Atmospheric Forcing of Decadal Climate Variability

William James Dow

Submitted in accordance with the requirements for the degree of Doctor of Philosophy

The University of Leeds
School of Earth and Environment

May 2023

UNIVERSITY OF LEEDS

Declaration of Authorship

The candidate confirms that the work submitted is his own, except where work which has formed part of jointly-authored publications has been included. The contribution of the candidate and the other authors to this work has been explicitly indicated below. The candidate confirms that appropriate credit has been given within the thesis where reference has been made to the work of others.

The first two results chapters form the basis for a paper that has already been peer reviewed and published. Content from the final results chapter is being prepared in a manuscript for submission to a suitable journal. The thesis contains an introductory chapter, a methods chapter, four results chapters, and a conclusions and recommendations chapter.

Work from the publication **Dow et al. (2021) The Effect of Anthropogenic Aerosols on the Aleutian Low**. *Journal of Climate*, *34*(5), 1725–1741. https://doi.org/10.1175/JCLI-D-20-0423.1 is included across chapters 3 and 4 of the thesis. The text was solely written by the candidate, with comments from co-authors. The candidate performed the data analysis and produced all the figures. A.C. Maycock contributed to the interpretation of the results. Model simulations were performed by the candidate (LUMA, FORTE 2.0), C.J. Smith (SOCRATES), and various members of the Precipitation Driver and Response Intercomparison Project (PDRMIP) group.

Acknowledgements

I would like to give a special thanks to my primary supervisor, Dr Amanda Maycock. Her guidance, insight, time, and professional and pastoral support have been of immense help to me throughout the PhD process, especially during the COVID-19 pandemic. 2020 and 2021 were especially challenging years, and without Amanda's great support, progress through the PhD would have been impossible.

I would like to thank my co-supervisors, Professor Piers Forster, and Dr Doug Smith. Piers was a great source of encouragement especially during the early stages of my PhD and at my first overseas workshop. Doug has been a great source of insight throughout my PhD, and I have really valued his constructive feedback and guidance whenever we have met.

A big thanks goes to Dr Marcus Lofverstrom, who provided great assistance in helping set up and coaching me in the use of the LUMA model. Similarly, a massive thanks must go to Professor Manoj Joshi and Dr Adam Blaker, who were always on hand to answer questions regarding the compilation and running of the FORTE 2.0 model and who were of further help answering questions about the source code during the development of my nudging code. I extend a further thanks to Dr Chris Smith, who assisted me by running simulations of the Met Office's SOCRATES model, the products of which I have used in chapter 4.

A huge thanks must go to Richard Rigby, who, especially during the COVID-19 pandemic, was always on hand and patient with me when I ran into

problems configuring the FORTE2.0 model on the Leeds system and any subsequent FORTRAN issues.

I have been lucky to be embedded within the PCC research group, and I'd like to thank all those who contributed feedback on my work over the years, as well as creating a positive working environment in which I felt comfortable.

Finally, to my family, especially my parents who have been an ever-present source of support and encouragement, and without whom this would not have been possible – thank you.

Abstract

There is an incomplete understanding of the processes influencing the Pacific Decadal Oscillation (PDO), including the role of anthropogenic forcing. It has been hypothesised that anthropogenic aerosol (AA) trends contributed to the transition of the PDO to its negative phase at the end of the 20th century. One proposed mechanism for this influence centres on the impact of AA on the strength of the Aleutian Low (AL), which precedes and modulates the PDO. This thesis seeks to improve our understanding of the role of AA emissions, and the associated teleconnection mechanisms, on the PDO.

The first stage of work analyses a multi-model dataset which includes idealised experiments of perturbations to sulphate and black carbon (BC) aerosols. It is found that global emissions of BC induce a robust weakening of the AL. This is primarily in response to BC from Asia; however, other regions contribute to the signal. The response is primarily governed by atmospheric adjustments, whereas the response to sulphates is less robust and more strongly mediated by sea surface temperature (SST) feedbacks. An idealised stationary wave model forced with instantaneous heating anomalies shows that the direct radiative effect of BC is a more important source of diabatic heating than anomalous latent heating, and that BC absorption can excite Rossby waves across the North Pacific, which supports the pathway elucidated from the multi-model analysis.

The second topic of work concerns the role of extratropical-tropical interactions on the PDO, building from the hypothesis that by inducing an anomalous AL, AA could perturb the entire Pacific basin. A nudged coupled

atmosphere-ocean model was developed and showed that an anomalous AL can produce sustained SST anomalies in the tropical Pacific that peak in boreal spring. This suggests a chain of processes which can connect AA emissions to decadal climate variability through the PDO.

Table of Contents

List of Abbreviations

(AO)GCM – (Atmosphere-Ocean) General Circulation Model

AA– Anthropogenic Aerosols

AL – Aleutian Low

AR5/AR6 – Assessment Report 5/6

BC – Black Carbon

CMIP5/6 – Fifth/Sixth Coupled Model Intercomparison Project

CO_2 – Carbon Dioxide

DJF – December, January, February

ENSO – El Niño-Southern Oscillation

EOF – Empirical Orthogonal Function

ERA5 – Fifth Generation ECMWF reanalysis data

ERF – Effective Radiative Forcing

FORTE 2.0 – Fast Ocean Rapid Troposphere 2.0

GHG(s) – Greenhouse Gas(es)

GMST – Global Mean Surface Temperature

IGCM4 – Intermediate General Circulation Model 4

IPCC – Intergovernmental Panel on Climate Change

IPO – Interdecadal Pacific Oscillation

IRF – Instantaneous Radiative Forcing

JJA – June, July, August

KE/KOE – Kuroshio (Oyashio) Extension

LR – Linear Regression

LUMA – Linear University Model of the Atmosphere

MAM – March, April, May

MLD – Mixed Layer Depth

MMM – Multi Model Mean

MOMA – Modular Ocean Model – Array

NAO – North Atlantic Oscillation

NDJFM – November, December, January, February, March

NPI – North Pacific Index

NPO – North Pacific Oscillation

PC – Principal Component

PDO – Pacific Decadal Oscillation

PDRMIP – Precipitation Driver Response Intercomparison Project

PDV – Pacific Decadal Variability

RWS – Rossby Wave Source

SFM – Seasonal Footprint Mechanism

SLP – Sea Level Pressure

SON – September, October, November

SST(A)(s) – Sea surface temperature(s) anomaly(-ies)

SSH – Sea surface height

TOA – top-of-atmosphere

WES – Wind-Evaporation-SST

Chapter 1 – Introduction

1.1 Motivation

The evolution of Earth's climate is determined by a complex interplay between the effects of external forcings and internal climate variability. The attribution of past changes in climate and the prediction of future behaviour is contingent on understanding the interplay between these factors on different spatial and temporal scales. In particular, internal climate variability can enhance or mask externally forced changes in climate on decadal timescales. A widely studied example is the period of a relatively weak trend in global surface temperature between the late 20th century and the first decade of the 21st century, which was attributed mainly to Pacific decadal variability (e.g. Watanabe et al., 2014; Meehl et al., 2013; Kosaka and Xie, 2013; Liu and Di Lorenzo, 2018). Therefore, developing a better understanding of the mechanisms that determine the nature of internal climate variability has the potential to improve our ability to skilfully predict the future state of the climate in the near and far term, which is of value to policy makers and other stakeholders (e.g. Mahmood et al., 2021; Meehl et al., 2009).

This thesis focuses on climate variability in the Pacific Ocean basin. Sea surface temperatures (SSTs) in the Pacific play a central role in the evolution of global and regional climate, for instance in determining the rate at which global mean surface temperature (GMST) changes (Meehl et al., 2016; Katjar et al., 2019), and teleconnections (a causal relationship between climate states in two remote regions) that originate in the Pacific and extend to almost all regions of the world (e.g. Amirudin et al., 2020; Yeh et al., 2018; Sprintall et al., 2020; Li et al., 2021). Decades of research has focussed on observing

and modelling the evolution of Pacific SSTs and patterns of spatiotemporal variability (e.g., Weare et al., 1976; Tourre et al., 1999, Guan et al., 2008). Developing a more complete understanding of the atmospheric and oceanic processes and mechanisms driving the evolution of SSTs across the Pacific continues to be an active area of research. For instance, recently, there has been great focus on global climate models' inability to accurately replicate the observed SST trends in the tropical Pacific Ocean over the recent past (e.g. Seager et al., 2021), which continues to be a concern given the strong influence of this region on large-scale climate, global ocean heat uptake and air-sea exchange of CO_2.

The characteristics of internal climate variability are frequently conceptualised via 'modes' of climate variability. The Pacific Decadal Oscillation (PDO) (Mantua & Hare, 2002) is defined as the leading mode of SST anomalies in the North Pacific over decadal timescales, usually isolated using Empirical Orthogonal Function (EOF) (or Principal Component, PC) analysis. The PDO is generally referred to as a component of wider Pacific Decadal Variability (PDV), which incorporates other modes such as the North Pacific Gyre Oscillation (NPGO) and the Southern Pacific Decadal Oscillation. The 'oscillation' implied by the name is more accurately described as an episodic change of sign, or phase.

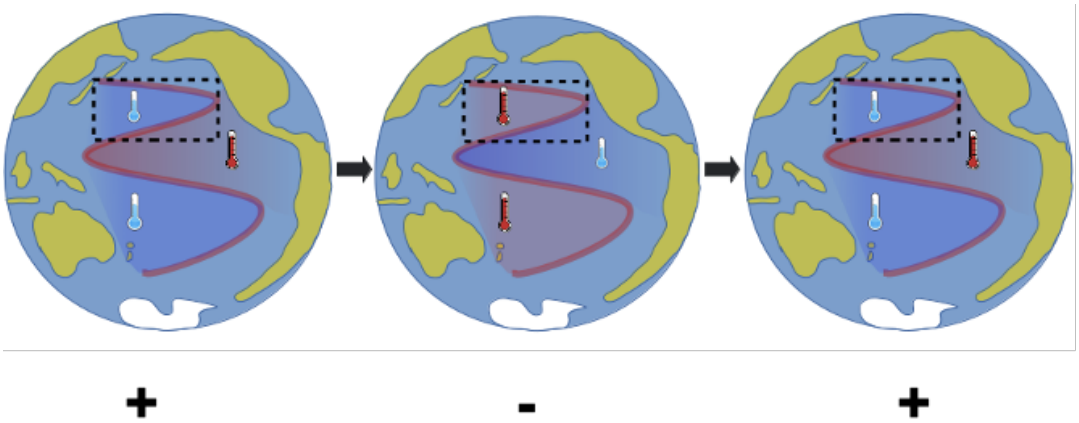

Figure 1.1 – Schematic representation of the spatial expression of the transition from a positive to negative to positive phase of the PDO. The black box represents the area in the North Pacific over which the PDO index is defined.

A positive PDO phase describes a surface ocean state as (relative to global means) warmer than average along the west coast of the Americas, and anomalously cool in the central North Pacific (Figure 1.1). Conversely, a negative PDO phase describes (relative to global means) a cooler surface ocean state along the west coast of the Americas, and anomalously warm in the central North Pacific. Furthermore, anomalously warm and cool surface ocean states across the tropical Pacific Ocean are associated with the positive and negative PDO states, respectively. The PDO has been demonstrated to play a key role in the evolution of global climate at decadal timescales (Trenberth, 2015). Over the last few decades, we have developed our understanding of the PDO: its climatic, ecological, and human impacts, and hypothesised the nature and magnitude of its controlling mechanisms (e.g. Mantua et al. 1997; Henson et al. 2006; Sen Roy, 2006; Newman et al. 2006; Ding et al. 2017). However, there remain substantial gaps in our understanding, for example, the degree to which external forcing agents may affect the modulation of the PDO. This uncertainty is illustrated when surveying the literature and is highlighted in studies such as Bonfils and

Santer (2011), Wu et al. (2011), Smith et al. (2016), Oudar et al. (2018), and Dittus et al. (2021). The increased abundance of observational data and improved modelling capabilities offer the opportunity to paint a more complete picture of the mechanisms driving the evolution of the PDO, whilst postulating the nature and timings of future phase changes under different future scenarios (e.g. Mochizuki et al. 2010; Li et al. 2019).

The aforementioned period marked by a slowdown (commonly referred to as a “hiatus”) in the rate of GMST increase (approx. 1998-2012) coincided with a change of phase of the PDO from positive to negative. This relationship has also been observed historically with previous changes in PDO phase (e.g. Mantua & Hare, 2001). The recent phase change has been a major focus as it coincided with increases in emissions of greenhouse gases (GHGs) and shifts in the pattern of anthropogenic aerosol (AA) emissions towards Asia with decreases in Europe and North America. The study by Smith et al. (2016) provided the initial motivation for this thesis in investigating the influence of atmospheric forcing on decadal climate variability. In the study, they focussed on the shift in PDO phase in the period 1998-2012 and challenged the prevailing view that the phase change was a consequence of internal climate variability (e.g. Meehl et al., 2001; Risbey et al., 2014). They showed that models contributing to the Fifth Coupled Model Intercomparison Project (CMIP5) robustly simulated a negative PDO phase change in response to AA forcing, implying a potential role for human influence and an interaction between external forcing and internal variability. The potential attribution of this phase change to AA has been supported by Takahashi and Watanabe (2016) and Dittus et al. (2021); however, a single model large initial condition ensemble study by Oudar et al. (2018) provided doubt to this view by

demonstrating that the CanESM2 ensemble members analysed by Smith et al. (2016) lay at the extreme end of a large spread when more ensemble members were analysed. Therefore, according to Oudar et al. (2018), the responses seen by Smith et al. (2016) were more likely to be 'spurious' model realisations rather than attributable to the effect of AA, which they found does not drive a negative PDO or slowdown in GMST trend. Ultimately, there is ongoing uncertainty about the effect of anthropogenic forcing on the PDO. Fundamental to this uncertainty is the poor understanding of how aerosol radiative forcing interacts with natural modes of climate variability (Verna et al. 2019).

The rationale for the work conducted in this thesis is to better understand the role of the atmospheric processes in driving coupled atmosphere-ocean changes in the Pacific that influence the PDO. To this end, the remainder of this chapter introduces the key concepts pertaining to this area of research, firstly introducing the climatic setting within which this thesis focuses – the Pacific ocean-atmosphere system. Then I will introduce climate variability, modes of climate variability (introducing the PDO), atmospheric and oceanic mechanisms affecting the PDO and the theoretical basis which underpins their behaviour, the relationship between different modes of climate variability, the forcing of the PDO (including introducing AA), ocean-atmospheric coupling and climate modelling and its utility and limitations.

1.2 Features of the Pacific ocean-atmosphere system

The Pacific Ocean is characterised by a number of features, for instance patterns of ocean circulation (ocean gyres) such as the North/South Pacific Gyre (also known as the Subtropical Gyre), the Subpolar Gyre, the Kuroshio

and Oyashio western boundary currents which converge into the Kuroshio-Oyashio Extention (KOE) extending eastwards across the North Pacific. In equatorial regions, the North and South Equatorial Currents straddle the Equatorial Countercurrent (see Figure 1.2 for a schematic representation of the gyres and currents). The surface gyres and currents manifest via the interaction between strong surface wind dragging the ocean surface and the Coriolis force induced by the Earth's rotation.

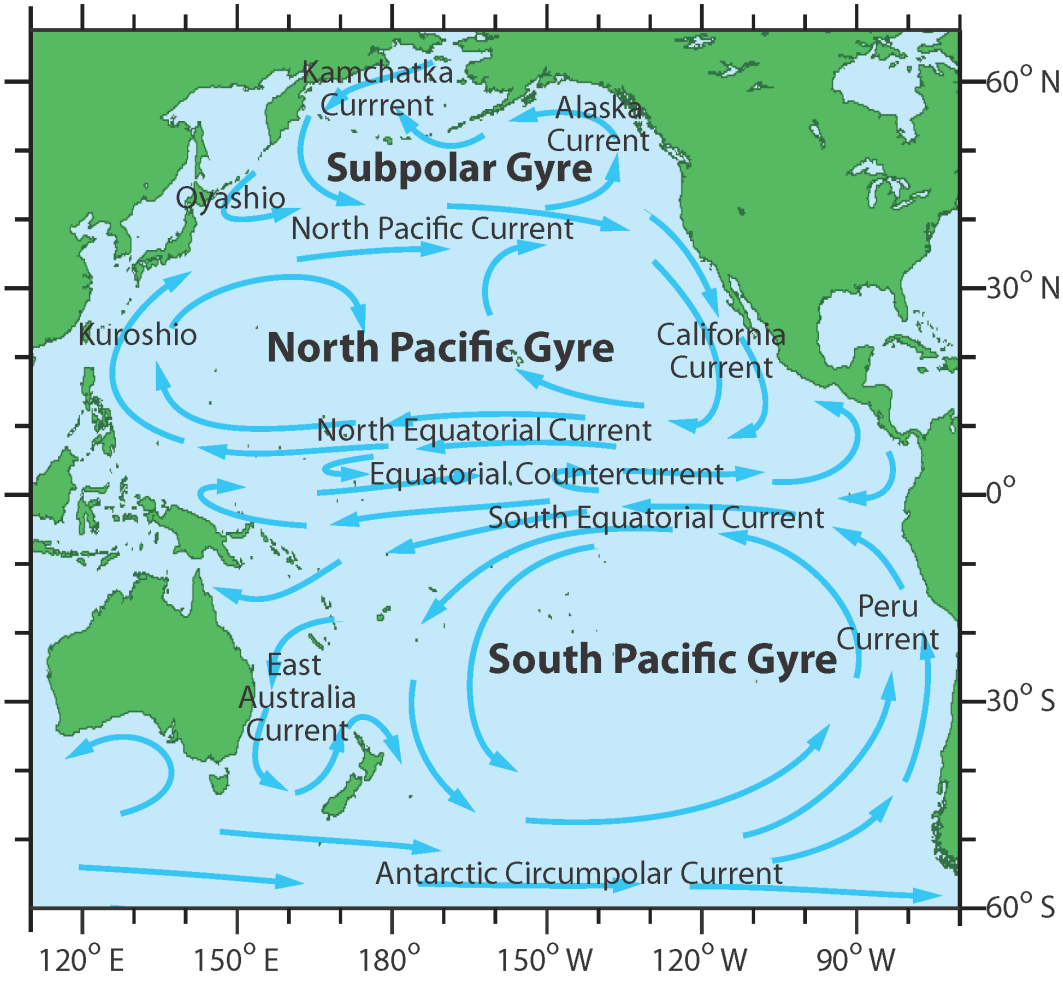

Figure 1.2: Schematic representation of the major features of ocean circulation in the Pacific basin. Taken from https://oceantracks.org/library/the-north-pacific-ocean/major-currents

Strong surface easterlies (known as the 'trades') flow along the equator as part of the lower branch of the Hadley cell. Variations in the strength of the

trade winds have been shown to influence the onset of El Niño-Southern Oscillation (ENSO) events (e.g. Philander, 1983). Cumulonimbus towers along with mesoscale convective systems (e.g. Saha et al. 2010) provide the mean ascent of the Hadley cell near the equator in the Inter-Tropical Convergence Zone (ITCZ), with air flowing poleward near the upper troposphere, terminating in the subtropical jet, and the subsiding limb of the cell, driven by radiative cooling, descending around 30^{o}N (see Figure 1.3). The circulation in the winter hemisphere is significantly stronger than the summer hemisphere (Nguyen et al. 2013). Figure 1.3 also shows extra-tropical baroclinic eddies, along with the eddy-driven polar jet make up the so-called polar front, which marks the position of the storm track and whose variability is related to the annular modes (Limpasuvan and Hartmann, 2000).

The Walker circulation is the major thermally-induced zonal circulation in the tropics, situated along the equator, where the lower branch flows from east to west and the upper branch from west to east (Figure 1.4). The rising branches coincide, in the western equatorial Pacific, with areas of maximum precipitation and its existence is owed to the sea surface temperature (SST) gradient created by the trade winds. The trade winds continually push water from east to west, moving relatively warmer water further west whilst inducing upwelling of cooler water in the east. The result is the Pacific Warm Pool in the western equatorial Pacific. The position of the upwelling and downwelling branch of the Walker cell is associated with El Niño and La Niña conditions (e.g. Lau and Nath, 2000).

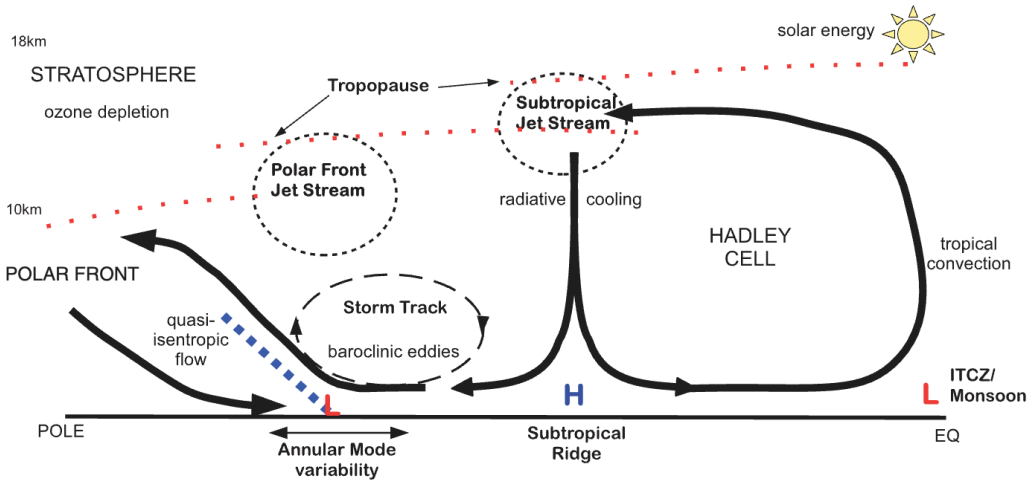

Figure 1.3: Schematic diagram detailing the components and physical processes of the mean meridional circulation. Diagram represents the hemispheric annual and zonal-mean flow. Taken from Lucas et al. (2014).

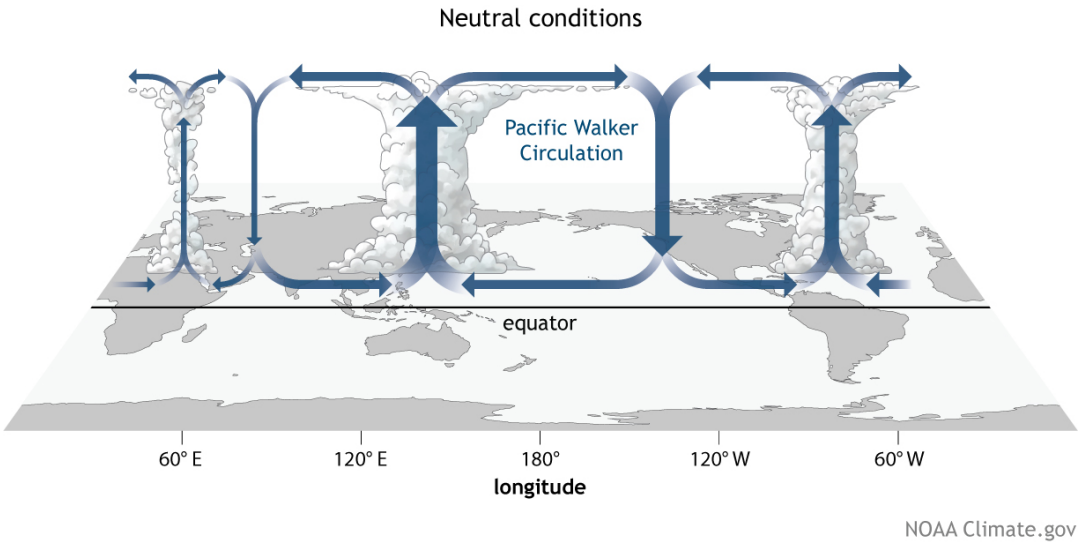

Figure 1.4: Schematic representation of the Pacific Walker cell circulation during ENSO neutral conditions. Taken from https://www.climate.gov/media/13542

1.3 Climate variability

The Earth is a highly complex system comprising a large variety of interacting components. The atmosphere, cryosphere, land, and oceans exchange energy, moisture and momentum across all time scales. As a result,

we observe fluctuations in global or regional climate variables, which have important impacts on human activities and ecosystems. Variations in the mean state of climatic variables on all temporal and spatial scales (beyond individual weather events) is referred to as climate variability (WMO, 2022). Climate variability is the result of either; internal processes involving interactions between different components of the earth system and/or external forcing mechanisms from independent environmental changes (for example, anthropogenic activity, volcanic activity, solar cycles). Accurately detecting and attributing the role of each remains a challenge and an active area of research (e.g. Imbers et al. 2014).

Evidence of climate variability is seen both directly from instrumental datasets and indirectly by historical and proxy datasets (e.g. Hernández et al. 2020; L'Heureux et al. 2013; Osterberg et al. 2014). Instrumental datasets, available to an increasing extent in the last couple of centuries, include data from sources such as aircraft, surface station measurements and satellites (Ghil and Lucarini, 2020). Climate proxies, which are biological, chemical or physical characteristics of the distant past that have been preserved in natural repositories, can be correlated with the state of the atmosphere, cryosphere or ocean at that time. Examples of proxies include ice-cores and marine sediment records, in better understanding the Quaternary Period (e.g. Hodgson et al. 2005), and tree-rings, coral records and geomorphic phenomena for the last few millennia (Geladof and Mantua 2002). The challenges of working with proxy data include its spatiotemporal heterogeneity as well as statistically combining the data with more recent instrumental data.

1.3.1 Modes of climate variability

Climate variability can follow distinctive patterns over a wide range of spatial and temporal scales, which are referred to as ‘modes’ of climate variability (Stephenson et al. 2004). A major focus of climate science research is on better understanding the behaviour of these global modes and the mechanisms contributing towards their evolution. Global modes, which include El Niño-Southern Oscillation (ENSO), the PDO, the North Atlantic Oscillation (NAO) and the Atlantic Multidecadal Oscillation (AMO) encapsulate multiple processes that govern their evolution over time, making it difficult to develop complete theories for their existence and evolution. Better understanding of the behaviour of the modes of climate variability will improve our ability to predict near-term global climate. This is of great importance for the scientific community and broader society, in providing more robust climate projections on which planning and policy decisions can be made.

While commonly identified by their unique statistical properties, modes of variability attempt to capture physical structures of variability, and though not exactly periodic (sometimes described as *quasi-periodic*), they are oscillatory in nature. The dominant periodicities of such modes are often difficult to identify as spectral peaks in instrumental observations (Liu and Di Lorenzo, 2018). Modes of climate variability are often tracked using climate indices, which are scalar values describing the magnitude of the mode at any given time. Statistical methods such as Empirical Orthogonal Function (EOF) analysis (Hannachi et al., 2006) can be utilised to derive such indices and the associated spatial patterns. Other simpler methods, such as area-weighted averages (e.g. North Pacific Indices, NPI) and the difference between fixed meteorological stations (NAO indices) are also employed to calculate indices.

On interannual timescales, the dominant mode of variability in the tropical Pacific is the ENSO, oscillating with a periodicity of between 2-7 years. The positive (warm) phase (El Niño) is characterised by a warming of SSTs in the central-eastern Pacific, peaking during boreal winter and is associated with a wide array of localised effects such as: reduced precipitation over northern Brazil and south-eastern Africa and warmer winters over areas of northern USA and colder winters in the southwest and south-eastern regions. The negative (cool) phase (La Niña) is characterised by episodes of cooler than average SSTs in the equatorial Pacific. La Niña conditions tend to be associated with the opposite tendencies which characterise localised effects of El Niño. Neutral years describe periods when SSTs are close to (within +/- 0.5^{o}C) the long term average.

On decadal timescales, climate variability can arise from internal interactions within the climate system and in combination with external forcing agents such as GHG's, volcanic forcing and AA's. The combination of internal variability and external forcing can act to amplify or diminish the impact of the forcing agent. Furthermore, decadal climate variability impacts the background state upon which, for example, modes of interannual variability occur and can thus affect their expression. The quasi-stochastic nature of the higher frequency variability may express itself as variability on decadal time scales.

Pertinent to this thesis are the modes of variability that encapsulate, what is referred to in the literature as PDV (e.g. Dong et al., 2014; Wang et al., 2012; Liu and Di Lorenzo, 2018), with particular emphasis on the PDO and the Aleutian Low, which are introduced next.

1.3.1.1 Aleutian Low

The Aleutian Low (AL) is a quasi-stationary trough located near the Aleutian Islands mainly during boreal winter. Its intensity can be represented by the North Pacific Index (NPI, Figure 1.5), defined as the area-weighted average of extended boreal wintertime (November, December, January, February, March (NDJFM)) sea level pressure (SLP) over the region bounded by 30°-65°N and 160°E-140°W (Trenberth & Hurrell, 1994). Positive NPI values describe a weaker AL and negative NPI values describe a stronger AL. The AL is associated with powerful extratropical cyclones (Rodionov et al. 2004) and also links closely with upper-level teleconnections such as the Pacific/North-American (PNA) pattern (Trenberth and Hurrell, 2004) and Arctic Oscillation (AO) - dominant modes of atmospheric circulation. The AL has a major effect on the North Pacific and North American continental winter climate, and the associated wind-stress and thermal forcing (e.g. Seager et al. 2001; Kwon and Deser, 2007) has an impact on fish stocks in the northeast Pacific (e.g. Chavez et al. 2003; Lehodey et al. 2006).

As well as having an impact on North Pacific weather and ecosystems on interannual timescales, the AL also shows variability in its intensity, latitudinal and longitudinal position on decadal and interdecadal timescales (Overland et al, 1999; Sugimoto and Hanawa, 2008) and plays a role in the evolution of the PDO (e.g. Newman et al. 2016; Schneider and Cornuelle, 2005). The evolution of the AL over longer historical time periods and the future under climate change has been the focus of recent research. Deser and Phillips (2009) found intensification in the AL during the second half of the twentieth century to be primarily attributable to changes in SST (particularly in the tropics). Drawing upon paleoproxies, studies using ice-cores from Alaska

and Yukon have been able to deduce that intensification of the AL began as far back as the mid 18th century and is unprecedented over the last 1200 years (Osterberg et al. 2017).

Studies such as Gan et al. (2017) and Choi et al. (2020) show a further deepening of the AL is to be expected as a result of future global warming. Giamalaki et al. (2021) investigated the response of the AL under the RCP8.5 future scenario and found that AL extremes become more frequent and persistent. These extreme events were associated with changes in precipitation and temperatures over north America, as well as changes to SST and heat fluxes in the Kuroshio extension region.

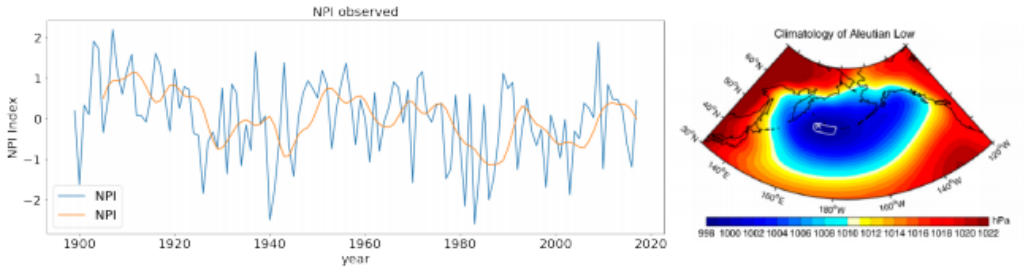

Figure 1.5 (Left) – NDJFM NPI (anomalies) standardized. Data provided by the Climate Analysis Section, NCAR, Trenberth and Hurrell (1994). Smooth orange line is a centred Gaussian weighted running average. (Right, taken from Gan et al. (2017)) Climatological-mean of boreal winter SLP from 1950-1999 based on reanalysis data. Cross marks the minimum SLP of 998.0 hPa and solid contour denotes the 999.0 hPa isobar.

1.3.1.2 Pacific Decadal Oscillation (PDO)

The PDO is the leading mode of Pacific decadal climate variability. The PDO can be defined (Mantua & Hare, 2002; Nidheesh et al., 2017) as the leading EOF of monthly SST anomalies over the North Pacific (110°E-110°W; 20°N-60°N), explaining around a quarter of the observed SST variance in this region (Trenberth et al., 2014) (Figure 1.6). It also accounts for the first mode

of sea-surface height (SSH) variability (Chhak et at., 2009). In addition to the PDO, the literature also describes the Interdecadal Pacific Oscillation (IPO) (McGregor., 2017; Kajtar et al. 2018; Liu & Di Lorenzo, 2018; Soon-Il An, 2018), which essentially displays the same interdecadal variability as the PDO but accounts for a wider signature of SST across the Pacific basin including into the Southern hemisphere. It is important to note the PDO and IPO are not considered to be independent modes; it has been argued that the IPO comprises of the PDO and the AMO (and to a much lesser degree ENSO) in various proportions depending on strength of the low-pass filter applied to the defining PC (Chen & Tung, 2017; Tung et al., 2018).

Figure 1.6, taken from Trenberth et al. (2014), shows the PDO as defined by EOF analysis of SST anomalies with the global mean removed from 1900 to 2012 in 20^{o}-70^{o}N, 110^{o}E-100^{o}W. The map shows that regression of the PC time series on global sea and land surface temperature anomalies also exhibits variance away from the North Pacific region. The structure of the variability across the Pacific and Atlantic basins closely represents that of the IPO (see Figure 3 in Tung et al, 2018), suggesting a significant contribution of the PDO to the IPO. Using the PDO index of Mantua et al. (1997), the correlation between the two has been shown to be very high ($r = 0.95$) (Tung et al, 2018).

A positive or “warm” PDO phase describes a surface ocean state as (relative to global means) warmer than average along the west coast of the Americas, and anomalously cool in the central North Pacific. Other characteristics of a positive PDO phase include lower SLP over the North Pacific, and higher SLP over the northern subtropical Pacific, and vice versa

for the cold phase. Observations of the PDO from instrumental data date back to 1854 (Mantua & Hare, 2002), and regime/phase shifts prior to 2013 have been identified circa 1925, 1947 and 1977, hence giving the PDO an estimated periodicity of around 50 years. It must be noted that estimating the periodicity based on the observational record further back in the historical record, due to fewer observational measurements, and estimates based on proxy data, must be done with caution. For example, MacDonald and Case (2005) highlight a significant absence of variability of periodicity within the 50-100 year range between 1600 and 1800 AD. Nevertheless, more recent phase shifts have been shown to correlate with ecological effects such as salmon production in the northwest US and Alaska (Mantua et al. 1997). Positive PDO phases are associated with positive air temperature anomalies and a deficit in precipitation in central and north-western US, and negative air temperature anomalies and an excess of precipitation in the southwestern US and northern Mexico. Additionally, according to Barlow et al. (2001), the PDO is in part, responsible for the long-term summertime drought events evident in the US over the last century.

Furthermore, like ENSO, the PDO can induce widespread global impacts (Wei et al., 2017). Examples include a proposed link between the PDO and decadal variability in the East Asian summer monsoon (EASM) (Dong and Xue, 2016). Additionally, the worst drought conditions in North China since the late 1970s have been reportedly connected to the PDO (Ma, 2007).

It is these global impacts (both climatic and ecological) which motivate research into the PDO, its driving mechanisms and its relationship to anthropogenic activity. In response to future climate change, Zhang and

Delworth (2015) show that the amplitude and duration of PDO phases is modulated - the periodicity becoming shorter and amplitude weaker as a result of global warming. Studies by d'Orgueville and Peltier (2009) and Fang et al. (2014) also show a weakening and increase in frequency of the PDO in a warmer world.

Whilst not the focus of my research, there exists an analogous mode of decadal variability across the South Pacific, known as the Southern PDO (or SPDO) - defined as the first EOF of SST anomalies poleward of 20^{o}S. Like the PDO, the SPDO integrates multi-decadal fluctuations of atmospheric forcing with contributions from internal variability of atmospheric circulation, tropical teleconnections, and annular modes. The PDO and SPDO are correlated at R = 0.46 (Liu and Di Lorenzo, 2018). There is coherence of decadal variability across the entire Pacific, as encapsulated in the IPO.

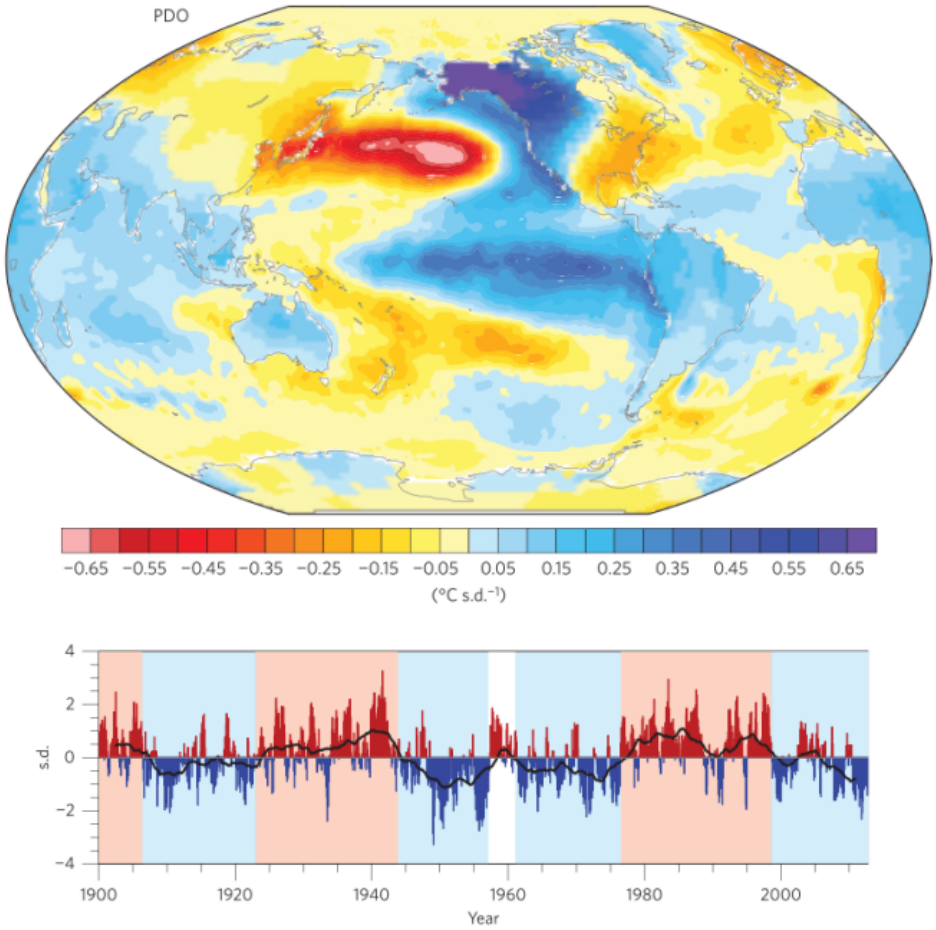

Figure 1.6: (Top) Spatial pattern of SST anomalies associated with the PDO. Calculated from the first EOF of SSTs in 20° - 70°N, 110°E, 100°W over the period 1900 to 2012 with global mean removed (25% variance explained). Global sea and land surface temperature anomalies are regressed on the PC time series to produce the map. (Bottom) PC timeseries of the PDO index. Black curve is a 61-month running average. The light red and blue colours depict the positive and negative phases of the PDO. Note the reversal of the colour key in the top panel so that blue colours are positive, and hence the current negative phase has below-normal SSTs in the blue areas. Here, s.d. is standard deviation. Taken from Trenberth et al. (2014).

1.3.1.3 Kuroshio Oyashio Extension

The Kuroshio Oyashio Extension (KOE) is a major component of North Pacific climate variability, characterised by decadal fluctuations of SST and SSH (e.g. Joh et al. 2021). It is a zonally-oriented SST and SSH frontal zone in the western North Pacific formed by the convergence of the Kuroshio and

Oyashio western boundary currents, extending from the coast of Japan near 35^{o}N, 140^{o}E, and associated with strong eastward surface currents which form the boundary of the subpolar and subtropical ocean gyres (Nonaka et al., 2005; Qiu 2002). It is observed as a meandering zonal jet accompanied by large-amplitude meanders and pinched-off eddies.

The KOE region exhibits two primary modes of SSH variability, associated with the decadal shift in the axis (KOE-meridional-mode) and the decadal modulation of the strength (KOE-zonal-mode). Atmospheric variability in the central and eastern North Pacific is considered as the drivers of these modes, driving large-scale oceanic Rossby waves westward (Taguchi et al., 2007). Over a period of around 2.5-4 years, the SSH anomalies associated with fluctuations to the AL/PDO propagate westward to modulate the KOE-meridional-mode, whereas changes to the North Pacific Oscillation (NPO)/NPGO modulate the KOE-zonal-mode (Kwon and Deser 2007).

1.4 Mechanisms affecting the PDO

Identifying the mechanisms that control the spatiotemporal evolution of the PDO is an active topic of research. The current view is that the PDO is a convolution of multiple mechanisms (Newman et al., 2016). Newman et al. (2016) detail how three groups of processes most likely explain the nature of the PDO: first, are processes related to the atmospheric bridge. The atmospheric bridge describes the connection between tropical Pacific and North Pacific SSTs.

According to Nidheesh et al. (2017) the chain of processes commences with warm SSTs in the equatorial Pacific causing enhanced rainfall and associated diabatic heating. The resulting upper tropospheric divergence

forces atmospheric Rossby waves toward the North Pacific (Trenberth et al., 1998), which causes the AL to strengthen. The subsequent increase in surface heat fluxes and advection by Ekman transport combine to drive ENSO-related cooling in the North Pacific. Herein lies a prevailing view that the PDO can be thought of a reddened response to changes in ENSO behaviour (Newman et al., 2016) and a body of research investigates the correlation and causation relationship of both phenomena (Nidheesh et al., 2017; Wei et al., 2018; Liu & Di Lorenzo, 2018).

Lead/lag statistical analysis is commonly employed to investigate how different climate modes interact with each other. Through this methodology, one can test whether modes demonstrate a precursory nature and over what time scales one impacts the other. For example, it has been observed that models participating in the CMIP5 tend to overestimate the time lag between ENSO and the PDO, which when accounted for exhibit maximum correlations between the respective indices of above 0.5 in the more reliable models (Nidheesh et al., 2017).

In addition to ENSO and the forcing of the PDO attributed to atmospheric white noise, the midlatitude re-emergence mechanism is thought to play a significant role in the evolution of the PDO. The changing year-round thermocline depth and thermal inertia of the ocean allows persistence of temperature anomalies from one winter to the next. These three mechanisms, when integrated into an auto-regressive model by Newman et al. (2003), were able to reproduce the PDO time series with an average correlation of 0.7 in the more reliable CMIP5 models (models which demonstrate a maximum lag

correlation between the ENSO and PDO indices of >0.5) and implied that these were the dominant mechanisms in describing the evolution of the PDO.

As mentioned in Section 1.3.1.3, decadal changes in the KOE system - forced by winds over the North Pacific driving westward-propagating oceanic Rossby waves, which manifest SST anomalies along the subarctic front in the western Pacific Ocean - has also been suggested as a contributor to the observed PDO (Qiu 2003; Joh & Di Lorenzo 2019; Zhao et al. 2021).

In summary, the PDO represents a combination of multiple processes, summarised by the schematic in Figure 1.7, acting over different time scales. In many cases in the literature, the PDO is posited as the cause of global impacts - this must be taken with caution in case they represent merely a correlational relationship. Hence, convincing arguments need to be put forward in establishing the PDO as a driving mechanism for non-oceanic responses.

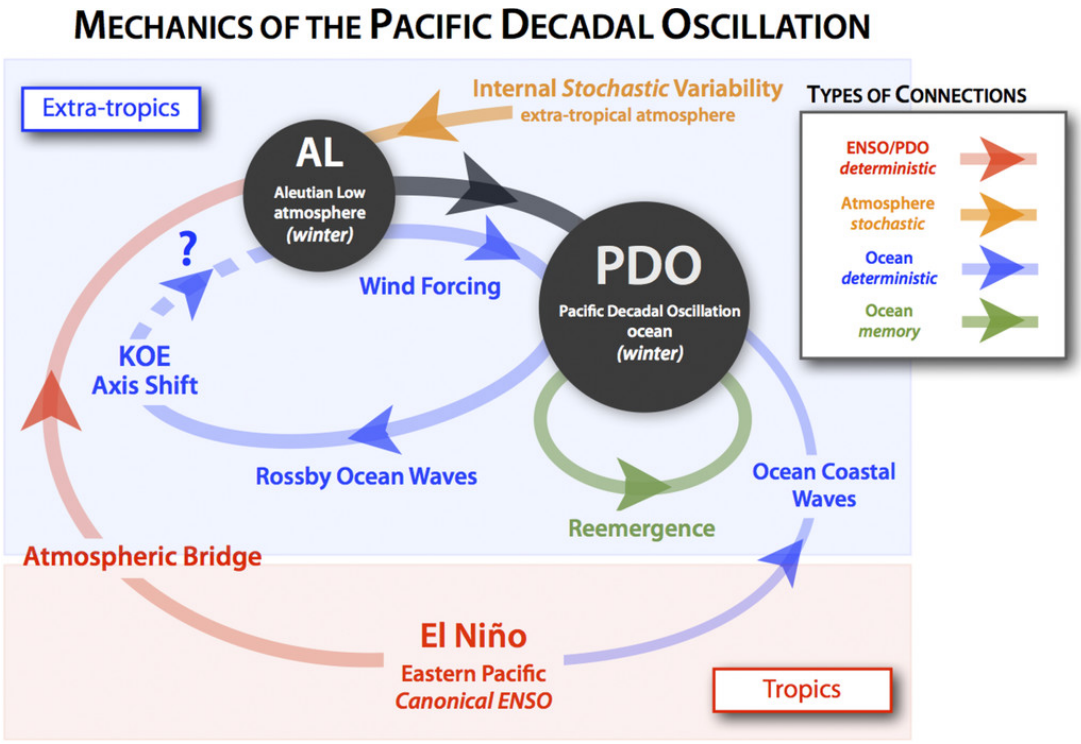

Figure 1.7 – Summary of the main processes involved in the PDO (Newman et al. 2016)

1.4.1 Atmospheric teleconnections

The term teleconnection is used to describe instantaneous or lagged relationships in climate variability and atmospheric circulation between geographically remote regions. Teleconnections are common, Trenberth et al. (1998) found 13 distinct teleconnection patterns in the northern hemisphere extratropics throughout the year, whereas in the southern hemisphere, only two have been identified (Mo, 2000). Teleconnections transport energy and momentum in an effort to restore imbalances in the energy budget of the climate system resulting from the heterogeneity in meridional distribution of solar insolation, SST anomalies associated with ENSO and internal variability of the climate system associated with midlatitude storms and ocean gyre circulations. As such, there has been a plethora of research that focuses on global teleconnections associated with ENSO and the AL (e.g Sen Roy, 2006; Alexander et al. 2002; Gan et al. 2017; Dong et al. 2018; Sprintall et al. 2020).

Interannual variation of the AL during boreal winter has been shown to have a close relationship with the Australian summer monsoon (Zhu and Wang, 2009). Choi and Cha (2017) demonstrated a link between summer tropical cyclone activity over the tropical western Pacific and variation in the preceding winter AL. Additionally, teleconnections of the AL have also been found as far away as the Mediterranean, where a deepening of the AL has been demonstrated to cause a cooling in SSTs a few days later (Li, 2006).

Upper-level divergence in the tropics, the interaction of the vorticity gradient and divergent flow and midlatitude barotropic and baroclinic instabilities are key mechanisms for generating poleward propagating Rossby wave trains that lead to teleconnections (Stan et al. 2017). Wallace and Gutzler (1981) identified the PNA pattern and noticed that teleconnections of SLP anomalies of opposite sign were predominantly between mid and high latitudes (e.g. NAO), while in the mid/upper troposphere the patterns had a more wavelike appearance and equivalent barotropic vertical structure. The PNA is of particular interest, as it arches from the tropical Pacific across North America and is a good example of a wave train, prominent during boreal winter, which is sensitive to tropical SSTs (e.g. Trenberth and Hoar, 1996; Straus & Shukla, 2002; Zhang et al. 2018). Here, in response to ENSO, the AL strengthens over the North Pacific, warm temperatures and high pressures develop over western Canada and there is an enhancement of precipitation along the west coast of the US during boreal winter. Teleconnections vary in the timeframe over which they affect regional climates, with the majority either prominent over either intraseasonal, inter-annual or decadal timescales (Esbensen, 1984; Liu and Alexander, 2007; Stan et al. 2017).

In addition to tropical-extratropical linkages, teleconnections can also facilitate communication from the mid and high latitudes to the tropics. Several hypotheses for PDV involve these teleconnections, either through the low-latitude portion of midlatitude atmospheric anomalies (e.g. Barnett et al., 1999, Vimont et al., 2001) or via the shallow subtropical cell in the ocean (e.g. Gu and Philander, 1997).

1.4.1.1 Rossby wave theory

Rossby waves (also known as planetary waves, Rossby et al., 1939), naturally occur in rotating fluids and are the most prominent waves in the atmosphere and ocean on large scales. On Earth, these waves form as a result of the rotation of the planet and variation in the Coriolis parameter, known as the β-effect. In a baroclinic atmosphere, a Rossby wave is a potential vorticity conserving motion that owes its existence to isentropic gradients of potential vorticity. In addition to latitude, topography is another source of a potential vorticity gradient. If a fluid parcel is displaced, its relative vorticity will change, creating a velocity field that displaces neighbouring parcels, whose relative vorticity changes and so on.

Rossby waves can be described mathematically using quasi-geostrophic theory, where the relevant equation of motion is the inviscid, adiabatic potential vorticity equation:

$$\frac{\delta q}{\delta t} + u.\nabla q = 0 \qquad \textit{Equation 1.1}$$

Where *q(x,y,z,t)* is the potential vorticity and ***u****(x,y,z,t)* is the horizontal velocity. The velocity is in turn related to a streamfunction by $u = -\delta\psi/\delta y$, $v = \delta\psi/\delta x$, and the potential vorticity is a function of the streamfunction. Linearising Equation 1.1 assuming small-amplitude motions on a steady, zonally-uniform basic state and neglecting terms involving products of primed (perturbed) quantities, the equation of motion can be expressed as:

$$\frac{\delta q'}{\delta t} + U\frac{\delta q'}{\delta x} + v'\frac{\delta \bar{q}}{\delta y} = 0 \qquad \textit{Equation 1.2}$$

Where U ≡ u. The particular dynamics of a Rossby wave are determined by the relationship between the wavevector and its frequency (known as the dispersion relation). Along with the group velocity (the velocity at which a fluid parcel of a group of waves will travel) and the phase speed (the speed at which the wave crests move), these Rossby wave characteristics, in a stratified quasi-geostrophic flow, can be described as:

$$\omega = Uk - \frac{\beta k}{k^2 + l^2 + m^2 f_0^2/N^2} \qquad \textit{Equation 1.3}$$

Where ω is the wave frequency, *U* is the zonal mean flow, *k, l* and *m* are the x-, y- and z- wavenumbers, f_0 is the Coriolis parameter and N^2 is a partial derivative of the vertical advection term, also known as the Brunt-Väisälä frequency.

It follows from Equation 1.3 that the group velocity of Rossby waves can be described as:

$$c_g^x = \frac{d\omega}{dk} = U + \frac{\beta[k^2 - \left(l^2 + \frac{m^2 f_0^2}{N^2}\right)]}{(k^2 + l^2 + m^2 f_0^2/N^2)^2} \qquad \textit{Equation 1.4}$$

$$c_g^y = \frac{d\omega}{dl} = \frac{2\beta kl}{(k^2 + l^2 + m^2 f_0^2/N^2)^2} \qquad \textit{Equation 1.5}$$

The group velocity is westward if the zonal wavenumber is sufficiently small, and eastward if the zonal wavenumber is sufficiently large.

In the ocean, Rossby waves play a critical role in the transient adjustment of ocean circulation to changes in large-scale atmospheric forcing and can effectively be coupled to the overlying atmosphere. Their effect on the vertical position of the thermocline facilitates convective processes at the surface and heat exchange and thus play a part in the coupling of the ocean to the atmosphere. As an example of their effect on global climate, Kirtman (1997) showed that the reflection of oceanic Rossby waves off the western boundary are required to explain the oscillation of ENSO cycles.

Furthermore, oceanic Rossby waves that develop along the subtropical gyres (e.g. in the North Pacific) are drivers of the rainfall oscillation on interannual to decadal timescales (Pinault 2012; Pinault 2018a) and therefore have a significant climate impact. Additionally, on a multi-decadal timescale, variability of the Atlantic Multidecadal Oscillation (AMO) is linked to the 64-

year-period Rossby wave winding around the North Atlantic gyre (Pinault, 2018b).

1.5 Relationship between the PDO and Aleutian Low

Schneider & Cornuelle (2005) demonstrated that the PDO can be recovered from a first-order auto-regressive model and forcing by variability of the AL (as well as ENSO and oceanic zonal advection anomalies in the Kuroshio-Oyashio Extension (KOE)). White noise forcing associated with large-scale weather patterns, such as the AL, generates much of the observed SST variability over the North Pacific (Frankingoul and Reynolds 1983). In this region interannual variability in SSTs and surface fluxes are closely linked to atmospheric circulation patterns (Cayan 1992; Iwasaka and Wallace 1995). A strong AL is associated with enhanced wind speeds and reduced air temperature and humidity along approximately 35^{o}N, which acts to cool the surface ocean via anomalous latent and sensible surface heat fluxes. In tandem, northward advection of warm moist air heats the upper ocean near North America, resulting in an SST pattern that resembles the PDO. In the case of a weak AL, the opposite fluxes are expected. Alexander and Scott (2008) show that Ekman transport tends to amplify this surface flux-driven pattern. Deser and Timlin (1997) highlight how these physical processes result in correlations in which atmospheric variability generally leads changes to SSTs in the North Pacific. Correlations between the NPI and PDO show that changes to the NPI both lead and are simultaneous to changes in PDO (Smith et al., 2016; Newman et al., 2016), suggesting a lagged ocean response and a precursory nature of the AL. However, identifying a causal role for the AL over relatively short timescales may be hampered by the large variability in

the extratropical atmospheric circulation (Xie et al., 2015). Hence, the AL is considered to govern, at least in part, the behaviour of the PDO.

1.6 External forcing of Pacific Decadal Variability

1.6.1 Aerosols

Atmospheric aerosols are solid, liquid or mixed particles with variable chemical composition and size distribution, suspended in the atmosphere (Myhre et al., 2013). Aerosols have manifold sources and formation mechanisms; however, they can be characterised as either ‘primary’ aerosols - emitted directly to the atmosphere - or ‘secondary’ aerosols produced in the atmosphere from precursor gases. Volcanic aerosols, mineral dust and sea spray constitute the inorganic primary aerosols, with atmospheric lifetimes of only a few days (Andreae, 2007), whilst biomass burning, combustion processes and plant materials make up carbonaceous primary aerosols, including organic carbon and black carbon (BC). Condensation of precursor gases onto pre-existing particles, or the nucleation of new particles, make up secondary aerosols, with a considerable mass forming through cloud processing (Ervens et al. 2011). The main components of secondary aerosols are sulphate, nitrate and organic carbon and originate from fossil fuel combustion, biogenic emissions, fires and other volatile organic compounds. Through condensation, coagulation, the uptake of water and other chemical reactions, aerosols evolve over time in the atmosphere and their numerous sources and compositions make quantifying their effects on the atmosphere difficult.

The burden of tropospheric aerosols has increased since preindustrial times due to anthropogenic activities (Bond et al., 2007; Smith et al., 2004). Even though aerosols represent a marginal fraction of the atmospheric mass, they play an important role in our climate because they are radiatively active species that interact with solar and infrared radiation.

Aerosols affect climate in different ways. The radiative forcing (the instantaneous change in energy flux caused by natural or anthropogenic drivers of climate change) from aerosol-radiation interactions (RFari in IPCC AR5, Randall et al. 2013) encompasses radiative effects from AA before any adjustment takes place and has been formerly referred to as the direct effect. This primarily results from scattering or absorption of solar radiation. The effective radiative forcing (ERF) is a measure of the total radiative forcing including rapid adjustments. As stated in IPCC WG1 AR6 (Szopa et al., 2021), aerosols contributed an ERF of -1.3 Wm^{-2} with a 90% range of certainty between -2 and -0.6 Wm^{-2} over the industrial era (1750-2014). This can be compared with the ERF from greenhouse gases and their precursors, which contribute 3.84 (90% range: 3.46 to 4.22) Wm^{-2}. The total anthropogenic ERF from 1750 to 2019 was 2.72 (90% range: 1.96 - 3.48] W m^{-2}. This estimate has increased by 0.43 W m^{-2} compared to IPCC AR5 estimates for 1750–2011 due to an increase in the GHG ERF that is partly compensated by a more negative aerosol ERF compared to AR5.

Rapid adjustments are modifications to the atmosphere and land system that occur prior to more slowly evolving changes in SSTs (Forster et al., 2016). Rapid adjustments to aerosol perturbations (indirect alterations to the global energy budget via changes to internal energy flow) include changes in the

surface energy budget, cloudiness and atmospheric profile; this contribution to the aerosol effective radiative forcing (ERFari) was previously known as the semi-direct effect. Interactions between aerosols and clouds (ERFaci), previously defined as indirect effects, can be split into either the instantaneous effect on cloud albedo due to changing concentrations of cloud condensation nucleii (RFaci) or the subsequent rapid adjustments to the cloud lifetime and thermodynamics.

Work by Zelinka et al. (2014) described and quantified the relative contributions of components of aerosol-radiation (ari) and aerosol-cloud interactions (aci) and concluded that 25% and 75% of total ERF (including ari + aci) comes from ERFari and ERFaci, respectively. This can be seen spatially by the comparison between panels a, b and c in Figure 1.8, and in the box plot in Figure 1.9. Furthermore, it is worth noting that in south-east Asia, particularly over the South China Sea, the largest magnitude ERFaci forcing is found, in the region and downstream of the largest emission sources.

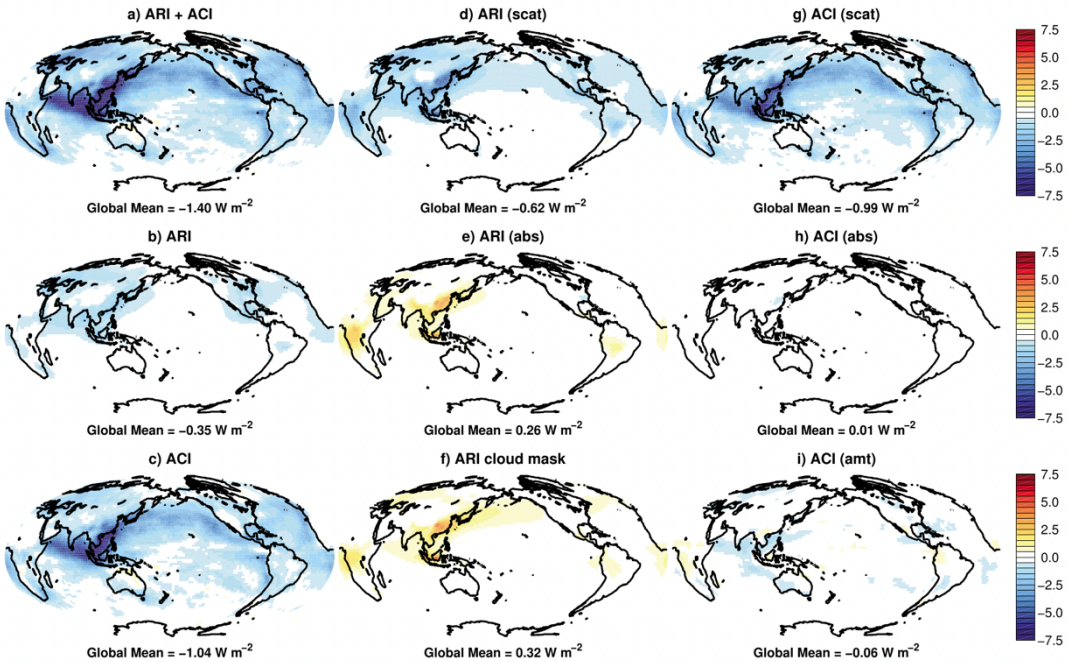

Figure 1.8: Taken from Figure 2 Zelinka et al. (2014) - (a) Ensemble mean SW ERF from their All-Aerosol run and its separation into (b) aci and (c) ari. ERFari is then separated into its (d) scattering and (e) and absorption components, and ERFaci is further separated into its cloud (g) scattering, (h) absorption, and (i) amount components. The ERFari (mask) term shown in panel f measures the effect of the presence of clouds on the ERFari, with positive values indicating that ERFari is less negative owing to the presence of clouds. The sum of panels b and c equals panel a. The sum of panels d and e equals panel b. The sum of panels g–i equals panel c.

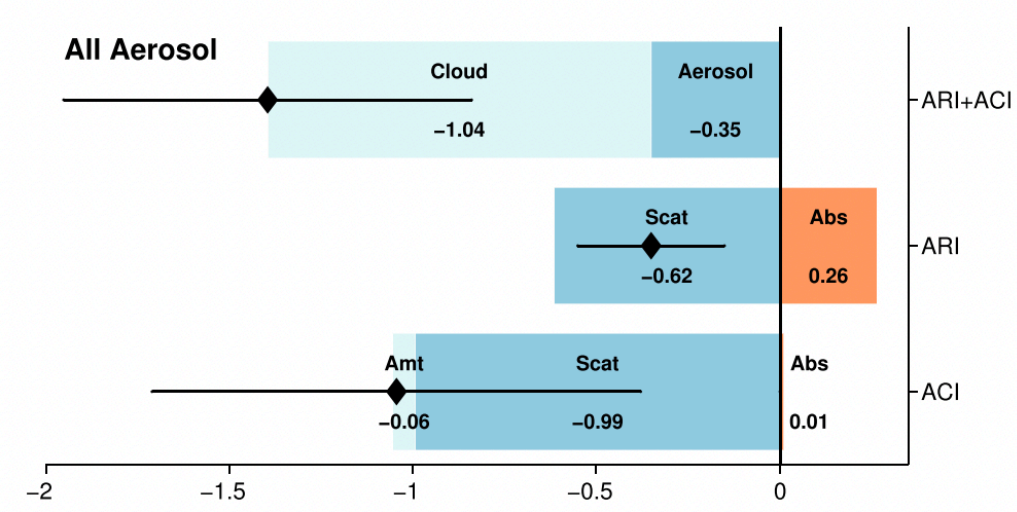

Figure 1.9: Figure 10 from Zelinka et al. (2014) showing the global, annual mean SW ERF values for their All-Aerosol runs, separated into ERFari and ERFaci. ERFari (middle bar) is separated into its scattering (blue) and absorption (orange) components. ERFaci (bottom bar) is separated into its amount (light blue), scattering (dark blue), and absorption (orange) components. The sum of terms is indicated by the black diamond, with the inter-model standard deviation of each sum indicated by the horizontal error bar.

Worldwide, aerosols have been found to play a major role in driving the late 20th century weakening of the monsoon over South Asia (Bollasina et al 2011, Undorf et al 2018b), East Asia (Song et al 2014), and West Africa (Undorf et al 2018b), as well as a suggested role in modulating multidecadal variability in the North Atlantic (Booth et al 2012, Undorf et al 2018a).

Aerosols represent the largest uncertainty in current estimates of anthropogenic climate change (Myhre et al., 2014) due to compounding uncertainties associated with model representations of poorly known aerosol

processes, and with the estimation of aerosol emissions. Climate model estimates of aerosol-cloud interactions carry large uncertainties, partly because their properties vary at scales significantly smaller than those resolved in climate models and must therefore be parametrised (e.g. microphysics). The magnitude and nature of the effect that aerosols have on the climate system varies depending on their constituents (Kasoar et al., 2018).

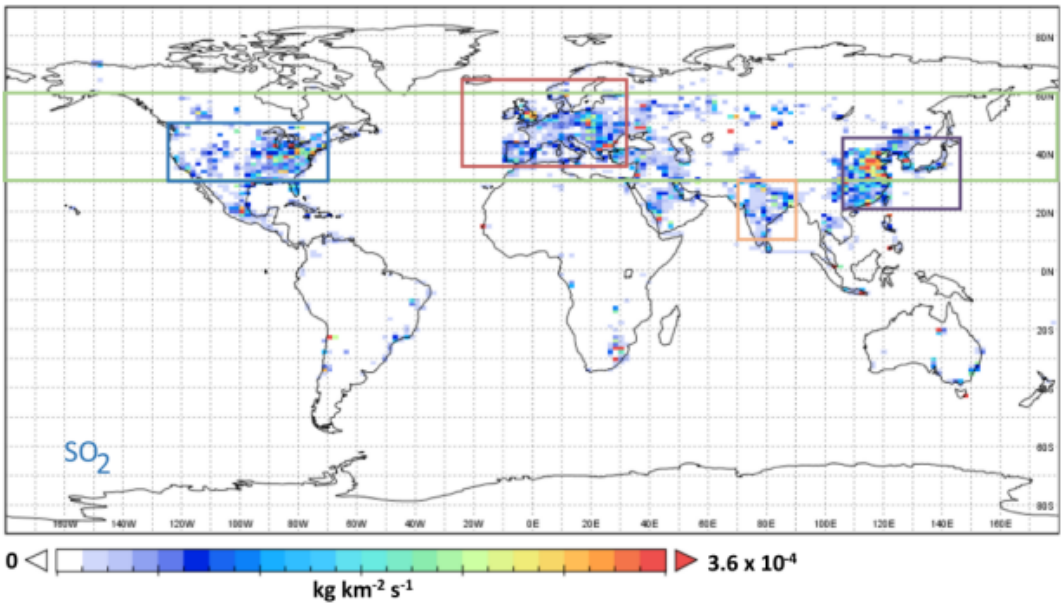

Figure 1.10 Annual mean anthropogenic SO_2 emissions circa year 2000. Boxes show regions in which aerosol emissions were applied in a suite of model experiments described by Kasoar et al. (2018).

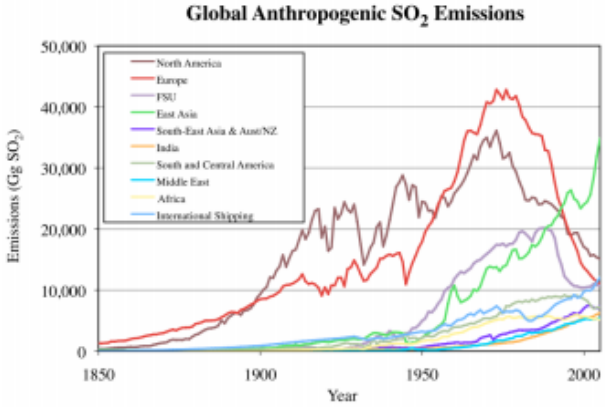

Figure 1.11 – Historical timeseries of estimated SO_2 emissions by region (North America = USA+Canada; East Asia = Japan, China and South Korea). From Smith et al. (2011).

In addition to complex variability in the nature of physical aerosol effects, there is and will continue to be spatial heterogeneities and uncertainties associated with the origin of aerosols (Smith et al., 2011, Bartlett et al., 2018). Figure 1.10 shows the major centres of aerosol emissions around the globe, with Asia, North America and Europe being the major contributors in the recent past. The relative and absolute contributions to the global aerosol burden from each region has also evolved and the effects of these transient heterogeneities has been studied (Kasoar et al. 2018, Smith et al., 2011). Kasoar et al. (2018) found that significant global warming across the northern hemisphere was found in the case of a reduction of SO_2 emissions from any of the aforementioned regions. The magnitude of the regional response was spatially dependent, however, the pattern of temperature response remained broadly comparable. This suggests that localised perturbations of AA have global effects. Figure 1.11 shows in more detail the shift in regional sulphate emissions that has occurred over the last 150 years. Most apparent is the acceleration in emissions from East Asia (defined as Japan, China, and South Korea) over the last half century and especially since around year 2000. Over the same period there have been rapid decreases in aerosol emissions over North America and Europe. More recently, emissions data from the Community Emissions Data System (O'Rourke et al., 2021) show a reduction in aerosol emissions over East Asia after 2010, which produces an overall negative trend when considering the full span of the 21st century. However, South East Asia, which includes India, still shows an increase in aerosol emissions over the same time period (Quaas et al. 2022).

Sulphate and BC are two of the most important radiatively active aerosols in the atmosphere and play opposite roles in their radiative effects. Their key characteristics are summarised below.

1.6.1.1 Sulphates (SO_4)

Over the 20th century, global radiative forcing due to sulphate aerosols is estimated to be of the same order of magnitude (but opposite in sign) to that of GHGs (Pachauri et al. 2014). Furthermore, in the next two decades, following stringent global climate and air pollution mitigation policies will likely cause a warming relative to 2019 predominantly due to sulphate aerosol reduction (Szopa et al., 2021). Sulphate aerosols can either be emitted directly or formed via oxidation of gas and aqueous phases of precursor gases (e.g. SO_2) in the atmosphere. They directly affect the climate system by either scattering solar radiation or absorbing longwave radiation, as well as indirectly by influencing cloud properties and precipitation (Boucher et al., 2013; Myhre et al., 2013). Additionally, sulphate aerosols and sulphate deposition have a large impact on air quality and ecosystems (Reis et al., 2012).

Sulphate aerosols are at their most abundant in the troposphere, however they can be transported to the stratosphere (including via volcanic eruptions) forming the stratospheric aerosol layer, which can affect global radiative forcing (Kremser et al., 2016; Myhre et al. 2004). Various uncertainties remain in the representation of key processes (e.g. emission heights, lifetime, cloud processes) that affect the simulated aerosol distributions (Yang et al., 2019).

The spatial distribution of sulphate emissions has changed significantly over the last hundred years, with reductions seen across North America and

Europe (since approximately 1980)(Smith et al. 2011) and increases seen across East Asia up to around 2005 and then a decline (Aas et al., 2019), with increasing trends persisting for longer in India (Bhaskar and Rao, 2017). Westervelt et al. (2015) project a decrease of global sulphate aerosol emissions by up to 80% by the end of the 21st century. Evidence for the changes in sulphate atmospheric concentrations is also deducible from ice cores (Engardt et al., 2017; Samyn et al., 2012, Iizuka et al., 2018).

Verma et al. (2019) showed that abrupt changes to anthropogenic sulphate aerosols over East Asia act to weaken the Walker cell and drive atmospheric subsidence over the equatorial west Pacific. The associated anomalous circulation imparts westerly momentum to the underlying tropical Pacific Ocean, leading to a transient warming of the east Pacific and an El Niño-like upper ocean response.

1.6.1.2 Black Carbon (BC)

BC aerosols form from the incomplete combustion of fossil fuels (such as for transportation, industrial and residential uses) and biomass burning; thus, a large fraction of atmospheric BC is the result of anthropogenic activities. Bottom-up inventories give an estimate of global BC emissions of circa 75000 Gg yr^{-1} in the year 2000 (Bond et al., 2013), and they are generally less than 1μm in diameter. BC absorbs solar radiation and, unlike sulphate aerosols, has a warming effect on the planet, though the magnitude of the global radiative forcing is still uncertain. BC can alter clouds through local heating or by acting as cloud condensation nuclei or ice nucleating particles (McGraw et al., 2020). Atmospheric concentrations of BC respond quickly to changes in emissions as BC is rapidly removed from the atmosphere (having an average lifespan of around a week) by either wet (i.e. in precipitation) or

dry deposition (Bond et al., 2013). Hansen et al. (2005) found the efficacy[1] of fossil fuel BC aerosols to be 0.93 when the ERF definition is used. The efficacy is closer to unity lower in the planetary boundary layer and lessens with altitude, due an enhancement in low cloud which reduces the direct warming effect (Sterjn et al. 2017). Even though efficacy is shown to decrease with height, radiative forcing due to the direct effect strengthens with height (Samset and Myhre, 2011, 2015).

The vertical distribution of BC also has impacts on convection (Wang et al., 2013), as BC heating in the boundary layer may limit shallow convection but enhance moisture build-up and convective available potential energy for later deep convection (Lin et al., 2016). Heterogeneous heating associated with BC has strong influences on moist dynamical processes at regional and global scales and therefore rapid adjustments dominate the global precipitation response to BC (Samset et al. 2016).

Absorption of BC has been demonstrated to impart changes in regional circulation, monsoon precipitation (e.g. Mahmood and Li, 2013; Hua et al., 2013) and global circulation (Johnson et al., 2019). Northward expansion of the northern hemisphere Hadley cell (Kovilakam and Mahajan, 2015) and poleward displacement of the mid-latitude jets (Allen et al., 2012; Wood et al., 2021) are associated with perturbations to BC emissions. Changes to the spatial distribution of tropical convection is also affected (Johnson et al., 2019), while a study by Zhao and Suzuki (2019) associated an increase in BC

[1] the ratio of the equilibrium global mean temperature change per unit forcing to the equilibrium temperature change per unit CO_2 forcing.

with a northward shift in the Inter-Tropical Convergence Zone (ITCZ) and a reduction in global mean precipitation. Remote impacts of BC aerosol via atmospheric teleconnections have been posited in a recent study by Amiri-Farahani et al. (2020), who attributed biomass burning in South Africa as a driver of tropical Pacific Ocean variability. Anomalous heating over the Atlantic was posited to trigger an atmospheric teleconnection to the tropical Pacific including an intensification of the Walker circulation.

Substantial uncertainties exist in the net climate forcing from BC, due to the limited understanding about cloud interactions with both BC and co-emitted organic carbon, as well as difficulty quantifying emissions from a diverse array of sources, atmospheric lifetime of BC and transport and BC mass concentrations in models (Bond et al., 2013). The ratio of concentrations of BC to sulphates has been shown to influence the direct heating effect of BC (Ramana et al., 2010), with a higher proportion of BC yielding stronger influence on net warming. Modak and Bala (2019) find a 60-fold increase in BC mixing ratio from present day levels has the same effect on GMST warming as doubling of CO_2, albeit with a lower efficacy driven by differences in the shortwave cloud feedback. Due to the complex nature of the sources of uncertainty mentioned above and disagreements among models, the role of BC in human-induced climate change remains uncertain and poorly understood (Johnson et al. 2019).

Takemura and Suzuki (2019) highlight the difference between BC and sulphates in the global mean temperature response to a top-of-atmosphere (TOA) instantaneous radiative forcing (IRF), with the mean GMST change due to BC approximately one-eighth of that of sulphates per unit IRF forcing. This

was attributed to the rapid atmospheric adjustment due to BC, whereas radiative imbalance due to sulphates drives a slower response over longer timescales. Heterogeneous spatial distributions make assessing regional climate responses to the short-lived BC emissions challenging. When BC is emitted, transported and deposited over snow or glacier surfaces it causes a change in surface albedo and this results in a series of feedbacks (e.g. Xu et al., 2009; Mahmood and Li., 2012).

1.6.1.3 Anthropogenic aerosol impacts on the PDO

The PDO has historically been considered as an internally generated mode of climate variability that emerges as a consequence of the mechanisms described in section 1.4. However, Smith et al. (2016) hypothesised that the change in global AA emissions over recent decades modulated the behaviour of the PDO and was in part responsible for its transition to a negative phase in the early 21st century. Smith et al. (2016) hypothesised that modulations in the Walker circulation and excitation of atmospheric Rossby waves as a consequence of local aerosol forcing over Asia are potential driving mechanisms of the AL and consequently the PDO. Other studies have also found a link between AA emissions and the PDO (e.g. Allen et al., 2014; Hua et al., 2018; Dittus et al., 2021), while Takahashi and Watanabe (2016) show that approximately one-third of the trade wind intensification in the Pacific at the end of 20th century could be attributable to changes in sulphate aerosols. Boo et al. (2015) demonstrate the impact that aerosol emissions have on North Pacific SST via the impact on changes to the intensity and position of the AL.

Despite the aforementioned evidence, the relationship between AA emissions and the PDO has been disputed by Dai et al. (2015) and Oudar et

al. (2018), who attribute the slowdown in GMST (and the transition of the PDO to its negative phase) exclusively to internal variability. One study found that the proposed link between evolving AA emissions and the change in phase of the PDO is not robust when examined across a large initial condition ensemble of historical simulations (Oudar et al., 2018). Similarly, a study by Kuntz and Schrag (2016) suggests that Asian AA cannot explain the enhancement of equatorial trade winds which are tied to the global hiatus in GMST increases. Therefore, there remain open questions around the influence of global and regional aerosol trends on the PDO.

1.6.2 Greenhouse Gas impacts on the PDO

Under future greenhouse warming scenarios, the amplitude and predictability of the PDO are projected to decrease (Li et al. 2020; Fang et al. 2013). The KOE region is where the greatest decrease in amplitude is evident, associated with a weakened meridional temperature gradient (Zhang and Delworth, 2016). The overall reduction in amplitude is shown to be associated with warming induced intensification of ocean stratification, which accelerates the propagation of oceanic Rossby waves (shown to be vital in the evolution of the PDO, especially at higher latitudes; Fang et al. 2013), increasing the frequency of the PDO and limiting its growth time. Furthermore, the rate of growth is larger under greenhouse warming due to the increased entrainment of upper ocean temperature anomalies into the upper ocean mixed layer in the KOE and North-East Pacific regions; however, the increased frequency is a more dominant factor causing the suppression the decadal variability of the PDO (Geng et al. 2019). Zhang and Delworth (2016) showed a reduction in PDO period from 20 to 12 years. Fang et al. (2013) demonstrated, for example, that if the ocean baroclinic Rossby waves sped up by 10,000 times,

there would be no decadal variability and hence no PDO. Reduced wind stress in the North Pacific in a warming world has been demonstrated to help weaken PDO amplitude through reducing the meridional displacements of the subtropical and subpolar gyres (Zhang and Delworth, 2016).

In contrast, in a scenario of global cooling the impact on the PDO is opposite to that in a warming scenario, where the ocean stratification becomes weaker and the decrease in ocean stratification acts to reduce the phase speed of the internal Rossby waves (increasing from 20 to 34 years; Zhang and Delworth., 2016), thereby altering the time scale of the PDO.

1.7 Ocean-atmosphere coupling

The coupling of the ocean and the atmosphere in the climate system is a major concept of climate dynamics and is essential in explaining the evolution of phenomena such as the PDO and decadal climate variability. Anomalous SSTs serve as the link between the ocean and the atmosphere, by altering atmospheric circulation through diabatic heating. Atmospheric changes alter wind stress and heat fluxes at the ocean surface, which in turn modifies ocean circulation and thermal structure. In the tropical Pacific, the convergence of moist air and the release of latent heat through deep convection drive direct thermal circulation, characterised by cumulonimbus clouds over the warmest regions and intense precipitation. Positive SST anomalies in the eastern equatorial Pacific results in anomalous diabatic heating of the atmosphere, convergence and a reduction in strength of the easterly winds. The local response to this heating is baroclinic, where warm SST anomalies induce a low pressure anomaly lower in the troposphere and high pressure anomaly in the upper troposphere (e.g. Gill, 1982; Battisti and

Hirst, 1989). The effect of diabatic heating on atmospheric circulation is stronger in the tropics as circulation is largely controlled by latent heat release driven by convective instability.

The response of the ocean to surface winds has a major role in determining surface temperatures. The surface winds affect the depth of the thermocline – the region separating the oceanic mixed layer from the deep ocean – and can expose cold water to the surface. For instance, a relaxation of intense easterly trade winds allows warm surface water to flow eastward, reducing the zonal temperature gradient, which creates positive feedbacks contributing to ENSO. One of the major positive feedbacks in the development of warm or cool ENSO states is known as the wind-evaporation-SST (WES) feedback (Xie and Philander, 1994), which reinforces anomalous temperature and SLP gradients induced across the equator by the following mechanism (shown in Figure 1.12). An initial asymmetry in SSTs either side of the equator (e.g. warmer to the north, cooler to the south) will induce an SLP gradient that drives southerly winds across the equator. The Coriolis force acts to turn the southerly winds in the southern hemisphere westward and in the northern hemisphere eastward. When these anomalous winds are imposed on the background easterly trade winds, the southerlies south of the equator increase the wind speed and therefore evaporative cooling. Conversely, in the northern hemisphere the wind speed is reduced, and the evaporative cooling also reduces. These feedbacks amplify the initial SST gradient.

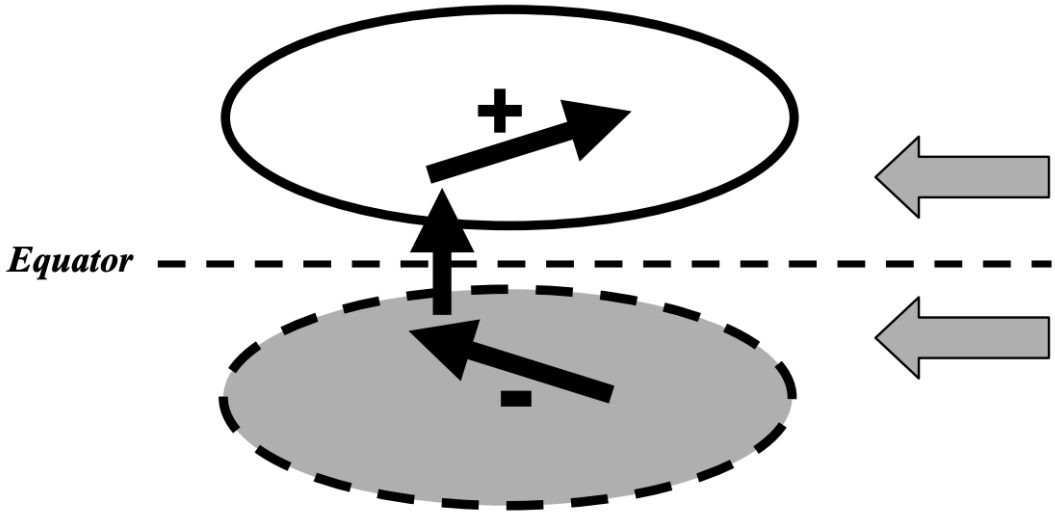

Figure 1.12: Schematic of the WES feedback. Anomalies of SST in contours (negative dashed) and surface wind velocity in black vectors. The grey vectors on the right signify the background easterly trades. Taken from Xie et al. (2004).

Positive feedbacks associated with ENSO maintain the meridional asymmetrical structure of tropical SSTs (e.g. Philander et al., 1996) and the seasonal cycle in the tropical Pacific (Chang and Philander 1994). The forcing by incoming solar radiation in the equatorial Pacific has a semi-annual cycle as the sun crosses the equator twice a year; however, in the eastern and central tropical Pacific the seasonal cycle is annual due to the SST's being controlled mainly by dynamical factors (such as upwelling). The ITCZ develops over the warmest waters and stays predominantly north of the equator. Seasonal variations in incoming solar radiation leads to meridional displacement of the ITCZ and annual variability in meridional winds and upwelling.

In the mid-latitudes, ocean-atmosphere coupling is believed to be determined, to a large extent, by stochastic atmospheric variability and the passive ocean response (e.g Frankignoul and Hasselmann 1977). However, modes of climate variability that manifest in the mid-latitudes, such as the NAO

and PDO, cannot be fully explained as a reddened response to atmospheric white noise and therefore suggests atmospheric variability can induce significantly large-scale SST anomalies in the ocean.

Zhang and Delworth (2015) demonstrate explicitly that, by using a 'partial coupling' approach where tropical and extra-tropical ocean-atmosphere coupling is activated separately, that the preferred multidecadal time scale of the model PDO is generated by extra-tropical North Pacific ocean-atmosphere coupling, and is further enhanced by tropical Pacific activity. This has been demonstrated in other studies on other models (e.g. Zhong et al., 2008). This work suggests that the tropical Pacific is not the origin of the PDO and acts as a relay to propagate decadal variability stemming from the North Pacific. To add credence to this claim, Zhong and Liu (2009) conducted Rossby wave 'partial blocking' experiments to suggest that the PDO relies on propagating Rossby waves in the subpolar Pacific, whereas those in the subtropics were less important. However, Newman (2007) suggests that climate models may underestimate the degree of tropical forcing of the North Pacific, therefore this must be kept in mind when comparing with observations and testing mechanisms using models.

Changes to heat fluxes resulting from evaporation, upwelling and ocean circulation all affect ocean-atmosphere coupling in the mid-latitudes with the thermal inertia of the ocean allowing such impacts to persist across seasons and interannually. A warm SST anomaly in the mid-latitudes is likely to induce a weaker baroclinic response compared to the tropics, with a more barotropic response resulting from the interaction between the initial perturbation and the mean atmospheric flow and mid-latitude storms (e.g.

Peng and Robinson 2001). These SSTs in the Pacific and Atlantic help generate the PNA and NAO patterns in SLP response, respectively.

Decadal climate fluctuations in the North Pacific are sustained by unstable interactions between the subtropical gyre and the AL according to Latif and Barnett (1994,1996). Over the mid-latitudes, the ocean can be considered to passively respond to forcing by the atmosphere. However, in the KOE region there is greater potential for coupling and ocean-atmosphere feedback. Latif and Barnett (1994) proposed a coupled feedback mechanism whereby wind-driven intensification of the North Pacific sub-tropical gyre would drive more warm water along the western boundary and into the KOE region, consequently feeding back to the large-scale atmosphere, weakening the AL which via a reduction in northward Ekman transport and mixing, influences the gyre and boundary current reinforcing the SST anomaly. However, evidence from observational data for this feedback is weak and that the SST anomaly is usually damped by air-sea heat fluxes and not amplified. Furthermore, Seager et al. (2001) and Schneider et al. (2002) have suggested that North Pacific decadal variability could be forced by stochastic Ekman pumping from the atmosphere with no active coupling necessary, where the ocean effectively acts as a low pass filter, integrating the high frequency wind stress forcing.

1.8 Climate Models

Climate models are numerical models that aim to simulate the climate system of the past, present, and future. They are the main tool used in forecasting near to long term future climate change and the findings from these models provide society and policy makers with vital information which

can be used to mitigate and adapt to predicted global and local effects (e.g. IPCC WGI AR6, 2021).

Climate models vary widely in their complexity, computational cost, and scientific scope. Therefore, different climate models are used to answer different scientific questions, often depending on the spatiotemporal scale (e.g. global/local, years/decades/centuries/millennia) and components (e.g. atmosphere, cryosphere, continents, oceans) of interest. Millennial scale experiments are run on coarse resolution simplified models which run quickly and at low computational cost (e. g. GENIE-1 (Edwards and Marsh, 2005), CLIMBER (Montoya et al., 2005), UVic (Ewen et al., 2004)) whereas high resolution models (<0.1°- 0.5° ocean) models (e.g. those contributing to the CMIP6 HighResMIP; Haarsma et al., 2016) are at the opposite side of the spectrum requiring large computational cost. The intermediate resolution models sit between these two extremes which include most of the coupled climate models contributing to CMIP5 (Taylor et al., 2012), CMIP6 (Eyring et al., 2016) and PDRMIP (Myhre et al., 2017).

Uncertainty in climate model simulations arises from unpredictable internal variability associated with the chaotic nature of geophysical flows, model formulation (including parameter and structural uncertainties), and uncertainties in characterising external forcing both in the past and in the future where actual emissions are not known. The extent to which these uncertainties are important sources of uncertainty in climate predictions varies as a function of time scale (Hawkins and Sutton, 2009).

Assuming the models are unbiased, understanding the uncertainty due to internal variability can be achieved by running a large ensemble of

simulations to produce a probabilistic distribution of how the system will evolve over time. For instance, the studies by Oudar et al. (2018) and Smith et al. (2016) use multiple realisations from the CMIP5 models, with Oudar et al. (2018) using an additional single model initial condition large ensemble (referred to as SMILEs, Maher et al. 2021) dataset from the CanESM2 model. These studies were able to investigate the role of different external forcing mechanisms by comparing simulations where only certain agents (e.g., GHG's, aerosols) were applied, with other forcing agents kept at pre-industrial levels. Furthermore, Dittus et al. (2020) used an array of ensembles to attempt to constrain the uncertainty of aerosol forcing on the decadal variability of the historical climate. Here, five ensemble members were run for five different aerosol forcings (25 in total). By setting up the ensemble simulations to sample a wide range of emission scenarios, the study allowed the authors to examine the role of aerosol forcing uncertainty in the absence of model structural diversity and, by scaling the members, provide the necessary signal to examine regional responses.

The value in using SMILEs such as the one used in Oudar et al. (2018) lies in the ability to quantify and separate internal variability of the climate system (e.g. Smith and Jahn, 2019; Dai and Bloecker, 2019) from the forced response due to external forcing (e.g. Maher et al. 2019). It also allows us to sample extreme events such as heatwaves and droughts and deduce their probability (e.g. Suarez-Gutierrez et al. 2018). Seven GCMs have provided SMILEs available for public use (Deser et al.,2020), many of which have been used in recent studies. For example, they have been used to investigate the role of internal variability and model differences in affecting future projections (Maher et al. 2020), trends in SST patterns (Olonscheck et al., 2020) and

decadal modulation of global warming (Liguori et al., 2020). Such large ensemble datasets are used to ascertain whether emissions reductions are likely to be detectable in the future, or whether internal variability will mask any signal (e.g. Marotze, 2019).

1.8.1 Modelling Pacific variability

The predictability of climate on decadal time scales depends on the ability of coupled climate models to capture the evolution of climate system components that are represented in the initial conditions and that respond realistically to prescribed external forcing (boundary conditions) (Kushnir et al., 2019, see Figure 1). Many challenges persist for operational near-term climate predictions, including reducing model biases, accounting for drift and using better observational datasets to constrain initial conditions. Improving upon the incomplete understanding of the physical processes that govern the behaviour of decadal phenomena, including the PDO, could enhance the utility of near-term climate predictions and give policy makers and other stakeholders more reliable information upon which more informed decisions could be made. It is for these reasons that the World Climate Research Programme (WCRP) initiated the Grand Challenge on Near Term Climate Prediction (NTCP) to 'support research and development to improve multiyear to decadal climate predictions and their utility to decision makers'.

A prominent characteristic in the observable behaviour of the Earth's climate is the rate at which the GMST has changed over time. When viewed as a time series, the behaviour of GMST can be decomposed into temperature 'surge' and 'hiatus' events. 'Surge' events are periods when the rate of GMST increases rapidly over decadal timescales, and conversely, 'hiatus' events, are periods when the rate of increase in GMST decreases or pauses over

decadal timescales. Energy has continued to be added to the climate system over the past half a century as a consequence of anthropogenic activity, with it being primarily stored in the ocean. Since 1960, the total planetary energy imbalance has increased by 36.0 ± 7.5 x 10^{22} J (Cheng et al., 2017). The most recent warming slowdown (lasting from 2001 (Fyfe et al., 2016) to between 2014-2016 (Hu & Fedorov, 2017)) is unique in modern times in that it is the only 'hiatus' period on record during a time of strongly increasing anthropogenic radiative forcing of the climate system. A plethora of research (e.g. Dai & Wang, 2018; England et al., 2014; Fyfe et al., 2016; Hu & Fedorov, 2017; Meehl et al., 2011; Watanabe et al., 2013) has aimed to improve our understanding of the mechanisms that governed the recent hiatus period. Research by Kosaka & Xie (2013) and England et al. (2014) attribute changes in the tropical Pacific to be the major component influencing the most recent hiatus. Intensification of surface tropical wind speeds over the past two decades and the resultant La Nina like cooling in the tropics is considered to be the most likely cause of the most recent hiatus.

The apparent discrepancy between observations and the CMIP5 models in simulating the most recent warming slowdown has been shown to be a consequence of, in part, quasi-random internal climate variability (Marotzke & Forster, 2015). Meehl et al. (2014) showed that 10 members out of 262 available uninitialized realisations produced the observed warming trend (defined as less than 0.04^{o}C per decade). A composite of these 10 realisations showed a change to a negative phase of the IPO. Given that the multi-model mean showed warming in the eastern tropical Pacific, the synchronisation, by chance, of the IPO with these 10 uninitialized realisations, lends additional

credence to the claim that natural variability in sea-surface temperatures in the Pacific Ocean is a major influencer on the rates of GMST change.

1.9 Thesis aims and Structure

The aim of this thesis is to advance understanding of the role of atmospheric forcing on decadal climate variability focusing on the role of the North Pacific. Through multi-model assessments the thesis will investigate the impact of different aerosol species, and the distribution of aerosol emissions, on the AL and differentiate the role of the ocean and atmosphere in driving these responses. The thesis will also investigate the role of the AL in driving basin-wide decadal variability across the Pacific by utilising a relaxation, also known as nudging, technique (developed as part of the thesis).

Chapter 2 outlines the methods used throughout the thesis, details of the models and multi-model datasets.

Chapter 3 presents an investigation of the role of idealised perturbations of AA emissions (Sulphate and BC) and CO_2 on the AL, utilising the multi-model dataset available from the Precipitation Driver Response Model Intercomparison Project (PDRMIP). The study builds on previous work, which has often focused on the atmospheric response to transient changes to external forcing (e.g. Smith et al., 2018; Dittus et al., 2021; Oudar et al., 2018), by analysing idealised, large step-change perturbations in each forcing agent to quantify the impact and significance of each response. The study allows a delineation of the ocean and atmosphere drivers of the response by analysing fixed-SST and fully coupled experiments. The study includes work that is published in Dow et al. (2021).

Chapter 4 builds on the findings from chapter 3 and seeks to further investigate the atmospheric mechanisms responsible for the AL responses evident in chapter 3. The chapter also seeks to validate the atmospheric mechanisms hypothesised to drive changes in the AL in previous work (e.g. Smith et al., 2016). The study uses a stationary wave model, forced by heating anomalies derived from precipitation anomalies and atmospheric absorption anomalies (calculated using an offline radiative-transfer model). The study includes work that is published in Dow et al. (2021).

Chapter 5 outlines the development and testing of a nudging functionality in a coupled GCM. The chapter is motivated by the findings from chapters 3 and 4, and the aim of the chapter is to develop a tool that can be used to investigate the communication between the AL and the tropical Pacific in an attempt to better understand the role of the extra-tropics on the tropics over decadal time scales. The grid-point nudging technique is analogous to, and takes inspiration from, those already used in other GCMs (e.g. Knight et al. 2017; Jung et al. 2010).

Chapter 6 utilises the grid-point nudging functionality developed in chapter 5 to investigate the role of an anomalous AL on the tropical Pacific. Literature suggests that the AL is modified by tropical Pacific SSTs via anomalous tropospheric Rossby waves, lending further support to the idea that variability in extra-tropics is predominantly a response to variability in the tropics (e.g. Newman et al., 2016). Therefore, the purpose of this study is to better understand the extent to which the extra-tropics can independently drive change in the tropics over decadal time scales. The findings from chapters 3 and 4 motivate the study conducted in this chapter, where I

examine the mechanisms through which anthropogenic forcing impact onto the extra-tropics in the North Pacific. In focusing on the communication between the extra-tropics and tropics in this chapter, I am able to hypothesise the degree to which the initial atmospheric forcing is able to modulate decadal climate variability across the Pacific basin.

Finally, chapter 7 synthesises the main findings from the thesis results, places them into the wider context of present scientific understanding and suggests areas for future work.

Chapter 2 - Methods

This chapter describes the methods and datasets used throughout this thesis. These include existing multi-model datasets used in chapters 3 and 4, reanalysis datasets, a linear stationary wave model used in chapter 4 and the atmosphere-ocean climate model used in chapters 5 and 6. Specific details of the experiments used to address the research questions will be given in each results chapter (Chapters 3 to 6). Also outlined below are the main data analysis techniques and diagnostics used in the results chapters, including Empirical Orthogonal Function (EOF) analysis, Rossby wave diagnostics, heat budget analysis and statistical methods.

2.1 Multi-model datasets

The Precipitation Driver and Response Model Intercomparison Project (PDRMIP; Myhre et al., 2017) was set up to investigate the role of various drivers of climate change for mean and extreme precipitation changes as simulated by multiple climate models. The dataset comprises output from 11 comprehensive coupled atmosphere-ocean climate models (listed in Tables 2.1 & 3.1) that perform a set of idealised aerosol (BC and Sulphate), CO_2, CH_4, solar constant and O_3 perturbation experiments. The control simulation in most of the models was run with observed year 2000 boundary conditions, including GHG concentrations, aerosol concentrations or emissions, and orbital parameters; the control simulation in HadGEM2 used preindustrial (year 1860) conditions, however, in the HadGEM2 scaled experiments (e.g. BCx10) it is emissions from year 2000 which are scaled (Lamarque et al. 2010). This presents a discrepancy between the spatial and vertical aerosol

distribution and load in the control simulations (and also in the difference between the scaled experiments and control experiment) across the models (see Figure 2 and S1 in Stjern et al., 2017), highlighting one of the challenges of using data from multi-model intercomparison projects.

The tier 1 PDRMIP experiments, denoted as highest priority, include global perturbations of black carbon (BC) and sulphate aerosols, with a 10 and 5 times (BCx10 and Sulx5) global instantaneous increase from the baseline state, respectively. Also in tier 1 are: a doubling of CO_2 (CO_2x2), a three-fold increase in methane and a change to the solar constant. Additional experiments performed by a subset of the models (see Table 3.1) applied a regional 10-fold increase in BC and sulphate over Asia (10°N-50°N, 60°E-140°E; BCx10a and Sulx10a) and Europe (35°N-70°N, 10°W-40°E; Sulx10e), respectively.

The control and perturbation experiments were run with two model configurations: (1) with a fully interactive ocean and sea ice models (except CESM1-CAM4 and ECHAM-HAM that used a simplified mixed-layer slab ocean), and (2) with prescribed monthly-varying climatological SSTs and sea ice extent from the control simulation. The two types of simulations were run for at least 100 and 15 years, respectively (see Table 3.1). Comparisons between these complementary simulations provide an assessment of the sensitivity to the ocean response for each forcing agent. The simulations with fixed SSTs allow the examination of rapid adjustments (i.e. the response in the absence of SST feedbacks) whilst the coupled simulations allow the examination of the importance of SST feedbacks for the response.

The representation of aerosol processes differs amongst the PDRMIP models (see Table 2.1). For models that prescribe aerosol concentrations, a common set of baseline concentration fields were used from phase 2 of the Aerosol Comparisons between Observations and Models (AeroCom) science initiative (Myhre et al., 2017). The remaining models prescribe aerosol emissions and use a detailed aerosol microphysical module to calculate the aerosol burden. Of the 11 models contributing to PDRMIP, indirect effects on clouds from BC and sulphates are included in CanESM2, NorESM1, CESM1-CAM5, SPRINTARS, and ECHAM-HAM, whilst IPSL-CM5A incorporates the Twomey effect only. Indirect effects of sulphate but not BC are included in HadGEM2 and HadGEM3, whilst CESM1-CAM4 and GISS do not include any indirect effects. MPI-ESM only ran the CO_2x2 experiment. Of the eleven models contributing to PDRMIP, six provided output diagnostics that enabled the analysis of the dynamical mechanisms contributing to the AL response (i.e., 3-D wind fields and geopotential height; see Table 3.1); the analysis presented in Section 4.4.2 uses this subset of six models.

Model	Version	Aerosol prescription	Indirect effects	Cloud scheme	Mixing State	Size Distribution	Key references
CanESM2	2010	Emissions	First, Second	One moment	Internal	Log-normal	[Arora et al., 2011]
CESM1-CAM4	1.0.3	Prescribed Concentrations	None	One moment	External	Log-normal	[Gent et al., 2011; Neale, 2004]
HadGEM2	6.6.3	Emissions	First*, Second*	One moment	External	Log-normal	[Martin et al., 2011]
HadGEM3	GA 4.0	Prescribed Concentrations	First*, Second*	One moment	External	Log-normal	[Bellouin et al., 2011; Walters et al., 2014]
NorESM1	NorESM1-M	Prescribed Concentrations	First, second	Two moment	Internal & External	Log-normal	[Bentsen et al., 2013; Iversen et al., 2013; Kirkevåg et al., 2013]
SPRINTARS	5.9.0	HTAP2 Emissions	First, Second	One moment	Internal & External	Log-normal	[Takemura et al., 2005; Takemura et al., 2009; Watanabe et al., 2010]
CESM1-CAM5	1.1.2	Emissions	First, second	Two moment	Internal	Log-normal	[Hurrell et al., 2013] This is the same model as [Kay et al., 2015], but with a coarser resolution [Otto-Bliesner et al., 2015]

ECHAM-HAM	ECHAM-6.3-HAM2.3-M7	Emissions	First, second	Two moment	Internal	Log-normal	[Zhang et al., 2012; Hodnebrog et al., 2019]
GISS	E2-R	Prescribed Concentrations	None	One moment	Internal & External	Log-normal	[Schmidt et al., 2014]
IPSL-CM5A	CMIP5	Prescribed Concentrations	First	Two moment	External	Log-normal	[Dufresne et al., 2013]
MPI-ESM	1.1.00p2	Climatology year 2000	First	Two-moment	Internal	Log-normal	[Giorgetta et al. 2013]

Table 2.1: Details of the aerosol processes across the models contributing to PDRMIP. Cloud scheme refers to the microphysical cloud scheme that describes cloud formation, where a one-moment scheme considers only change in mass and a two-moment scheme considers changes in mass and number concentration. The first indirect effect refers to the aerosol effect on cloud albedo, and the second indirect effect refers to the aerosols effect on cloud lifetime. The sixth column describes the assumptions made by each model of the aerosol mixing state. Asterisk denotes where indirect effects of sulphate but not BC are included.

Validation of the PDRMIP models was performed on the control runs to investigate each model's representation of the AL. Figures 2.1-2.3 show the control run NPI indices across the models throughout the control run simulations. Figure 2.1 shows the mean state of the AL throughout the control run, which shows each model does a good job capturing its quasi-permanent nature. The IPSL model and the HadGEM2 model depict the strongest and weakest magnitudes for the mean state AL, respectively. Although they are out of phase which is to be expected due to internal variability, inspecting the periodograms in Figure 2.3 shows the dominant frequencies to be <0.02 cycles per month, translating to dominant periods of AL oscillation > 50 months. This instils confidence that the AL is characterised by low frequency variability in the models. There is some discrepancy between the observational and reanalysis dataset, as the reanalysis dataset manifests a secondary peak around 0.06 cycles/month not evident in the observational dataset. At higher frequencies (periods >0.1 cycles per month) there is good agreement between the observational and reanalysis datasets. The discrepancy at lower frequencies could raise questions of how well models represent lower frequency variability of the AL and with what accuracy are we capturing low frequency variability of the AL in the observational datasets.

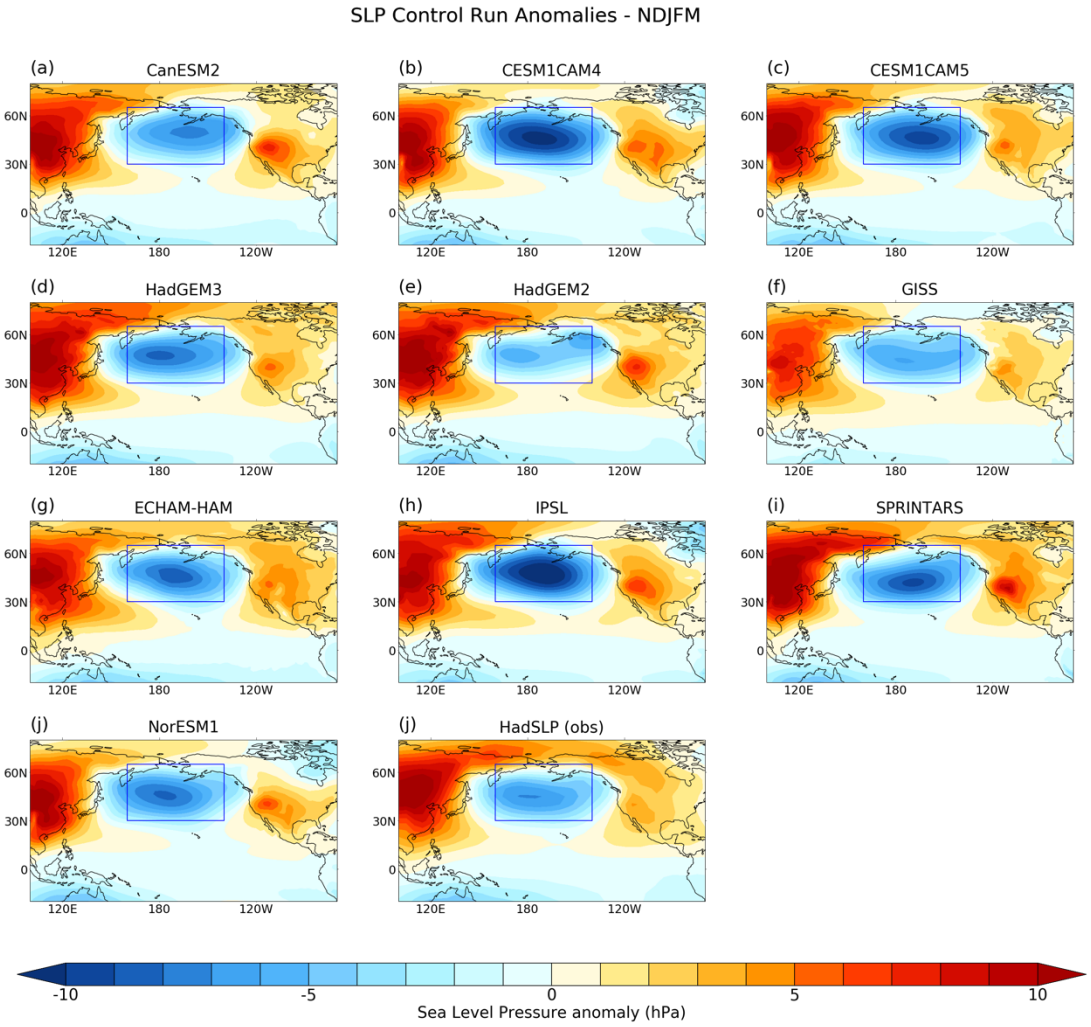

Figure 2.1: Each model's representation of the AL in the control simulation. The blue box depicts the region over which the AL is defined across the literature (30°N-65°N, 160°E-140°W (Trenberth and Hurrell, 1994))

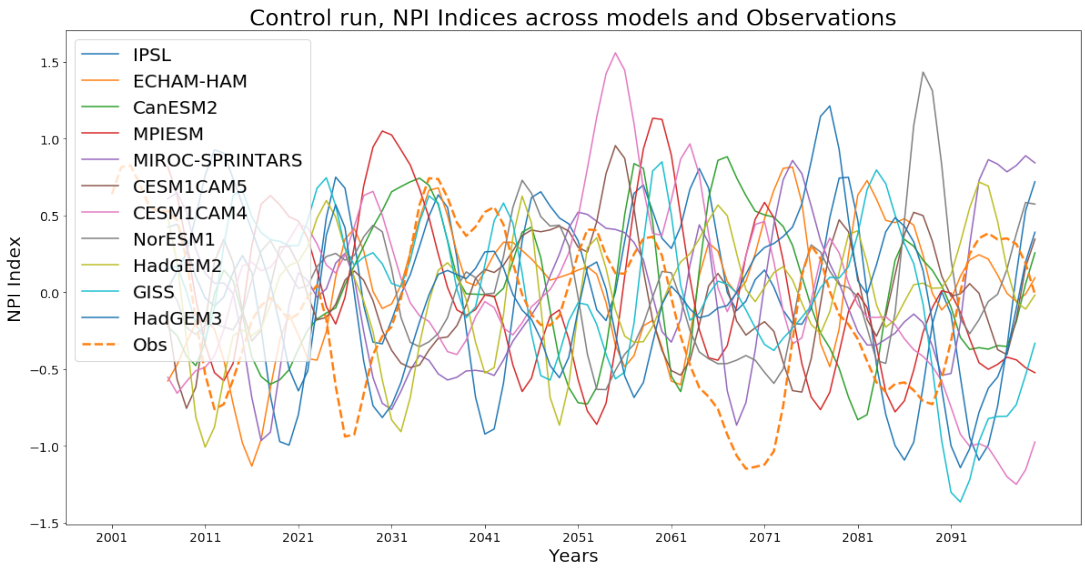

Figure 2.2: Extended boreal winter (NDJFM) average NPI Index in the PDRMIP control simulations. NPI is defined within the region 30°N-65°N, 160°E-140°W. A weighted running average has been applied with weights [1,3,5,6,5,3,1]. The observational data (from 1920-2020, provided by NCAR Climate Analysis Section) is plotted on the same x-axis to allow comparison.

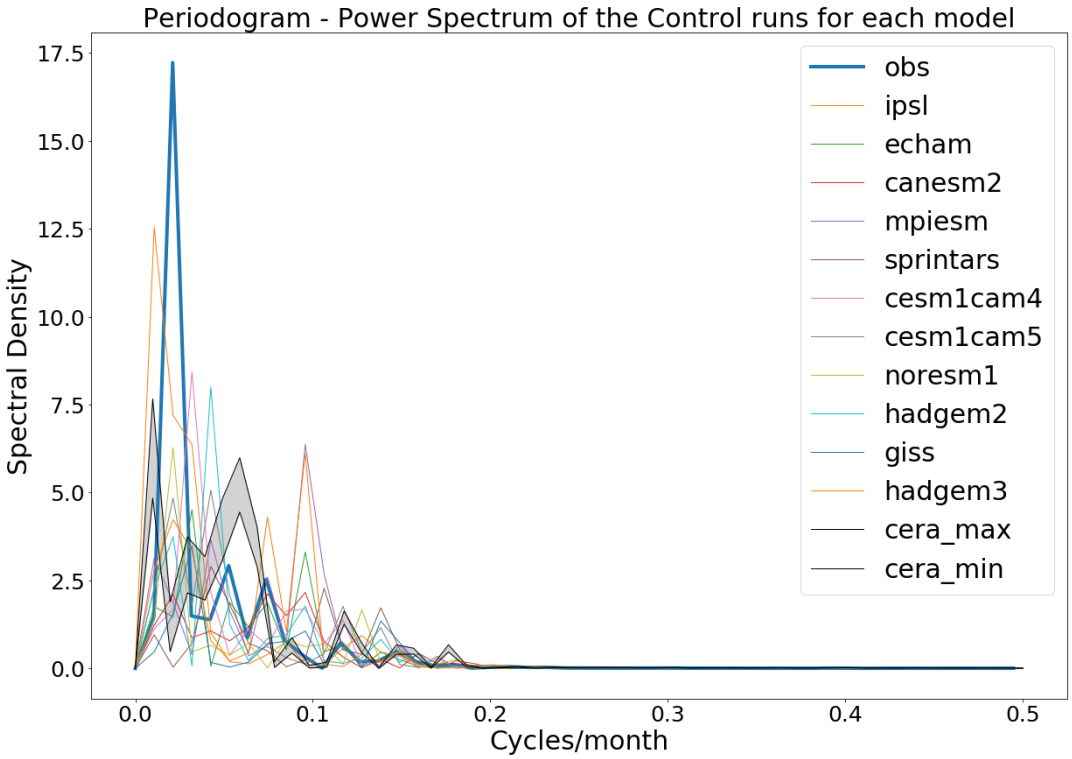

Figure 2.3: Power spectrum (Periodogram) of the NPI index in the PDRMIP control simulations. For comparison and validation, observational data (blue; provided by the Climate Analysis Section, NCAR) and a reanalysis ensemble (black and shaded range; CERA-20C ECMWF 10-member ensemble) are overlain.

2.2 Linear stationary wave model (LUMA)

The Linear University Model of the Atmosphere (LUMA) is a global, stationary wave model that solves the linearized dry, primitive equations on terrain-following sigma-levels (Hoskins and Simmons 1975). It is a linearized version of the Portable University Model of the Atmosphere (PUMA; Fraedrich et al. 2005) and the concepts of the model are adapted from Ting (1994). The basic equations on which the model is based include those for vorticity (ζ), divergence (D), temperature (T), and log of surface pressure (lnP_s). Geopotential height (Φ) and the sigma dot vertical velocity (σ) are also treated as independent variables in the hydrostatic and mass balance equations, respectively. The adiabatic form of the dynamical equations in the σ coordinates can be written as:

$$\frac{\delta\zeta}{\delta t} = -\nabla\cdot\{(f+\zeta)\boldsymbol{V}\} - \boldsymbol{k}\cdot\nabla\times\left\{RT\nabla lnP_s + \dot{\sigma}\frac{\delta\boldsymbol{V}}{\delta\sigma}\right\} \qquad \textit{Equation 2.6}$$

$$\frac{\delta D}{\delta t} = -\boldsymbol{k}\cdot\nabla\times\{(f+\zeta)\boldsymbol{V}\} - \nabla\cdot\left\{RT\nabla lnP_s + \dot{\sigma}\frac{\delta\boldsymbol{V}}{\delta\sigma}\right\} \qquad \textit{Equation 2.7}$$

$$-\nabla^2\left\{\frac{1}{2}(u^2+v^2)+\phi\right\}$$

$$\frac{\delta T}{\delta t} = -\boldsymbol{V}\cdot\nabla\mathrm{T} - \sigma\frac{\delta T}{\delta\sigma} + \frac{\kappa T}{\sigma}\dot{\sigma} + \kappa T\left\{\left(\boldsymbol{V}-\widetilde{\boldsymbol{V}}\right)\cdot\nabla lnP_s - \widetilde{D}\right\} \qquad \textit{Equation 2.8}$$

$$\frac{\delta lnP_s}{\delta t} = -\tilde{V}\cdot\nabla lnP_s - \widetilde{D} \qquad \textit{Equation 2.9}$$

Where a tilde denotes vertically integrated quantities and other notations are standard (see Ting (1994) for a comprehensive description). The primitive equations are linearised around a zonally symmetric atmospheric state, *[Y]*, which contains spectral coefficients of the aforementioned fields. The model solves for a steady state implying that the stationary-wave induced eddies, contained in *Y**, are obtained by solving the following equation (Ting 1994; Liakka et al., 2012).

$$L([Y], \epsilon)Y^* = F^* \qquad \textit{Equation 2.10}$$

The stationary wave response to a given forcing – which can include transient vorticity and heat flux convergences, radiative, sensible and latent heating and orographic uplifting - is obtained by inverting the linear operator that is a function of the zonally symmetric background state and on ε (which is the dissipation through diffusion, Rayleigh friction and Newtonian cooling), and the spectral tendencies of the primitive equations solved sequentially with one spectral wavenumber perturbed by a non-zero value (see details in Liakka et al., 2012). The magnitude of the spectral wavenumber perturbation is an unconstrained parameter that controls the amplitude of the stationary wave response; the spatial patterns of the response are invariant to this parameter. The spectral resolution of LUMA is T21 and vertically represented by 10 sigma levels. The size of the linear operator with this resolution is 7,161 x 7,161 elements. The model uses a ∇^4 type diffusion and the diffusion coefficient is set to 2 x 10^{17} m^4 s^{-1}. The time scales for Rayleigh friction and Newtonian cooling are adopted from Ting (1994): they are 0.9 days at σ = 0.95 and 15 days at all other levels. LUMA is used in chapter 4 to build on the PDRMIP analysis from chapter 3 and investigate further the perturbation to large scale

atmospheric dynamics as a consequence of aerosol perturbations. I installed and set up the model on the Leeds network.

2.3 Met Office SOCRATES model

In Chapter 4, the shortwave heating associated with BC absorption is quantified using the UK Met Office SOCRATES version 15.04 (Suite of Community RAdiative Transfer codes; based on Edwards and Slingo, 1996), using a two-stream (short and long wave) delta-Eddington solver. The code takes in a spectral file (the decomposition of the spectrum into bands), a pre-defined physical state of the atmosphere and the code runs to calculate radiances, fluxes and heating rates. The reader is referred to Edwards and Slingo (1996) for a full description of the model's equations, and to Manners et al. (2017) for a technical description and instructional manual for running the codes.

2.4 FORTE 2.0

FORTE2.0 is an intermediate resolution coupled Ocean Atmosphere General Circulation Model (AOGCM) consisting of the IGCM4 (Intermediate General Circulation Model 4) atmospheric model (Joshi et al., 2015) coupled to the MOMA (Modular Ocean Model – Array) (Webb, 1996) ocean model. The ocean and atmospheric components of the model are coupled once per day using OASIS version 2.3 (Terray et al., 1999) and PVM version 3.4.6 (Parallel Virtual Machine). The model code is readily accessible from the FORTE2.0 Github repository, linked to the Zenodo archive at:

http://doi.org/10.5281/zenodo.3632569. The reader is referred to the model development paper by Blaker et al. (2020) for a complete description.

The model was chosen for its accessibility, local expertise, runtime, and the ease of its configurability. Furthermore, the model did a satisfactory job in simulating the climatology of the Pacific – the region over which my study area focuses. The reader is referred to Chapter 5 for a demonstration of the model's accuracy in representing Pacific climatology. This instilled confidence in the applicability of the model moving forward.

2.4.1 IGCM4

The atmospheric component of FORTE2.0 is IGCM4. IGCM4 is a global spectral primitive equation model based on the configuration of Hoskins and Simmons (1975) with a sigma terrain following vertical coordinate. Two configurations of IGCM4 exist, the standard configuration which is a spectral truncation of T42 (a longitudinally regular grid is used for advection and diabatic processes, with a grid spacing of 2.8^{o}, and a Gaussian grid in latitude, with an irregular grid spacing of approximately 2.8^{o}) and 20 vertical layers, and the version with 35 vertical layers. The former enables studies on troposphere processes whilst the latter enables additional investigations on troposphere-stratosphere processes. The 20-level version is used for the work contributing to this thesis and reaches from the surface to 50 hPa (around 25 km altitude). IGCM4 has been used extensively in research to understand atmospheric dynamical processes (e.g. Wood et al., 2020; McKenna 2019; O'Callaghan et al., 2014). The model is used here because it offers a flexible framework for implementing techniques such as atmospheric nudging and is computationally efficient enabling large ensemble simulations to be performed

on the local HPC at Leeds. The reader is referred to Joshi et al. (2015) for a full description of the model, its development and nuances.

2.4.2 MOMA

MOMA solves the primitive equations discretized using finite differences on an Arakawa B grid (Arakawa and Lamb, 1977). In this configuration, the horizontal resolution is 2^o x 2^o with 15 z-layer levels which increase in thickness with a depth of 30 m at the surface and 800 m at the bottom. It encompasses a linear free surface and uses 'full cell' bathymetry. The vertical diffusion term in MOMA has been set to be stability dependent in the FORTE2.0 configuration, such that the term takes a maximum value at the sea floor and high latitudes and lower values in the upper ocean at low latitudes. Additionally, starting from 5^oN/S the horizontal diffusion in the surface layer increases towards the equator from its default to 20 times this value at the equator. This is set to counteract equatorial upwelling and parameterise the eddy heat convergence associated with tropical instability waves, highlighted by Shaffrey et al. (2009). The reader is referred to Blaker et al. (2020) and Webb (1996) for a full description of the configuration and model, respectively.

2.5 Observational and Reanalysis Datasets

The observational dataset (datasets of direct measurements of climate variables such as SST or precipitation) used in Chapters 5 and 6 is HadISST version 1.1 – which is a combination of monthly globally-complete fields of SST and sea ice concentration on a 1 degree latitude-longitude grid from 1870

to data. The temperatures are reconstructed using a two stage reduced-space optimate interpolation procedure, followed by superposition of quality-improved gridded observations onto the reconstructions to restore detail at a local level. SSTs near sea ice are estimated using statistical relationships between SST and sea ice concentration (Rayner et al. 2003). SLP observational data presented earlier in this chapter is taken from the NCAR Sea Level Pressure dataset, which cover 1899 to present for latitudes 30^{o}N-90^{o}N. Here, the raw data is quality controlled with empirical corrections to take into account changes in instrumentation and station location.

Where reanalysis datasets are used in Chapters 4 and 5, I use data from ERA5, which is the fifth generation of ECMWF atmospheric reanalysis of the global climate covering the period from 1940 to the present day. The reanalysis data presented in this Chapter, CERA-20C (an ECMWF product) which included 10 ensemble members of coupled climate reanalysis, allows an uncertainty envelope to be visualised and quantitied. Reanalysis datasets such as ERA5 combine large amounts of historical observational data and global estimates using advanced modelling and data assimilation systems. The benefits of using reanalysis data include having a more complete spatial and temporal record of the climate versus using observations alone. Furthermore, as model resolution improves, more data can be assimilated into reanalysis datasets. However, they are not without limitations, including observational constraints which can hamper the reanalysis ability to model the climate in certain areas and at certain times. Additionally, different

observational datasets carry different biases which can introduce spurious variability and trends in the reanalysis data.

2.6 Diagnostics

2.6.1 North Pacific Index

The North Pacific Index (NPI) is defined as the area-averaged SLP anomaly in the region 30°N-65°N, 160°E-140°W (Trenberth and Hurrell, 1994).

2.6.2 Rossby Wave Source

The Rossby wave source (RWS) is calculated following Sardeshmukh and Hoskins (1988) as:

$$RWS = -\boldsymbol{v_x}.\nabla\zeta - \zeta D \qquad \textit{Equation 2.11}$$

where $\mathbf{v_\chi}$ is the divergent component of the horizontal wind, ζ is the absolute vorticity, and D is the divergence ($D = \boldsymbol{\nabla}.\mathbf{v_\chi}$). The first term represents the rate of change of vorticity due to vorticity advection by the divergent wind, and the second term represents the rate of change of vorticity due to vortex stretching. Vortex stretching describes the change in length of vortices and the associated change in vorticity due to the conservation of angular momentum. Vortex stretching helps to explain the formation of features such as mesocyclones and tornadoes, which are vertically oriented vortex tubes.

2.6.3 EOF analysis

Empirical Orthogonal Function (EOF) analysis (or Principal Component Analysis) as a technique is employed in this thesis and is used extensively in the literature in the study of Pacific climate variability (e.g., Zhao et al., 2021; Newman et al., 2006; Zhang and Delworth, 2016). For spatial data over time, EOF analysis can be used to extract spatial modes or patterns of variability, which are referred to as EOFs. They are assumed to be stationary and do not evolve with time. The time series associated with each EOF is termed the principal component (PC), with each PC being uncorrelated with other PCs by construction. The technique is purely mathematical, and each extracted mode is orthogonal, implying independence between each mode. There is no physical basis to the method, yet the mode has been shown to be effective in describing modes of climate variability, such as the PDO and PNA patterns (e.g., Newman et al., 2006; Straus and Shukla, 2002; Wei et al., 2018).

Computationally, the EOFs and PCs are calculated in python using a technique called singular value decomposition, which takes a 2-dimensional matrix, *Y,* with time information in the first dimension and spatial information in the second, as:

$$Y = L\Lambda R^T \qquad \textit{Equation 2.12}$$

Where L is a *p x p* matrix containing the left singular vectors, R is a *n x n* matrix containing the right singular vectors and Λ is a diagonal matrix of the same dimension as Y. The EOFs are provided by the columns of L and the PCs by the columns of R.

2.6.4 PDO loading pattern and index

The PDO is calculated as the first EOF of monthly upper-level ocean temperature or sea surface temperature anomalies (SSTAs), calculated as deviations from the climatological seasonal cycle, over the region [20-65^{o}N, 120-260^{o}E]. Before calculating the leading EOF, the temperature anomalies are weighted by the square-root of the cosine of latitude to account for the decrease in area towards the pole. The monthly PC is normalised by the standard deviation to give it unit variance. The larger-scale pattern of temperature anomalies that covaries with the PDO outside of the domain [20-65^{o}N, 120-260^{o}E] is found by calculating at each latitude and longitude the linear regression (LR) between the time series of the monthly mean temperature anomalies and the monthly PDO index. Therefore, this loading pattern shows the temperature anomalies associated with a PDO index of 1. In the presentation of the PC time series, a running mean with a window of 12-months is applied in cases where multi-decadal data is shown, to emphasise the multi-decadal component of the variability.

2.6.5 Mixed Layer Heat Budget Analysis

The mixed layer is a quasi-homogenous region in the upper ocean where there is little variation in temperature or density with depth. The regions owe its existence to turbulent mixing generated from wind stress and heat fluxes at the ocean surface (Kara et al., 2000). The mixed layer depth (MLD) varies regionally and seasonally. Various criteria have been used to define the MLD, mainly using either a temperature (e.g. Alexander et al., 2002) or density gradient (e.g. Chhak et al., 2009) threshold.

Chapter 6 includes the results from a mixed layer heat budget analysis, which isolates the contributions from different processes to the upper ocean (or mixed layer) temperature tendency. The mixed layer heat budget equation may be written as (Murata et al. 2020):

$$\frac{\delta T_M}{\delta t} = -\frac{1}{h}\int_{-h}^{0} u\frac{\delta T}{\delta x}dz - \frac{1}{h}\int_{-h}^{0} v\frac{\delta T}{\delta y}dz - \frac{1}{h}\int_{-h}^{0} w\frac{\delta T}{\delta z}dz + \frac{Q_{net} - Q_{sw}(-h)}{\rho c_p h} - \frac{1}{h}\left(\kappa_v \frac{\delta T}{\delta z}\right)_{z=-h} + \frac{1}{h}\int_{-h}^{0}\left\{\frac{\delta}{\delta x}\left(\kappa_H \frac{\delta T}{\delta x}\right) + \frac{\delta}{\delta y}\left(\kappa_H \frac{\delta T}{\delta y}\right)\right\}dz - \frac{1}{h} w_e \Delta T \quad \textit{Equation 2.13}$$

Where T is the temperature at the domain edges (e.g. at the sea surface), T_m is temperature averaged over the mixed layer; u, v, and w are the zonal, meridional and vertical velocities, respectively; h is the MLD; Q_{net} is the net surface heat flux; $Q_{sw}(-h)$ is the penetrative shortwave radiation at the base of the mixed layer; ρ is the density of seawater (1024 kg m^{-3}); c_p is the specific heat capacity of water (c_p = 3,940 J kg^{-1} K^{-1}); k_H is the horizontal diffusion coefficient and k_v is the vertical diffusion coefficient. The entrainment rate, w_e, and the difference between T_M, and the temperature of entrained water, ΔT, are explicitly calculated.

Summarising, the right-hand side of the equation contains terms for zonal, meridional, and vertical advection, surface heat fluxes, diffusion terms and entrainment. In some studies (e.g., Fathrio et al., 2018), the terms other than advection and surface heat fluxes are referred to as *residual* terms. In this case, equation 2.3 is simplified to the form (where all terms are averaged over the mixed layer).

$$\frac{\delta T}{\delta t} = -u\frac{\delta T}{\delta x} - v\frac{\delta T}{\delta y} - w\frac{\delta T}{\delta z} + \frac{Q}{\rho_o C_p H} + residual \qquad \textit{Equation 2.14}$$

2.7 Statistical Methods

2.7.1 Anomalies

Throughout the thesis, when comparing the responses of perturbed model simulations (e.g., in response to an increase in BC emissions) to control simulations, the term ‘anomaly’ is used. The term is also used in cases when analysing control run simulations when investigating variations about the climatology.

2.7.2 Student’s t-test

The Student’s t-test, employed in results Chapter 3, is a method of determining the statistical significance of a normally distributed population when the population standard deviation is unknown. The t-test tests for the null hypothesis that 2 independent samples have identical average values (assuming the same variances by default). It quantifies the difference between the arithmetic means of two samples (for example, a reference case and perturbed case) and the p-value quantifies the probability of observing the difference in mean assuming the null hypothesis is true. A p-value greater than 0.05 is commonly adopted as a threshold for not rejecting the null hypothesis with a high level of confidence.

2.7.3 Statistical Significance of multi-model and large ensemble data

The method for calculating statistical significance of multi-model mean (MMM) or large ensemble perturbed responses compares the responses to the magnitude of internal variability. For each model or ensemble member, variability is calculated by multiplying the standard deviation of overlapping means of a predefined length (e.g., 50 years) from the control simulation(s) by $\sqrt{2}$. This estimates the variation of the difference in standard deviation between two independent averages, which have the same variance, that would be expected due to internal variability. The median value of the standard deviation across the models or ensemble members is used and a result is said to be statistically significant at the 95% level if the MMM or ensemble mean value lies outside of the bounds ±1.96xSD. This is similar to the method used in IPCC AR5 (2013) to show where a MMM change is large compared to internal variability.

2.7.4 Temporal least squares linear regression

Least squares LR is employed to find the linear relationship between an independent variable, X, and dependent variable, Y, where there are n pairs of observations of X and Y in time $\{(\mathbf{x},\mathbf{y}) = (x_i,y_i) : i=1,...,n\}$. Python function 'scipy.stats.linregress' is utilised. This methodology is used numerous times throughout the thesis, including calculating the PDO loading pattern in Chapter 5 as well as in results Chapter 6, investigating the relationship between AL variability and modulation of heat fluxes.

Chapter 3 - The effect of anthropogenic aerosols on the Aleutian Low - a multi-model analysis

This chapter's contents, along with the contents of chapter 4, have been published as a paper in AMS Journal of Climate (Dow et al., 2020). This paper appears across both chapters with some edits. For example, more detailed explanations of the research process have been provided where helpful, and material has been moved from the Supplementary Information to the main text. The paper has also been edited to avoid overlap with other chapters – specifically, parts of the introduction and method sections instead appear in Chapters 1 and 2 – and to be consistent with the results of other chapters – for example, parts of the method and discussion/conclusions sections have been added to or edited for consistency with Chapters 4, 5 and 6.

3.1 Introduction

The PDO has traditionally been thought of as an internally-generated mode of climate variability, which is a product of the convolution of multiple atmospheric and oceanic processes and feedbacks (Newman et al., 2016; Chen and Wallace, 2016; Newman, 2007). However, recent studies have suggested that the PDO may also be influenced by regional trends in AA through modulation of the North Pacific AL (Smith et al., 2016; Dittus et al., 2021).

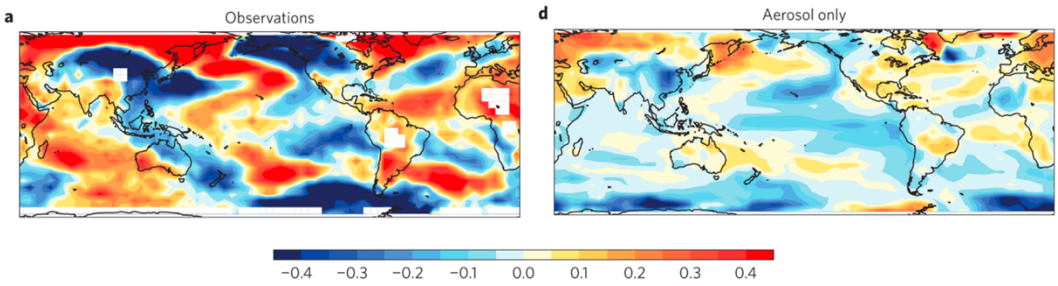

Figure 3.1: Taken from Smith et al. (2016), Figure 2. Panels a,d. Near surface temperature trends for the 15-year period 1998 to 2012. a – observations (averaged over 3 datasets). c – CMIP5 multi-model mean of the effects of AA. Units are ^{o}C per decade.

Smith et al. (2016) examined the transition to a negative phase of the PDO during the early 21st century, and concluded, based on results from coupled CMIP5 climate model simulations forced with different combinations of external forcings, that this was driven in part by changes in AA emissions over recent decades (Figure 3.1). They hypothesised that, in response to the negative aerosol radiative forcing over Asia, modulations in the strength of the Walker circulation and excitation of atmospheric Rossby waves caused a weakening of the AL, inducing a transition to a negative PDO phase through atmosphere-ocean coupling. Other studies have also provided evidence for a causal effect of AA emissions on the strength of the Walker circulation and PDO-like SST variability (e.g. Takahashi and Watanabe, 2016; Allen et al., 2014; Hua et al., 2018). However, this connection was challenged by Dai et al. (2015) and Oudar et al. (2018), who attributed the early 21st century slowdown in GMST trends, and the associated transition of the PDO to its negative phase, to internal variability. Oudar et al. (2018) analysed, using the CanESM2 model, a 50-member initial condition large ensemble forced with AA changes and showed a robust local weakening of the AL (by up to ~0.5 hPa) between 1998-2012 in the ensemble mean; however, they also found non-robust changes in the PDO and GMST trends. The studies by Smith et

al. (2016) and Oudar et al. (2018) analyse the response of the Pacific to transient changes in AA, which help ascertain their contribution to historical climate trends. Taking these studies in isolation, the contrasting results are another example of how aerosols continue to be a major source of uncertainty in understanding past and future climate change (Boucher et al., 2013). Dittus et al. (2021) investigated the importance of the uncertainty in historical AA forcing for the North Pacific using idealised scenarios with scaled AA and precursor emissions. Using a version of the Met Office's HadGEM3-GC3 model, they found that scaling the historical anthropogenic emissions by five factors, ranging from 0.2-1.5, drives a response in the AL through the propagation of a Rossby wave train across the North Pacific. Here, an increase in aerosol emissions is associated with a weaker AL and conversely, a decrease in emissions is associated with a strengthening of the AL. Additionally, using historical ensembles of CMIP6 they concluded that AA likely contributed to an increase in North Pacific SLP over the period 1981-2012, in agreement with Smith et al. (2016) and Oudar et al. (2018). Furthermore, Dittus et al. (2021) provide evidence associating the changes in AA emissions between 1998-2012 to a more negative PDO phase, in agreement with Smith et al. (2016) but counter to the results of Oudar et al. (2018). None of the simulations used in Smith et al. (2016) and Dittus et al. (2021) separated the roles of different aerosol types for historical trends. Johnson et al. (2019) showed that in an idealised experiment with a global increase in BC, the AL weakened. Therefore, it remains unclear as to the relative influence of scattering and absorbing aerosols on the AL.

It is this uncertainty of the impact of AA on the PDO across studies which motivates the work conducted in this chapter. I focus on simulations which perform idealised step change perturbations, rather than transient changes, in order to isolate different aerosol species and a clean signal.

3.2 Aim and research questions

This chapter aims to better understand the proposed effects and mechanisms for a possible influence of AA on the PDO. To this end, I analyse global climate model data from a set of idealised experiments that include large global and regional perturbations of AA with the aim of addressing the following research questions:

1. Do changes in AA, globally and regionally, have a robust impact on the AL?
2. Does any response of the AL to idealised perturbations of AA agree with the findings of Smith et al (2016), Oudar et al (2018) and Dittus et al. (2021) who examine the AL response to transient changes in emissions?
3. What are the relative influences of scattering and absorbing aerosols on the AL?
4. What is the role of ocean feedbacks for the AL response to aerosol forcing?

3.3 Methods

3.3.1 Global climate model simulations

The analysis uses climate model simulations from the Precipitation Driver and Response Model Intercomparison Project (PDRMIP; Myhre et al., 2017), which were introduced in detail in Section 2.1. All model data are interpolated to a common 2.5° x 2.5° longitude-latitude grid. The analysis focuses on the PDRMIP experiments that applied a step-increase in AA from a baseline state at global (BCx10 and Sulx5) and regional scales (BCx10a, Sulx10a, Sulx10e), whilst analysing the impact of a doubling of CO_2 (CO_2x2). The regional 10-fold increase in BC and sulphate over Asia is constrained to [10°N-50°N, 60°E-140°E; BCx10a and Sulx10a] and in Europe over [35°N-70°N, 10°W-40°E; Sulx10e], respectively. The MMM change in aerosol burden in each experiment, along with the zonal mean burden change for each model, is shown in Figure 3.2.

The analysis focuses on years 51-100 from the coupled experiments and all years except the first year in the prescribed SST simulations, which was discarded for spin-up. Table 3.1 contains an overview of the models and experiments analysed in the study. Table 2.1 provides further detail on the aerosol processes across the models. All the analysis presented in the study refers to the extended boreal winter season November through March (NDJFM) as this is the season when the AL is most prominent and has been connected to the PDO (Trenberth et al., 2014; Smirnov et al., 2013).

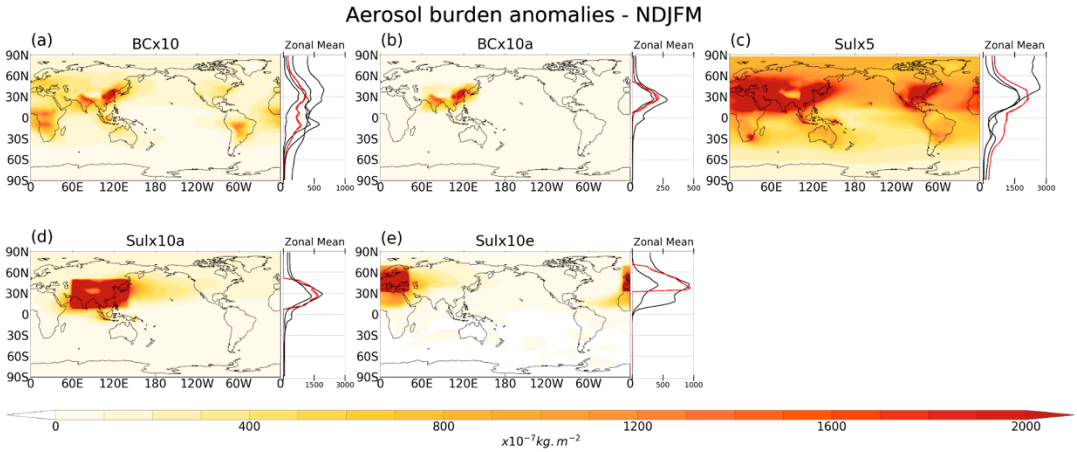

Figure 3.2: NDJFM mean MMM aerosol burden anomalies [x10^{-7} kg m^{-2}] in the (a) BCx10, (b) BCx10a, (c) Sulx5, (d) Sulx10a and (e) Sulx10e experiments. Side panels show the zonal mean aerosol burden anomalies in individual models; note the different x-axis scales. The red lines denote the prescribed aerosol concentration models (identical by construction) and the black lines show models with prescribed emissions (see Table 3.1).

Most of the figures in this chapter show the PDRMIP MMM responses. The significance of the MMM responses is assessed by comparing them to the magnitude of internal variability using the method described in Section 2.6.3. Where results from individual models are presented, the statistical significance of the simulated changes with respect to the control simulations is assessed using a two-sided Student's t-test ($p<0.05$), described in Section 2.6.2.

Model	**Prescribed SST length (years)**	**Aerosol prescription**	**Experiments**	**Key references**
CanESM2	*15*	Emissions	*BCx10, Sulx5, CO_2x2*	*[Arora et al., 2011]*
CESM1-CAM4	*30*	Prescribed Concentrations	*BCx10, Sulx5, Sulx10a, Sulx10e, CO_2x2*	*[Gent et al., 2011; Neale, 2004]*
HadGEM2	*30*	Emissions	*BCx10, Sulx5, CO_2x2*	*[Martin et al., 2011]*
HadGEM3	*15*	Prescribed Concentrations	*BCx10, BCx10a, Sulx5, Sulx10a, Sulx10e, CO_2x2*	*[Bellouin et al., 2011; Walters et al., 2014]*
NorESM1	*30*	Prescribed Concentrations	*BCx10, BCx10a, Sulx5, Sulx10a, Sulx10e, CO_2x2*	*[Bentsen et al., 2013; Iversen et al., 2013; Kirkevåg et al., 2013]*
SPRINTARS	*15*	HTAP2 Emissions	*BCx10, BCx10a, Sulx5, Sulx10a, Sulx10e, CO_2x2*	*[Takemura et al., 2005; Takemura et al., 2009; Watanabe et al., 2010]*
CESM1-CAM5	24	Emissions	BCx10, BCx10a, Sulx5, Sulx10a, Sulx10e, CO_2x2	[Hurrell et al., 2013] This is the same model as [Kay et al., 2015], but with a coarser resolution [Otto-Bliesner et al., 2015]
ECHAM-HAM	30*	Emissions	BCx10, Sulx5*, CO_2x2	[Zhang et al., 2012; Hodnebrog et al., 2019]
GISS	15	Prescribed Concentrations	BCx10, BCx10a, Sulx5, Sulx10a, Sulx10e, CO_2x2	[Schmidt et al., 2014]
IPSL-CM5A	30	Prescribed Concentrations	BCx10, BCx10a, Sulx5, Sulx10a, Sulx10e, CO_2x2	[Dufresne et al., 2013]
MPI-ESM	15	Climatology year 2000	CO_2x2	[Giorgetta et al. 2013]

Table 3.1: List of the models and experiments used in this study. HTAP2 = Hemispheric Transport Air Pollution, phase 2. The subset of the models which included the necessary diagnostics for more detailed analysis of the dynamical mechanisms in Chapter 4 are highlighted by italics. Asterisks indicate experiments that performed the prescribed SST simulation only.

3.4 Results

3.4.1 Large-scale climate response to forcings

3.4.1.1 Surface air temperature response

The spatial patterns of the surface air temperature responses across the PDRMIP simulations are shown in Figure 3.3 and have been presented in Richardson et al. (2019). There is an increase in global mean surface air temperature associated with the CO_2x2, BCx10 and BCx10a experiments, whilst the sulphate experiments are associated with global cooling. The spatial pattern of the temperature change is broadly comparable across the BCx10, BCx10a, Sulx5 and Sulx10a aerosol experiments, which show a positive east-west temperature gradient across the extra-tropical North Pacific. More broadly, the largest change in surface air temperatures is evident in the northern polar regions, with significant increases associate with BCx10, BCx10 and CO_2x2 and decreases with Sulx5, Sulx10a and Sulx10e. Similarly, the largest temperature increases and decreases are evident across land regions in the northern hemisphere, such as North America and Eurasia. The Sulx10e experiment is associated with less of a significant response over the Pacific Ocean, which could be attributed to its reduced aerosol burden and more remote source region in comparison with the Sulx10a experiment.

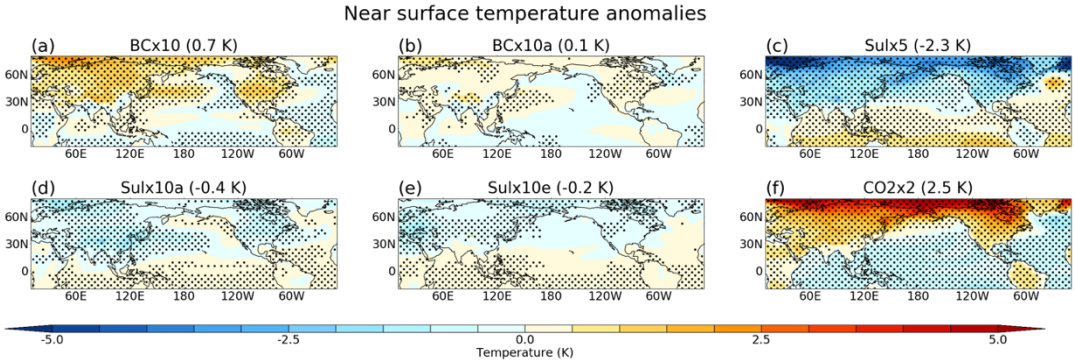

Figure 3.3: MMM annual mean surface air temperature [K] anomalies in the six coupled perturbation experiments. Stippling indicates differences that are significant at the 95% confidence level (see Methods). The GMST change in each experiment (see headers) has been subtracted to highlight the regional patterns.

3.4.1.2 Precipitation responses

The precipitation responses (Figure 3.4) in the PDRMIP simulations, and their driving mechanisms, have been described in detail in e.g., Samset et al. (2016), Liu et al., (2018), Richardson et al., (2018). Here I briefly summarise the key changes in precipitation that are relevant for interpreting the AL response to the aerosol perturbations and the role of teleconnections in the response. BCx10 and the two sulphate perturbation experiments show a reduction in annual global mean precipitation, with Sulx5 showing the largest decrease of ~0.2 mm day^{-1} (-7%). BCx10 shows increased precipitation at high northern latitudes and decreases across the northern midlatitudes. Tropical precipitation is substantially reduced (by ~1 mm day^{-1}, equivalent to a 10% local reduction) in Central and South America, as well as in the equatorial Indian Ocean, indicating a northward shift of the ITCZ away from the cooler hemisphere (c.f. Kang et al., 2008). In the southern extratropics, there is a dipole pattern of precipitation change that is associated with a poleward shift of the southern hemisphere storm track (Wood et al., 2020). BCx10a shows a near-zero change in global precipitation, which suggests that regions of net increased and decreased precipitation are of comparable

magnitude. Generally, regional precipitation changes are weaker and less robust in BCx10a, but there is a coherent decrease in the tropical Indian Ocean by 0.2-0.4 mm day^{-1} (-3% local reduction).

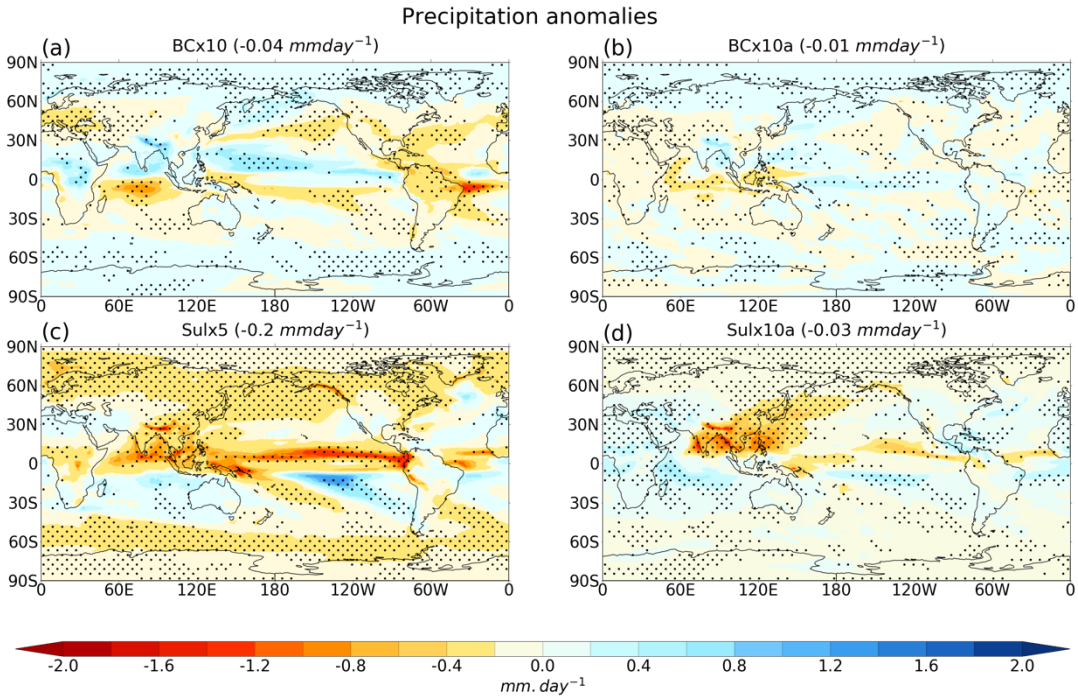

Figure 3.4: Annual mean MMM precipitation [mm day^{-1}] anomalies in four coupled aerosol perturbation experiments. Stippling indicates differences that are significant at the 95% confidence level. The global average precipitation anomaly is given in brackets.

In Sulx5 the regional precipitation changes are generally larger and more robust across the models. There are reductions in precipitation across the northern and southern high latitudes, over India, south-east China and in the Indian Ocean, in the equatorial Pacific indicating a southward shift of the ITCZ, and in the North Pacific, with local anomalies exceeding 1.6 mm day^{-1} (up to -27% of the local mean). In Sulx10a, there is increased precipitation across Africa, the Middle East and the western Indian Ocean, and decreased precipitation over India, China and in the northern subtropics and the North Pacific. The precipitation anomalies in Sulx10a reach up to around ±1.5 mm day^{-1} locally, with significant reductions in precipitation over Asia and into the

North Pacific caused by a combination of factors including: a weakening monsoon circulation, a decrease in surface temperature over the North Pacific, and a southward shift of the ITCZ (Liu et al., 2018). Note there is generally greater inter-model spread in the precipitation responses to BC as compared to the sulphate perturbations, as indicated by the smaller amount of stippling in Figure 3.4.

3.4.2 North Pacific response to global and regional climate perturbations

Figure 3.5 shows the near-surface air temperature anomalies, focused on the North Pacific, from the coupled perturbation experiments. To compare the aerosol responses to the effect of well-mixed GHGs, I also show results from an instantaneous doubling of carbon dioxide (CO_2x2) experiment.

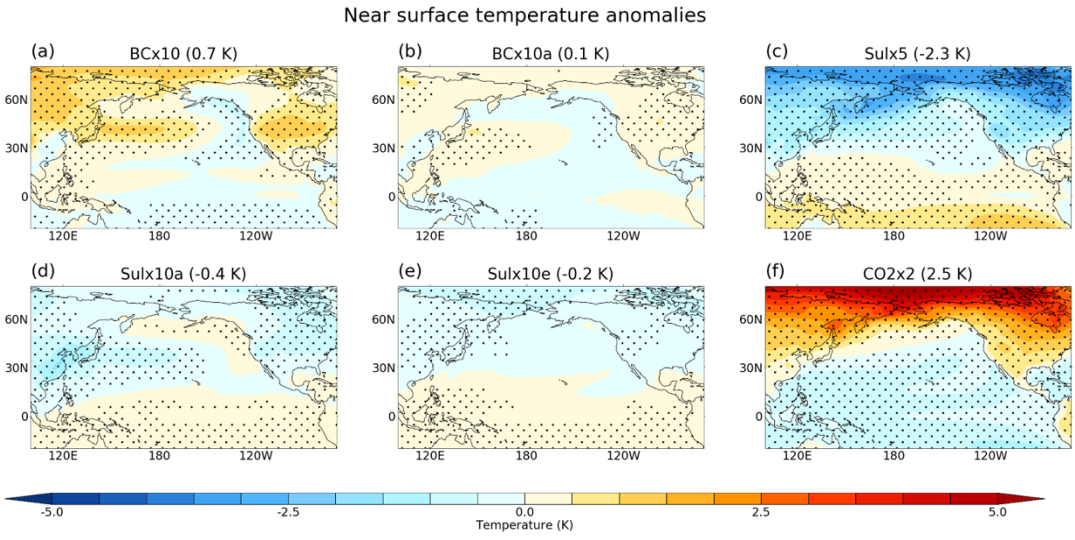

Figure 3.5: MMM annual mean surface air temperature [K] anomalies in the coupled perturbation experiments. Stippling indicates differences that are significant at the 95% confidence level (see Methods). The GMST change in each experiment (see headers) has been subtracted to highlight the regional patterns.

The BC and CO_2 perturbations drive global average warming, while the sulphate perturbations drive global cooling. The magnitude of global temperature change varies across the experiments mainly due to different ERFs induced by each perturbation (Richardson et al., 2019). All the experiments show enhanced temperature changes over land areas and in the Arctic, broadly consistent with the canonical surface temperature response to anthropogenic forcings (e.g., Joshi and Gregory, 2008). Interestingly, the BCx10, Sulx10a and, to a lesser extent, the BCx10a show a horseshoe-like pattern of anomalous temperature in the North Pacific that is reminiscent of the PDO. The patterns correspond to a negative PDO-like anomaly for the BCx10 and BCx10a experiments, and a positive PDO-like anomaly for Sulx10a.

Figure 3.6 shows the SLP responses in the experiments; individual model responses in the BCx10, BCx10a, Sulx5 and Sulx10a experiments are also shown in Figures 3.7-3.10, respectively. The BCx10 perturbation induces a robust weakening of the AL (Fig. 3.6 panel a). The AL also weakens in the BCx10a experiment (Fig. 3.6 panel b), but the magnitude is only about 25% of the change in BCx10 and the response is less consistent across models (Figure 3.7). Positive SLP anomalies over the North Pacific are only evident in ~50% of the models for BCx10a, and only CESM1-CAM5 shows a statistically significant response in the North Pacific (Figure 3.8). Furthermore, with the exception of SPRINTARS, which does not show a significant response in the North Pacific in either BCx10 or BCx10a, all models that performed both experiments show a larger and more robust weakening in response to the global BCx10 perturbation (also shown later in Figure 3.11).

Therefore the multi-model mean across both experiments does not appear to be sensitive to the composition of models making up the groups. The results of the MMM implies that sources of BC and associated climate interactions outside of Asia are important contributors to the AL response in BCx10.

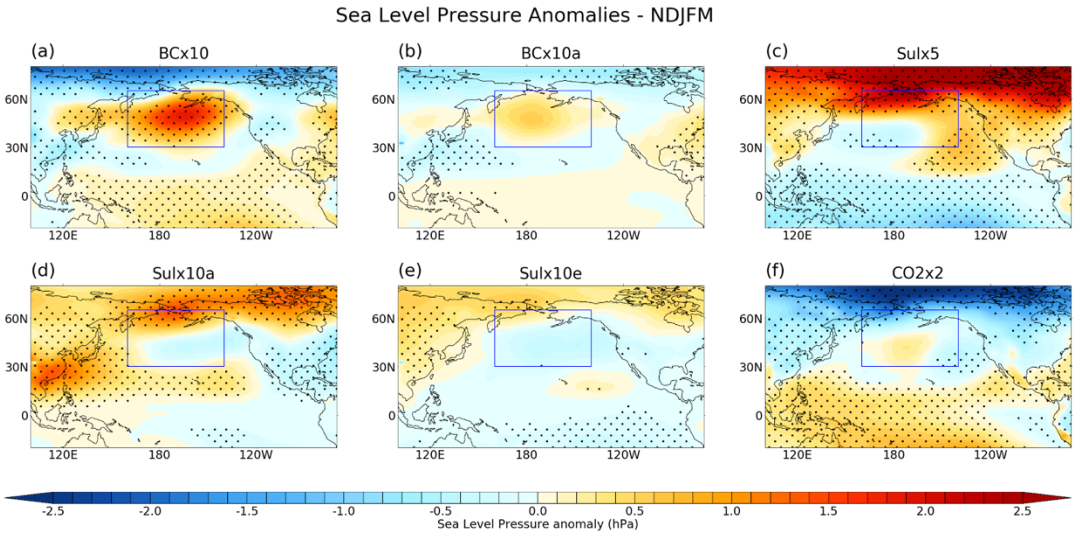

Figure 3.6: MMM NDJFM SLP [hPa] anomalies in the coupled perturbation experiments: (a) BCx10, (b) BCx10a, (c) Sulx5 (d) Sulx10a, (e) Sulx10e, (f) CO_2x2. Stippling indicates differences that are significant at the 95% confidence level. The box is the region used to define the NPI.

The SLP response in Sulx5 (Fig. 3.6 panel c) does not project strongly onto the climatological AL structure, while the regional sulphate experiments (Sulx10a and Sulx10e; Fig. 3.6 panels d,e) exhibit a meridional dipole SLP pattern in the North Pacific, with reduced pressure to the south and increased pressure over the Arctic. The SLP response to Sulx5 (Fig. 3.6 panel c) also displays a significant latitudinal dipole across the North Pacific, with reduced pressure to the west and increased pressure to the east; this pattern of SLP anomalies in the North Pacific is broadly similar to that found by Qin et al. (2020) when assessing the surface patterns associated with aerosol forcing over the historical period. There is agreement across the models that SLP increases in the Arctic in response to Sulx5 and Sulx10a. The CO_2x2

experiment shows a comparatively small increase in SLP over part of the AL sector; however, the largest changes occur in the Arctic, where there are stronger negative SLP anomalies (Fig. 3.6 panel f), though not all of the models show this pattern.

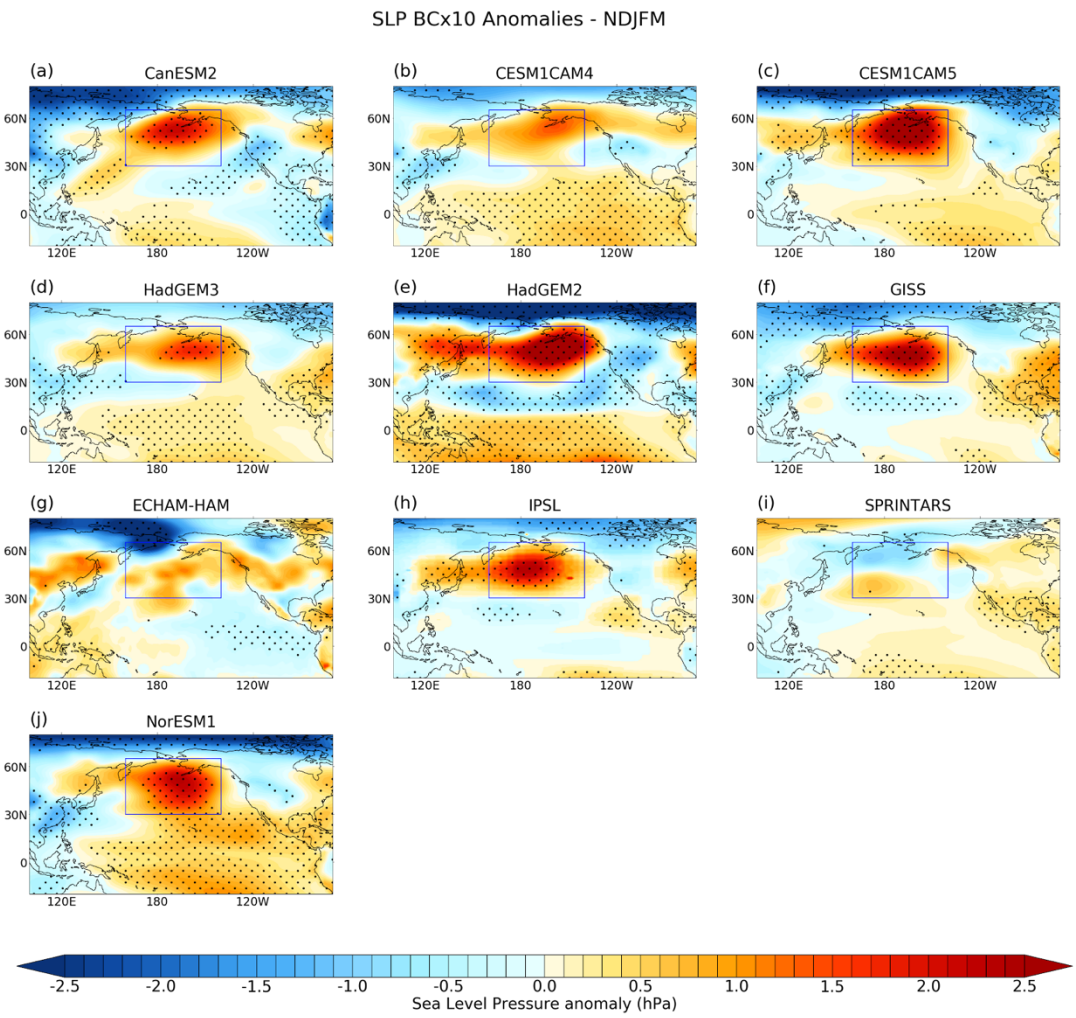

Figure 3.7: Individual model NDJFM mean SLP [hPa] anomalies in the coupled BCx10 perturbation experiment. Stippling shows regions of significant differences based on a Student's t-test with p<0.05. The box is the region used to define the NPI.

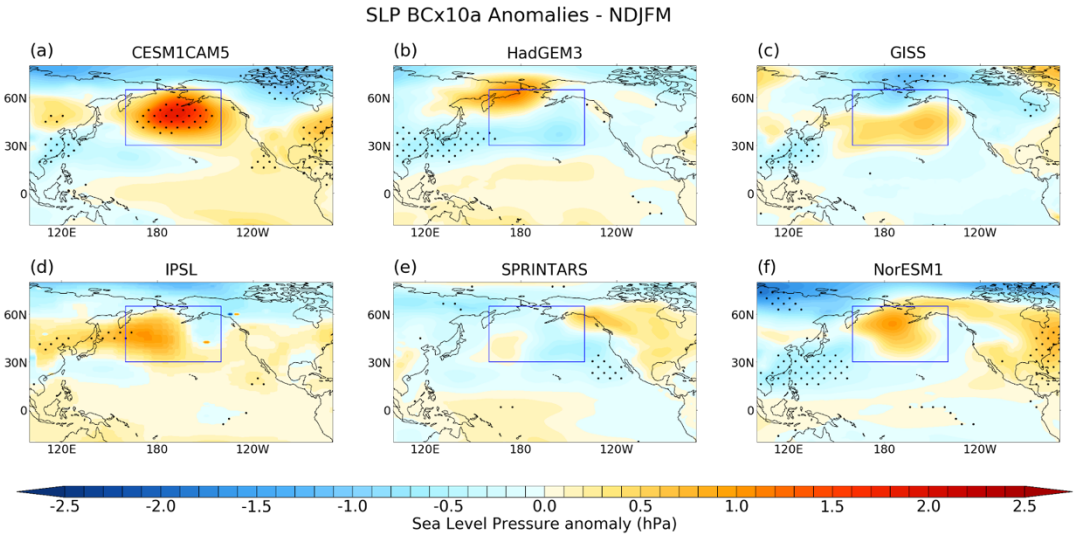

Figure 3.8: As in Figure 3.7 but for the BCx10a perturbation experiment. Note that different models are shown (see Table 3.1).

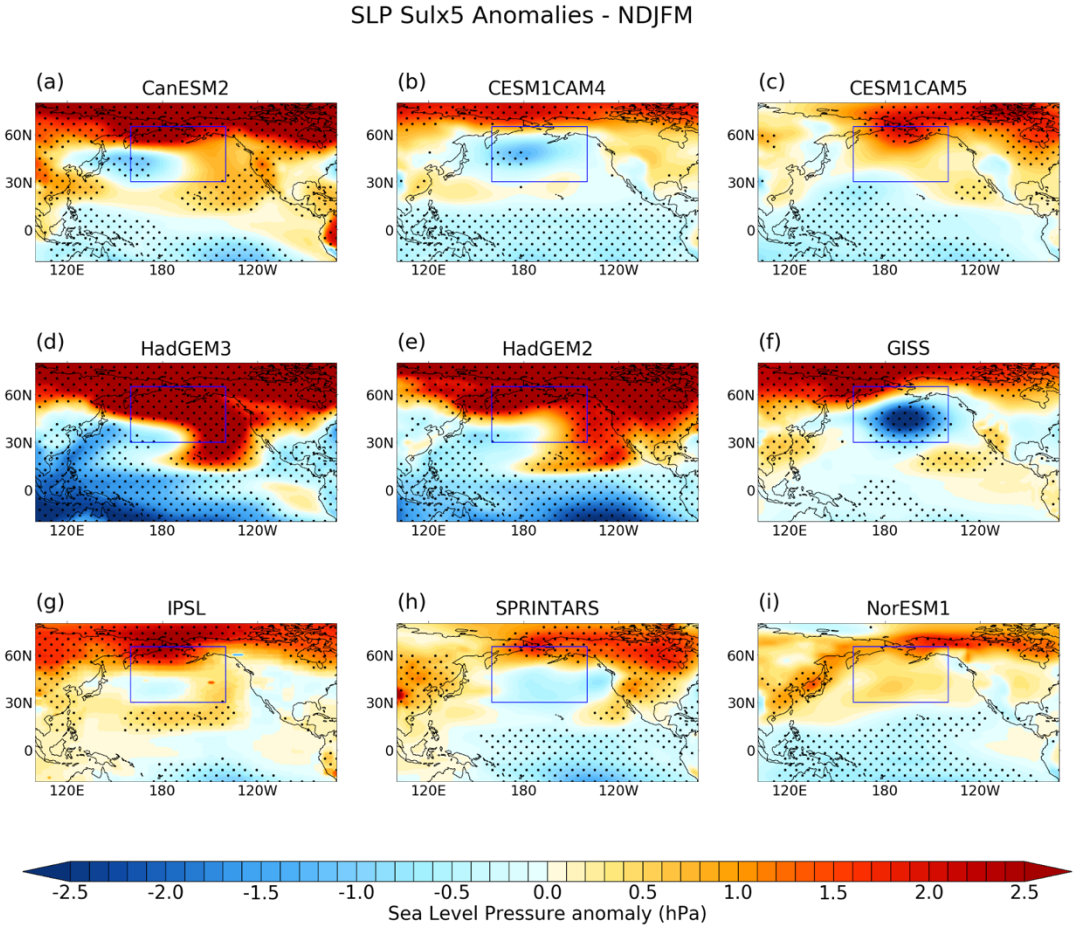

Figure 3.9: As in Figure 3.7 but for the Sulx5 perturbation experiment. Note that different models are shown (see Table 3.1).

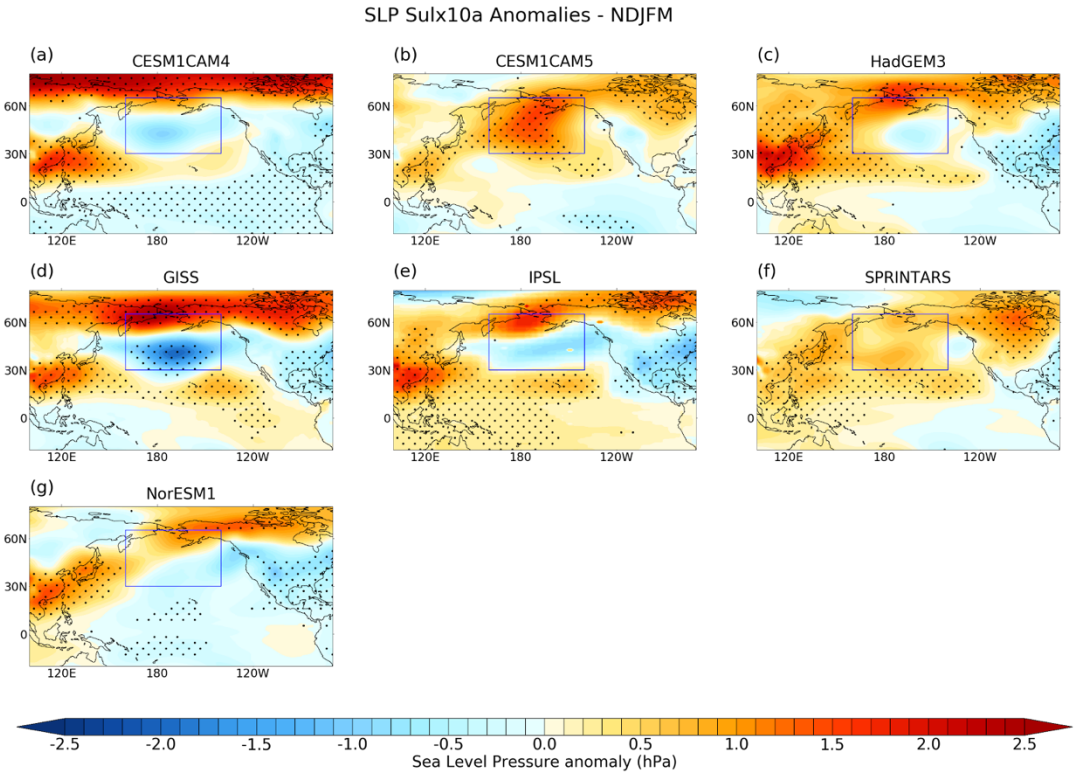

Figure 3.10: As in Figure 3.7 but for the Sulx10a perturbation experiment. Note that different models are shown (see Table 3.1).

The NPI anomalies for individual models in both the coupled and prescribed SST experiments are shown in Figure 3.11. A comparison between the coupled and prescribed SST experiments enables an assessment of the role of atmosphere-ocean coupling for the long-term NPI response to each perturbation. The MMM North Pacific spatial SLP anomalies in the prescribed SST experiments are shown in Figure 3.12 for reference. For BCx10, seven out of ten models show a significant increase in the NPI when SSTs are held prescribed; there is no discernible difference in NPI response between the fully coupled (left column) and prescribed SST (right column) simulations, implying that atmosphere-ocean coupling plays a relatively minor role for the NPI response to BCx10. In BCx10a, the NPI response is weaker and generally less significant in the models, though the MMM anomaly is positive and around 25% of the magnitude in BCx10.

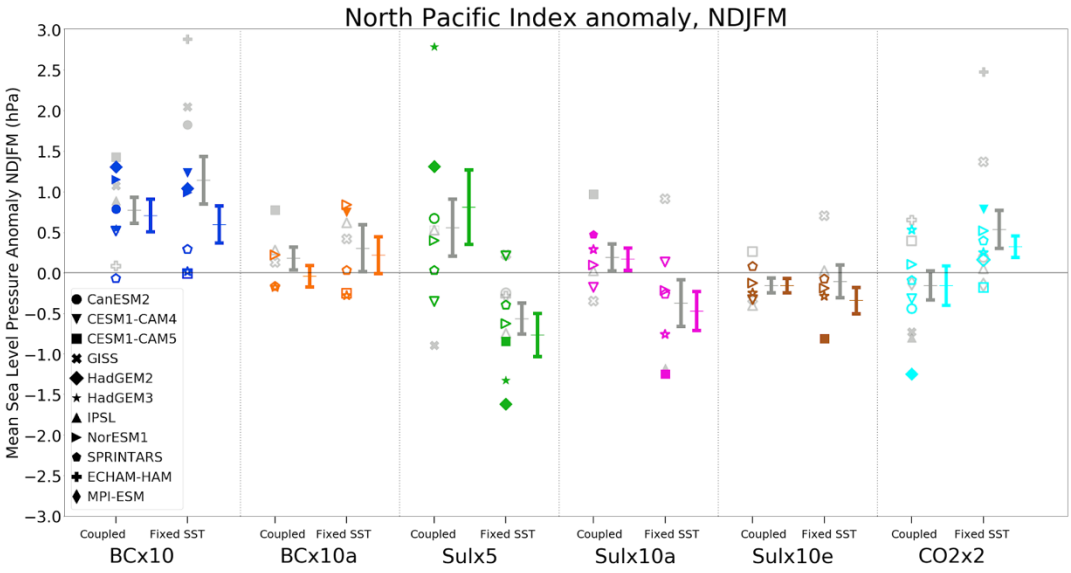

Figure 3.11: The NPI anomaly (averaged over 30°N-65°N, 160°E-140°W) [hPa] averaged for NDJFM. For each experiment (column), values are shown for coupled (average years 51-100; left) and prescribed SST experiments (average after year 1; right). Coloured symbols show the model subsets used to create input fields for LUMA (Chapter 4), with grey symbols showing other models. Filled symbols represent differences that are significant at the 95% confidence level, and vice versa for open symbols. The line-whisker symbols show the MMM ±1 standard error for each experiment.

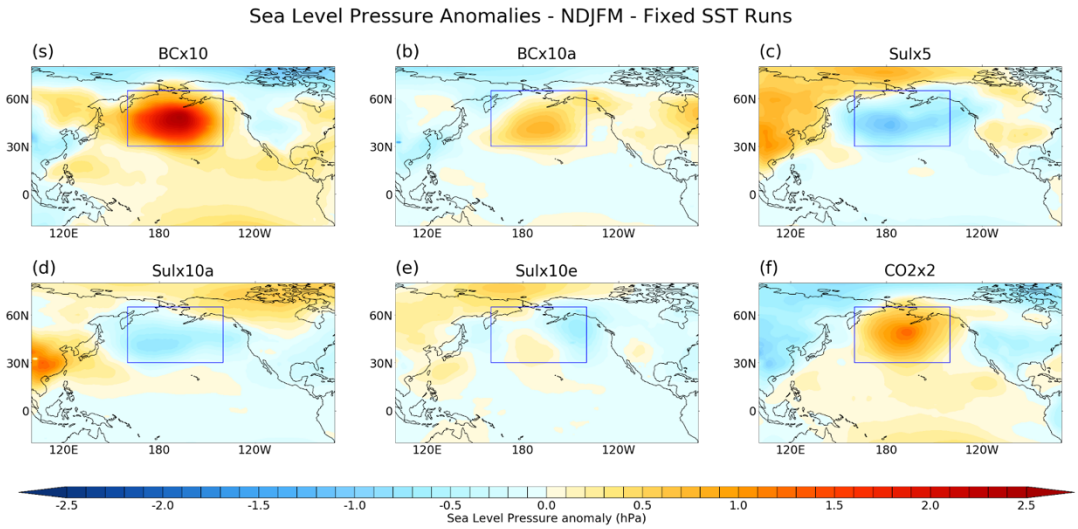

Figure 3.12: As in Figure 3.6, but for the prescribed SST experiments. Note that given the shorter averaging period, the MMM differences in the prescribed SST experiments are generally smaller than internal variability (i.e. no stippling is shown). However, note that individual models do show significant North Pacific responses in these experiments (see Figure 3.11).

The intermodel spread is largest in the coupled Sulx5 experiment, where two models out of nine show a significant increase in NPI, one shows a significant decrease and six show no significant change from the control experiment. The coupled MMM response to Sulx10a shows a small increase in the NPI, which is qualitatively consistent with the weakening of the AL identified by Smith et al. (2016) and Oudar et al. (2018). However, only two out of seven models for Sulx10a show an NPI response that is significant relative to internal variability. Furthermore, the pattern of SLP anomalies in Sulx10a does not strongly project onto a modulation in the strength of the AL, with the NPI area-average reflecting a cancellation of opposite sign anomalies between the southern and northern parts of the NPI region (Fig. 3.6 panel d). Interestingly, both Sulx5 and Sulx10a show an opposite sign of NPI response between the prescribed SST and coupled simulations, with a clear shift in the distribution of models from generally negative to positive NPI anomalies. The CO_2x2 experiment also exhibits a similar behaviour but in the opposite sense, implying that the ocean plays an important role in the long-term AL response to sulphate and CO_2 forcing and that ocean feedbacks counteract the rapid atmospheric adjustment in the North Pacific. Since these forcings induce larger surface temperature changes than BC (Figure 3.3), this suggests the NPI response is mediated by surface temperature driven feedbacks. Lastly it is noted that in every experiment there is substantial intermodal spread in the NPI response, with at least one model having an opposite sign of response to the MMM.

3.4.2 Upper tropospheric response to external drivers in North Pacific

The analysis so far has focused on the surface response in the PDRMIP perturbation experiments. This section investigates the response in the upper troposphere focusing on the coupled model experiments that isolate the effects of global and Asian aerosol forcing: BCx10, BCx10a, Sulx5 and Sulx10a.

3.4.2.1 Upper tropospheric geopotential height responses

The 300 hPa eddy geopotential height anomalies in the four selected aerosol perturbation experiments are shown in Figure 3.13. In BCx10 (Fig. 3.13 panel a), across the North Pacific sector, there is an anomalous ridge with two local maxima of around 25-30 m over China and in the North Pacific and an anomalous trough of around 15-20 m centred off the west coast of North America. Comparison with the surface response (Fig. 3.6 panel a) shows a westward tilt that resembles the vertical structure of stationary Rossby waves. In the BCx10a experiment, the anomalous upper tropospheric ridge over China is weaker (~10 m) and located further south than in BCx10. This suggests that remote BC aerosols are contributing substantially to the ridge over China in BCx10. Within the North Pacific region itself, there is an anomalous ridge with a local maximum of ~10 m on the western side of the basin, and a trough with a similar amplitude to the east in BCx10a. These midlatitude anomalies are weaker and shifted westward by around 20° longitude compared to BCx10. In Sulx5, there is a ridge with a local maximum of around 20 m extending across the North Pacific sector, a trough with a local maximum of around 10 m to the south, and downstream a reversal in the meridional pattern with a trough over the northern USA (local maximum ~20

m), and a ridge with similar amplitude over the southern USA. The midlatitude response to sulphate aerosols is generally more baroclinic than for BC aerosol. For example, in both Sulx5 and Sulx10a there is a trough in the upper troposphere over the northern USA and Canada, whereas at the surface the experiments show a ridge in this region.

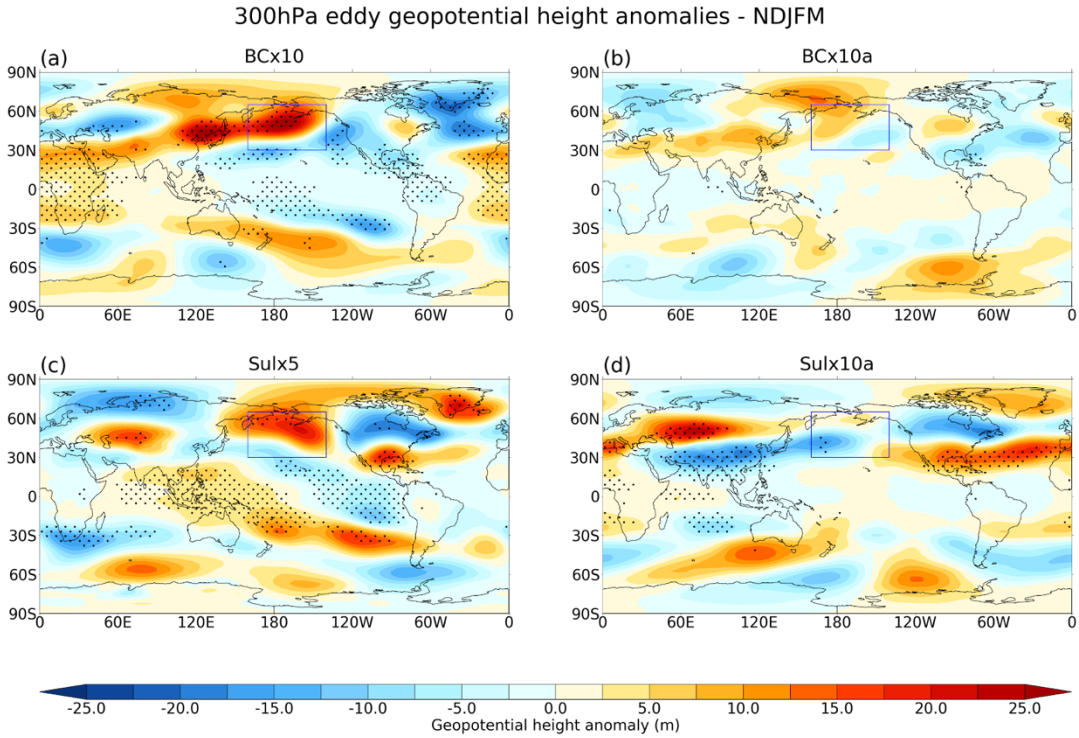

Figure 3.13: MMM NDJFM 300 hPa eddy geopotential height [m] anomalies in the (a) BCx10, (b) BCx10a, (c) Sulx5 and (d) Sulx10a experiments. The MMM is constructed using the subset of models that provided 3-D output variables used as inputs to LUMA in Chapter 4 (see Table 3.1). Stippling indicates differences that are significant at the 95% confidence level. The box is the region used to define the NPI.

3.4.2.2 Rossby wave source responses

Changes in the upper level flow such as those shown in Figure 3.13 may be associated with anomalous stationary wave activity (e.g. Wills et al. 2019). Figure 3.14 shows the anomalous Rossby wave source (RWS; Eq. 2.6 in Methods) in the four aerosol perturbation experiments. The RWS represents anomalous sources and sinks of vorticity, which can induce meridionally

propagating Rossby wave trains (e.g., Hoskins and Karoly, 1981; Sardeshmukh and Hoskins 1988). Smith et al. (2016) found that AA caused a negative trend in RWS east of Japan between 1998-2012 (their Fig. S9). They proposed that, in line with studies by Ming et al. (2011) and Lewinschal et al. (2012), changes to AA emissions impacts the direct and indirect radiative effects of AA. The combined radiative forcing due to the direct and indirect effects act to alter tropospheric convection, therefore inducing anomalous upper-tropospheric divergence. Rossby waves emanating from this region propagate north-eastward across the North Pacific, and thereby weaken the AL.

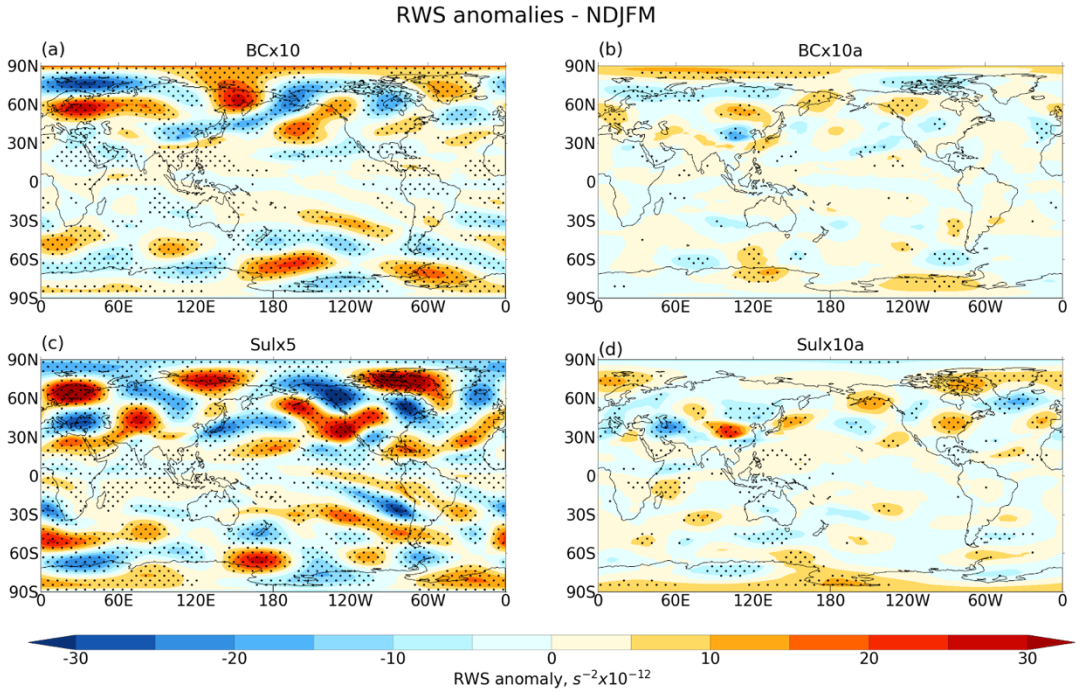

Figure 3.14: NDJFM RWS [x10^{-12} s^{-2}] anomalies in the coupled experiments, calculated using the NDJFM MMM zonal and meridional wind fields. The BCx10 and Sulx5 responses are scaled by 0.5x for display purposes. Stippling indicates differences that are significant at the 95% confidence level.

Figure 3.14 panel d shows that in the Sulx10a experiment there is a positive RWS anomaly east of Japan – which is opposite in sign to the anomaly highlighted by Smith et al. (2016) – but the largest positive RWS

anomalies occur further upstream in central China. In Sulx5, the RWS anomaly to the east of Japan has the opposite sign (Fig. 3.14 panel c), suggesting that the response to local forcing from Asian aerosols is overwhelmed by the response to aerosols outside of this region. Large RWS anomalies across the northern extratropics suggest that remote sources may also help influence the circulation response over the North Pacific region. The BCx10a experiment shows dipole RWS anomalies upstream of the North Pacific over eastern China and Russia, with a positive anomaly around 45-60°N and a negative anomaly around 30-45°N (Fig. 3.14 panel b). The negative node of this pattern is present in BCx10 but is around twice the magnitude and extends further east over Japan and into the North Pacific sector (Fig. 3.14 panel a). In addition, the BCx10 experiment demonstrates a positive RWS node further downstream in the central-eastern North Pacific, around 30-45ºN which extends north-east over north-west Canada. This represents the second major node visible across the North Pacific, not apparent in the BCx10a experiment, and suggests sources of BC outside of Asia affect North Pacific tropospheric dynamics. Further analysis indicates that for all experiments the anomalous RWS in the northern extratropics is predominantly caused by changes in upper-level divergence rather than by changes in the meridional gradient in absolute vorticity. Figure 3.15 demonstrates this for the case of the BCx10 coupled experiments by showing the contribution by the changes in upper-level divergence ($\zeta_0 D'$, panel c) to the change of vorticity due to vortex stretching (ζD, panel b), which explains most of the change to the RWS anomaly (panel a).

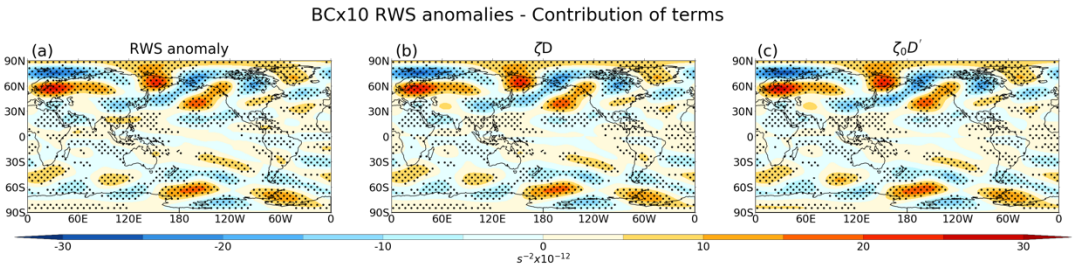

Figure 3.15: NDJFM RWS [x10^{-12} s^{-2}] anomalies for the BCx10 MMM coupled experiments (a) and the contribution to the anomaly by the change in vorticity due to vortex stretching (b). The contribution to (b) from the changes to upper-level divergence are shown in panel c. The responses are scaled by 0.5x for display purposes. Stippling indicates differences that are significant at the 95% confidence level.

3.5 Discussion and Conclusions

Smith et al. (2016) found that models participating in CMIP5 simulated a weakening of the AL over the period 1998-2012 in response to a transient increase in AA emissions from East Asia. This weakening corresponded to an increase in SLP in the North Pacific over the 15 year period of up to 0.75-0.9 hPa. Dittus et al. (2021) also found that models participating in the Coupled Model Intercomparison Project phase 6 (CMIP6) simulated a weakening of the AL over the early 21st century, similar to Smith et al. (2016). Caution should be taken when comparing the long-term centennial response in the PDRMIP coupled experiments with the decadal trends considered by Smith et al. (2016) and Dittus et al. (2021), particularly given the idealised, large step increases in aerosol applied here, which have a strongly contrasting pattern to the observed reduction in emissions over Europe and North America and concurrent increase over Asia in the past few decades (Smith et al. 2016). The sign of the NPI response to a step sulphate aerosol forcing changes between the prescribed SST and coupled experiments and the decadal response falls somewhere between these two timescales (i.e. transient rather than equilibrium). Furthermore, the pattern of aerosol forcing

in Sulx10a (Fig. 3.2) is different from that observed in recent decades (Samset et al., 2019). Nevertheless, the multi-model mean NPI anomaly in the Sulx10a experiment is only 0.2 hPa, which is considerably weaker than the change identified by Smith et al. (2016) despite the regional aerosol perturbation in Sulx10a being many times larger than the trend over 1998-2012. Only CESM-CAM5 produces an NPI anomaly in the coupled experiments with a comparable magnitude to the changes found by Smith et al. (2016).

Oudar et al. (2018) used the CanESM5 model to investigate drivers of AL trends over the same period as Smith et al. (2016). They showed that a 50-member historical ensemble including only anthropogenic aerosol forcing produced a weakening of the AL over 1998-2012 by up to around 0.45-0.5 hPa locally, but this had no robust effect on the PDO or GMST trends. One of the contributing models to PDRMIP is CanESM2, a predecessor version of the Canadian Earth System Model. CanESM2 did not perform the Sulx10a experiment, but in the Sulx5 experiment the model does show an increased NPI by 0.7 hPa that is consistent with a weakening of the AL.

The hypothesis proposed by Smith et al. (2016) posits that weakening of the AL is, in part, due to modulation of the Walker circulation. I find significant near surface temperature warming in the North Atlantic relative to the North Pacific resulting from differential sulphate loading (evident in the Sulx10a coupled experiment, Figure 3.3 panel d). These conditions have been shown to be conducive to a strengthening of the Walker circulation (McGregor et al., 2014, Qin et al., 2020). Therefore, the mechanism posited by Smith et al. (2016) could explain the difference in strength of AL response between the prescribed SST and coupled model set-ups; a comparison of the dynamical

processes operating in the prescribed SST and coupled experiments would be an area ripe for future work (see Chapter 7).

The transient simulations used by Smith et al. (2016) and Oudar et al. (2018) incorporated multiple aerosol species with the combined effect being considered to be primarily a consequence of increasing sulphate emissions in China. Given the much larger change in sulphate emissions with respect to BC emissions worldwide, this is a reasonable assumption; however, here I have shown that increased BC emissions over Asia drives a weakening of the AL, and this could compound any effects from increasing sulphate emissions. For instance, Smith et al. (2016) found a horseshoe pattern in near surface temperature trends over the North Pacific in response to transient changes in aerosol emissions, corresponding to a negative-PDO (their Figure 2d) which resembles most closely the response seen to BCx10 (Fig. 3.3).

The weakening of the AL in response to BC is in agreement with the results of Johnson et al. (2019), who showed that in response to 10-fold increase in BC emissions with SSTs held constant, a pattern of lower tropospheric zonal wind anomalies in the North Pacific that is indicative of a weakened AL. The studies of Johnson et al. (2019) and Mahajan et al. (2013) found that under two different experimental set-ups (atmosphere only and mixed-layer ocean, respectively), diagnostics such as top-of-atmosphere radiative forcing, GMST, precipitation and cloud cover scale linearly in response to different BC scaling factors. This allows us to make tentative assumptions regarding the linearity of the AL response to a spatially constant change in BC loading. Additionally, my results concur with Teng et al. (2012) who showed, using a fully coupled atmosphere-ocean model, a weakened AL

in boreal winter in response to a 10-fold increase in Asian carbonaceous aerosol concentrations. My finding of a more robust weakening of the AL to BCx10 in comparison with BCx10a suggests that sources of BC outside of Asia and their complex climate processes and feedbacks also play a fundamental role in modulating the strength of the AL.

The diversity of model responses to the sulphate perturbations in tandem with the findings from Oudar et al. (2018) highlight the difficulty in identifying robust regional responses to sulphate aerosol forcing. It is difficult to ascertain whether any of the responses identified here are likely to be realistic, since each model differs in its climatology and representation of aerosol processes, including the representation of aerosol-radiation and aerosol-cloud interactions. Richardson et al. (2019) used results from “double call” radiation experiments for a subset of PDRMIP models to show that the TOA IRF from aerosol-radiation interactions in BCx10 has considerable spread across models (see variable “IRF_{toa}” in their Fig. 1). Richardson et al. (2019) also found considerable inter-model spread in the ERF across PDRMIP models in response to both sulphate and BC perturbations, which may cause uncertainty in the North Pacific response. However, there is no systematic disparity in North Pacific responses between models that do and do not include indirect aerosol effects for both BC and sulphate aerosols. It is plausible that the more robust response of the AL to BC aerosol is due to the dominance of the aerosol shortwave absorption, whereas for sulphate aerosols the pattern of anomalous precipitation is important (cf. Wilcox et al., 2019) and this differs across models.

Past literature has provided an inconsistent picture of the influence of AA emissions on the North Pacific atmospheric circulation and the PDO. Overall, my results show a robust weakening of the AL due to a global 10-fold increase in BC, which is partly driven by local emissions from east Asia but also shows a significant role for BC sources outside of east Asia in influencing the North Pacific. However, a 5-fold increase in global sulphate aerosol and a 10-fold increase in sulphate aerosol over Asia both produce responses that do not project strongly onto the climatological AL. This differs from the findings of Smith et al. (2016) and Oudar et al. (2018), who showed that in coupled climate models a transient increase in AA over Asia leads to a weakening of the AL, though there are differences in the magnitude, pattern and timescale of the aerosol forcing imposed in my experiments which prevents a like-for-like comparison with those studies.

The relative importance of ocean feedbacks for the responses to the BC and sulphate perturbations experiments was identified from the comparison of the coupled and prescribed SST PDRMIP simulations. The robust weakening of the AL in response to BCx10 and BCx10a in the coupled and prescribed SST experiments indicates a small role for ocean feedbacks. This is in contrast to the sulphate perturbation experiments where the MMM changes in NPI reverse sign from negative to positive in the prescribed SST and coupled experiments, respectively.

My results show that aerosols, and in particular BC, can modulate the strength of the AL and induce surface temperature anomalies in the North Pacific that resemble the PDO. Chapter 4 focuses on understanding the

mechanisms responsible for the North Pacific response to BC and sulphates seen in the PDRMIP models using a simplified stationary-wave model.

Chapter 4 – The effect of anthropogenic aerosols on north Pacific tropospheric dynamics – dynamical understanding

This chapter's contents, along with the contents of chapter 3, have been published as a paper in AMS Journal of Climate (Dow et al., 2020). The contents of the paper appears across both chapters with some edits. For example, more detailed explanations of the research process have been provided where helpful, and material has been moved from the Supplementary Items to the main text. The paper has also been edited to avoid overlap with other chapters – specifically, parts of the introduction and method sections instead appear in Chapters 1 and 2 – and to be consistent with the results of other chapters – for example, parts of the method and discussion/conclusions sections have been added to or edited for consistency with Chapters 3, 5 and 6.

4.1 Introduction

The results of Chapter 3 have shown that aerosol perturbations, in particular BC, can impact on the strength of the AL and promote surface temperature anomalies in the North Pacific that resemble those associated with the PDO. The analysis of the upper tropospheric flow in chapter 3 revealed significant anomalies in eddy geopotential height and RWS over East Asia and into the North Pacific in response to the aerosol perturbations. This chapter seeks to better understand the mechanisms underlying the dynamical response to aerosols across the North Pacific.

To recap, there has been a substantial increase in AA and their precursors in Asia since the 1950s (e.g. Lin et al, 2016), whilst aerosol emissions in Europe and North America have been decreasing since the 1970s (e.g. Kasoar et al., 2018). Numerous physical and chemical removal processes prevent aerosols from having a residence time in the atmosphere greater than a couple of weeks (e.g. Stohl and Sodemann, 2010; Papastefanou 2005). Hence, spatiotemporal heterogeneity in global aerosol emission trends have ever changing effects on both global and regional climate. Aerosols have the capacity to impart substantial changes in atmospheric circulation and their influence can extend over large distances, which may outweigh the response to local forcing (Rotstayn and Lohmann, 2002; Ramanathan et al., 2005; Allen et al., 2015; Shindell et al., 2012; Lewinschal et al., 2013).

There have been limited studies on the boreal winter (DJF) response to Asian AA, despite this being the season when the AL is found, with the majority focused on boreal summer (JJA). The aim of these studies has been to examine the impact of aerosols on the summer monsoon (Bollasina et al., 2011; Bartlett et al., 2018) or annual mean climatic changes (e.g. Richardson et al., 2016; Kasoar et al., 2016, 2018; Liu et al., 2018; Grandey et al., 2016). Remote responses to Asian aerosols in JJA have been identified in studies by Menon et al. (2002) and Liu et al. (2018). Remote responses to global aerosol emissions in DJF, particularly at high latitudes have been identified in studies by Allen and Sherwood (2011), Lewinschal et al. (2013) and Chung and Seinfeld (2005). Wilcox et al. (2019) found using a linear stationary wave model that the radiative effect of Asian AA modifies the extra-tropical stationary wave pattern, with the response characteristic of the positive PNA

pattern. Additionally, they found that North American and European responses to Asian AA arise primarily in the extratropics. Teng et al. (2012) similarly found a PNA pattern in response to Asian BC aerosol, which they concluded was not tropically-excited.

Absorption of BC has been demonstrated to impart changes in regional circulation, monsoon precipitation (e.g. Mahmood and Li, 2013; Hua et al., 2013) and global circulation (Johnson et al., 2019). Northward expansion of the northern hemisphere Hadley cell (Kovilakam and Mahajan, 2015) and poleward displacement of the mid-latitude jets (Allen et al., 2012) are associated with perturbations to BC emissions. Changes to the spatial distribution of tropical convection is also affected (Johnson et al., 2019), while a study by Zhao and Suzuki (2019) associated an increase in BC with a northward shift in the ITCZ and a reduction in precipitation globally. Remote impacts of BC aerosol via atmospheric teleconnections have been posited in a recent study by Amiri-Farahani et al. (2020), who attributed biomass burning in South Africa as a driver of tropical Pacific Ocean variability. Anomalous heating over the Atlantic was posited to trigger atmospheric teleconnection to the tropical Pacific including an intensification of the Walker circulation.

Hoskins et al. (1977) and Hoskins and Karoly (1981) showed that an extra-tropical response to tropical heating can be initiated through the propagation of Rossby waves from areas of anomalous tropical upper tropospheric divergence. Scaife et al. (2016) showed a few ‘hotspots’ for Rossby wave generation arising in regions of large meridional vorticity gradients in the upper troposphere, with the same forced wave trains being associated with a variety of different rainfall anomalies (forcings).

Considering all the above, this chapter seeks to investigate the mechanisms responsible for the North Pacific circulation responses seen in the PDRMIP models in response to BC and sulphate aerosol emissions from Asia and globally. This is achieved using a linearized stationary-wave model which builds on the multi-model analysis in chapter 3. Similar approaches have been utilised by Teng et al. (2012) and Ming et al. (2011) to investigate the influence of Asian emissions of BC on temperatures in the US and northern hemisphere, respectively. Lewinschal et al. (2013) also used this approach to explain the northern hemisphere response to changes in global aerosol emissions.

4.2 Aim and research questions

This chapter aims to better understand the dynamical mechanisms through which BC and sulphate emissions influence the AL. To this end, I run and analyse a linearised steady-state primitive equation model forced with diabatic heating and precipitation anomalies derived from the PDRMIP models, with the aim of addressing the following research questions:

1. Does diabatic heating resulting from the absorption of atmospheric BC and latent heating from the precipitation anomalies, derived from the PDRMIP BC experiments, induce atmospheric dynamics associated with a weakening AL?
2. Which regions of BC emissions contribute to the dynamics associated with a weakening of the AL?
3. Does the stationary wave model driven by latent heating associated with precipitation anomalies from the PDRMIP global and Asia-only

sulphate experiments reproduce the PDRMIP MMM response over the North Pacific?

4.3 Methods

4.3.1 PDRMIP Models

Of the eleven models that contributed to the PDRMIP project (see Tables 2.1 & 3.1), six provided diagnostics that enabled a more in depth analysis of the dynamical mechanisms contributing to the AA response (i.e. 3-D wind fields and geopotential height; see Table 3.1); the analysis presented in Section 4.4.2 uses this subset of six models. For comparison with Figure 3.6, Figure 4.1 shows the PDRMIP MMM SLP response in the North Pacific to the aerosol perturbations in the fully coupled configurations in these six models. The overall responses are very similar to those described in chapter 3.

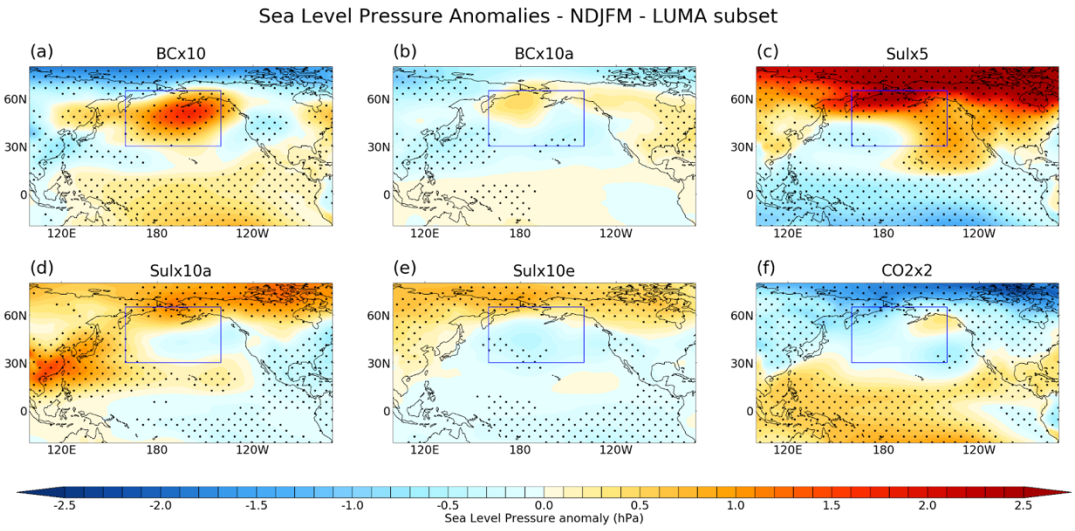

Figure 4.1: As in Figure 3.6 in Chapter 3, but for the subset of models that provided 3-D output fields and are used to create input fields for LUMA.

4.2.1 Linear stationary wave model (LUMA)

The Linear University Model of the Atmosphere (LUMA) is a global, stationary wave model that solves the linearized dry, primitive equations on

terrain-following sigma-levels (Hoskins and Simmons 1975). More details are given in the Methods chapter, section 2.2 as well as Liakka et al. (2012). Studies, such as Wilcox et al. (2019), who have used LUMA to investigate far-field midlatitude responses to Rossby waves generated over China, providing confidence in using the model. The experimental set-up in Wilcox et al. (2019) is comparable with the methodology presented here, where diabatic heating inferred from precipitation anomalies is used to derive the stationary wave response. Here, LUMA is linearized around the MMM extended winter climatology of the PDRMIP control experiments (taking in temperature, relative vorticity, divergence and surface pressure fields to initiate the basic state), and the forcing consists of diabatic heating anomalies derived from the PDRMIP perturbation experiments.

For the BC perturbation experiments, we include anomalous heating from both the absorbing aerosol and the anomalous latent heating that forms part of the hydrological cycle response; both effects can drive planetary Rossby wave trains (Hoskins and Karoly, 1981). The direct heating due to the absorbing aerosol is estimated from the PDRMIP MMM BC fields, which are input to the UK Met Office SOCRATES version 15.04 (Suite of Community Radiative Transfer codes; based on Edwards and Slingo, 1996), using a two-stream delta-Eddington solver; more details are given in Section 2.3. Due to the availability of the necessary variables, atmospheric and surface state variables (including clouds and ozone) were used from the ERA5 reanalysis dataset for the year 2014 (Hersbach et al., 2020). Optical properties of BC are used from the HadGEM2 model parameterisation, obeying a lognormal size distribution with mean radius 40 nm and geometric standard deviation of 2.0 nm. No other aerosols are specified in the SOCRATES calculations. Monthly

mean shortwave heating rates are calculated using five representative solar zenith angles and Gaussian quadrature (Figure 4.2). The instantaneous heating rate anomalies derived from SOCRATES are then input to LUMA as an external forcing of the thermodynamic energy equation.

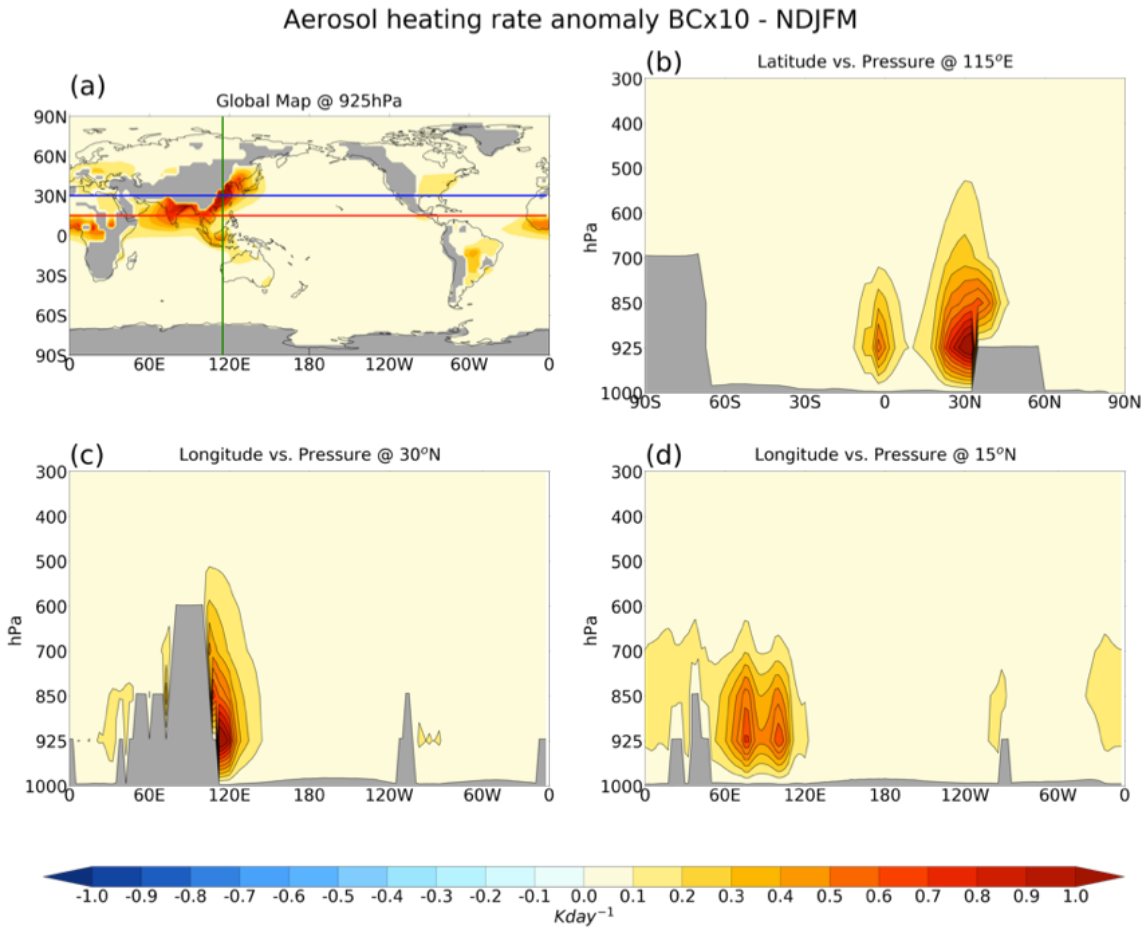

Figure 4.2: NDJFM mean heating rate [K day^{-1}] anomalies due to the MMM BCx10 aerosol perturbation. (a) Global distribution of instantaneous heating rate at 925 hPa. Regions where the surface pressure is below 920 hPa are masked in grey. The green, blue and red transects relate to the vertical heating profiles in b, c and d, respectively. (b,c,d) Longitude-pressure transects showing the instantaneous heating rates due to the BC aerosol. Contours are at 0.1 K day^{-1} intervals.

For all experiments, a 3-D anomalous latent heating field is estimated following Chan and Nigam (2008) using the PDRMIP MMM mean precipitation

anomalies (Figure 4.3), which are converted to a tropospheric column average heating rate [K s^{-1}] by multiplying by (g L ρ_w 10^{-5})/[$C_p(P_0 - 125)$], where L is the latent heat of condensation (2.5 x 10^6 J kg^{-1}), g is gravity (9.81 m s^{-2}), ρ_w is the density of water (10^3 kg m^{-3}), C_p is the specific heat of air at constant pressure (1004 J kg^{-1} K^{-1}), and P_0 is a reference surface pressure calculated from the PDRMIP models. The heating is distributed in the vertical using a Gaussian profile centred at 500 hPa (following Lewinschal et al., 2013).

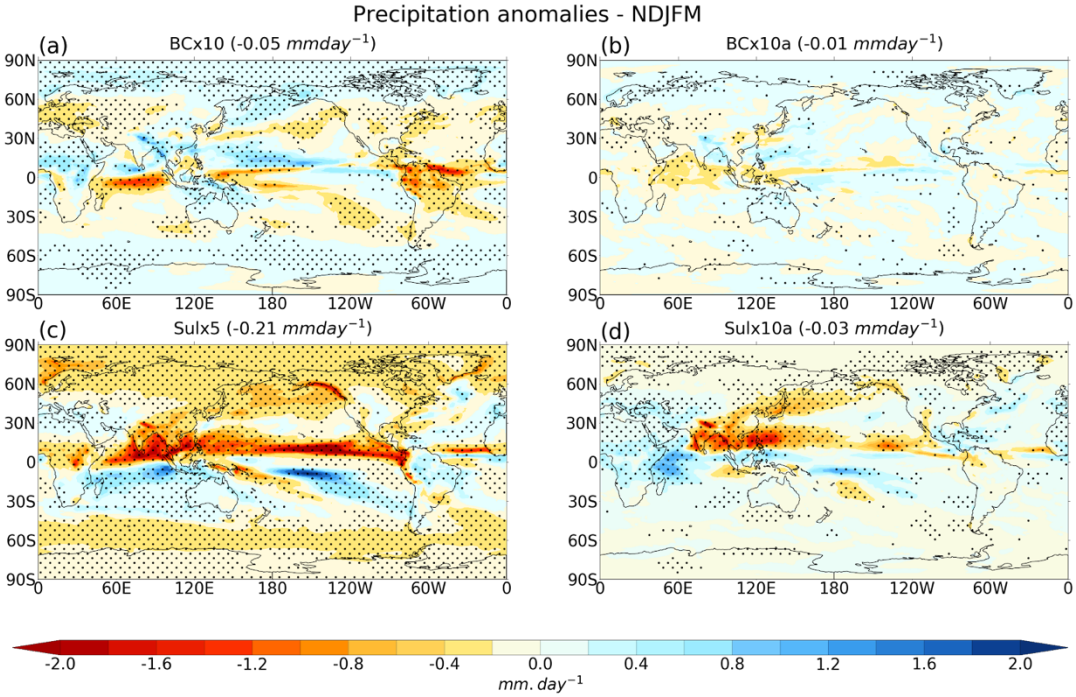

Figure 4.3: NDJFM mean PDRMIP MMM precipitation [mm day^{-1}] anomalies in four coupled aerosol perturbation experiments. Stippling indicates differences that are significant at the 95% confidence level. The global average precipitation anomaly is given in brackets.

In the LUMA experiments, the magnitude of the spectral wavenumber perturbation (an unconstrained parameter) is set to unity. This means that the output from LUMA cannot be quantitatively compared to the PDRMIP results. Thus, while we include colour scales on the figures in order to clarify units, we

focus on the qualitative comparison of LUMA forced with diabatic heating anomalies and the PDRMIP simulations (cf. Wilcox et al., 2019).

By construction, the LUMA model does not capture all of the processes present in the PDRMIP models. This must be borne in mind when comparing the LUMA results to the PDRMIP models. Nevertheless, this type of model has proven useful in isolating the steady-state stationary wave response to diabatic forcing (e.g., Held et al., 2002), including that due to aerosol perturbations (e.g., Lewinschal et al., 2013; Wilcox et al., 2019), and we therefore use LUMA alongside the PDRMIP models to investigate some of the underlying dynamical mechanisms and teleconnections.

4.4 Results

4.4.1 LUMA Model Validation

To validate that the LUMA model was fit for purpose, I conducted test case simulations based on those described by Hoskins and Karoly (1981) using the primitive equation, baroclinic, sigma-coordinate multi-layer (5 levels) spectral model of Hoskins and Simmons (1975). The model they describe uses the spectral-transform technique in the horizontal and second-order finite differences in the vertical and has been thoroughly tested and used in many studies of atmospheric dynamics. Hoskins and Karoly (1981) explore the responses to various thermal (and orographic) perturbations with varying latitudinal and vertical distributions of the forcing.

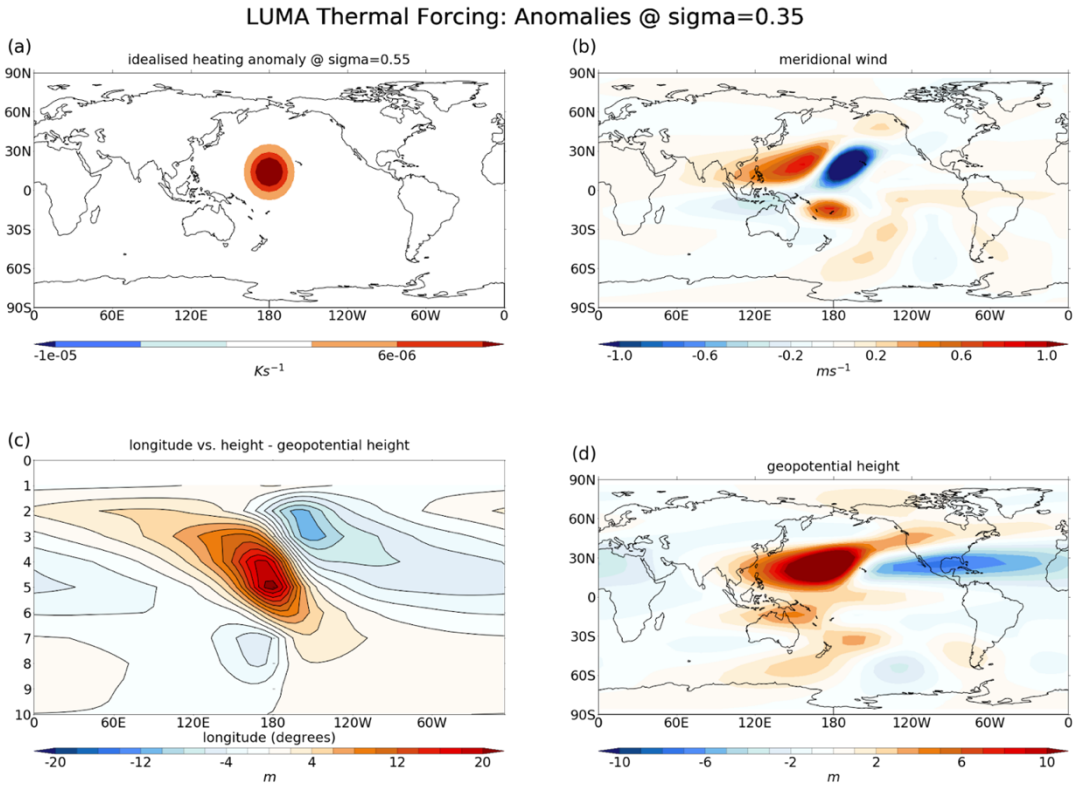

Figure 4.4: Linear Stationary Wave model (LUMA) response to an idealised isolated tropical thermal forcing centred at σ=0.55. Panel (a) shows the location of the thermal forcing, (b) shows the meridional wind anomaly, (c) shows a height-longitude cross section of geopotential height anomaly and (d) shows the geopotential height anomaly at σ=0.35.

Figure 4.4 shows the steady-state response generated by LUMA to an isolated thermal forcing in the sub-tropics (like Hoskins and Karoly, 1981; Figure 3). Here a vertically-integrated diabatic heating anomaly of 3 K s^{-1} is imposed on a background state derived from the PDRMIP MMM (Figure 4.6). The PDRMIP MMM fields were converted to sigma-coordinates and interpolated onto LUMA sigma-levels. The horizontal distribution of the heat source is that of a cosine squared in an ellipse on the tangent plane at 15ºN, with zonal and meridional half-widths of the heating anomaly set at 10º. The vertical heating profiles throughout testing were proportional to $\sin\pi\sigma$, with a maximum at σ = 0.55. When comparing the vertical structure of the geopotential height field (Figure 4.4 panel c) at 19ºN with Figure 3a from Hoskins and Karoly (1981), there are notable similarities especially with

respect to the westward longitudinal tilt. There is less evidence of poleward propagation initiated by a subtropical thermal forcing as that seen in Hoskins and Karoly (1981), though this may be influenced by base state model biases (e.g. Di Carlo et al. 2022; Harvey et al. 2020). There is evidence of a PNA-like response across the North Pacific in response to the central Pacific thermal forcing, albeit with a weak projection to the northern latitudes in the Pacific. Tests were also conducted by placing the thermal forcing anomaly in the mid-latitudes, at 45^{o}N (Figure 4.5), simulating an East Asian source of atmospheric heating. The geopotential height field perturbation is shown in the longitude-height section at 47^{o}N in Figure 4.5 panel c. Comparing Figure 4 in Hoskins and Karoly (1981), the surface low pressure and upper-level maximum are both found east of the heating source. Consistent with their results, the westward tilt is less evident than seen in response to a subtropical heat source.

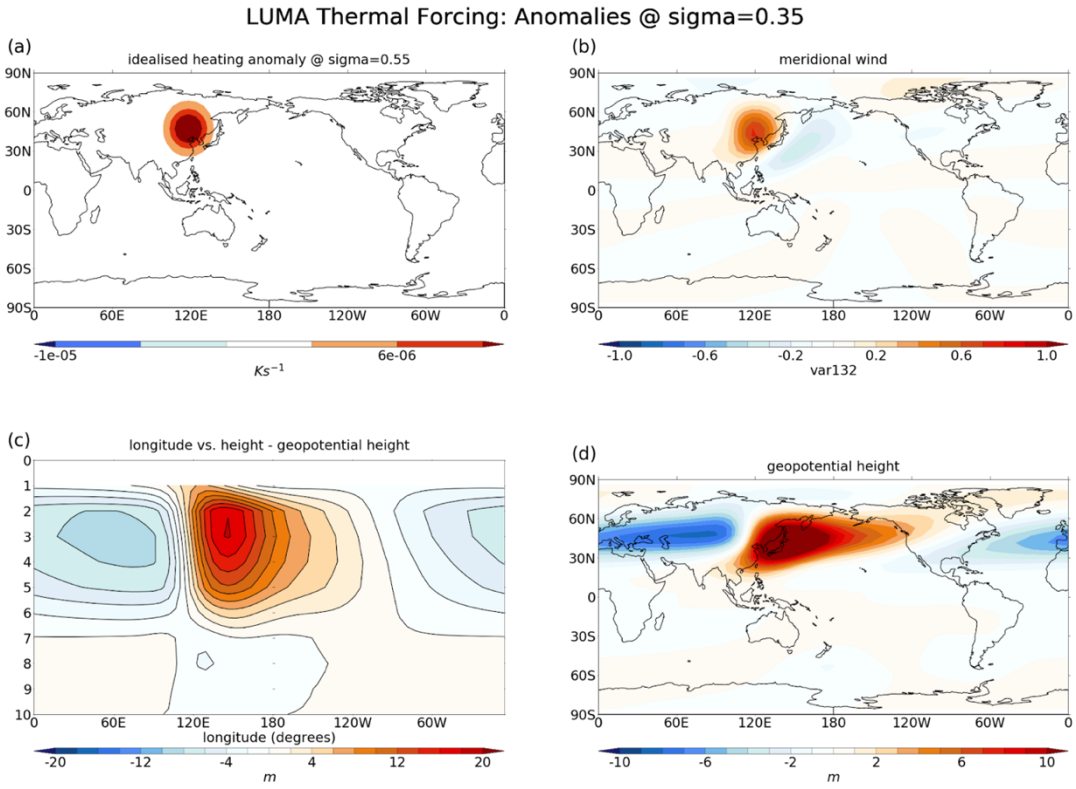

Figure 4.5: LUMA response to an idealised sub-tropical isolated thermal forcing centred at σ=0.55. Panel (a) shows the location of the thermal forcing, (b) shows the meridional wind anomaly, (c) shows a height-longitude cross section of geopotential height anomaly and (d) shows the geopotential height anomaly at σ=0.35.

The mean background states from PDRMIP MMM for the zonal and meridional fields are given in Figure 4.6, which shows a weaker than usual northern hemisphere upper tropospheric wind speeds when compared to reanalysis data (ERA5) and a bias towards a stronger southern hemisphere upper troposphere subtropical jet.

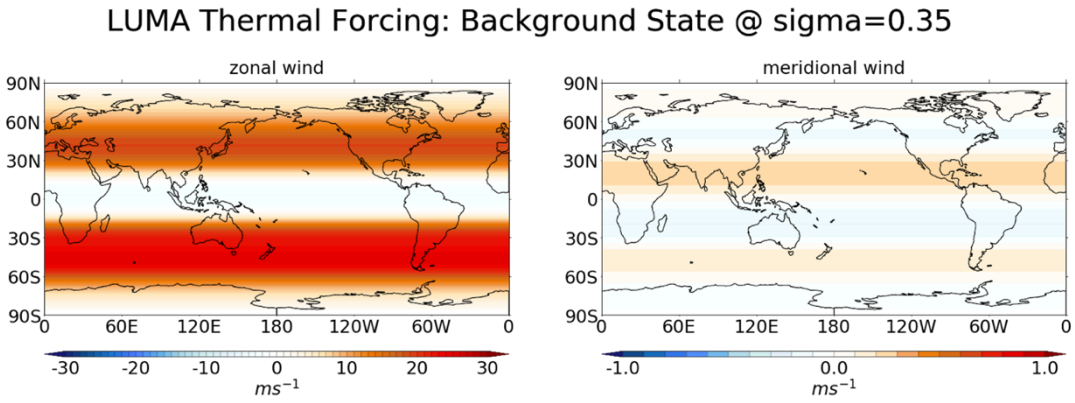

Figure 4.6: (a) Zonal and (b) meridional wind zonal mean fields used as background states in the LUMA simulations.

The similarity of the idealised test case results to other published studies, such as Hoskins et al. (1977) and Hoskins and Karoly (1981), gives confidence in employing LUMA to investigate planetary wave modulation and propagation in response to thermal forcing initiated by anthropogenic emission of aerosols.

4.4.2 LUMA simulations driven by PDRMIP responses

We run LUMA with diabatic heating anomalies derived for the absorbing BC aerosol and precipitation anomalies induced by the different aerosol species. Figure 4.2 shows the pattern of heating rate anomalies due to the BCx10 absorption calculated in the SOCRATES radiative transfer model. The anomalous heating rates (up to 1 K day^{-1}) driven by BC absorption are largely confined to pressures greater than 500 hPa, closely following the distribution of the PDRMIP BC burden (Chapter 3; Fig. 3.2). In addition, the precipitation anomalies in Figure 4.3 are used to estimate a 3-D distribution of anomalous latent heating for all experiments (see details in Section 4.3.2). We further investigate how the North Pacific stationary wave response is influenced by diabatic heating anomalies in different regions.

For comparison with the upper tropospheric responses at 300 hPa in the PDRMIP models, we show results from LUMA at σ = 0.35. The upper tropospheric circulation responses in the linear model are presented in Figure 4.7. BCx10 heating causes the largest anomalous divergence in the tropics, with enhanced divergence over the equatorial Indian Ocean, the Philippines, the tropical Pacific, and over China (Fig. 4.7 panel a). Conversely, anomalous convergence is present along the equator in the Pacific and northern South America. The largest increases in geopotential height are located over China, extending in a southwest-northeast tilted pattern from India across the North Pacific to northern Canada. This response is predominantly driven by the direct radiative heating from the absorbing aerosol. To ensure this, simulations were performed including either direct radiative heating or latent heating. The pattern of geopotential height anomalies over China and the North Pacific qualitatively resembles the PDRMIP response seen in Figure 3.13(a); however, the upper level ridge near the Aleutian Islands is similar in magnitude to over eastern China in PDRMIP, while in LUMA it is proportionately weaker suggesting the stationary wave model is missing a process that amplifies the North Pacific ridge.

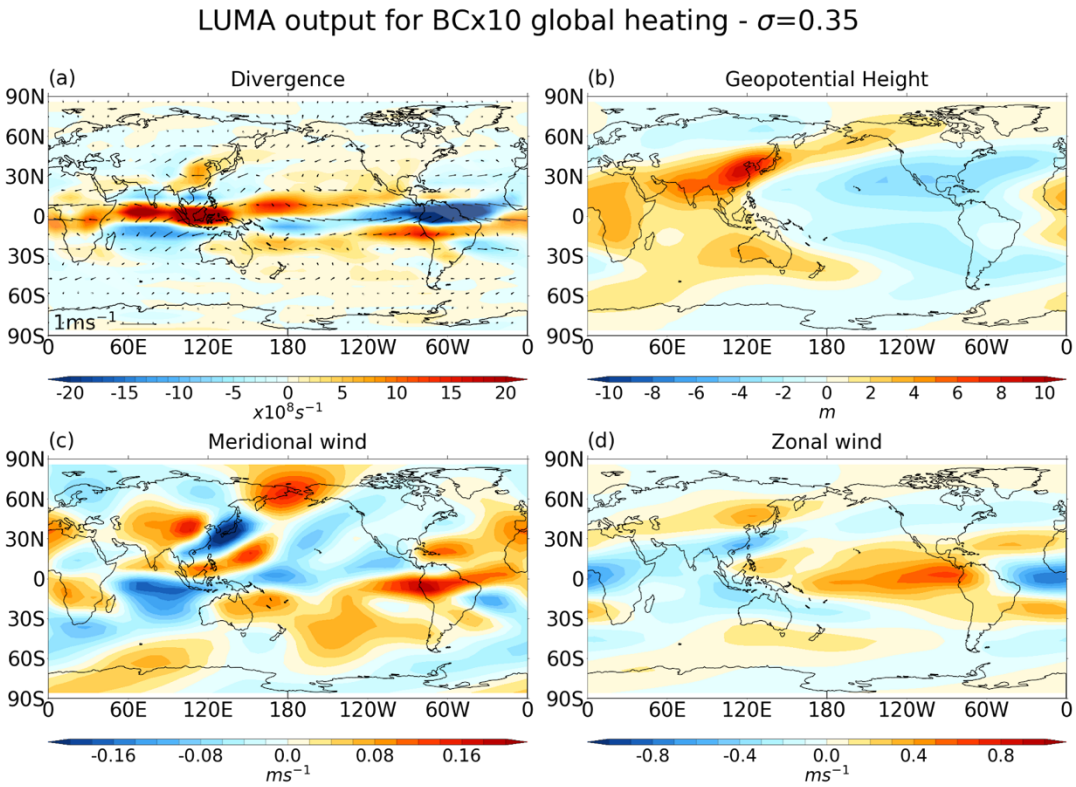

Figure 4.7: LUMA steady-state response (σ=0.35) to diabatic heating anomalies from the NDJFM global atmospheric absorption and precipitation for the BCx10 experiment: (a) divergence [s^{-1}], (b) geopotential height [m], (c) meridional wind [m s^{-1}], (d) zonal wind [m s^{-1}]. Wind vectors are also shown in (a).

Similarly, the anomalous meridional winds in LUMA show a wave train emanating from central China and propagating north-eastwards towards the North Pacific and Arctic (Fig. 4.7 panel c). There is also a wave train emanating from central China that propagates south-eastwards towards the equatorial Pacific. The zonal wind anomalies show a poleward shift in the upper tropospheric North Pacific jet maximum near Japan (cf. Johnson et al., 2019), and a weakening near the jet exit region further downstream (Fig. 4.7 panel d).

To further explore the importance of local and remote BC forcing on the North Pacific upper tropospheric circulation, Figure 4.8 shows geopotential

height anomalies resulting from regional heating applied over China, Equatorial Africa, Indonesia and Nepal/India. These regions represent areas with the largest radiative heating from the BC absorption (Figure 4.2). The majority of the geopotential height increase over China and India is associated with local heating anomalies. Both regional forcings excite Rossby wave trains that propagate downstream in a north-easterly direction (Figure 4.9 panel a-d) and project onto an increase in geopotential height near 60^{o}N in the North Pacific and a decrease near 30^{o}N, thereby contributing to the overall North Pacific response in Fig. 4.7(b). Conversely, localised heating over equatorial Africa and Indonesia have a negligible impact on circulation in the North Pacific, only inducing local wave trains (Figure 4.9 panel b-c). However, these four regions do not explain the full linear response to the global heating anomaly in BCx10. Figure 4.10a shows the sum of the geopotential responses for the four regions and Figure 4.10b shows the difference between the total response (Fig. 4.7 panel b) and this sum. This residual shows that heating outside of China, India, equatorial Africa and Indonesia also contributes to the increased upper tropospheric geopotential height over Japan.

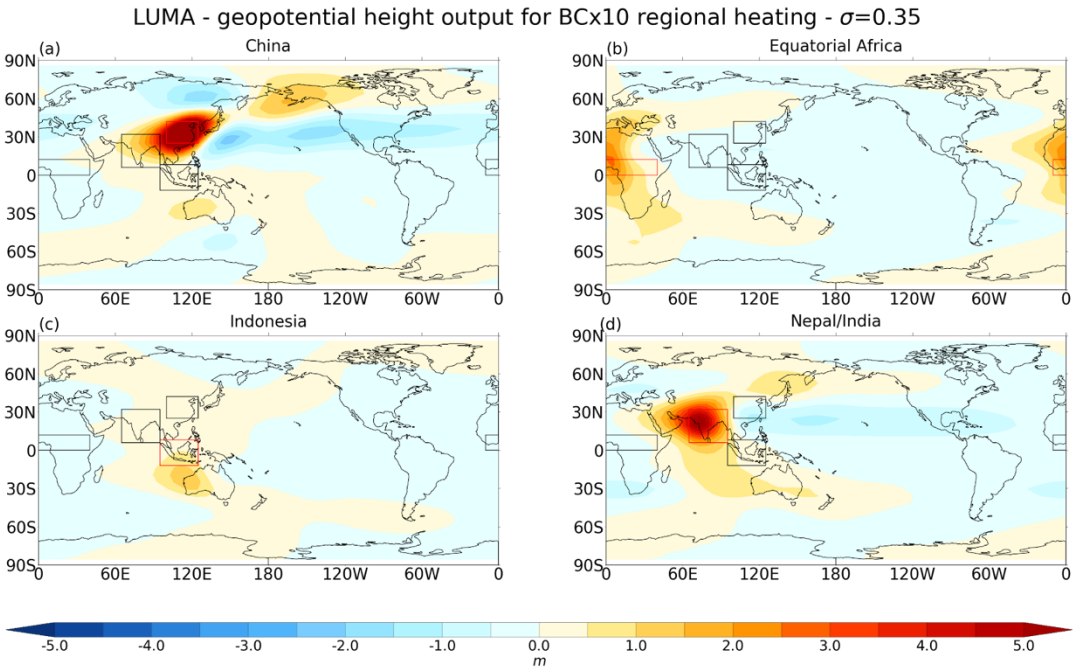

Figure 4.8: LUMA steady-state NDJFM geopotential height [m] anomalies (σ=0.35) due to regional diabatic heating from the BCx10 experiment. The regions, defined by areas with the largest radiative heating from BC absorption (Figure 4.2), are: (a) China [100°E-125°E, 25°N-42°N], (b) Equatorial Africa [10°W-40°E, 0°-12°N], (c) Indonesia [95°E-125°E, 12°S-8°N] and (d) Nepal/India [65°E-95°E, 6°N-32°N].

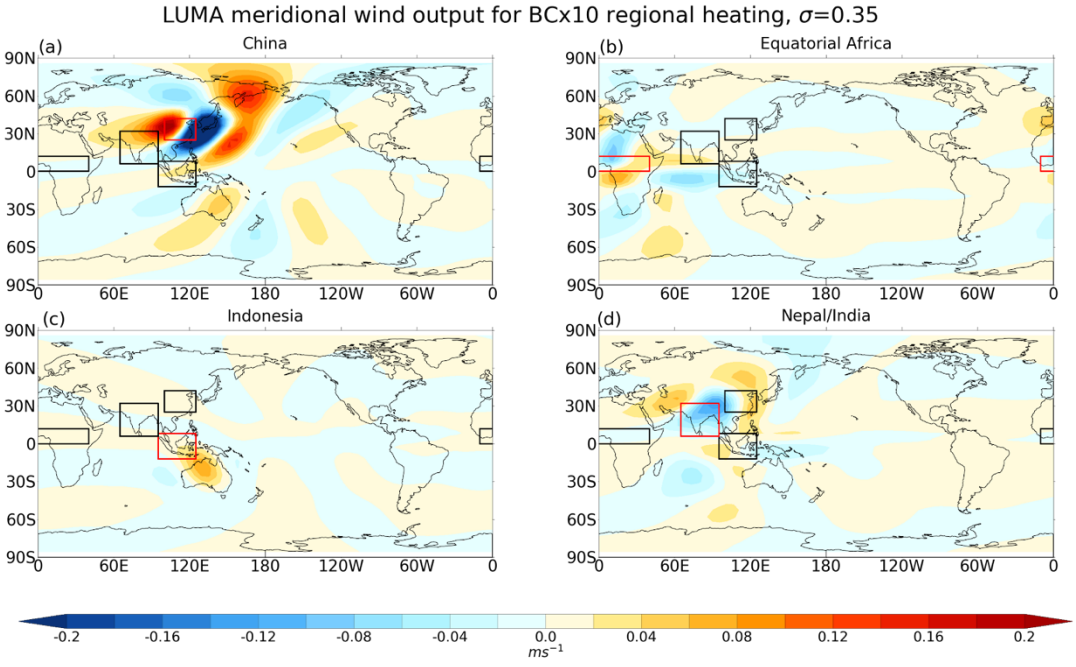

Figure 4.9: LUMA steady-state NDJFM meridional wind [m s^{-1}] anomalies (σ=0.35) due to regional diabatic heating from the BCx10 experiment. The regions are: (a) China [100°E-125°E, 25°N-42°N], (b) Equatorial Africa [10°W-

40°E, 0°-12°N], (c) Indonesia [95°E-125°E, 12°S-8°N] and (d) Nepal/India [65°E-95°E, 6°N-32°N].

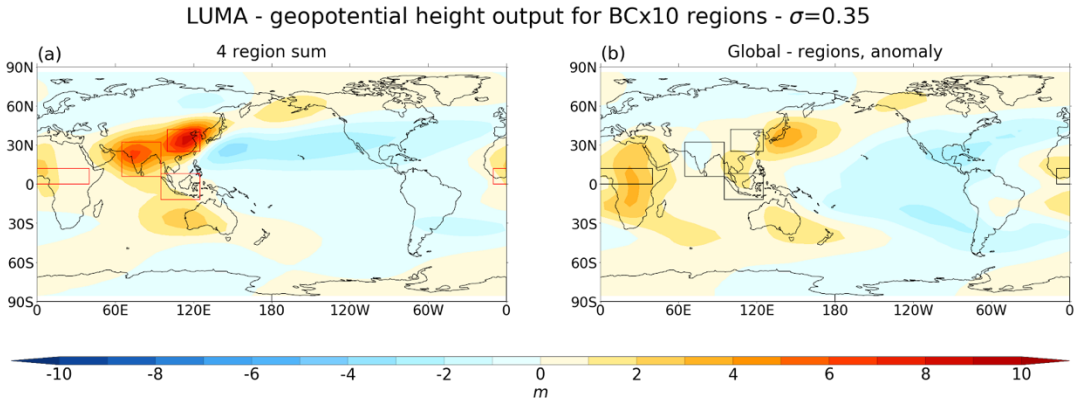

Figure 4.10: LUMA steady-state NDJFM geopotential height anomalies (σ=0.35) due to diabatic heating from the BCx10 experiment. (a) Sum of responses to the four regions shown in Fig. 4.8 (China, Equatorial Africa, Indonesia and Nepal/India). (b) Difference between the response to the global diabatic heating field in Fig. 4.7 panel b and the sum of the four subregions in panel (a).

Figure 4.11 shows the upper tropospheric meridional wind and geopotential height anomalies diagnosed from the linear model for: Sulx5, Sulx10a and BCx10a. The linear model does not reproduce the PDRMIP MMM response over the North Pacific in Sulx5 (Fig. 4.11 panels a,b). It does, however, reproduce the height anomalies over North America. We note that precipitation anomalies north of 45°N contribute to the split-trough over North-West North America, where we see a local geopotential height minimum of around -2 m. In contrast, the PDRMIP pattern of response to Sulx10a is relatively well captured by the linear model (cf. Fig. 3.13 panel d and Fig. 4.11 panels c,d). The precipitation anomalies over China and Nepal/India generate a trough over continental Asia. Further sensitivity simulations reveal that the trough around 25°N extending north-east over the North Pacific is excited by precipitation anomalies over China and Nepal/India (Figure 4.12). Heating

from remote regions, such as Africa, the western and eastern Indian Ocean and the equatorial Pacific Ocean have a smaller influence on the circulation changes in the North Pacific, but in combination, deepen the trough over Asia (Figure 4.13). Latent heat anomalies north of 45°N affect the anomalies in the Sulx10a experiment by broadening and enhancing the trough over the North Pacific. Heating from precipitation anomalies over Nepal/India compound the ridge over the subtropical east Pacific near 25°N, with its effect extending downstream over the Atlantic Ocean.

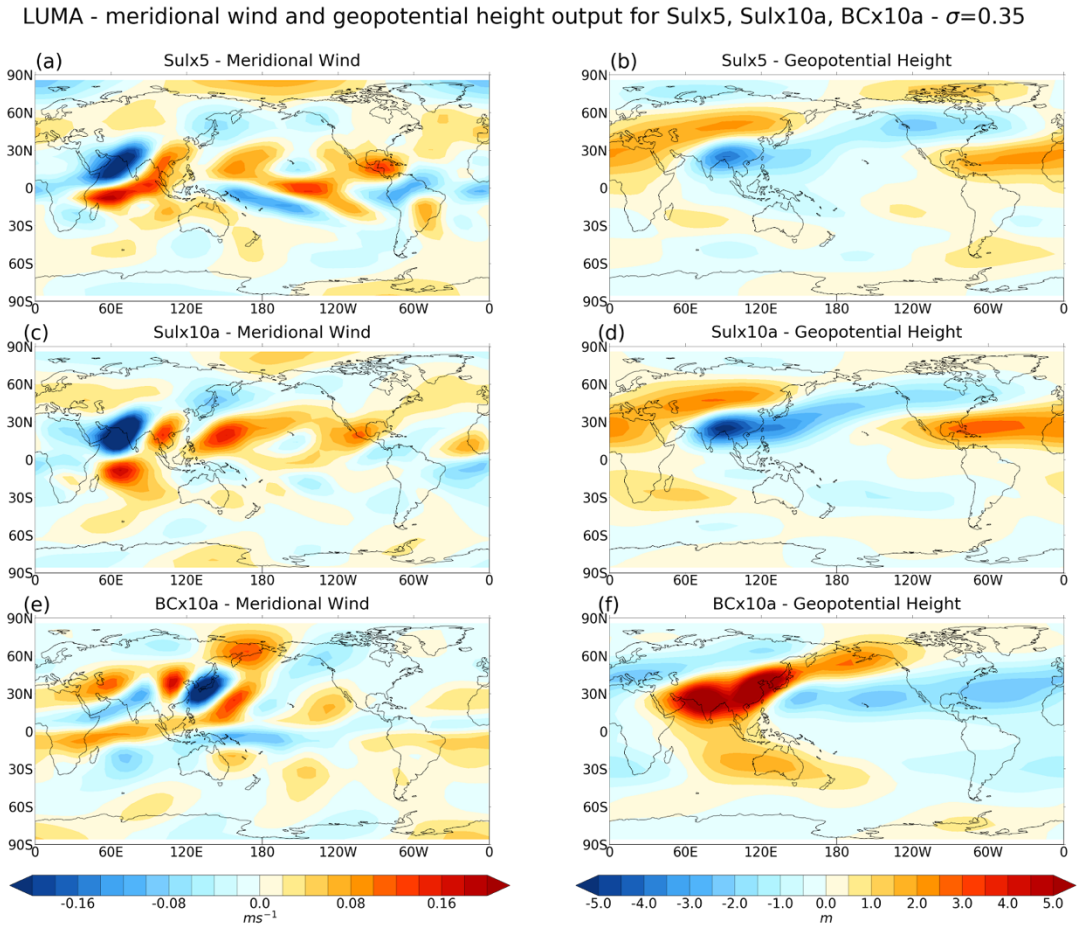

Figure 4.11: LUMA steady-state responses (σ=0.35) of (a, c, e) meridional wind [m s^{-1}] and (b, d, f) geopotential height [m] due to diabatic heating from the NDJFM mean precipitation responses in the (a, b) Sulx5, (c, d) Sulx10a and NDJFM mean precipitation and atmospheric absorption in the BCx10a (e, f) experiments.

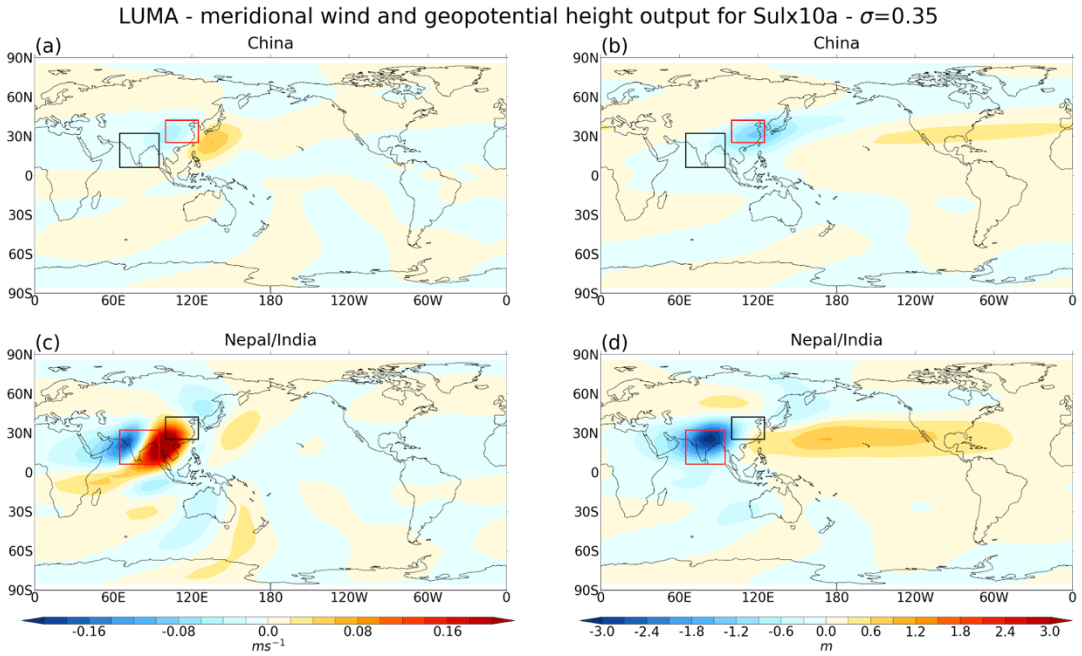

Figure 4.12: LUMA steady-state responses (σ=0.35) of (a, c) meridional wind [m s^{-1}] and (b, d) geopotential height [m] due to diabatic heating from the regional NDJFM mean precipitation responses in the Sulx10a experiments. Regions shown are (a,b,e,f) China [100°E-125°E, 25°N-42°N] and (c,d,g,h) Nepal/India [65°E-95°E, 6°N-32°N].

The linear response to the combined aerosol and latent heating for BCx10a broadly resembles the PDRMIP MMM over the North Pacific (cf. Fig. 3.13b and Fig. 4.11e,f), though with a more pronounced south-west north-east tilt of the ridge/trough pattern. Moreover, the response to BCx10a is structurally similar to that for BCx10. Much of the North Pacific response to both BCx10 and BCx10a is due to aerosol heating over India and China, with a comparatively smaller contribution from latent heating.

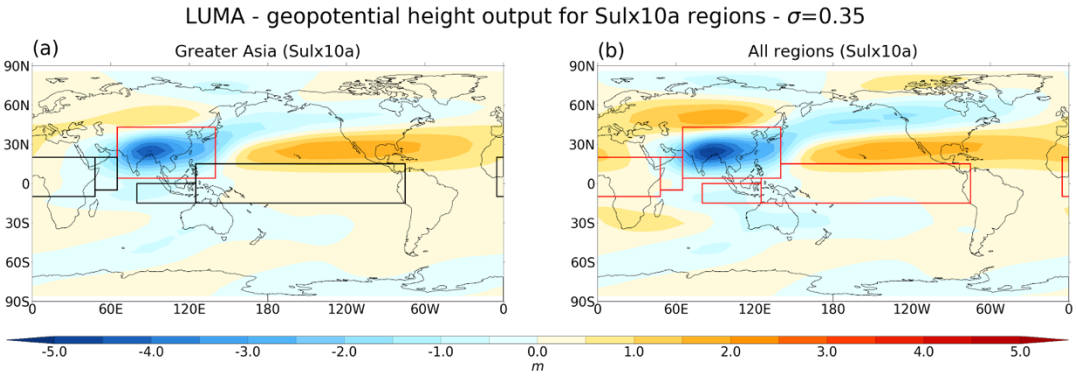

Figure 4.13: LUMA steady-state response (σ=0.35) of geopotential height [m] due to diabatic heating from the regional NDJFM mean precipitation responses in the Sulx10a experiments. (a) Response to Greater Asia region [65°E-140°E, 4°N-43°N]. (b) Responses to Greater Asia region plus Africa [5°W-48°E, 10°S-20°N], the western Indian Ocean [48°E-75°E, 5°S-20°N], equatorial Pacific Ocean [125°E-285°E, 15°S-15°N], tropical east Indian Ocean [80°E-125°E, 15°S-0°N] and north of 45°N (no box shown).

4.5 Discussion and Conclusions

Previous studies have provided a varying picture of the influence of AA emissions on North Pacific atmospheric circulation. I have used simplified model experiments with large, idealised aerosol forcings to investigate potential mechanisms through which changes in aerosol emissions affect the North Pacific.

The discrepancies between the steady-state response to the diabatic heating anomalies in the linear stationary wave model and the results from the PDRMIP models in Chapter 3 should be contextualised by reminding the reader of the limitations of the linear model. One limitation is the absence of a fully integrated ocean model, which has been shown to be integral in assessing aspects of the climate response to aerosol forcing (Zhao and Suzuki, 2019). Another limitation is that the heating from BC absorption was estimated using a single offline radiative transfer model that differs from that used in most of the PDRMIP models. Another factor is that, for the sake of convenience, the mean precipitation anomalies were imposed even if they

were not statistically significant, which raises the potential for a component of climate noise to influence the LUMA results. Therefore, these simplifications must be taken into account when comparing the results of the linear model with the comprehensive climate models. Nevertheless, LUMA is useful for demonstrating aerosol-induced teleconnections from remote regions that have the potential to influence the AL.

It must be acknowledged that there are some differences between the stationary wave pattern obtained from LUMA in response to the Sulx10a forcing (Fig. 4.11d) and the response seen in Wilcox et al. (2019) (their Figure 8d). The sign of the stationary wave anomaly is opposite across the northern North Pacific, which is the key region in this analysis. There are distinct differences between the precipitation patterns derived from PDRMIP MMM and those used in the study by Wilcox et al. (2019) (their Fig. 6b) – notably the large negative precipitation anomalies south of the equator in Wilcox et al. (2019) are north of the equator in Sulx5 and Sulx10a in the PDRMIP MMM. Comparing with Sulx10a more specifically, the anomalies have opposite sign over India and China, however both are negative south of Japan and over the northern North Pacific. The difference in precipitation anomalies imposed over east Asia could be a source of the discrepancy in stationary wave response over the northern North Pacific and other regions.

I have shown, using a linearized steady-state primitive equation model, that diabatic heating from the absorption of atmospheric BC over both Nepal/India and China, alongside latent heating from precipitation anomalies over India and East Asia generates Rossby wave trains that propagate downstream into the North Pacific sector. The response in the North Pacific

displays a similar barotropic nature compared with the results from the PDRMIP MMM in Chapter 3. The ridge evident, which extends into the North Pacific, is indicative of a weakening AL, whilst the increase in divergence anomalies in the tropical Pacific is commensurate with the early studies by Hoskins et al. (1977) and Hoskins and Karoly (1981) in affirming the hypothesised mechanism for tropical-extra-tropical communication.

I have shown that the most important regions of BC emissions impacting on the North Pacific circulation are China and Nepal/India. I have shown that equatorial Africa and Indonesia have negligible impact on circulation in the North Pacific, however regions outside of these four study regions also impact on North Pacific upper troposphere dynamics in response to global BC perturbations. I conclude that the linear model does a relatively good job at capturing the response seen in the PDRMIP MMM in the Sulx10a experiment, however it does not reproduce the PDRMIP MMM response over the North Pacific in Sulx5, which indicates that the linearised primitive equation model neglects some key processes that determine the North Pacific response to a global increase in sulphate aerosols. The response to BCx10a in the linear model broadly resembles the PDRMIP MMM over the North Pacific albeit less robustly and is structurally similar to that for BCx10.

I find the direct radiative effect is a considerably more important source of diabatic heating than the anomalous latent heating induced by the aerosol's role in cloud formation and associated modification to precipitation patterns. The aerosol heating induces remote responses through anomalous RWS regions. This has also been found in a study by Yan et al. (2021), who demonstrated two mid-to-high latitude Rossby wave trains - propagating from

the subtropical Atlantic across Europe and Siberia, and from the Middle East across Asia and the Pacific Northwest – resulting from atmospheric heating caused by BC emissions from wildfires in equatorial Africa.

The assessment of the relative importance of latent and radiative heating induced by aerosols must be further caveated with the fact that most global climate models are only partially capable of investigating the complex interaction between aerosols and shallow and deep convective cloud systems (Wang et al., 2014). The authors further highlighted discrepancies in the North Pacific between a climate model that uses cloud parameterization to represent deep convection and an embedded regional cloud-resolving model that can explicitly resolve cloud updrafts. Hence, the development of improved cloud-aerosol microphysical schemes will facilitate future investigation of the dynamical responses to aerosol forcing.

There remain substantial uncertainties in the global and regional forcing from AA. For example, at least 20% of the present uncertainty in simulated direct radiative forcing from BC is due to diversity in the vertical distribution of aerosol mass (Samset et al., 2013). Idealised sensitivity studies can therefore provide insights to the potential mechanisms that induce remote effects from aerosol forcing and have the advantage of achieving a larger signal that can be identified thereby overcoming some of the challenges of investigating the historical period when aerosols and GHGs have been changing simultaneously.

Chapter 5 - Developing regional nudging capability in FORTE2.0

5.1 Introduction

Chapters 3 and 4 focussed on using multi-model datasets to examine the role of external forcing in modulating North Pacific circulation, with a focus on the AL due to its intrinsic association with the PDO. The next two chapters of this thesis focus on developing a more general mechanistic insight to the processes underlying PDV, with a focus on the interactions between the extratropics and tropics. This is motivated by the hypothesis of Smith et al. (2016) that external modification of the AL can lead to a basin scale coupled atmosphere-ocean response that resembles the structure of the PDO. Studies such as those of Smith et al. (2016), Newman et al. (2016), Oudar et al. (2018), Dow et al. (2021) and Dittus et al. (2021) analyse the change to the AL (hence extra-tropics) resulting from either external forcing (e.g. AA emissions) or variability initiated in the tropics (e.g. ENSO). Therefore, even though modulation of the AL is considered precursory to subsequent tropical variability (e.g. PDO), the mechanism for AL variability is often traced back to tropical (Pacific) variability. To fully isolate the role of the AL in driving PDO-like variability, this chapter documents the implementation of a nudging technique (also referred to as Newtonian relaxation) into a global atmosphere-ocean climate model (FORTE2.0; see Section 2.4). The technique introduces extra terms to the equations that govern the tendencies of, for example, horizontal winds and temperature fields, in order to constrain the fields towards a pre-defined reference state (e.g. from reanalysis data). Nudging enables the study of the relationship between two remote regions by constraining one region and ‘nudging’ it towards a pre-defined state (e.g.

Watson et al., 2016; Pohl et al. 2014; Knight et al., 2017). Nudging is also utilised across meteorological and climate studies concerning climate model development and evaluation (e.g., Kooperman et al., 2012; Telford et al., 2008; Schmidt et al., 2006). Nudging has proven to be useful in the development and evaluation of physical parameterizations and chemistry modules (e.g., Zhang et al. 2014; Ma et al., 2014; Zhang et al., 2012) because it enables a more meaningful comparison between model output and observations, including case study events, as a test of model performance (Zhang et al. 2014). In constraining a particular region, nudging allows us to isolate specific effects that may otherwise require very long simulations to be able to discriminate between signal and noise (e.g. Kooperman et al., 2012).

There have been numerous studies in the climate dynamics community that have employed nudging to elucidate interconnections between remote regions. For example, Knight et al. (2017) used nudging (referred to in the paper as ‘relaxation’) to assess contributions of tropical regions to the record-breaking observed winter rainfall in the UK in 2013-2014. Similarly, Watson et al. (2016) examined the impact of the tropical West Pacific on extreme meteorological events during 2013-2014 winter and concluded that this region had an important influence on remote regions through the excitation of Rossby waves. Other studies where nudging is applied include in the investigation into variability in mid-latitude blocking (Gollan et al., 2015), and understanding tropical convection in the context of the Madden-Julian Osciallation (MJO) (Pohl and Crétat, 2013). The relationship evident in observations between the tropospheric MJO and the stratospheric quasi-biennial oscillation is explored using a set of spectrally-nudged ensemble simulations in Martin et al. (2021). Here, zonal-mean zonal and meridional wind fields in the stratosphere are

relaxed and the troposphere is left to evolve freely. Similar simulations with stratospheric relaxation have been examined by Chrysanthou et al. (2019) investigating the effect of nudging towards reanalysis datasets on the stratospheric residual circulation. Thus, the widespread application of nudging in atmospheric models and the documented methodologies allows confidence to be taken for the implementation of an equivalent method in the FORTE2.0 model. While models with this capability exist, they are generally computationally expensive to run and need to be compiled on large High Performance Computing platforms (e.g. ARCHER). FORTE2.0 is a much more computationally efficient model, enabling different configurations and large ensembles of experiments to be integrated quickly. Furthermore, the model code is sufficiently tractable and flexible that the model can be developed by a small team rather than the vast team of developers required for the Met Office Unified Model.

This chapter outlines the steps taken to develop a nudging code in the FORTE2.0 coupled climate model, firstly from the compilation of the model onto the Leeds HPC, to testing and implementation of the newly developed code. The final code is presented in the Appendix.

5.2 Aim and research question

The motivation is to develop a tool to explore the mechanisms that drive the communication between the tropical and extra-tropical Pacific Ocean through the atmospheric bridge (e.g. Newman et al. (2016)). To achieve this, I aim to develop and test a nudging capability in the atmospheric component (IGCM4) of the FORTE 2.0 model.

5.3 Background

5.3.1 FORTE 2.0

FORTE 2.0 was compiled from the model source code from the publicly available github page (https://github.com/NOC-MSM/FORTE2.0) onto the Tier 3 ARC4 HPC cluster. ARC4 has 149 standard nodes with 40 cores each. The integration of the model on the ARC4 HPC cluster is relatively fast, where 1 model year takes around 7 minutes to compile. Further details of the model and its components is given in Chapter 2 section 2.4.

5.3.2 Model Validation

Prior to developing the nudging code, I first validated the representation of Pacific climate and climate variability in FORTE 2.0 against reanalysis data to assess its suitability for my intended application. A 250-year control simulation was performed using the configuration described in Chapter 2 section 2.4 with the analysis using the final 100 years of the integration. Figure 5.1 shows timeseries of the PDO index and maps of the PDO expression in surface temperature in FORTE2.0 and the HadISST version 1.1 observational dataset from 1920-2019. The method for calculating the spatial signature of the PDO is described in Section 2.5.4. Figure 5.1 shows similarities between the modelled and observed PDO structure across the North Pacific, with the characteristic horse-shoe pattern extending out eastwards from Japan. In both cases, the PDO is shown in its negative phase. The magnitude of the oscillation in the tropical regions is less pronounced in FORTE2.0 but is still evident. There is good qualitative agreement extending down into the subtropical south Pacific. The PDO index time series shows decadal scale variability, consistent with observations.

To assess the model's representation of the atmospheric bridge and the communication between the tropical Pacific and extra-tropical Pacific, Figure 5.2 shows the lead-lag relationship of SSTs in both regions regressed onto the PDO index. As one would expect, the largest correlation between the PDO and North Pacific SST occurs at lag-0. SST variability in the tropical Pacific exhibits a leading tendency in relationship with the PDO, concurring with the general consensus that the tropical Pacific drives substantial variability in the extratropics (e.g. Newman et al., 2016). This is further highlighted in Figure 5.3 where the greatest surface ocean anomalies in the tropical Pacific are found to lead the PDO by 7 months. However, the presence of a 'shoulder' at positive lag values up to +6 months (red line, Figure 5.2) highlights that there is a positive correlation where the extratropics leads the tropics, implying a potential role for the extratropics in driving SST variability in the tropics.

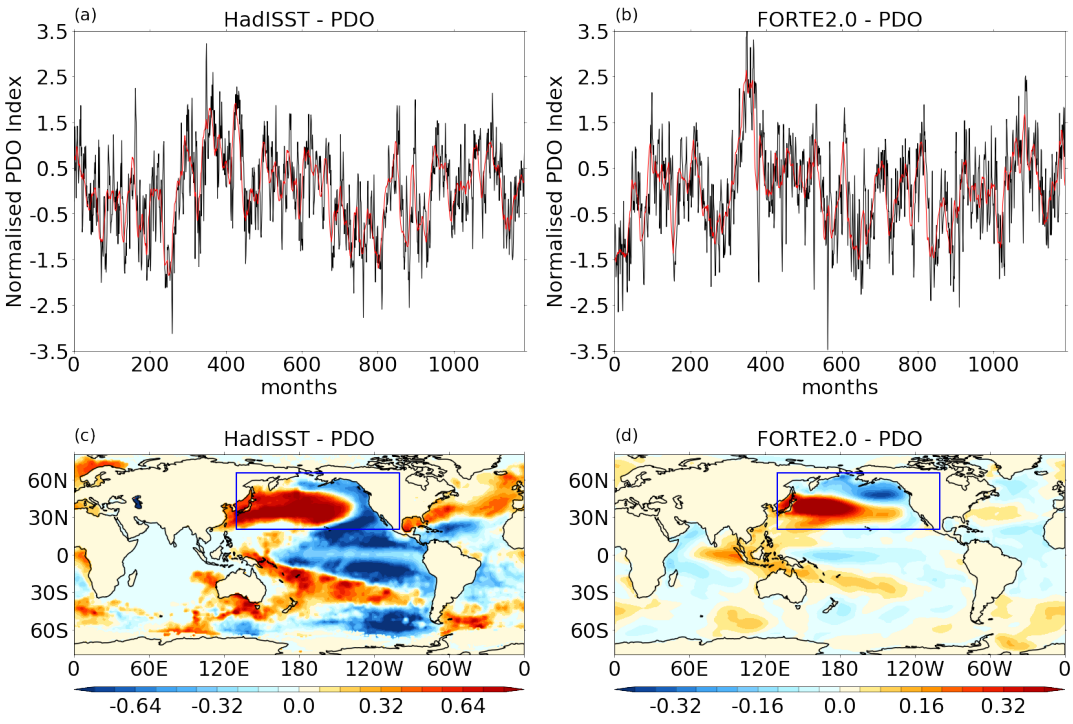

Figure 5.1: Upper two panels: (left) Normalised PDO index from the HadISST observational dataset (months spanning 1920-2019). (right) Normalised PDO

index from the FORTE 2.0 control run (final 100 years). Black line represents monthly values, red line represents the 12-month running mean. Bottom two panels: (left) Linear regressed SSTAs from observations onto the PDO index of HadISST version 1,1. (right) Linear regressed SSTAs onto the PDO index from the FORTE2.0 control experiment. Both of the bottom two panels show the PDO in its negative phase.

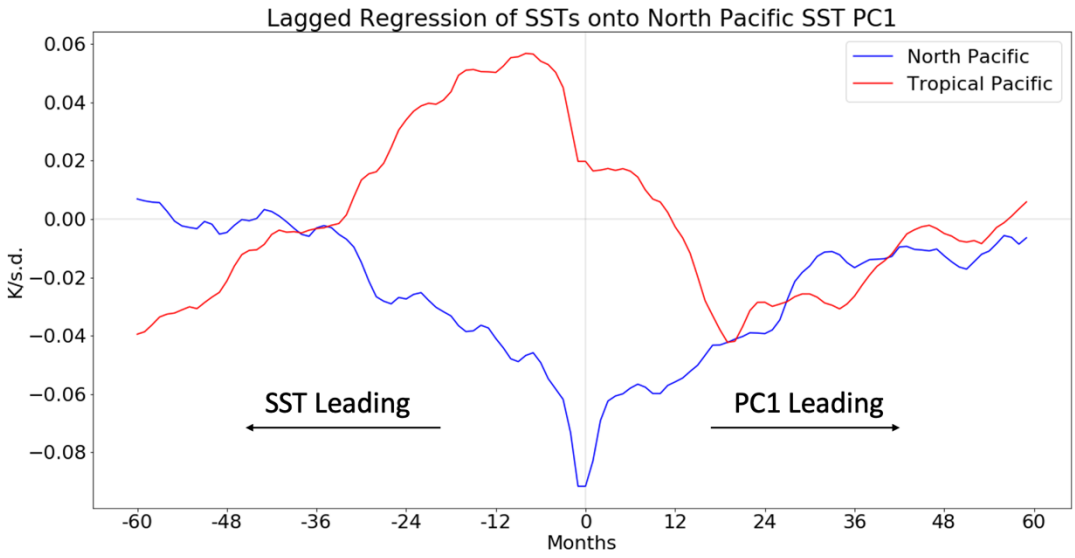

Figure 5.2: Lagged regression of FORTE2.0 SSTs onto North Pacific SSTs PC1 (PDO indices). The regions defining the North and Tropical Pacific are shown in the blue and red boxes in Figure 5.3, respectively.

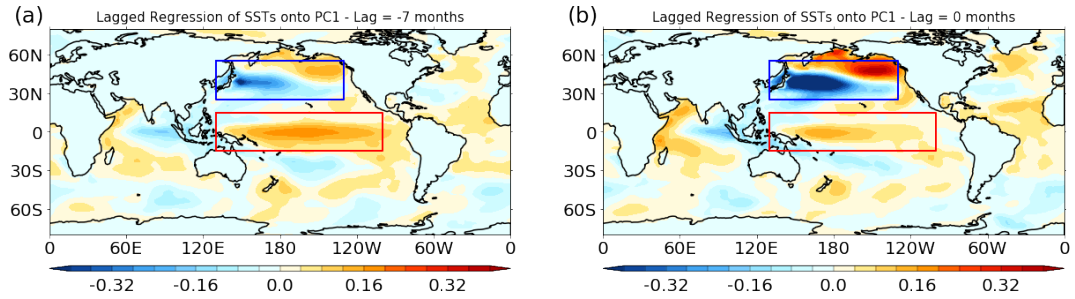

Figure 5.3: Lagged regression of SSTs onto North Pacific SSTs PC1 (PDO indices). Bottom panels show LR at lag=0 months and lag=-7 months. Red box – Tropical Pacific, Blue Box – North Pacific

In addition to simulating PDO-like variability, I validated the ability of FORTE2.0 to represent the AL. Figure 5.4(b) shows the representation of the AL as an extended boreal winter season (NDJFM) anomaly from the annual mean. For comparison, Figure 5.4(a) shows the ERA5 reanalysis dataset.

While the climatological AL is deeper in the reanalysis dataset there is an area of sustained low pressure in the north Pacific over the Aleutian Islands representative of the AL.

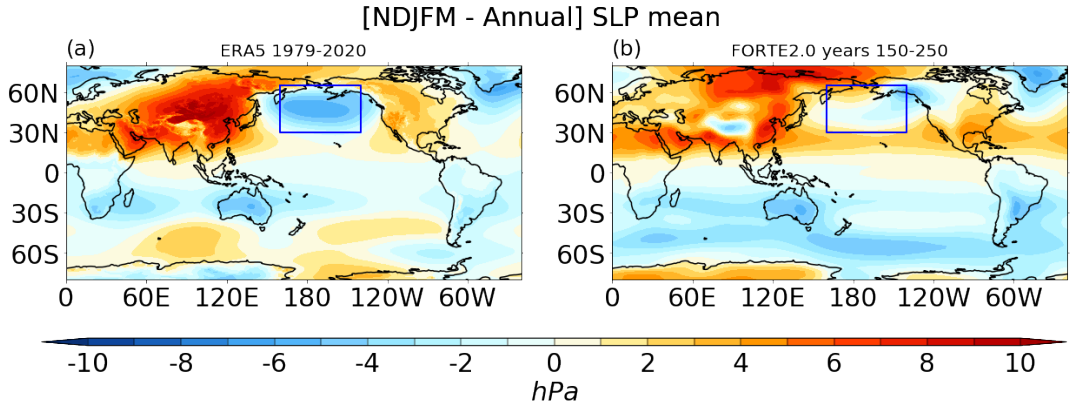

Figure 5.4: Comparison between climatological AA in ERA5 reanalysis data and in FORTE2.0. The annual mean SLP is subtracted from the extended boreal winter [NDJFM] to produce the anomalies.

Assessing the relationship between the PDO and the AL in FORTE 2.0 was accomplished by calculating the lead-lag correlation between the PDO and AL indices and linearly regressing the AL anomalies onto the first PC of SST anomalies in the region defining the PDO. Figure 5.5 shows a simultaneous relationship between PDO and NPI indices, implying that simultaneous variability in both indices, which is also in agreement with Newman et al. (2016).

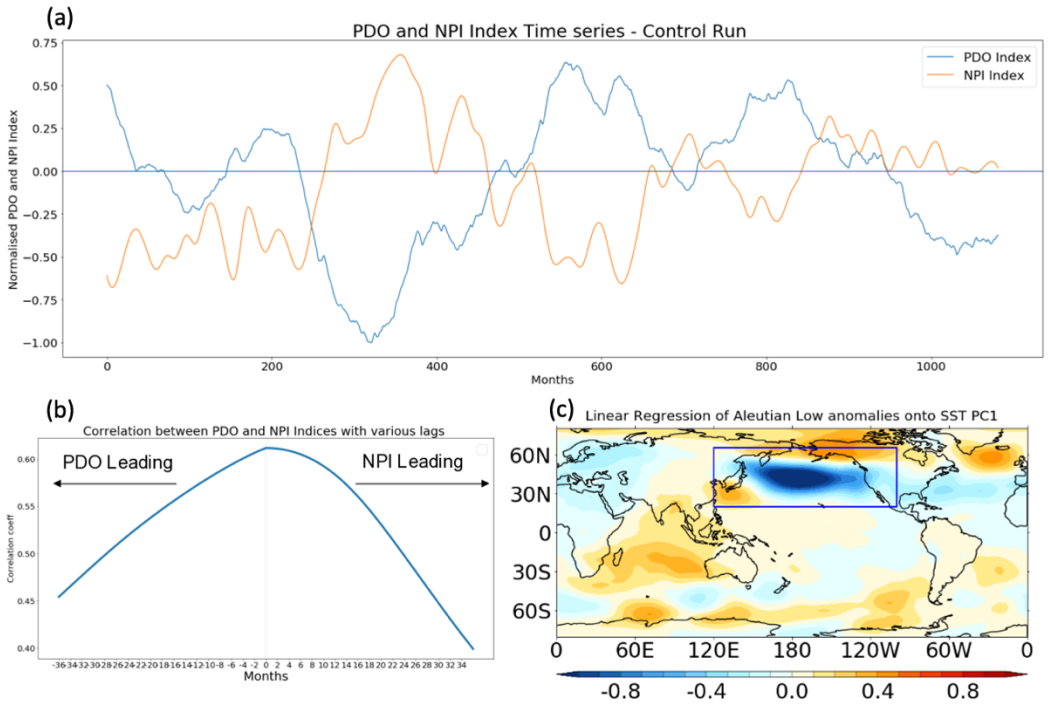

Figure 5.5: Top - time series of PDO and NPI Index from years 150-250 of control run. Bottom left- Correlation between PDO and NPI Indices with various time lags. Bottom right – LR of SLP anomalies onto SST PC1 at lag=0.

In summary, FORTE2.0 produces PDO-like variability with a similar spatial pattern to observations but a weaker amplitude in the tropical and South Pacific. The climatological AL is weaker in FORTE2.0 than in reanalysis data, but the relationship between the AL and the PDO is similar to that found in observations. The satisfactory representation of these aspects of variability gave me confidence to proceed with developing the nudging code within the atmospheric component of FORTE 2.0

5.4 Nudging code development

5.4.1 IGCM4 Model Structure

The structure of the IGCM4 model is shown in Figure 5.6. The key routines that make up the code are shown, as well as the points where spectral to grid point space transformations are performed.

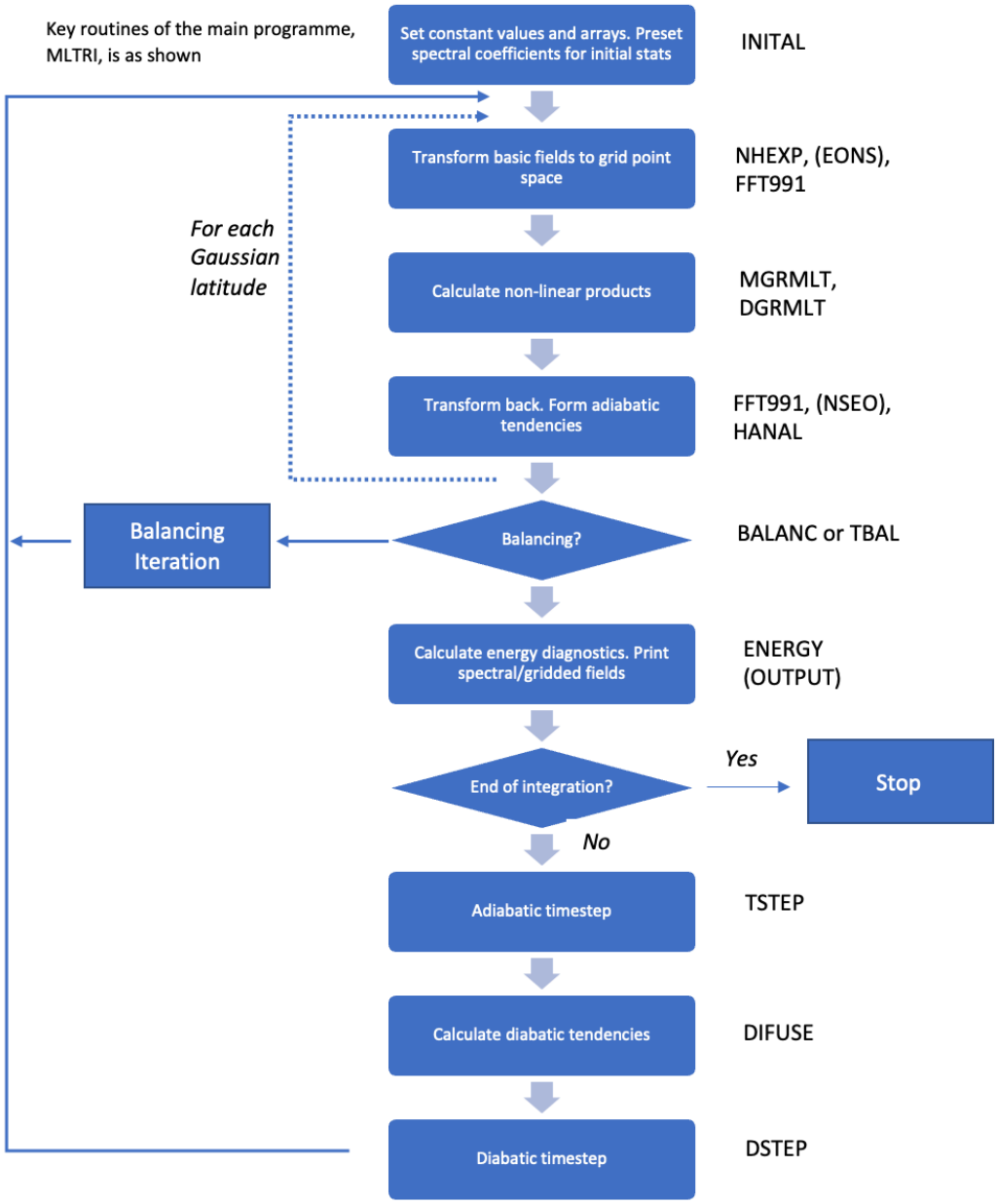

Figure 5.6: Adapted from the IGCM original documentation. Overall model structure of IGCM. For descriptions of the individual routines, see the original documentation.

5.4.2 Code development

The first challenge in code development was remotely compiling the model onto the ARC4 HPC at Leeds during the COVID-19 pandemic. Learning FORTRAN on the fly whilst ironing out bugs in the compilation with limited assistance was a major challenge, but one that allowed me to learn the fundamentals of the model architecture.

The nudging code is implemented in the atmospheric component of the model (IGCM4). IGCM4 is a spectral primitive equations model, which uses a spherical geometry with representation of the fields at each level as a truncated series of spherical harmonics. Given how the code has been annotated and updated, navigating, and developing the IGCM4 code was very challenging. Previous edits had been made in IGCM4 to implement nudging of zonal mean fields (wavenumber-0 in spectral space) in the stratosphere (in the DIFUSE routine). However, initial attempts to modify this existing code to enable regionally varying nudging in grid point space proved unsuccessful. Extensive testing revealed that the DIFUSE routine could not accurately perform the multiplication of nudging coefficients. This was due to the limitations of performing the operation in spectral space in which the required operation was an array convolution. Figure 5.7 shows a comparison between a convolution (representing spectral space) of spectral coefficients and a multiplication (representing grid point space). Therefore, due to the requirement to nudge across all spectral wavenumbers in a specified region (spatially and vertically), and re-engineering the code to allow matrix multiplication in grid-point space, the routines DGMRLT and MGMRLT were chosen to add the gridpoint tendencies to U,V,T, and surface pressure fields. As shown in Figure 5.6, these routines are performed after the prognostic variable fields have been transformed into grid-point space.

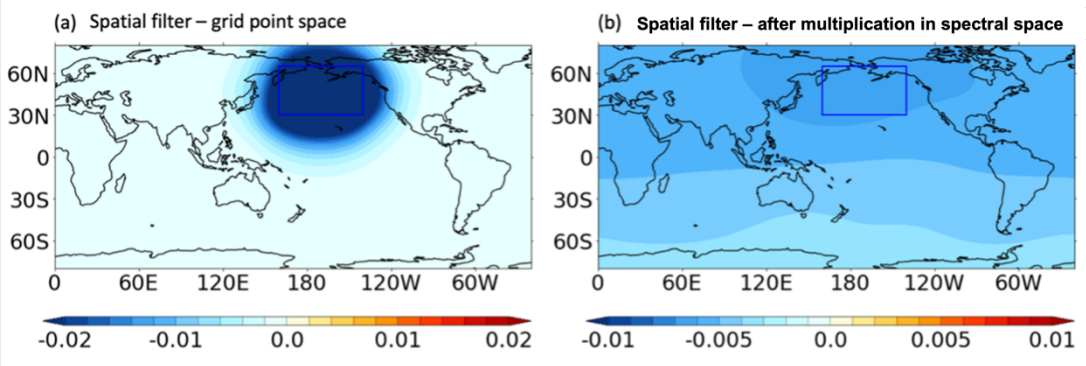

Figure 5.7: Using spharms python package, panel (a) shows the spatial filter in grid-point space after multiplication by a latitude/longitude mask. (b) shows the spatial filter in spectral space after convolution with a latitude/longitude mask.

The mathematical form of the nudging equation is similar to that in Jung et al. (2010) and Watson et al. (2016), with two additional terms to account for vertical dependence (α) and seasonal dependence (β) in the nudging strength:

$$\delta x = -\gamma(\Phi, \lambda, \alpha, \beta)(x - x_{ref})/\tau \qquad \textit{Equation 5.15}$$

where x is the variable being relaxed, x_{ref} is the reference value, and τ is the nudging strength (set to 6hr). The spatial extent, $-\gamma(\Phi,\lambda)$, of the nudging was tested extensively, aiming to avoid any shock effects at the boundaries and spurious effects of nudging near polar regions. α and β represent the vertical and temporal variability in the nudging coefficients, respectively. The regional extents were determined as

$$\gamma(\Phi, \lambda) = f(\Phi, \Phi_1, \Phi_2) f(\lambda, \lambda_1, \lambda_2) \qquad \textit{Equation 5.16}$$

where,

$$f(\Phi, \Phi_1, \Phi_2) = \left[\frac{1}{1 + e^{-\frac{(\Phi - \Phi_1)}{\delta_1}}}\right]\left[1 - \frac{1}{1 + e^{-\frac{(\Phi - \Phi_2)}{\delta_2}}}\right] \qquad \textit{Equation 5.17}$$

$$f(\lambda,\lambda_1,\lambda_2) = [\frac{1}{1+e^{-\frac{(\lambda-\lambda_1)}{\delta_1}}}][1-\frac{1}{1+e^{-\frac{(\lambda-\lambda_2)}{\delta_2}}}] \qquad \textit{Equation 5.18}$$

with Φ_1 and Φ_2 representing the southern and northern limits of the latitude, respectively. λ_1 and λ_2 represents the western and eastern limits of the longitude, respectively.

The vision for the application of this nudging code was to test the effect of an anomalous lower tropospheric, North Pacific state in an extended boreal winter on Pacific modes of variability. Therefore, the strength of the tropospheric nudging is set to its maximum value at the lowest pressure level (sigma = 0.96), which decreases to zero in the uppermost level of the 20-level IGCM4 atmosphere. The target region for the nudging is the extent of the region in which the climatological AL is defined [30^{o}N-65^{o}N, 160^{o}E-140^{o}W]. Additionally, the nudging code was designed so that the nudging would only take place during the extended boreal winter (NDJFM), peaking on January 15th. A Gaussian function, based on the evolution of NPI strength in ERA5 (Figure 5.8), was implemented to ramp up/down the strength of the nudging throughout the extended winter.

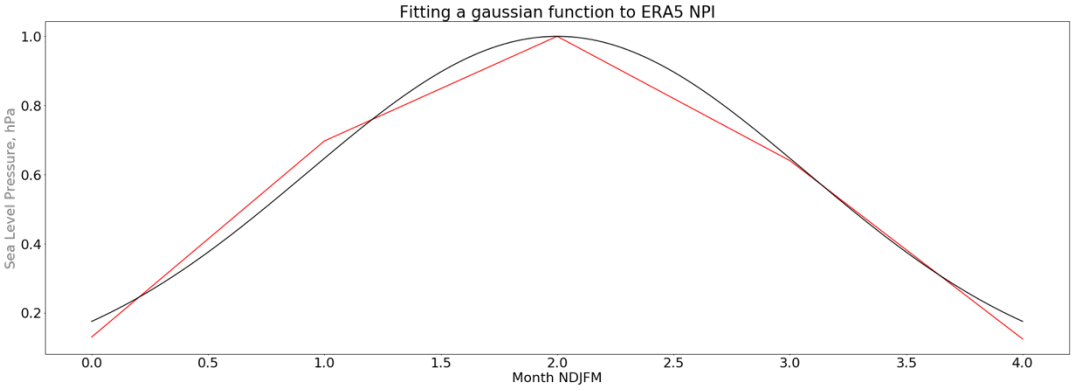

Figure 5.8: Fitting a gaussian function (black line) to the average strength of the NPI across the 4-month extended boreal winter in ERA5 (red line). The Gaussian fitting process shown here was used for the testing of the ramp up/down of temporal nudging coefficient.

5.4.3 Choice of reference state, x_{ref}

Figure 5.4 showed the climatological AL in FORTE2.0 is weaker than in ERA5; however, there are individual winters within which the NPI anomaly falls within the spread of the reanalysis data. A reference state was chosen from the FORTE2.0 control run that represented an anomalously strong AL state. Year 163 of the spin-up run shows the strongest NPI, and this was chosen to represent the test case in the analysis (Figure 5.9). The SLP anomaly peaks in January of year 163 (Figure 5.9), in agreement with the anomaly seen in ERA5. Therefore, January of year 163 was taken as the reference anomaly.

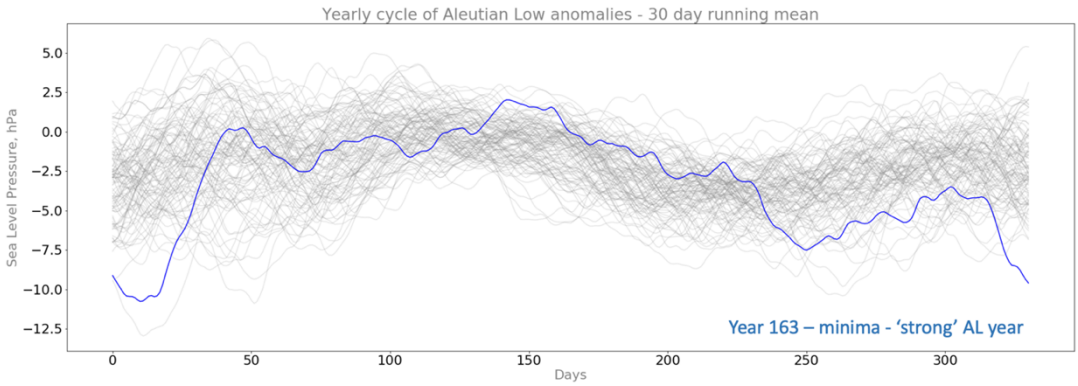

Figure 5.9: SLP anomalies [hPa] in years 150-250 of the FORTE2.0 control run (thin grey lines). Days (x-axis) represent day of the year, e.g. 0 = January 1st. Blue line represents the strongest AL year used as the reference state for the nudged simulation.

5.5 Nudging code testing and implementation

To test that the nudging code was implemented correctly, various test simulations were performed.

In the first instance, a global nudged run was performed with nudging applied at each timestep (20 minutes) through the extended boreal winter. Figure 5.10 shows surface pressure anomalies over the first four timesteps of a case where nudging was applied globally to surface pressure only. The comparison is made with the anomaly in the reference state, x_{ref}.

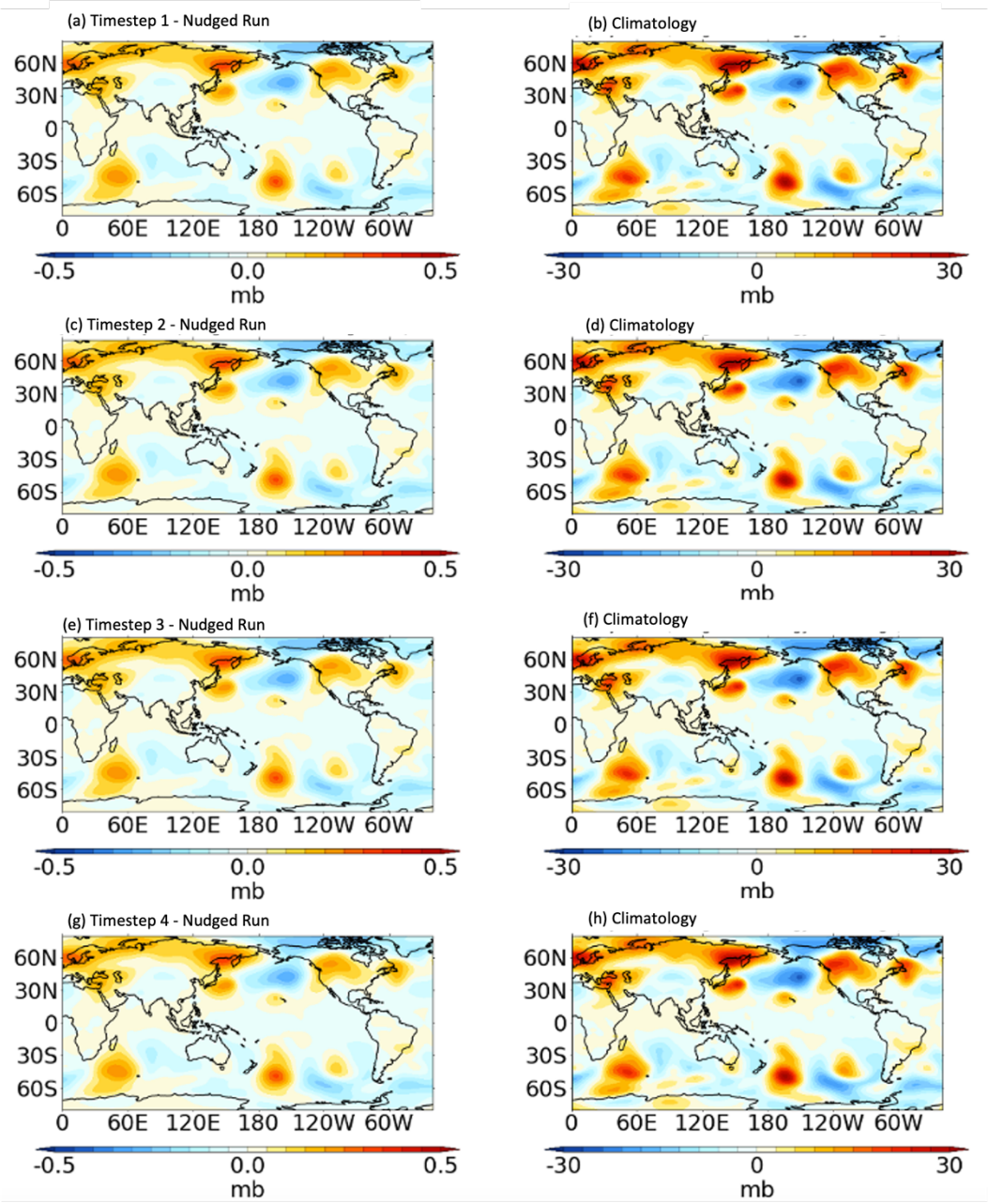

Figure 5.10: Model validation. (Left hand column) The first 4 timesteps of a globally nudged model (where only surface pressure is nudged) [Nudged run

– Control Run] compared against (Right hand column) the nudging climatology. Panels b, d, f and h are identical to aid comparison with panels a, c, e and g.

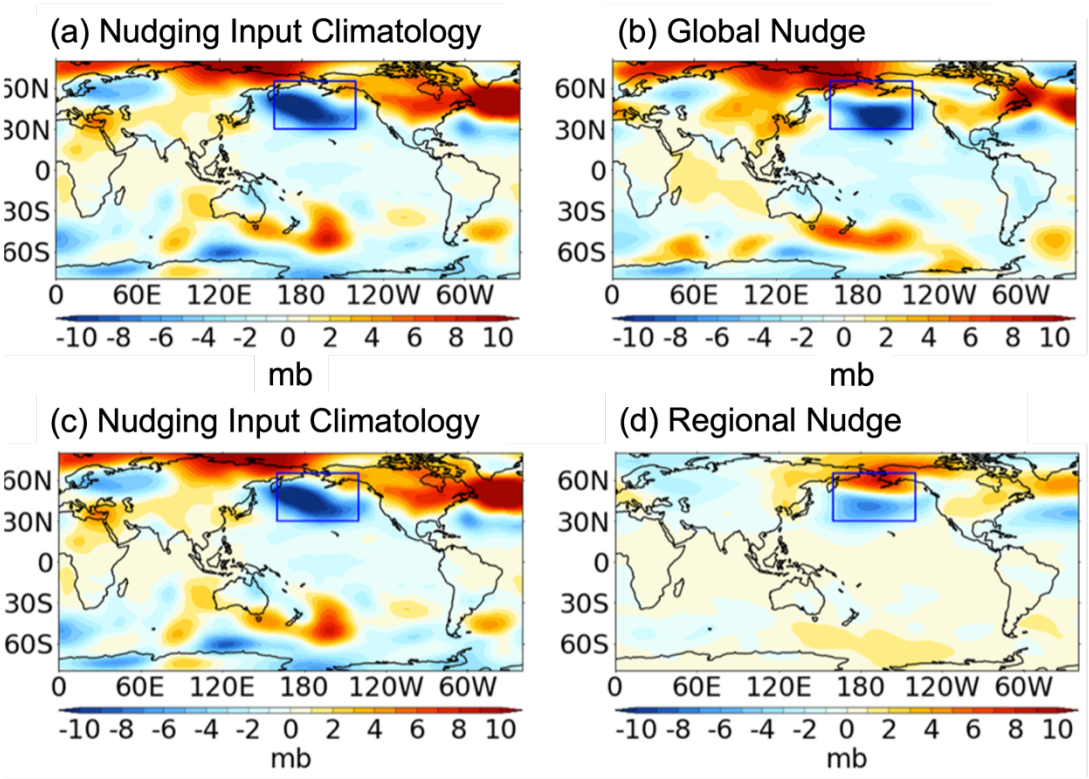

Figure 5.11: Comparison of surface pressure anomalies [hPa] between a globally nudged simulation (b) and a regionally nudged simulation in the North Pacific (d) [Nudged run – Control] using the same x_{ref}. Left hand represents the climatology towards which the simulations are being nudged (panels a and c are identical). In each simulation τ = 48hr.

Given that nudging the variables globally was producing a satisfactory representation of the nudging reference state, Figure 5.11 shows the comparison between a globally and regionally nudged simulation. The aim of this test was to assess the result of applying a spatial filter to the nudging reference state where the nudging coefficients would taper to 0 at the margins. Various filters were tested aiming to minimise any 'shock' when the predominantly zonal moving trade winds impinge on the nudging domain, whilst encompassing the full domain over which the AL forms. Comparing Figure 5.11 panels b and d shows the expected effect of the spatial filter with the

largest anomalies present within and downstream of the spatial filter selected (i.e. across the extratropical North Pacific and into the North Atlantic).

The effect of varying the nudging timescale (τ) between 6hr and 48hr was tested. Figure 5.12 shows the results of a set of three experiments where the τ was set to 48hr (in panel a,d) and 6hr (in panels b,e and c,f), in each case the model is stable with the North Pacific being drawn towards the nudging reference state. In Figure 5.11, which displays the difference between a model nudged globally and in the region of the North Pacific only, a value of τ was also set to 48hr. After further testing, a value of 6hr was chosen for future work to align with previous studies such as Jung et al. (2010), Watson et al. (2016) and Knight et al. (2017). It became evident during testing that the preferred approach was, in focussing on an extended boreal winter, that all simulations would commence nudging in November of year 1 of the simulation, rather than on 1 January when the model is initialised.

Figure 5.12 shows the effect of different spatial filters (with varying latitudinal and longitudinal forms) on the performance of the nudged simulation. The results of applying these filters in the nudged simulations is shown in Figure 5.12 d, e and f. Panels a, b and c show three different spatial filters. Here, the simulation in panel a, d has τ = 48hr, the simulations in panels b, e and c, f have τ = 6hr. Comparing the nudged simulations to the target reference state, it is clear that with τ = 6hr and the spatial filter extending further poleward, the reference state is more accurately reproduced. Key features which provide confidence in the methodology include the absence of strong anomalies in regions outside the North Pacific. The shape of the Gaussian function that applied weights to the temporal nudging coefficients

throughout this season was tested. To maximise the nudging signal, a 'super' Gaussian function, which has a more persistent maximum coefficient throughout the season, was tested and applied to the simulations shown later in the chapter. In order to impart maximum nudging strength in the lower troposphere whilst nudging throughout the 20-level tropospheric column, the vertical nudging strength decreases with height. Various vertical tapers were tested to ensure no undesirable effects manifest and to ensure model stability. Figure 5.13 shows a comparison between the input reference state (panel a) and the output anomaly (panel b) at the upper troposphere, demonstrating a reduction in nudging strength with height in the tropospheric column. Panel c shows vertical profiles of various tapers that were tested with the results in panels a and b corresponding to KNUDGx1 in panel c. Figure 5.14 shows the strength and shape of the finalised spatial, vertical, and temporal tapers that are used in the subsequent simulations.

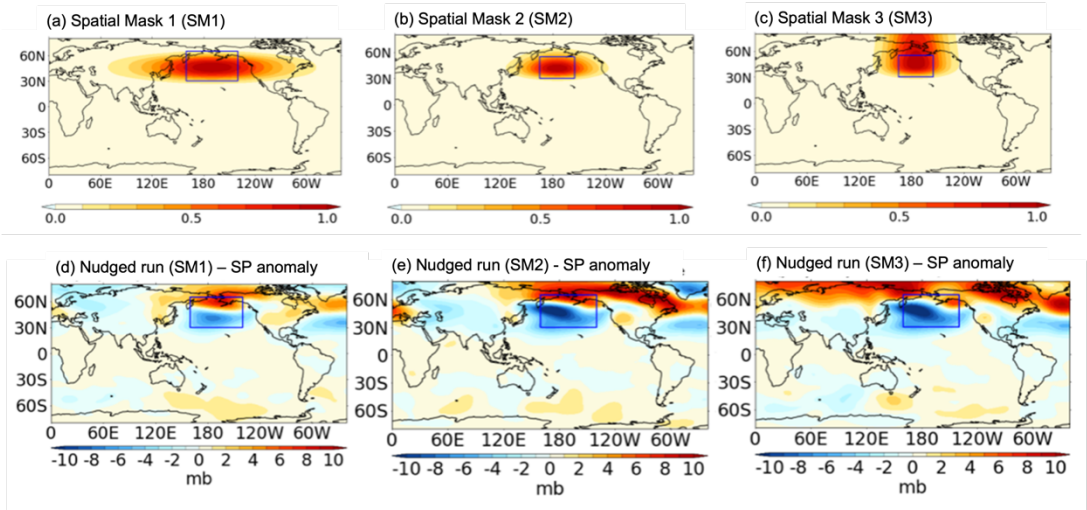

Figure 5.12: Panels a,b,c show three different spatial masks (SM1, SM2, SM3) applied in the testing phase of model development. Panels d,e,f show the surface pressure response to nudging experiments [Nudged run – Control] with these spatial masks a, b and c, respectively. τ = 48hr for panel d and τ = 6hr for panels e and f.

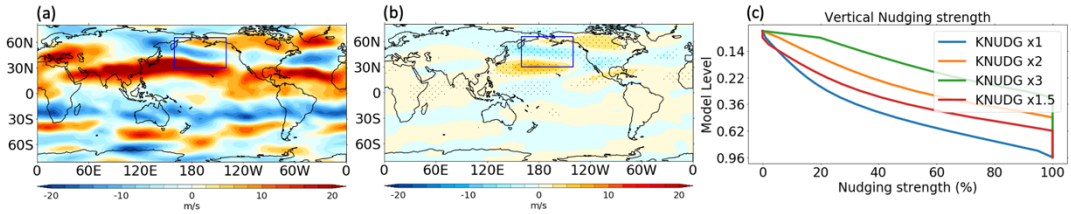

Figure 5.13: (a) Upper troposphere zonal wind input reference state (b) Upper troposphere zonal wind anomaly corresponding to vertical nudging strength KNUDGx1 in panel (c). (c) Vertical profiles of vertical nudging tapers tested.

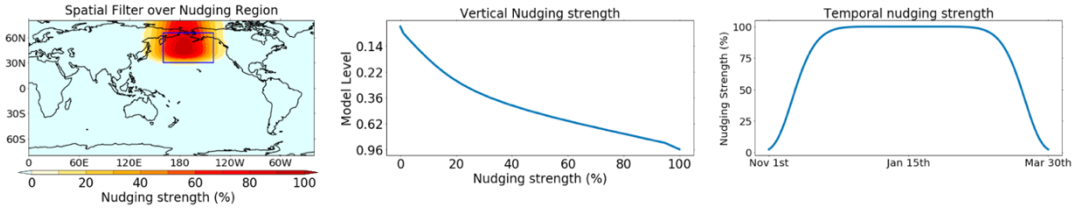

Figure 5.14: Details of the nudging kernel optimised through testing. (a) Spatial nudging strength (corresponds to SM3, Figure 5.12), (b) vertical profile of nudging strength and (c) temporal shape of nudging strength.

To assess the stability of the model with the additional nudging tendencies applied, the temporal evolution of the TOA energy budget was analysed. In an equilibrium climate, there is a global balance between incoming and outgoing radiation. Applying additional tendencies through a forced perturbation has the potential to disrupt this equilibrium state, however the evidence from Figure 5.15 suggests that, although there is an initial response of the system in the first 2-3 years amounting to an increase in GMST of around 0.1 K, the climate reaches a new equilibrated state with no evidence of longer-term model drift.

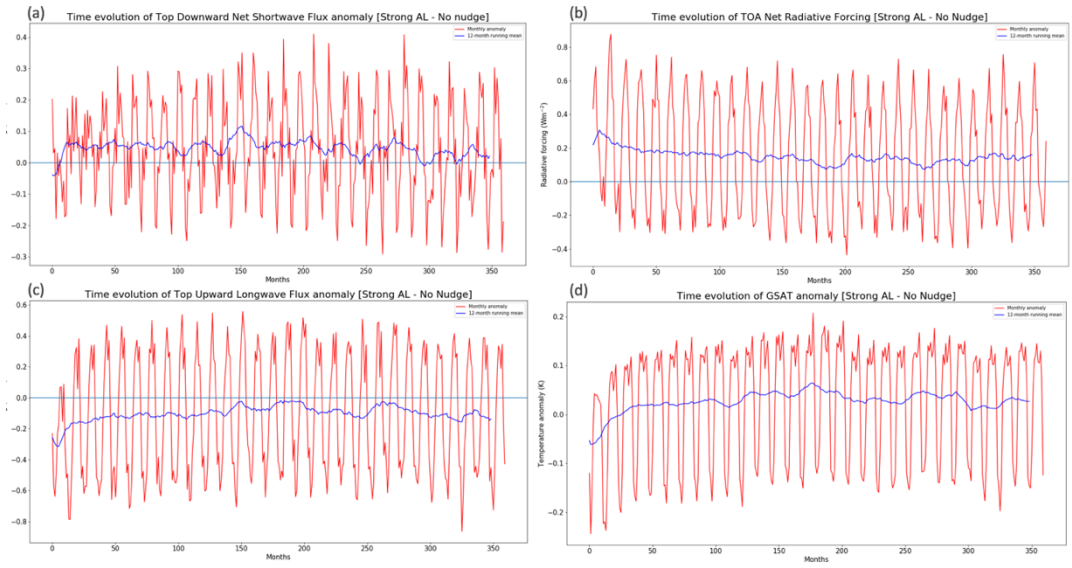

Figure 5.15: a - Time evolution of Top Downward Net Shortwave Flux anomaly [Strong AL – No Nudge]. Red = monthly anomaly. Blue = 12-month running mean. b – Same as a but Time evolution of TOA Net Radiative Forcing anomaly [Strong AL – No Nudge]. c – same as a but Top Upward Longwave Flux anomaly [Strong AL – No Nudge]. d - same as a but Time evolution of GSAT anomaly [Strong AL – No Nudge].

Given the focus of this work is on decadal variability, I decided on an experiment design whereby individual ensemble members would be integrated for 30 years, with nudging applied each winter and then terminated. This would simulate a scenario in which there is a persistent AA anomaly that is externally-driven over decadal timescales, but does not build up spurious signals over many decades from applying the same anomaly year-on-year. To implement this experiment strategy, I developed shell scripts that allow large ensembles of nudged simulations to be performed, with each simulation spinning off from different initial conditions taken from the control run. A schematic representation of the ensemble simulations is depicted in Figure 5.16. Here, initial conditions are taken from a given year and the subsequent ensemble member retrieves the initial conditions by cycling backwards in time in one-year increments. This differs from other methods in which ensemble members are generated (e.g. perturbed parameter or stochastic physics), for

which the reader is referred to Chapter 1, section 1.8 for a comprehensive overview. Nonetheless, the result of this method is that nudging towards the same state is applied to different climate states, facilitating a measure of internal variability.

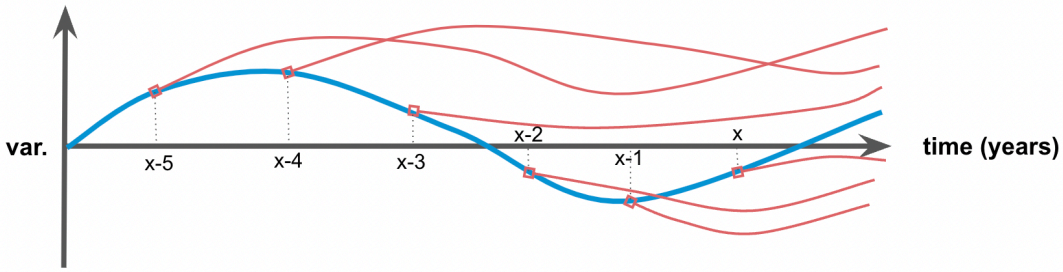

Figure 5.16: A schematic representation of ensemble simulations. Initial conditions for each ensemble member are taken from one point in time (e.g. starting at time t = x).

To demonstrate results of ensemble generation, Figure 5.17 shows the comparison between the surface temperature nudging reference state (derived from January of year 163 from the control run) and the anomaly calculated from the ensemble mean of a 50-member nudged run with respect to the control run. Similar broad patterns are evident in the North Pacific, but the ensemble mean exhibits much less noise meaning a clear signal from the influence of the intensified AL can be extracted. Similarly, Figure 5.18 shows the upper tropospheric wind anomalies generated from the nudged run ensemble, when compared with the extended control run.

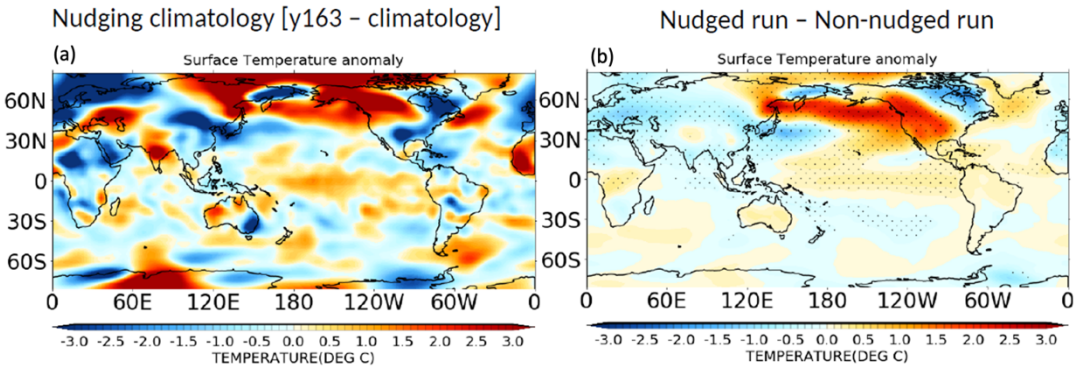

Figure 5.17: Surface temperature anomaly. Left: Nudging reference state (towards which the model is drawn). Right: [Strong AL – No Nudge] ensemble mean anomaly. Stippling indicates regions of 95% significance where ensemble mean value lies outside of bounds +/- 1.96 times S.D.

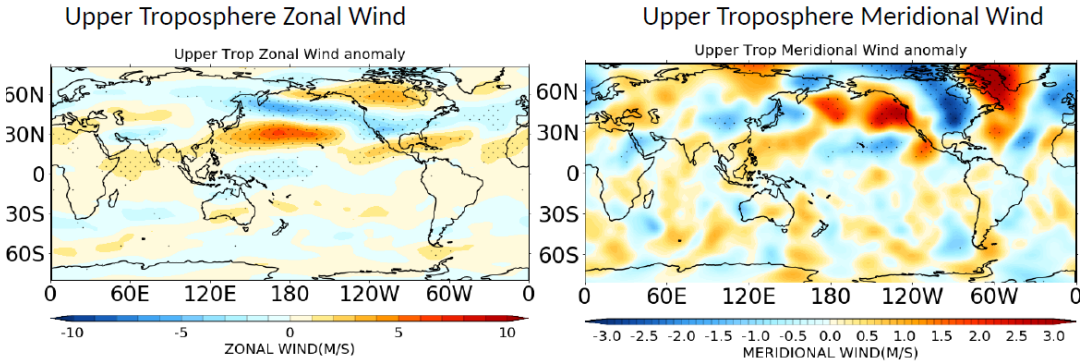

Figure 5.18: Upper Troposphere Wind anomalies. Left: Upper Troposphere Zonal Wind [Strong AL – No Nudge], Right: Upper Troposphere Meridional Wind [Strong AL – No Nudge]. Stippling indicates regions of 95% significance where ensemble mean value lies outside of bounds +/- 1.96 times S.D.

I have demonstrated the development of new functionality for the FORTE 2.0 model which, through extensive testing has been proven to be stable and functional. The nudging code (given in full in the Appendix) is ported in the CREATE.basic.L20 script and toggled on with the LNUDGGP switch in the namelist. Additional python scripts were written to pre-process the data into the correct (.dat) format. The python scripts are interactive and allow adjustments to be made to the spatial nudging strength as well as conditioning the state towards which the model will be nudged. Upon execution of the model with the new nudging code, the model slows down, taking around 15 minutes to complete one model year or double the simulation

time of the original model. However, this is still relatively fast for a GCM meaning the full ensemble experiment could be performed in less than one week.

While nudging is a powerful tool to explore climate interactions and isolate specific parts of the system, a limitation is that it breaks the dynamic-thermodynamic coupling and introduces an inconsistency between the model dynamics and physics. The solutions by construction have the potential to violate normal constraints on global circulation, such as the conservation of momentum and energy. In some cases, the model may be drawn towards a solution that is different from its own steady state (e.g. if being drawn towards observational data). Furthermore, nudging can induce non-negligible changes to the hydrological cycle (Kooperman et al. 2012) whilst Zhang et al. (2014) noted changes in the radiation budget arising from nudging. These caveats must be borne in mind when interpreting results derived from nudging experiments and one must be sensitive to the potential for introduction of new biases and unrealistic fields. Nevertheless, the extensive testing carried out in the development of the nudging capability in FORTE2.0 lends confidence that it can be a useful tool to investigate the wider impacts of anomalous atmospheric circulation in the North Pacific on the Pacific basin.

Chapter 6 - Tropical Pacific warming forced by strong Aleutian Low via the seasonal footprint mechanism

6.1 Introduction

Chapter 1 described how the AL is a precursor to the oceanic expression of the PDO in the North Pacific (Newman et al. 2016; Smith et al. 2016), including the North Pacific subpolar gyres (e.g. Pickart et al. 2008), upper ocean temperatures (e.g. Latif and Barnett, 1996) and sea surface height (e.g. Nagano and Wakita, 2019). On interannual to decadal timescales, the AL is modified by tropical Pacific SST anomalies that excite upper tropospheric Rossby waves which propagate to the extratropics as part of the 'atmospheric bridge'. The prevailing model for the PDO therefore regards the extratropical atmosphere-ocean response to be predominantly driven from the tropical Pacific (e.g. Newman et al., 2016; Zhao et al. 2021). Nevertheless, decadal changes in the AL may be driven by mechanisms other than the tropics, including Arctic sea ice changes (Simon et al. 2021; Deser et al. 2016), the stratosphere (Richter et al., 2015) and regional radiative forcing (Smith et al, 2016; Dow et al. 2021; Dittus et al. 2021). In these cases, it is less understood the extent to which an anomalous AL can itself drive tropical Pacific SSTs and may therefore generate basin-scale SST anomalies that are not confined to the North Pacific. Some studies have proposed that low frequency variability can originate from the extratropical North Pacific (e.g. Lysne et al., 1997) due to oceanic integration of stochastic atmospheric forcing, seasonally-insulated ocean temperature anomalies (e.g. Alexander and Deser, 1995), wind-driven adjustment of the ocean gyre circulation (Taguchi et al. 2007) and Rossby wave adjustment (Schneider et al. 2002; Kwon and Deser, 2007). Modulation

of the North Pacific subtropical gyre (Gu and Philander, 1997; Zhang and McPhaden, 2006) has also been shown to impact extratropical to tropical communication. Here, changes to the overturning circulation affect the degree to which cooler surface waters are advected equatorward and subsequently upwelled (McCreary and Lu, 1994).

Pierce and Barnett (2000) examined mechanisms linking the midlatitudes and the tropics in the Pacific on decadal timescales. They found a low frequency relationship between patterns of North Pacific SST and surface wind stress reaching the equator, implying extratropical modulation of the trade winds in the tropics on decadal timescales. This finding is supported by Barnett et al. (1999). A role for atmospheric forcing is also elucidated in a modelling study by Clement et al. (2011), who hypothesised that tropical decadal variability does not require interactive ocean dynamics and is consistent with stochastic atmospheric forcing. Therefore, the nature of the forcing from the extratropical Pacific is still not fully understood.

Sun and Okumura (2019) imposed anomalous surface heat fluxes associated with the NPO in a coupled model and found that North Pacific variability could, albeit weakly, affect decadal variability in the tropics. The causal mechanism found is known as the seasonal footprint mechanism (SFM). Winter net surface heat flux anomalies associated with large-scale extratropical atmospheric variability can cause SST anomaly persistence through spring-summer. Atmospheric circulation anomalies (i.e. zonal wind-stress), driven by the subtropical portion of the SST footprint, then modulate tropical SSTs through coupled atmosphere-ocean dynamics. The SFM can account for up to 70% of interdecadal tropical Pacific SST variability (Vimont

et al., 2003). Liu et al. (2021) highlighted the role SFM plays in communicating anomalous North Pacific SSTs to the tropical Pacific where modulation of the PNA pattern causes modulation of the Atlantic Warm Pool.

In this chapter, I aim to build on the work of Sun and Okumura (2019) to further investigate the mechanisms that drive communication between the wintertime extratropical North Pacific atmosphere and the tropics over decadal timescales. This will lead to better understanding of the role the AL plays in governing basin-scale PDV. To this end, I design and run an ensemble of nudging simulations in an intermediate complexity coupled climate model (FORTE2.0) to isolate the impact of an anomalous AL on climate. I compare the nudging simulations with a free running control simulation to allow me to isolate the mechanisms resulting from the anomalous AL.

6.2 Aim and research questions

This chapter aims to increase the understanding of the relationship between the extratropical North Pacific and tropical Pacific by answering the following research questions:

1. Do nudging simulations where the North Pacific is nudged towards an anomalous AL state during an extended boreal winter produce a significant signal in tropical Pacific climate over interannual to decadal timescales?
2. If so, which mechanism(s) facilitate this communication between the regions and, over what timescale(s) do these mechanisms operate?

6.3 Methods

6.3.1 Model simulations

All simulations in this chapter were performed using the nudging configuration of FORTE2.0 described in chapter 5. The reference state was an anomalously strong AL state simulated in a winter from the FORTE2.0 control run. An ensemble of 50 members was integrated for 30 years with nudging towards the reference state applied in each winter; this is referred to as NUDGED. The analysis uses all 1500 years of the NUDGED simulation and compares this to a control run.

6.3.2 Mixed Layer Heat Budget Analysis

To analyse the mechanisms that contribute to any change in the upper ocean (~30 m) temperature, I perform a mixed layer heat budget analysis in the regions shown by the green and black boxes in figure 6.2 (representing North Pacific subtropics and the Nino 3.4 region, respectively). Daily temperature tendencies due to advection, vertical and horizontal diffusion and convection are output from FORTE2.0. The vertical diffusion term represents the contribution due to surface heat fluxes. As described in the FORTE2.0 development paper (Blaker et al. 2020), starting from 5^{o}N/S the horizontal diffusion term increases from its default value to 20 times this value at the equator to counteract equatorial upwelling and parameterise the eddy heat convergence. The advection term is composed of vertical, zonal, and meridional terms which can be expressed as:

$$adv. = u\frac{\delta T}{\delta x} + v\frac{\delta T}{\delta y} + w\frac{\delta T}{\delta z} \qquad \textit{Equation 6.19}$$

I linearize the constituent terms of Equation 6.1 to investigate the relative role of the changes to ocean current velocity and temperature gradient in the form (demonstrated for meridional advection):

$$\left(v\frac{\delta T}{\delta y}\right)' = v'\frac{\delta T_0}{\delta y} + v_0\left(\frac{\delta T}{\delta y}\right)' + v'\left(\frac{\delta T}{\delta y}\right)' \qquad \textit{Equation 6.20}$$

where the subscript 0 denotes control run values and the prime denotes the deviations from the control run in the nudging experiment.

6.4 Results

As expected, the atmospheric circulation anomalies in the North Pacific in NUDGED closely follow those of the imposed reference state. There are cyclonic surface wind anomalies (max ~5 m s^{-1}) and an extension and narrowing of the subtropical jet over the North Pacific (Figure 6.1). The upper tropospheric meridional wind anomalies show a northward surface anomaly extending from the central northern subtropics to the coast of North America. Analysis into changes in RWS activity show anomalies in the western and central North Pacific (not shown). Interestingly, nudging the AL also generates surface and upper tropospheric zonal wind anomalies in the North Atlantic sector that resemble the reference state; however, further investigation of this downstream influence is beyond the scope of this chapter.

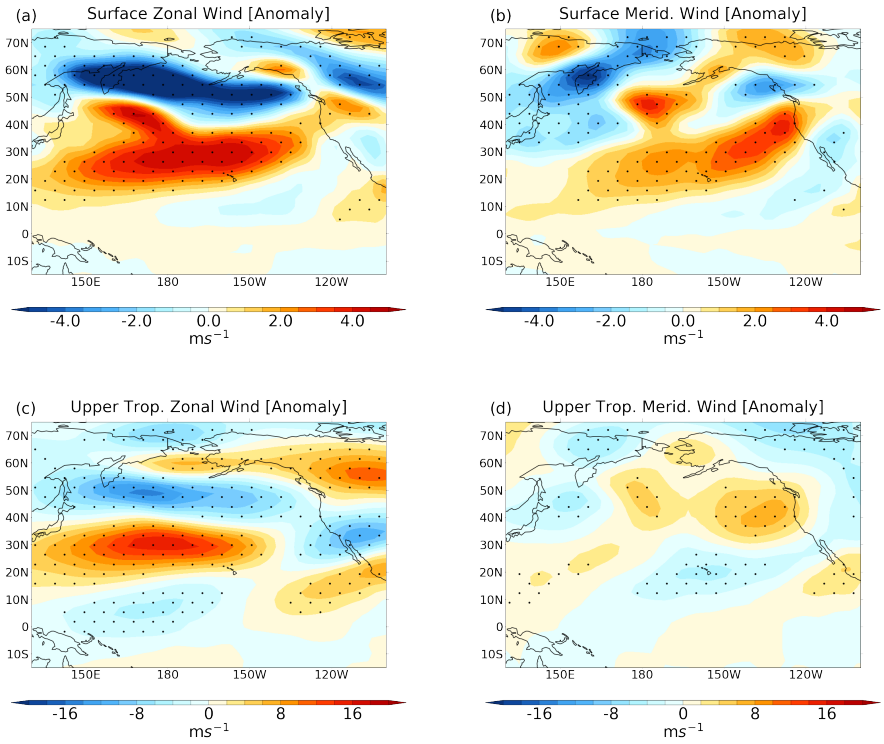

Figure 6.1: a-d: Annual anomaly [NUDGED – Control] mean (a,b) surface and (c,d) upper tropospheric (a,c) zonal wind and (b,d) meridional wind fields. Stippling denotes anomalies that are statistically significant at the 95% confidence level.

The ensemble mean difference in Pacific near-surface air temperature, expressed as an anomaly per unit PDO index anomaly, in the NUDGED simulation is shown in Figure 6.2b. There is a horse-shoe pattern of temperature changes across the North Pacific comprising of warming in the north and eastern Pacific and along the west coast of North America, and cooling in the western North Pacific/KOE region. The strongest warming (0.2-0.3 K/s.d.) is seen over the North Pacific and western North America. There is weaker (0.02-0.04 K/s.d.), but statistically significant warming simulated in the eastern and central equatorial Pacific. There are weaker changes in temperature that are not statistically significant in the Southern hemisphere. There is a high degree of agreement between the spatial pattern of the NUDGED anomaly and the PDO in the control run (Figure 6.2a), demonstrating that anomalies in the AL alone can generate a response that

resembles the basin scale mode of Pacific variability, but with a weaker signature in tropical temperatures.

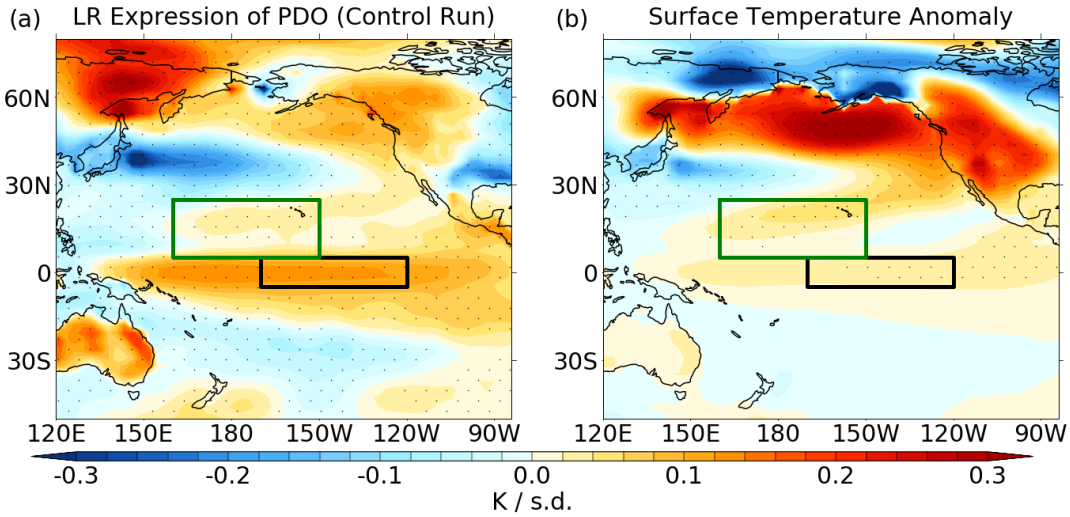

Figure 6.2: Near surface air temperature anomalies for (a) regression onto the PDO index in the control experiment and (b) ensemble mean composite anomaly for all years of the NUDGED strong AL experiment. Units are K per standard deviation. Stippling denotes anomalies that are statistically significant at the 95% confidence level.

The seasonality of the internally generated PDO in FORTE2.0 shows that the largest tropical temperature anomalies occur in boreal spring (MAM) and then dissipate in JJA (Figure 6.3, panels a-d). This seasonality agrees with that in the HadISST dataset (Figure 6.3, panels e-h). Wang et al. (2013) attribute the seasonality of the PDO to surface wind variability in the tropics and seasonal variability in the MLD across observational and model datasets, with strong surface wind variability in early spring responsible for the increased variability in the PDO. Other processes, such as variability in solar radiation, clouds and SST gradients in the North Pacific may affect the seasonality of the PDO.

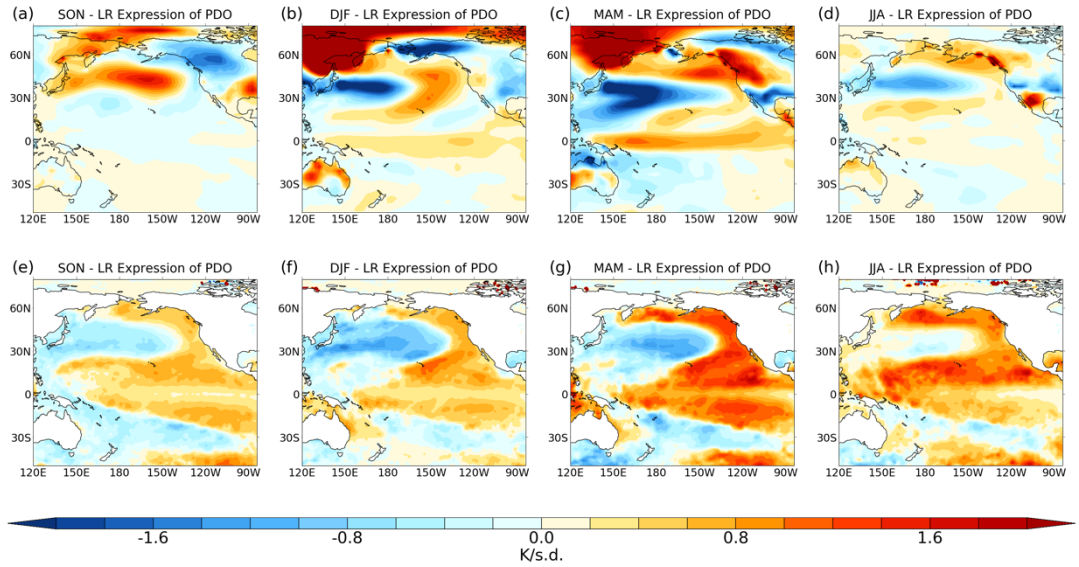

Figure 6.3: Panels a-d - Seasonal mean near surface temperature anomalies regressed onto the PDO index in the control experiment. Scaled by 5x for comparison with HadISST data (panels e-h). Units: K per standard deviation.

The seasonality of the temperature anomalies in the NUDGED experiment is shown in Figure 6.4 for years 1-2 and years 3-4 followed by the remainder of the run (years 5-30). The initial response to the intensified AL is a warming in the subpolar gyre in SON. This amplifies in DJF, where a tongue of warming also extends into the subtropical North Pacific. This pattern persists into MAM, but is also accompanied by warming in the eastern tropical Pacific. By JJA, the tropical and subtropical temperature changes have weakened leaving warming in the subpolar gyre. The positive temperature anomaly dissipates quicker over North America due to the differences in land-sea specific heat capacities. A similar seasonal evolution occurs in years 3-4, but the tropical warm anomaly emerges earlier in DJF and extends further westward at its peak in MAM. The anomalies in years 5-30 show a similar spatiotemporal pattern to the first 4 years, suggesting the mechanism(s) by which the anomalies manifest are consistent throughout the nudged run. Slight differences between the years 1-4 and 5-30 are the extent of the robust signal in the tropical Pacific – there is a slight reduction in the warming region

in JJA and no significant western tropical Pacific warming in MAM for years 5-30. The signal of peak tropical warming occurring in MAM in NUDGED qualitatively agrees with observations of the PDO (Figure 6.3).

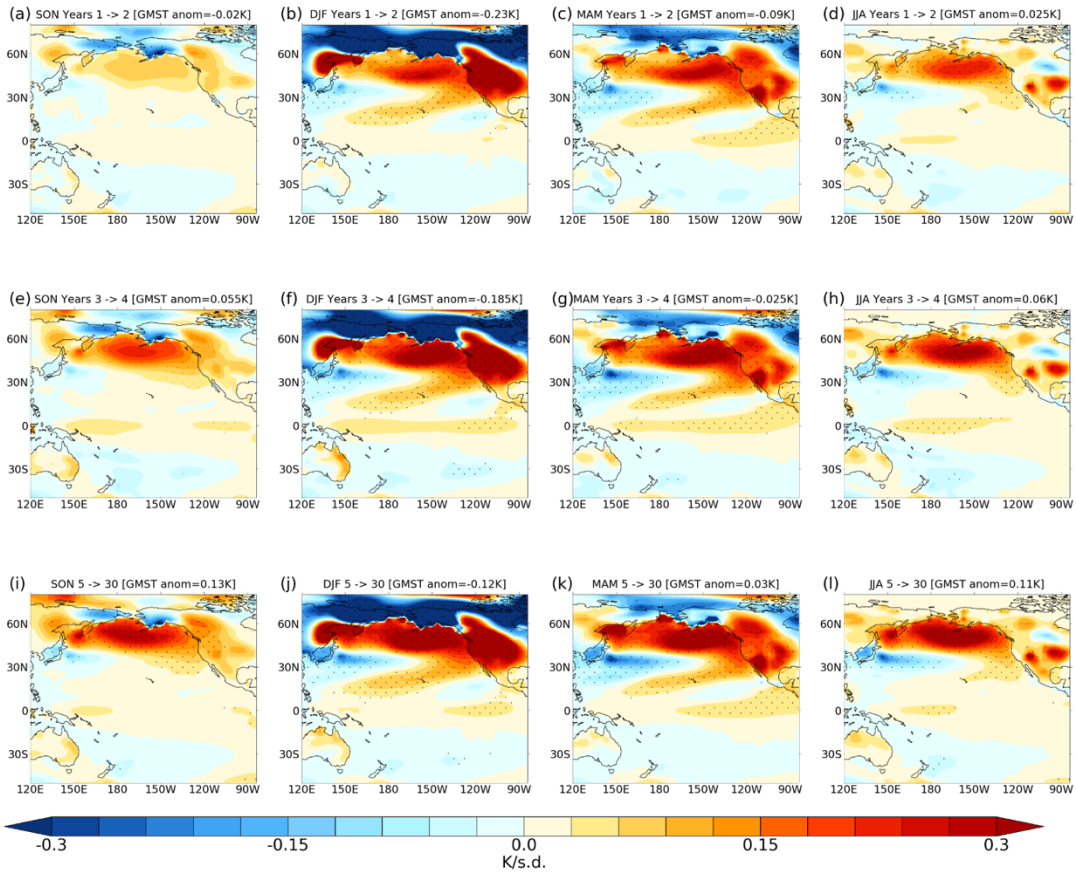

Figure 6.4: Ensemble mean near surface air temperature anomaly [K/s.d.] in the NUDGED strong AL experiment. Anomalies are shown for seasonal means over years 1-2 (panels a-d), years 3-4 (panels e-h) and the remainder of the simulation (years 5-30; panels i-l). Stippling denotes anomalies that are statistically significant at the 95% confidence level.

To investigate the mechanisms behind the subtropical and tropical temperature anomalies evident in Figure 6.4 and in Figure 6.2, I conducted a mixed layer heat budget analysis in these regions. The subtropical and Niño 3.4 regions show different annual cycles with respect to their mixed layer temperature tendency anomalies (Figure 6.5 a,b). The peak surface temperature tendency in the subtropical northern Pacific occurs during the nudging period (boreal winter), whereas the peak warming tendency in the

tropical Pacific region occurs later in FMA. For the subtropical region, the vertical diffusion term (contribution from surface heat fluxes) is offset by advection in driving the temperature tendency. The anomalous advection term is dominated by the meridional component. The maximum tendency due to vertical diffusion is in DJF (~0.28 K/month) and the minimum tendency from advection is in JFM (~ -0.24 K/month). In the Niño 3.4 region, anomalous advection contributes to a warming tendency year-round, with the maximum (~0.3 K/month) in MAM. Here too, the meridional component of the advection dominates. This warming is offset by anomalous vertical diffusion and convection terms, which remain negative year-round. Meridional advection therefore contributes to cooling in the subtropical North Pacific, whereas it causes warming in the Niño 3.4 region.

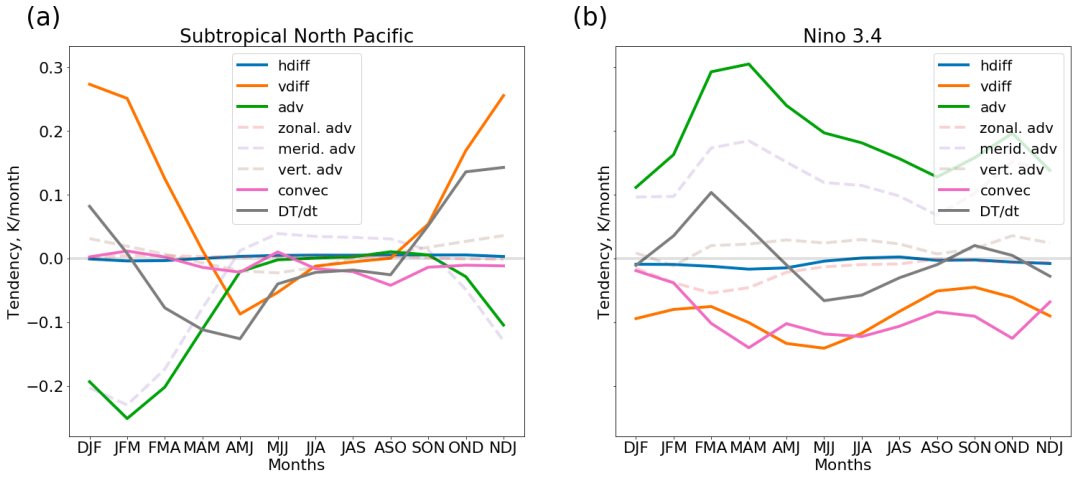

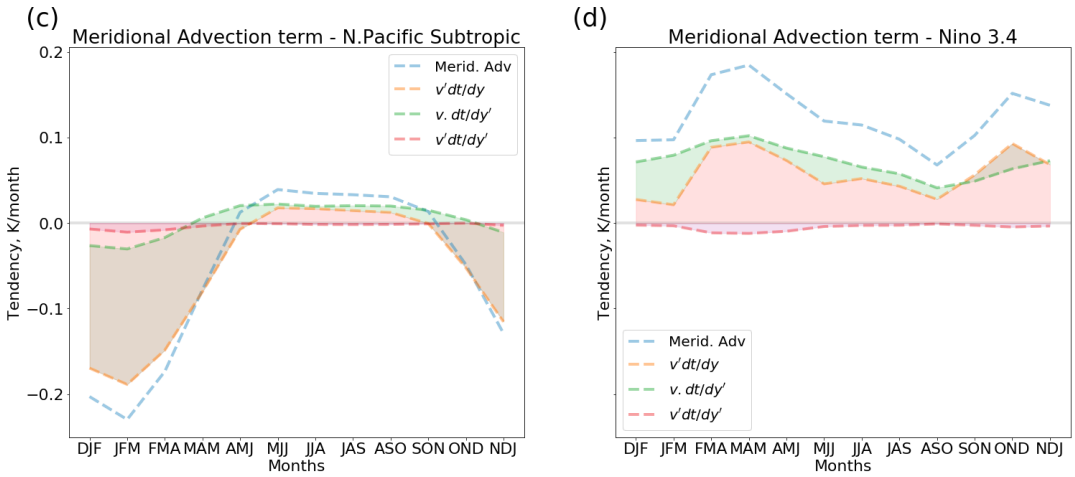

Figure 6.5: a,b: Subtropical North Pacific (a) and Niño 3.4 (b) region heat budget analysis and constituent terms. c,d: Linearised meridional advection terms. Each value represents a moving 3-month moving average.

Given the importance of meridional advection for the anomalous mixed layer temperature tendencies in both the subtropical and equatorial Pacific regions, I further decompose these into changes associated with differences in the meridional velocity and temperature gradient (Equation 6.2). The subtropical North Pacific region is dominated by the change in meridional velocity whilst in the Niño 3.4 region the change in meridional temperature gradient is the largest contributor throughout most of the year (apart from in Sept-Dec). Furthermore, the increase in temperature tendency seen from Feb-June in the Niño 3.4 region is driven by changes to the meridional velocity. The difference in contributing terms implies different mechanisms governing the changing mixed layer temperatures in the two regions.

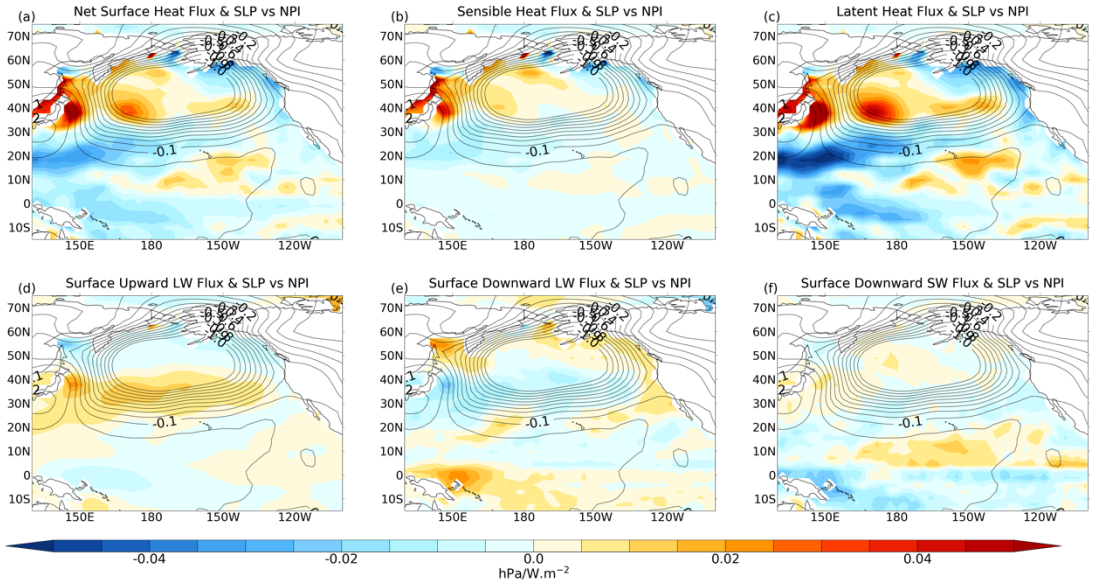

Figure 6.6: a-f: LR of NDJFM surface heat flux anomalies onto the NPI in the control run (shading). Contours show SLP anomalies regressed onto NPI anomaly (interval = 0.1 hPa/hPa).

Further findings from the heat budget analysis in figure 6.5 shows the importance of the surface heat flux term (vdiff) in contributing to warming in the subtropical North Pacific in boreal winter and cooling year-round in the Niño 3.4 region. To better understand the changes in surface heat fluxes associated with variability in the AL, I performed LR of the net surface heat flux anomalies onto the NPI in the control run (Figure 6.6). This shows a strengthened AL corresponds to an increase in anomalous downward net surface heat flux throughout the extended boreal winter (Fig. 6.6a). In the equatorial and subtropical regions around 25ºN, a strong AL corresponds with a decrease in anomalous downward net surface heat flux, apart from around 150ºW. Separating the total heat flux into its constituent terms shows that latent heat flux anomalies dominate the overall signal, with large positive (negative) values seen in the northern (subtropical) western Pacific. Analysing the seasonality of the latent heat fluxes in the control run, I find that throughout Jan-May there is a statistically significant negative relationship between the AL strength and the SW-NE oriented band of subtropical latent heat anomalies

(Figure 6.7). This indicates warming due to latent heat anomalies in boreal spring across the subtropics.

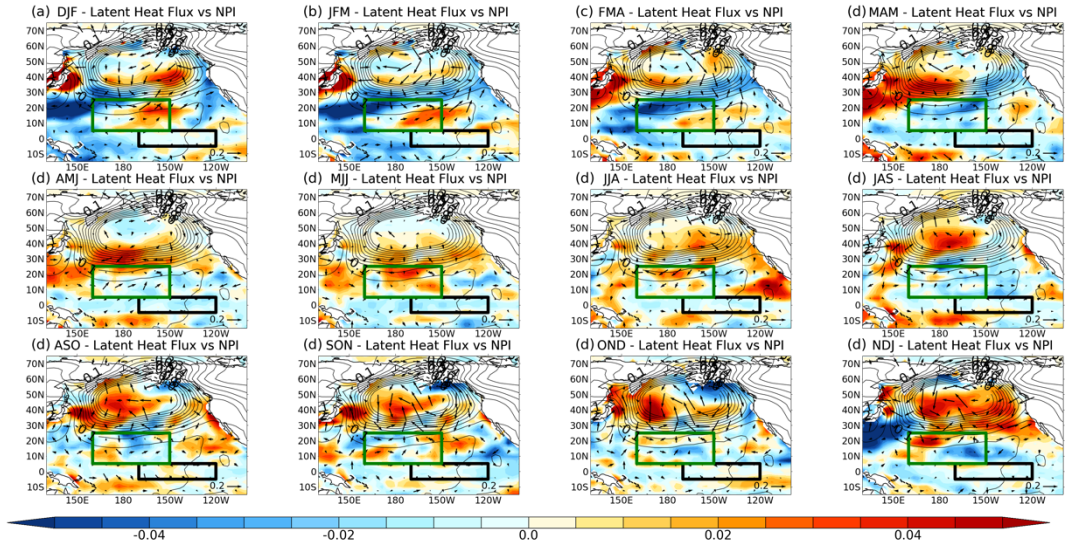

Figure 6.7: Rolling seasonal mean of latent heat and surface wind anomalies (in each season) regressed onto the NPI. Shading shows the latent heat regression gradient [W.m^{-2} / S.D.], contours show the SLP regression gradient [hPa / S.D.] and the arrows represent the surface wind regression gradient [m.s^{-1} / S.D.]. Green and black boxes represent the two regions over which heat budget analysis was conducted in Figure 6.6.

The total and latent heat flux anomalies in the NUDGED experiment are shown in Figure 6.8. In the same way as the surface temperature anomaly associated with the nudged simulation resembles the internally generated PDV (Figure 6.2), the total and latent heat anomalies in NUDGED are also similar to those in figures 6.6 and 6.7. There is an increase in downward total and latent heat fluxes across the North Pacific and across a band in the SW-NE orientation in the subtropical North Pacific. The largest heat flux anomalies occur during DJF, with values in excess of 4 W.m^{-2}/s.d., with persistence year-round. The pattern of total and latent heat flux anomalies in JJA across the extra-tropical North Pacific resembles the PDO structure, with an increase in downward heat flux extending eastward from the KOE region, which are enveloped by negative anomalies in the northeast Pacific and subtropical

North Pacific. The persistence of surface flux anomalies year-round is expected given the surface temperature persistence and alludes to ocean-atmosphere feedbacks.

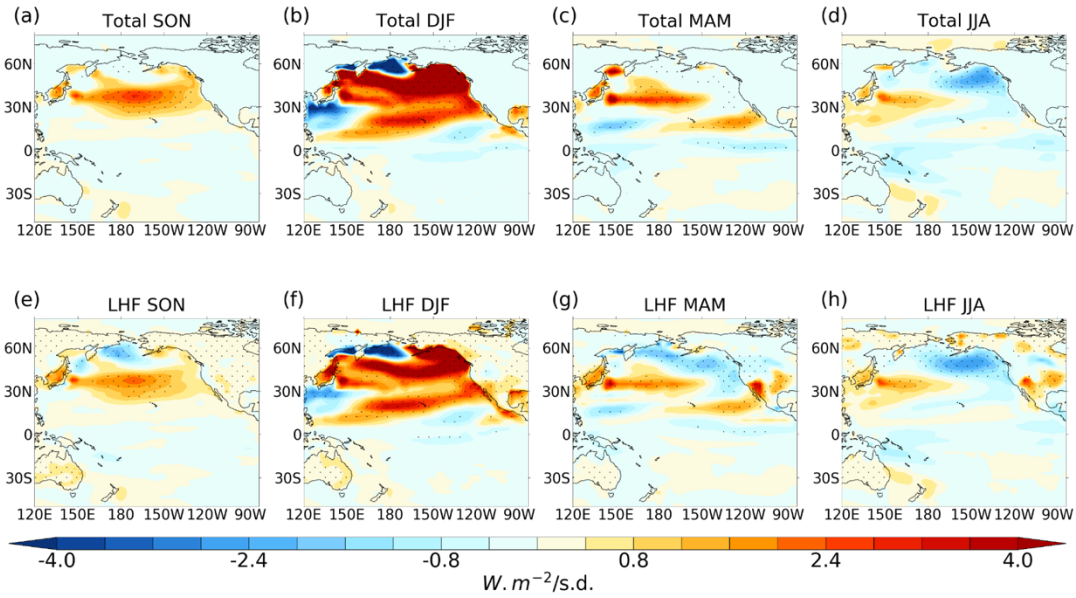

Figure 6.8: (a-d) Mean seasonal downward heat flux anomaly into the ocean in NUDGED. (e-h): Mean seasonal latent heat flux anomaly in NUDGED. Stippling denotes anomalies that are statistically significant at the 95% confidence level.

To further investigate the source of the anomalous heat advection seen in Figure 6.5, Figure 6.9 shows the anomalous northward and vertical velocities in the upper-most ocean layer alongside the surface wind anomalies. In the annual mean (Fig. 6.9a,b), there is a westerly surface wind anomaly (~0.2 m s^{-1}) across the tropical Pacific, which coincides with a decrease in upwelling (~1 x 10^{-6} m s^{-1}) and convergence at the equator. The decrease in upwelling is maximum in MAM and migrates from east to west from DJF-SON. This coincides with the maximum anomalous zonal wind across the equatorial Pacific which occurs in MAM. Furthermore, additional testing shows that in moving from west to east, the contribution of the vertical advection to the tropical warming increases, coincident with a deepening of

the thermocline in the east Pacific, which is evident in all seasons excluding SON (Figure 6.10).

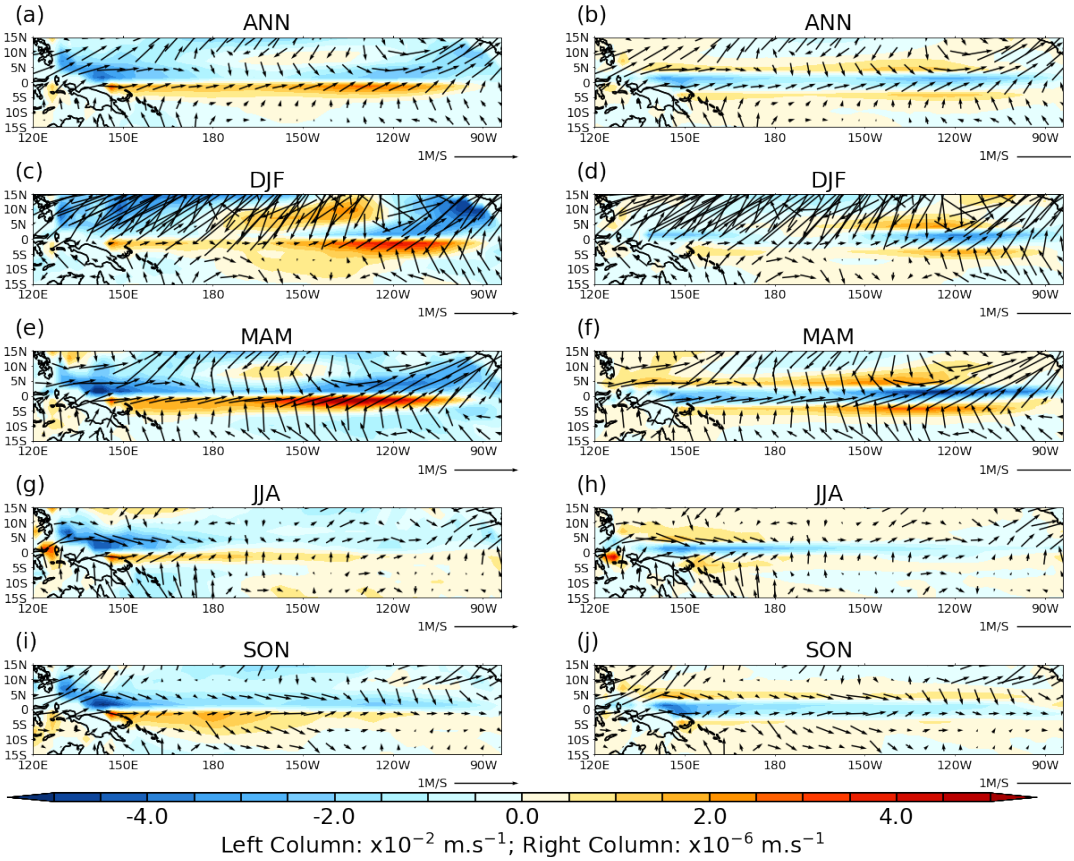

Figure 6.9: Left: Seasonal mean northward velocity anomaly in upper-most ocean layer. Right: Seasonal upward velocity anomaly in upper-most ocean layer. Vectors denote anomalous surface winds.

Figure 6.11 shows the seasonal evolution of the anomalous zonal and meridional surface wind fields in NUDGED compared with the control run. As expected, the largest anomalies occur in the period over which nudging is applied (DJF), where the positive subtropical westerly zonal wind anomaly reaches a maximum of ~0.5 ms^{-1}/s.d. and the anomalous subpolar extratropical easterly zonal wind reach a similar magnitude. Evidence of a change to the atmospheric Rossby wave train in the upper troposphere is evident in the surface meridional anomalies with an alternating southerly-

northerly anomaly orientated with a north-easterly tilt propagating across the North Pacific. Comparing the control run climatology (contours) with the anomalies through the seasons, the subtropical westerly zonal wind anomalies show a southerly shift throughout the year with significance persisting into the season after nudging (MAM). Interestingly, there is also more significance in the zonal equatorial westerly wind anomalies in MAM, extending further west across the equatorial region. Although anomalies are evident in JJA, they are not strongly statistically significant.

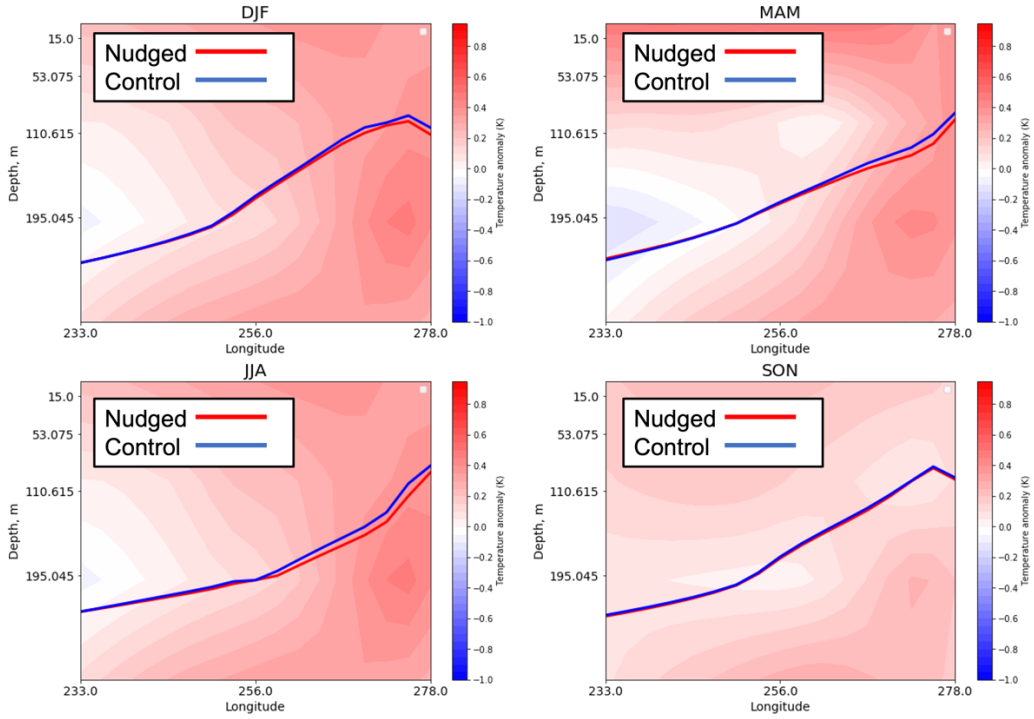

Figure 6.10: Cross-section along the equatorial Pacific (averaged between 5°N-5°S) of upper ocean temperature anomaly (colours) and the thermocline calculated as the depth of the 20°C isotherm. Blue line = control run. Red line = NUDGED.

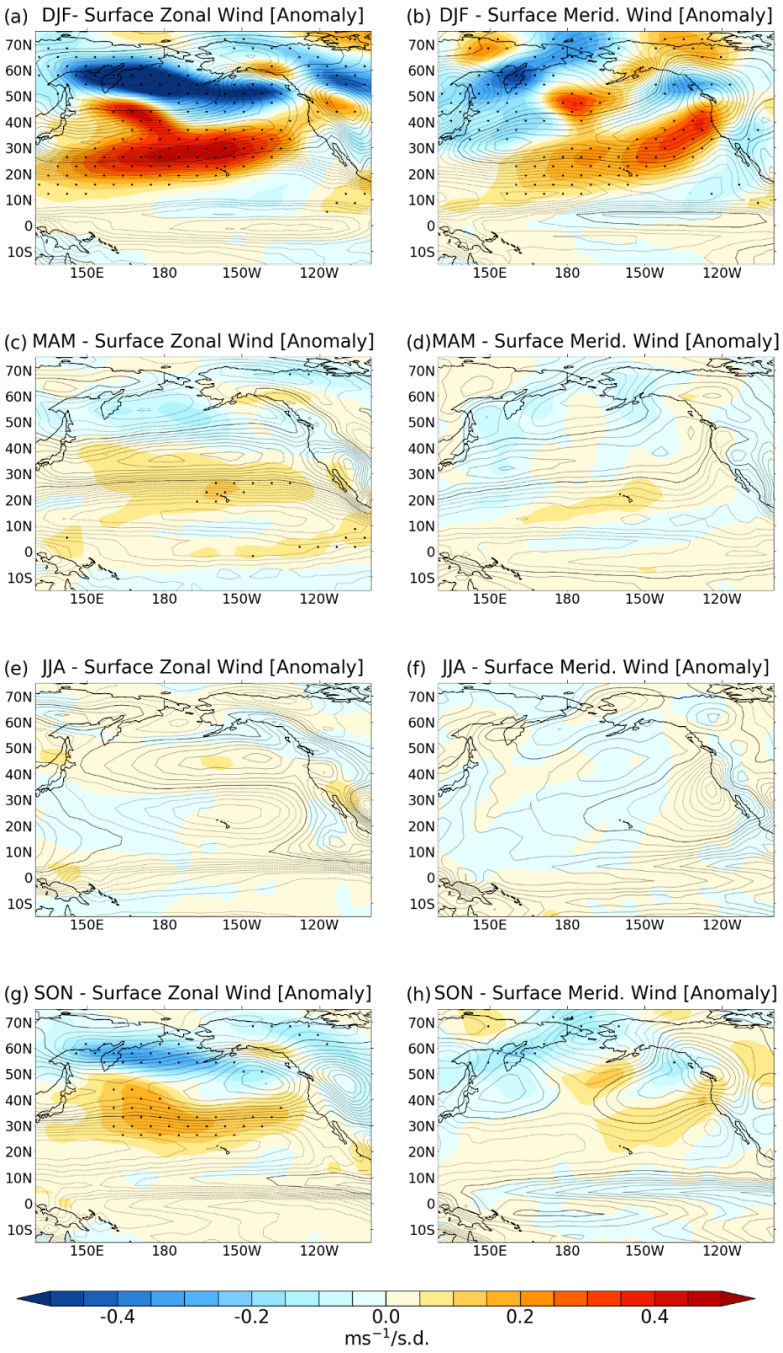

Figure 6.11: Seasonal evolution of the ensemble mean NUDGED surface wind anomalies: (left) zonal wind and (right) meridional wind. Contours represent the climatology of the control run (dashed lines are negative values, contour interval 1 m s^{-1}). Stippling denotes anomalies that are statistically significant at the 95% confidence level.

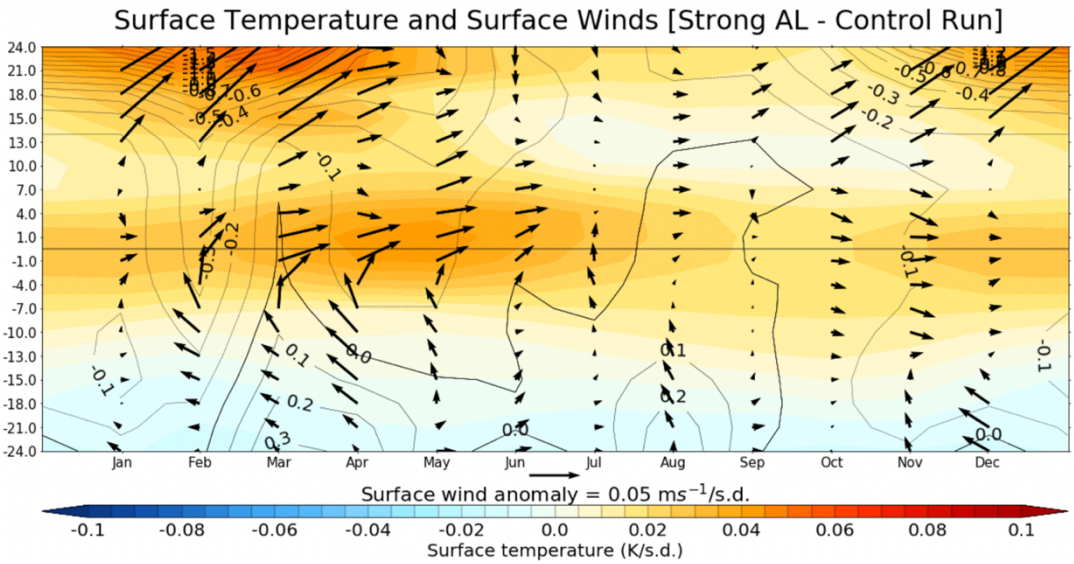

Figure 6.12: Latitude-time section of monthly mean response of SST anomaly (K/s.d.; shading), surface pressure (hPa; contours) and surface wind anomaly (m s^{-1}/s.d.; vectors) averaged over the central-eastern tropical Pacific (205°-80°W).

The monthly evolution of the surface temperature, surface wind and surface pressure anomalies in the NUDGED experiment averaged over the central-eastern tropical Pacific are shown in Figure 6.12. There is a consistent year-round warming evident in subtropical and equatorial regions, with the largest magnitude in the subtropics from November through April (~0.05 K/s.d.) and in the equatorial region from March through July (~0.3 K/s.d.). The nudging invokes concurrent warming in the subtropics, while there is a seasonal delay in the emergence of warming in the equatorial Pacific. From July to November in the subtropics (around 15°N) there is substantially less warming than during the rest of the year, with values close to zero. The westerly wind anomalies coincide with the timing of the temperature anomalies, with south-westerly anomalies of ~0.05 m s^{-1}/s.d. in the subtropics and ~0.03 m s^{-1}/s.d. in the equatorial region. In addition to the cross-equatorial temperature gradient generated by the subtropical anomaly, the lower surface pressure in the subtropical northern hemisphere (~1.5 hPa), which is largest

in February and March, creates a pressure gradient across the equator. In the Southern hemisphere subtropics there is evidence of cooling in the sub-tropical region (south of 15^{o}S).

To summarize, an ensemble of simulations which are nudged towards a strong AL state produce near-surface air temperature patterns similar to the spatial expression of the PDO. This comprises of warming across the north and eastern Pacific and into North America, and cooling in the western North Pacific/KOE region. Notably, there is warming simulated in the central and eastern equatorial Pacific, demonstrating the ability the AL anomalies to generate a basin-wide response. A mixed layer heat budget analysis shows that peak warming in the tropics occurs the season after nudging, whilst the subtropics warm most during the nudging period (boreal winter). Vertical diffusion (subtropics), which represents the surface heat flux, and the meridional component of advection (equatorial) are the major contributors to surface warming in the two regions, whilst the meridional component of advection acts to cool the subtropical North Pacific. Generally, different factors drive the meridional advection term in each region, with the change in meridional velocity dominating in the subtropical region and the meridional temperature gradient dominating in the Niño 3.4 region. Latent heat anomalies, which drive warming across the subtropics, dominate the surface heat flux term in both the control and NUDGED experiments, with the largest values evident in boreal winter, yet are persistent year-round. Persistent zonal wind anomalies across the equatorial Pacific and a deepening of the thermocline are shown to contribute to the anomalous heat advection term whilst there is evidence that nudging towards a strong AL causes a southerly shift of the subtropical westerly zonal wind anomalies which persist

significantly into MAM. Consistent year-round surface warming coincides with the westerly wind anomalies whilst the formation of a cross-equatorial temperature and surface pressure gradient acts to produce a pressure gradient across the equator.

6.5 Discussion and conclusions

The AL is known to be an integral component of Pacific climate variability over interannual and decadal timescales. However, disentangling what impact the AL has within the broader context of PDV has yet to be fully achieved. Recent evidence suggests a change in relationship between the AL and the PDO (Litzow et al., 2020) occurred in the period after 2014, therefore better understanding the specific mechanisms initiated from the AL is needed when considering changes to the PDO under future climate change.

Nudging simulations have been used widely to investigate the relationship between different climate and weather phenomena (e.g. Martin et al., 2021; Knight et al., 2017; Watson et al., 2016). This chapter has investigated the relationship between the extra-tropical and tropical Pacific through relaxing the North Pacific towards an anomalously strong AL state derived from the model's own internal variability. Sun and Okumura (2019) conducted a similar investigation centred on imposing heat flux anomalies associated with the NPO throughout the year; however, I impose the anomalous AL throughout extended boreal winter only, which is more representative of its observed variability.

To pursue this investigation, I performed a large ensemble experiment using a coupled atmosphere-ocean climate model, in which the winter-time AL was nudged to an anomalously strong state during successive winters.

The results of this ensemble were compared to a free-running simulation to isolate the impacts of the anomalous AL. The strong AL experiment produces a basin-scale SST response with a similar pattern to the PDO in the free running simulation albeit with a weaker amplitude by around a factor of 5. Tropical Pacific SSTs are significantly warmer in the strong AL experiment, demonstrating that North Pacific atmospheric forcing can impart a signature in tropical SSTs. The largest tropical Pacific warming occurs in the season following nudging (boreal spring), though anomalies persist year-round. A heat budget analysis shows the subtropical and tropical Pacific SST responses are predominantly driven by anomalous surface heat fluxes in boreal winter and meridional advection in boreal spring, respectively.

The impact of the anomalous AL on the tropical Pacific suggests an excitation of the SFM mechanism proposed as means for extratropical forcing of the tropics (e.g. Vimont et al 2003; Alexander et al. 2010; Chen and Yu, 2020; Sun and Okumura, 2019). In accordance with the SFM, the SST anomalies persist into the summer season, with anomalous temperatures found in the North Pacific year-round. The nudging season and season thereafter (MAM) (Figure 6.4) show a spatial signature clearly replicated in the study by Liguori and Di Lorenzo (2019), who show the same SST precursor in the sub-tropics considered to affect ENSO dynamics.

The westerly subtropical zonal wind anomalies show a southerly shift throughout the year (Figure 6.11) which, in agreement with Liu et al. (2021), acts to prevent heat loss from the surface due to reduced evaporation. This in turn drives the SST anomaly towards the equator. Liu et al. (2021), show the SFM as the mechanism that propagates the SST anomalies southward,

through a change in latent heat fluxes. That being said, in DJF (peak nudging season) the westerly winds imposed by the nudging create a weakening of the subtropical trade winds - therefore the southerly shift of the wind anomalies starts to occur within the first season of nudging. Here, I show anomalous latent heat fluxes are responsible for the change in subtropical North Pacific SSTs. One limitation of the Liu et al. (2021) study is that the atmosphere was coupled to a thermodynamic slab-ocean, whereas I integrate a fully coupled ocean model, thereby enabling an active role for ocean dynamics.

In the tropical Pacific, the dominant mechanism responsible for the increase in SSTs is enhanced meridional advection, with a change in meridional velocity driving the accelerated warming during the spring. Figure 6.12 shows a northward cross-equatorial SST gradient, which coincides with the development of an anomalous cross-equatorial southward pressure gradient. Cross-equatorial winds are generated, which, due to Coriolis force act to weaken the trade winds in the northern equatorial region, decreasing the latent heat flux and leading to a local warming. A comprehensive review of this mechanism, commonly referred to as the WES mechanism is provided in Chapter 1, as well as in Mahajan et al. (2008). Furthermore, the WES mechanism was hypothesised as a process through which southern Pacific extra-tropical cooling imparts a change in tropical Pacific SSTs, through the modulation of the south-easterly trades, triggering the zonal SST contrast and associated change in stratocumulus clouds. Here, I demonstrate the WES mechanism is at play in the development of tropical SSTs induced by an extratropical North Pacific atmospheric anomaly. Investigation into equatorial thermocline depth shows a slight deepening of the thermocline associated

with reduced upwelling in all seasons apart from SON, which is supported by the sensitivity of vertical advection to the zonal gradient of the thermocline.

The evidence presented here of extratropical atmospheric variability driving coupled atmosphere-ocean changes in the deep tropics further supports the findings of Xie and Tanimoto (1998) who investigated the effect of extratropical wind forcing on the tropics in the Atlantic and were able to reproduce observed decadal oscillation in both SST and wind velocity over the tropics. Other studies, such as those by Czaja et al. (2002) have also identified influences from the midlatitude variability on the tropics.

Furthermore, my results show that the effect of a strong anomalous AL is a weakening of the trade winds across the tropical Pacific, which appears to occur in the season after nudging, commensurate with the SFM and WES mechanisms. The schematic in Figure 6.13 illustrates the mechanisms involved. To build on the work in this chapter, a more detailed analysis of the impact of an extra-tropical anomalous AL on the modulation of the Walker cell, including the effect of cloud feedbacks, position of deep convective regions, and the zonal-SST gradients under different experimental set ups (such as fully coupled AOGCMs and simpler atmosphere-only models - like those conducted in Kang et al. 2020) would elucidate further the degree to which the aforementioned mechanisms play a role in the evolution of the basin-wide Pacific SST’s when initiated by an anomalous AL.

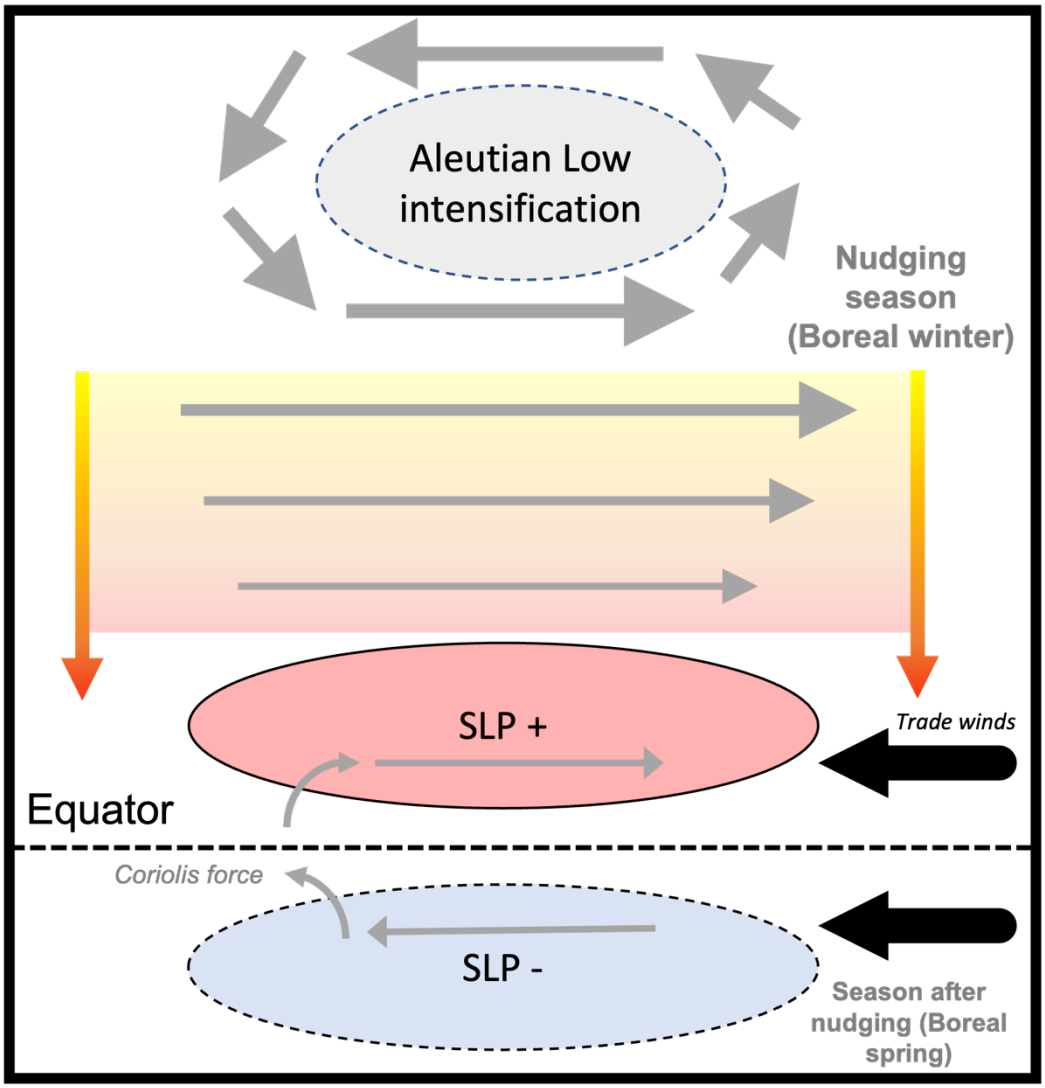

Figure 6.13: Schematic depicting the mechanisms involved in the tropical SST anomalies manifest as a result from an intensification of the AL. An intensified AL imposed during boreal winter is associated with intensified westerlies in the extra-tropics and reduced upward latent heat transfer. The migration of the SST anomalies southward during boreal winter is associated with a southerly shift in the westerly anomalies. The westerly anomalies act to weaken the background trades (black arrows) which reduces latent heating due to evaporation and hence an increase in tropical Pacific SST's. In the season after nudging, the temperature asymmetry either side of the equator (red and blue ellipsoids) induces an SLP gradient (solid line – positive SLP; dashed line – negative SLP) that drives southerly winds across the equator. The Coriolis force acts to turn the southerly winds in the southern hemisphere westward and in the northern hemisphere eastward. When these anomalous winds are imposed on the background easterly trade winds (black arrows), the southerlies south of the equator increase the wind speed and therefore evaporative cooling.

The findings presented here support the claim made by studies such as Smith et al. (2016) that PDV can, at least in part, be driven by extratropical

variability independent of the tropics. Future investigation into the mechanisms through which the AL impacts on modes such as the NAO and regions such as the tropical Atlantic will provide a more complete understanding of the wider climatic impacts of North Pacific variability.

Chapter 7 – Conclusions and Future Work

7.1 Summary and Conclusions

The climate system exhibits multiple large-scale modes of variability on interannual to decadal timescales. These modes of variability are understood to be internally-generated, largely arising from coupled atmosphere-ocean interactions; however, there is a potential for this variability to be modified by external drivers including anthropogenic activity. This thesis has concerned Pacific Decadal Variability (PDV) and several factors that have been hypothesised to influence its characteristics. Improving our understanding of the mechanisms governing the behaviour of the PDO is of great importance in the context of improving the ability to predict the global climate on decadal timescales. There has been a plethora of literature that has focussed on how anthropogenic forcing agents can modulate the PDO, for example, with the studies by Smith et al. (2016), Oudar et al. (2018) and Dittus et al. (2021) focussing on the phase transition that took place at the end of the 21st century. There is still considerable uncertainty around to what degree anthropogenic forcing agents, especially AA emissions, may have impacted onto the evolution of the PDO, owing to uncertainty in the aerosol radiative forcing trend and the poor simulation of recent Pacific trends in climate models (e.g., Seager et al., 2022; Wills et al., 2022).

This thesis has examined processes related to the PDO focusing on the role of the North Pacific. Firstly, I have investigated whether large, abrupt changes to AA could cause a modulation in the AL (considered precursory to the PDO) and secondly I have investigated the mechanistic pathways through

which local and remote atmospheric forcing could cause changes in the PDO across the extra-tropical and tropical Pacific.

Chapter 3 investigated the impact of perturbations in different aerosol species (sulphate and BC) on the AL and North Pacific atmospheric circulation in a multi-model ensemble from PDRMIP. In comparison to Smith et al. (2016), Oudar et al. (2018) and Dittus et al. (2021), who found that a transient increase in AA emissions during the period 1998-2012 is associated with an increase in SLP in the AL region, I find that a 5-fold increase in sulphates globally and 10-fold increase in sulphates over Asia is associated with only a small increase in SLP over the AL region, despite the aerosol perturbation being far larger than in those studies. An important distinction is that the previous studies do not delineate between aerosol species, though it is generally assumed that any signal is likely to be dominated by sulphate aerosol (e.g. Zhang et al. 2016). A further caveat is that my investigation focussed on the long-term centennial response in coupled atmosphere-ocean simulations, whilst Smith et al. (2016), Oudar et al. (2018) and Dittus et al. (2021) focussed on decadal trends. It is possible that on multi-decadal timescales, other feedback processes are enacted that modify the surface response. For this reason, in addition to the differences in the magnitude and pattern of forcing, a like-for-like comparison with these studies is difficult to make with much fidelity.

The results from chapter 3 show that a 10-fold increase in BC emissions globally and over Asia drives a weakening of the AL, which could compound any effects from increasing sulphate emissions. The response to BC also shows surface temperature changes in the North Pacific that resemble the

PDO pattern. My findings of the AL response to a global and Asia-only increase in BC agree with Johnson et al. (2019), who showed a pattern of lower-tropospheric zonal wind anomalies in the North Pacific indicative of a weakened AL in response to a tenfold increase in BC emissions. My findings also agree with Teng et al. (2012) who showed a weakened AL in boreal winter in response to a tenfold increase in Asian carbonaceous aerosol concentrations; however the findings from chapter 3, which analyse global and regional perturbations of BC, provide new information that sources of BC outside of Asia play a fundamental role in modulating the strength of the AL. Chapter 3 hypothesised that the robustness of the AL response to BC may be due to the dominance of aerosol shortwave absorption, whereas the lack of consistency among models in response to sulphate forcing could be a function of anomalous precipitation. The fixed-SST runs also confirmed a small role for ocean feedbacks in the response to BC forcing, whereas the ocean plays a more fundamental role in governing the response to the sulphate experiments, which may be expected given the larger surface forcing due to sulphate aerosol.

Chapter 4 built on chapter 3 by using a linearised stationary-wave model to investigate the atmospheric mechanisms through which changes to aerosol emissions affect the North Pacific. The model was forced with diabatic heating anomalies derived from the PDRMIP precipitation anomalies and shortwave heating by BC absorption, which was estimated using an offline radiative transfer model. I found that the radiative heating by BC is more important than latent heating for inducing remote responses through anomalous RWS regions. Additionally, regions of heating over India and China are important contributors to the North Pacific response to a ten-fold global BC perturbation.

The linear model did not reproduce the pattern in response to the Sulx5 experiment, indicating the model likely neglects key processes that determine the local dynamical response to a global increase in sulphate aerosols. This could include other effects resulting from surface temperature change, such as changes in large-scale temperature gradients. Following on from studies such as Wilcox et al. (2019) and Lewinshcal et al. (2013), I have shown that the radiative effect of a BC perturbation modifies the extra-tropical stationary wave patterns inducing a response over the North Pacific. Elucidating a relationship between BC emissions and a modulation in the strength of the AL must be caveated by acknowledging the existing uncertainties associated with BC forcing, for instance in the vertical distribution of aerosol mass (Samset et al., 2013) and BC optical properties. However, the approach of this study is able to delineate atmospheric forcing from an aerosol perturbation without considering the interplay between other forcing agents, such as CO_2.

Chapter 5 lays the foundations for the work in chapter 6, by developing a grid-point nudging functionality in the FORTE2.0 AOGCM. The motivation underpinning this development was to investigate the communication between the extra-tropical and tropical North Pacific in the context of the mechanisms contributing to the modulation of the PDO. Chapters 3 and 4 highlighted that large changes in BC can robustly modulate the AL through the excitation of upper tropospheric Rossby waves. This, in addition to what we understand about the relationship between the AL and the PDO from the literature (e.g., Newman et al. 2016; Litzow et al., 2020), provides an avenue through which BC emissions could affect the PDO over decadal periods. The development of the grid-point nudging methodology allowed me to isolate the impact of a sustained, anomalous AL state on the tropical Pacific and detect

the mechanisms through which any change takes place. The FORTE2.0 model used for this exercise demonstrated its ability to represent the climatology of the Pacific to a satisfactory level and through extensive testing I was successful in implementing the code in preparation for Chapter 6. With foresight, I also developed the functionality to perform large ensemble experiments in FORTE2.0 using shell scripting, to achieve a high signal-to-noise level. Through testing, each ensemble member would take initial conditions from different years of the model spin-up run prior to nudging.

Chapter 6 utilised the grid-point nudging capability developed in chapter 5 to investigate the relationship between the AL and the PDO. The study was conducted with the aim of investigating the mechanisms initiated by a modulation of the AL, focusing on the potential for extra-tropical Pacific variability to impact on the tropics; this was distinct from the majority of literature that takes the perspective of a tropically initiated pathway to the extratropics. Comparing an ensemble of 50 members with an extended control run, the findings show that an anomalously strong AL excites the SFM mechanism which acts to force tropical atmosphere-ocean changes through the associated processes (e.g. Sun and Okumura, 2019; Chen and Yu, 2020). The pattern of SST anomaly induced by the nudging and associated with the SFM is in agreement with Liguori and Di Lorenzo (2019), who considered a similar SST precursor in the sub-tropics to affect ENSO dynamics. The southerly shift of the westerly wind anomalies evident during the period of nudging manifests changes in the latent heat fluxes, in agreement with Liu et al. (2021). Through a heat budget analysis, I showed that, in the tropics, meridional advection is primarily responsible for the increase in SSTs, with changes to the shallow meridional current velocity driving the accelerated

warming during spring. The SFM mechanism acts to excite the WES mechanism across the tropical (equatorial) Pacific, whilst the change to the surface trade winds produces a slight deepening of the thermocline in all seasons apart from SON. Additionally, weakening of the trade winds is evident in the season after nudging. The main conclusions drawn from this study support evidence that decadal variability in the Pacific can be affected by anomalous activity originating outside the tropical region. This raises the possibility that atmospheric teleconnections that induce signals in the North Pacific, for example associated with changing external forcing (e.g., aerosols, see chapter 3 and 4), Arctic sea ice and the stratosphere can initiate basin-scale anomalies in the Pacific that resemble the PDO.

7.2 Future Work Recommendations

7.2.1 Large ensemble investigation into the role of BC on the North Pacific under transient forcing

One key finding from my thesis is the role that BC plays in modulating the AL through the excitation of Rossby waves in the upper troposphere. This finding was based on investigations of idealised, large, and persistent perturbations of BC across an array of climate models. The comparisons made herein between my findings and those from literature are made challenging by the difference in experimental design. In an ideal scenario, parsing out the different species of aerosol (e.g. sulphates and BC) in a transient simulation would allow a more comprehensive picture of the role of BC over the historical period, and a more accurate comparison to be made to the studies of Smith et al. (2016), Oudar et al. (2018) and Dittus et al. (2021).

It is also clear that large ensemble of simulations are required to confidently detect a forced signal from internal variability (Oudar et al., 2018). As discussed in section 7.1, the PDRMIP study outlines the centennial response, therefore studying the response to transient emissions of BC isolated from other aerosol species will provide insight into whether any response is evident and significant over decadal timescales.

In pursuing this line of investigation, I started analysis on the CESM1 large ensemble dataset (Kay et al., 2015), which includes a 40-member ensemble of fully coupled CESM1 simulations for the period 1920-2100 (historical followed by the RCP8.5 scenario) under different external forcings. The study includes single forcing experiments, including GHGs, however I focussed on all aerosols (XAER) and biomass burning aerosols (XBMB). For investigating the response to all BC, the separation of species here is awkward as BC from other sources is still active and evolves as normal when the sources of biomass burning are switched off. Of the other 6 CMIP5 class models contributing to the US CLIVAR Working Group on Large Ensembles data archive, only HadGEM3-GC3.1 (Dittus et al., 2020) and CanESM5 (Yu et al., 2022) have performed single forcing aerosol experiments. Even so, there is no delineation amongst aerosol species in these experiments, therefore isolating the role of BC in modulation of the North Pacific over decadal timescales would not be achievable.

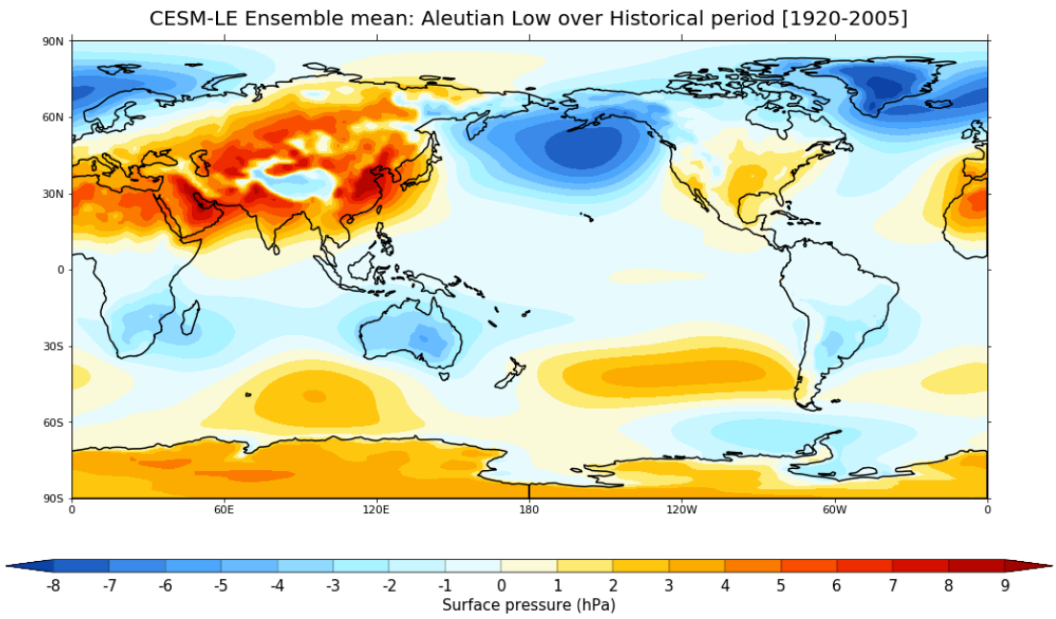

Figure 7.1: CESM-LE NDJFM ensemble mean representation of the AL over the historical period [1920-2005]. Contours every 1 hPa. Demonstration of aptitude of the large ensemble dataset to represent the AL.

Figure 7.1 shows the CESM-LE NDJFM ensemble mean historical climatology, demonstrating the large ensemble represents the AL. Figures 7.2 and 7.3 show the difference in aerosol burdens between the historical and the XAER and XBMB experiments (here, I focus on the years 1998-2012 to coincide with the period of study of Smith et al. (2016)). To demonstrate that these burden anomalies impact on the NPI anomaly, figure 7.4 shows the deviation of the SLP anomaly from the historical ensemble mean. The aerosol forcing appears to affect the strength of the AL over the historical period in both XAER and XBMB, with the removal of biomass burning aerosols causing an increase in NPI in up to circa 2005 before a reversal to a negative anomaly by the end of the simulation. Comparatively, the removal of all AA causes a strengthening of the AL between circa 1945 and circa 1980 before the anomaly is positive signifying a weakening of the AL for the rest of the historical record. Under RCP8.5 conditions, the anomaly is largely positive (weakening NPI). As mentioned, with the aim of disentangling the role of all

BC sources, the analysis of these runs can only provide limited insight because the perturbation is limited to biomass burning.

[XAER – Historical]

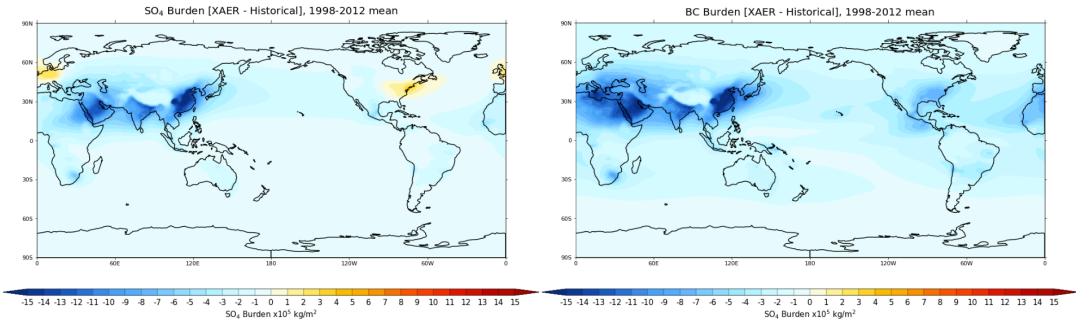

Figure 7.2: 1998-2012 means (Left) Difference in the sulphate aerosol burden between the XAER (Simulation with all forcings except AA) and Historical (All forcing) simulation. (Right) Difference in the BC burden between the XAER (Simulation with all forcings except AA) and Historical (All forcing) simulation.

[XBMB – Historical]

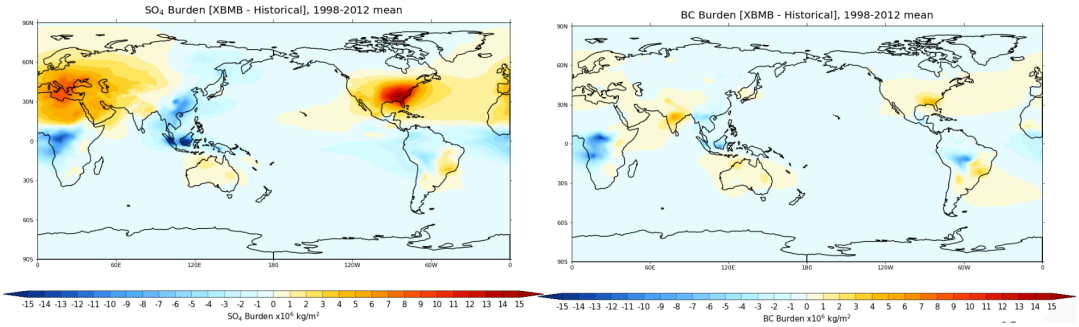

Figure 7.3: 1998-2012 means (Left) Difference in the sulphate aerosol burden between the Historical (All forcing) simulation and XBMB (Simulation with all forcings except biomass burning). (Right) Difference in the BC burden between the Historical (All forcing) simulation and XBMB (Simulation with all forcings except biomass burning).

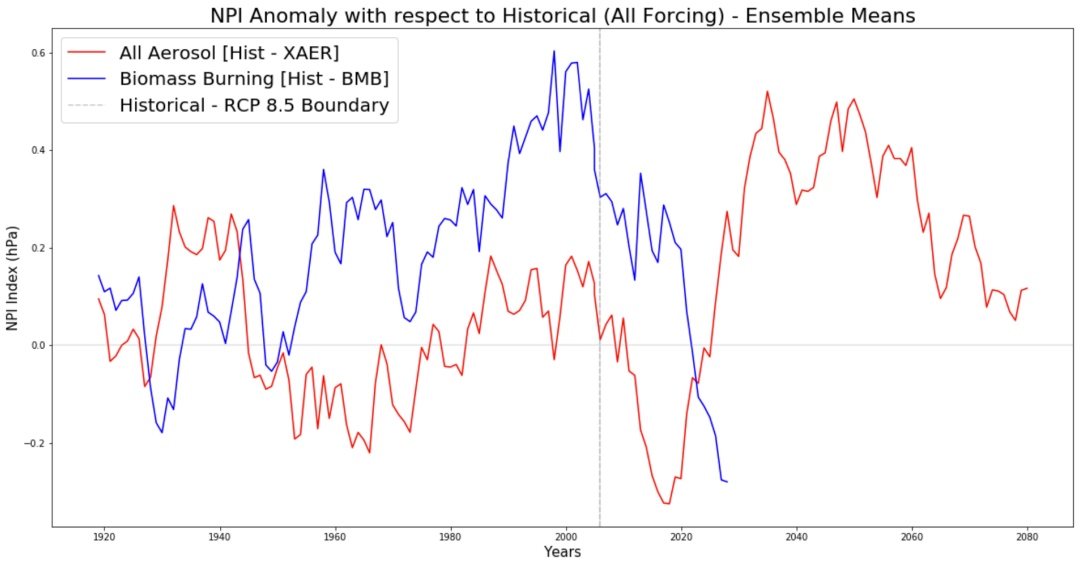

Figure 7.4: NPI anomaly with respect to historical (all forcing) – Ensemble Means. Red line – All Aerosol [Hist – XAER]; Blue line – Biomass Burning [Hist – XBMB]. The grey dashed line signifies the date at which the historical forcing changes to scenario RCP8.5.

A logical continuation of this work would be to conduct a single forcing large ensemble simulation where BC and sulphates are perturbed separately. Furthermore, amongst the BC runs, this could even be separated further into anthropogenic BC and all sources of BC to address the spatial heterogeneities of the two sources – the larger sources of biomass burning are centred in the tropics in regions such as sub-Saharan Africa and South America (Pan et al. 2020), whereas anthropogenic BC sources are confined predominantly to industrial regions (Klimont et al. 2017). One could mimic the set-up of the HadGEM3-GC3.1 LE single forcing experiment performed by Dittus et al. (2020), where aerosol emissions were scaled over the historical period (i.e. 0.2x, 0.4x, 0.7x, 1.0x, and 1.5x), to - firstly, shed further light on the work conducted by Johnson et al. (2019) and Mahajan et al. (2013), who found the diagnostics such as TOA radiative forcing, GMST and precipitation scaled linearly under different BC scaling factors. This would permit an investigation into the linearity of the response of the AL in response to BC. Secondly, in

scaling the transient emissions of sulphate and BC under single forcing experimental design, one could scrutinize the initiation of the mechanisms considered to drive the modulation of the surface climate across the north Pacific and into the tropical Pacific.

7.2.2 - Testing the sensitivity of the extra-tropical tropical communication to the strength of AL anomaly under future warming scenarios

Chapter 6 investigated the impact of an extreme anomalous AL on the Pacific basin and the mechanisms through which the extra-tropical North Pacific communicates with the tropics. An open question remaining from this study is whether variability in the AL anomaly induces the same mechanisms and whether the impact onto tropical SSTs is proportional to the size of the AL anomaly. Research shows that the AL intensity is projected to increase and expand northwards under future global warming scenarios (Gan et al. 2017), therefore understanding the sensitivity of these mechanisms to various AL states would provide insight into the role of the extra-tropics in contributing to global climate variability in a warming world.

This research could be conducted on a more complex AOGCM, such as HadGEM3-GC3.1 (Ridley et al. 2018), as one of the limitations to FORTE2.0 is its absence of a dynamic sea-ice representation. Given that these relaxation experiments can be applied in the NH extratropics, a more sophisticated representation of dynamic sea-ice could also allow investigation into additional teleconnections such as between the AA and the Arctic Oscillation, which has weakened over the last couple of decades (Hwang et al. 2022). Likewise, this would provide more confidence in investigating the relationship between variability in AL intensity and other extra-tropical modes of variability,

for example the NAO, which are linked via the stratospheric polar vortex (e.g. Fereday et al. 2020). Furthermore, as it stands, the nudging code in FORTE2.0 is limited to the troposphere only component, therefore more development would be required to facilitate stratospheric nudging to investigate this AL-NAO relationship.

The experimental design could take inspiration from Dittus et al. (2021), where future AL variability and intensity could be scaled against existing modelled scenarios (e.g. RCP8.5), and diagnostics assessed for their linearity of response.

7.2.3 – Nudging the Aleutian Low to investigate remote impacts, feedbacks, and teleconnections outside of the Pacific

The idealised aerosol experiments in the PDRMIP project, and the relaxation of the North Pacific towards an anomalous AL state in FORTE 2.0 produced signals in regions outside of the Pacific basin. For example, I found significant near surface warming in the North Atlantic relative to the North Pacific in the PRDMIP Sulx10a coupled experiment. The relative difference in temperature between the two basins is conducive to a strengthening in Walker circulation (McGregor et al., 2014; Qin et al. 2020). This mechanism could be investigated further by imposing varying states of the AL towards which FORTE2.0 simulations could be nudged. Furthermore, this would build on the recent study from Kang et al. (2020), who investigated the role of the northern and southern extra-tropics in modulating the Walker circulation and found that atmospheric and oceanic mechanisms initiated by a cooling in the extra-tropics projects onto a modulation of the Walker circulation via processes such as the WES feedback, cloud feedbacks and ocean upwelling. A study imposing an atmospheric anomaly instead of a more idealised change to

surface fluxes would allow inferences about the far-field effects of an anomalous AL through the mechanism outlined in Kang et al. (2020) to be tested. Diagnostics such as SST, vertical and zonal wind velocity would allow determinations to be made about the effect of the AL on the Walker cell.

Furthermore, recent research suggests competing influences on the evolution of the AL under future GHG-induced warming. Utilising observational data and CMIP5 simulations, Gan et al. (2017) show that the AL will likely deepen under future GHG-induced warming through the mechanisms associated with tropical Pacific heating and the resulting atmospheric bridge - described in chapter 1. Counter to this projection, Orihuela-Pinto et al. (2022) describes how a projected weakening (or collapse) of the Atlantic Overturning Circulation under global warming is associated with a weakening of the AL (driven by a cooling equatorial Pacific). Therefore, developing a better understanding of how these two factors shape the evolution of the AL under future climate projections could be achieved by framing the study from the perspective of the anomalous extra-tropical North Pacific. In doing so, one could develop a better insight into the robustness and interplay of these competing feedbacks in a warming world.

References

Aas, W., Mortier, A., Bowersox, V., Cherian, R., Faluvegi, G., Fagerli, H., Hand, J., Klimont, Z., Galy-Lacaux, C., Lehmann, C. M. B., Myhre, C. L., Myhre, G., Olivié, D., Sato, K., Quaas, J., Rao, P. S. P., Schulz, M., Shindell, D., Skeie, R. B., Xu, X. (2019). Global and regional trends of atmospheric sulfur. *Scientific Reports*, *9*(1), 1–11. https://doi.org/10.1038/s41598-018-37304-0

Alexander, M. A., Bladé, I., Newman, M., Lanzante, J. R., Lau, N. C., & Scott, J. D. (2002). The atmospheric bridge: The influence of ENSO teleconnections on air-sea interaction over the global oceans. In *Journal of Climate* (Vol. 15, Issue 16). https://doi.org/10.1175/1520-0442(2002)015<2205:TABTIO>2.0.CO;2

Alexander, M. A., & Deser, C. (1995). A mechanism for the recurrence of wintertime midlatitude SST anomalies. *Journal of Physical Oceanography*, *25*(1), 122–137. https://doi.org/10.1175/1520-0485(1995)025<0122:AMFTRO>2.0.CO;2

Alexander, M. A., & Scott, J. D. (2008). The role of Ekman Ocean heat transport in the northern hemisphere response to ENSO. *Journal of Climate*, *21*(21), 5688–5707. https://doi.org/10.1175/2008JCLI2382.1

Alexander, M. A., Vimont, D. J., Chang, P., & Scott, J. D. (2010). The impact of extratropical atmospheric variability on ENSO: Testing the seasonal footprinting mechanism using coupled model experiments. *Journal of Climate*, *23*(11), 2885–2901. https://doi.org/10.1175/2010JCLI3205.1

Allan, R. P. (2017). Global energy budget: Elusive origin of warming slowdown. *Nature Climate Change*, *7*(5), 316–317. https://doi.org/10.1038/nclimate3282

Allen, R. J., Sherwood, S. C., Norris, J. R., & Zender, C. S. (2012). Recent Northern Hemisphere tropical expansion primarily driven by black carbon and tropospheric ozone. *Nature*, *485*(7398), 350–354. https://doi.org/10.1038/nature11097

Allen, R. J., Evan, A. T., & Booth, B. B. B. (2015). Interhemispheric aerosol radiative forcing and tropical precipitation shifts during the late Twentieth Century. *Journal of Climate*, *28*(20), 8219–8246. https://doi.org/10.1175/JCLI-D-15-0148.1

Allen, R. J., Norris, J. R., & Kovilakam, M. (2014). Influence of anthropogenic aerosols and the Pacific Decadal Oscillation on tropical belt width. *Nature Geoscience*, *7*(4), 270–274. https://doi.org/10.1038/ngeo2091

Allen, R. J., & Sherwood, S. C. (2011). The impact of natural versus anthropogenic aerosols on atmospheric circulation in the Community Atmosphere Model. *Climate Dynamics*, *36*(9–10), 1959–1978. https://doi.org/10.1007/s00382-010-0898-8

Allen, R. J., Sherwood, S. C., Norris, J. R., & Zender, C. S. (2012). Recent Northern Hemisphere tropical expansion primarily driven by black carbon and tropospheric ozone. *Nature*, *485*(7398), 350–354. https://doi.org/10.1038/nature11097

Amiri-Farahani, A., Allen, R. J., Li, K. F., Nabat, P., & Westervelt, D. M. (2020). A La Niña-Like Climate Response to South African Biomass Burning Aerosol in CESM Simulations. *Journal of Geophysical Research: Atmospheres*, *125*(6). https://doi.org/10.1029/2019JD031832

Amirudin, A. A., Salimun, E., Tangang, F., Juneng, L., & Zuhairi, M. (2020). Differential influences of teleconnections from the Indian and Pacific oceans on rainfall variability in Southeast Asia. *Atmosphere*, *11*(9), 13–15. https://doi.org/10.3390/ATMOS11090886

An, S. Il. (2018). Impact of Pacific Decadal Oscillation on Frequency Asymmetry of El Niño and La Niña Events. *Advances in Atmospheric Sciences*, *35*(5), 493–494. https://doi.org/10.1007/s00376-018-8024-7

Anderson, B. T., Perez, R. C., & Karspeck, A. (2013). Triggering of El Niño onset through trade wind-induced charging of the equatorial Pacific. *Geophysical Research Letters*, *40*(6), 1212–1216. https://doi.org/10.1002/grl.50200

Andreae, M. O. (2007). Aerosols before pollution. *Science*, *315*(5808), 50–51. https://doi.org/10.1126/science.1136529

Arakawa, A., & Lamb, V. R. (1977). *Computational Design of the Basic Dynamical Processes of the UCLA General Circulation Model* (Vol. 17, pp. 173–265). Elsevier. https://doi.org/10.1016/b978-0-12-460817-7.50009-4

Arora, V. K., Scinocca, J. F., Boer, G. J., Christian, J. R., Denman, K. L., Flato, G. M., Kharin, V. V., Lee, W. G., & Merryfield, W. J. (2011). Carbon emission limits required to satisfy future representative concentration pathways of greenhouse gases. *Geophysical Research Letters*, *38*(5). https://doi.org/10.1029/2010GL046270

Barlow, M., Nigam, S., & Berbery, E. H. (2001). ENSO, Pacific decadal variability, and U.S. summertime precipitation, drought, and stream flow. *Journal of Climate*, *14*(9), 2105–2128. https://doi.org/10.1175/1520-0442(2001)014<2105:EPDVAU>2.0.CO;2

Barnett, T. P., Pierce, D. W., Latif, M., Dommenget, D., & Saravanan, R. (1999). Interdecadal interactions between the tropics and midlatitudes in the Pacific basin. *Geophysical Research Letters*, *26*(5), 615–618. https://doi.org/10.1029/1999GL900042

Barnett, T. P., Pierce, D. W., & Planck, M. (1999). Interdecadal interactions between the tropics and midlatitudes in the Pacific basin. *Geophysical Research Letters*, *26*(5), 615–618.

Bartlett, R. E., Bollasina, M. A., Booth, B. B. B., Dunstone, N. J., Marenco, F., Messori, G., & Bernie, D. J. (2018). Do differences in future sulfate emission pathways matter for near-term climate? A case study for the Asian monsoon. *Climate Dynamics*, *50*(5–6), 1863–1880. https://doi.org/10.1007/s00382-017-3726-6

Battisti, D. S., & Hirst, A. C. (1989). Interannual variability in a tropical atmosphere-ocean model: influence of the basic state, ocean geometry and nonlinearity. *Journal of the Atmospheric Sciences*, *46*(12), 1687–1712. https://doi.org/10.1175/ 1520-0469 (1989)046<1687:IVIATA>2.0.CO;2

Bellouin, N., Collins, W. J., Culverwell, I. D., Halloran, P. R., Hardiman, S. C., Hinton, T. J., Jones, C. D., McDonald, R. E., McLaren, A. J., O'Connor, F. M., Roberts, M. J., Rodriguez, J. M., Woodward, S., Best, M. J., Brooks, M. E., Brown, A. R., Butchart, N., Dearden, C., Derbyshire, S. H., … Wiltshire, A. (2011). The HadGEM2 family of Met Office Unified Model Climate configurations. *Geoscientific Model Development Discussions*, *4*(2), 765–841. https://doi.org/10.5194/gmdd-4-765-2011

Bentsen, M., Bethke, I., Debernard, J. B., Iversen, T., Kirkevåg, A., Seland, Ø., Drange, H., Roelandt, C., Seierstad, I. A., Hoose, C., & Kristjánsson, J. E. (2012). The Norwegian Earth System Model, NorESM1-M – Part 1: Description and basic evaluation. *Geoscientific Model Development Discussions*, *5*(3), 2843–2931. https://doi.org/10.5194/gmdd-5-2843-2012

Bhaskar, V. V., & Rao, P. S. P. (2017). Annual and decadal variation in chemical composition of rain water at all the ten GAW stations in India. *Journal of*

Atmospheric Chemistry, *74*(1), 23–53. https://doi.org/10.1007/s10874-016-9339-3

Blaker, A., Joshi, M., Sinha, B., Stevens, D., Smith, R., & Hirschi, J. (2020). FORTE 2.0: a fast, parallel and flexible coupled climate model. *Geoscientific Model Development Discussions*, 1–22. https://doi.org/10.5194/gmd-2020-43

Boers, N., Ghil, M., & Rousseau, D. D. (2018). Ocean circulation, ice shelf, and sea ice interactions explain Dansgaard–Oeschger cycles. *Proceedings of the National Academy of Sciences of the United States of America*, *115*(47), E11005–E11014. https://doi.org/10.1073/pnas.1802573115

Bollasina, M. A., Ming, Y., & Ramaswamy, V. (2011). Anthropogenic aerosols and the weakening of the south asian summer monsoon. *Science*, *334*(6055), 502–505. https://doi.org/10.1126/science.1204994

Bollasina, M. A., Ming, Y., & Ramaswamy, V. (2011). Anthropogenic aerosols and the weakening of the south asian summer monsoon. *Science*, *334*(6055), 502–505. https://doi.org/10.1126/SCIENCE.1204994/SUPPL_FILE/BOLLASINA.SOM.PDF

Bond, T. C., Doherty, S. J., Fahey, D. W., Forster, P. M., Berntsen, T., Deangelo, B. J., Flanner, M. G., Ghan, S., Kärcher, B., Koch, D., Kinne, S., Kondo, Y., Quinn, P. K., Sarofim, M. C., Schultz, M. G., Schulz, M., Venkataraman, C., Zhang, H., Zhang, S., … Zender, C. S. (2013). Bounding the role of black carbon in the climate system: A scientific assessment. *Journal of Geophysical Research Atmospheres*, *118*(11), 5380–5552. https://doi.org/10.1002/jgrd.50171

Bond, T. C., Bhardwaj, E., Dong, R., Jogani, R., Jung, S., Roden, C., Streets, D. G., & Trautmann, N. M. (2007). Historical emissions of black and organic carbon aerosol from energy-related combustion, 1850-2000. *Global Biogeochemical Cycles*, *21*(2). https://doi.org/10.1029/2006GB002840

Bonfils, C., & Santer, B. D. (2011). Investigating the possibility of a human component in various pacific decadal oscillation indices. *Climate Dynamics*, *37*(7–8), 1457–1468. https://doi.org/10.1007/s00382-010-0920-1

Chan, S. C., & Nigam, S. (2009). Residual diagnosis of diabatic heating from ERA-40 and NCEP reanalyses: Intercomparisons with TRMM. *Journal of Climate*, *22*(2), 414–428. https://doi.org/10.1175/2008JCLI2417.1

Chavez, F. P., Ryan, J., Lluch-Cota, S. E., & Ñiquen, C. M. (2003). Climate: From anchovies to sardines and back: Multidecadal change in the Pacific Ocean. In *Science* (Vol. 299, Issue 5604, pp. 217–221). American Association for the Advancement of Science. https://doi.org/10.1126/science.1075880

Chen, S., & Yu, B. (2020). The seasonal footprinting mechanism in large ensemble simulations of the second generation Canadian earth system model: uncertainty due to internal climate variability. *Climate Dynamics*, *55*(9–10), 2523–2541. https://doi.org/10.1007/s00382-020-05396-y

Chen, X., & Tung, K. K. (2018). Global-mean surface temperature variability: space–time perspective from rotated EOFs. *Climate Dynamics*, *51*(5–6), 1719–1732. https://doi.org/10.1007/s00382-017-3979-0

Chen, X., & Wallace, J. M. (2016). Orthogonal PDO and ENSO indices. *Journal of Climate*, *29*(10), 3883–3892. https://doi.org/10.1175/JCLI-D-15-0684.1

Chen, X., Wallace, J. M., & Tung, K. K. (2017). Pairwise-rotated EOFs of global SST. *Journal of Climate*, *30*(14), 5473–5489. https://doi.org/10.1175/JCLI-D-16-0786.1

Cheng, L., Trenberth, K. E., Fasullo, J., Boyer, T., Abraham, J., & Zhu, J. (2017). Improved estimates of ocean heat content from 1960 to 2015. *Science Advances*, *3*(3). https://doi.org/10.1126/ SCIADV.1601545/SUPPL_FILE/ 1601545_SM.PDF

Cherian, R., Quaas, J., Salzmann, M., Tomassini, L., Cherian, R., Quaas, J., Salzmann, M., & Tomassini, L. (2017). Black carbon indirect effects in a climate model. *Tellus B: Chemical and Physical Meteorology*, *0889*, 1–10. https://doi.org/10.1080/16000889.2017.1369342

Chhak, K. C., Di Lorenzo, E., Schneider, N., & Cummins, P. F. (2009). Forcing of low-frequency ocean variability in the Northeast Pacific. *Journal of Climate*, *22*(5), 1255–1276. https://doi.org/10.1175/2008JCLI2639.1

Choi, H. Y., Lee, H. J., Kim, S. Y., & Park, W. (2020). Deepening of Future Aleutian Low in Ensemble Global Warming Simulations with the Kiel Climate Model. *Ocean Science Journal*, *55*(2), 219–230. https://doi.org/10.1007/s12601-020-0017-7

Choi, J. W., & Cha, Y. (2017). Anomalous variation in summer tropical cyclone activity by preceding winter Aleutian low oscillation. *Atmospheric Science Letters*, *18*(6), 268–275. https://doi.org/10.1002/asl.752

Chrysanthou, A., Maycock, A. C., Chipperfield, M. P., Dhomse, S., Garny, H., Kinnison, D., Akiyoshi, H., Deushi, M., Garcia, R. R., Jöckel, P., Kirner, O., Pitari, G., Plummer, D. A., Revell, L., Rozanov, E., Stenke, A., Tanaka, T. Y., Visioni, D., & Yamashita, Y. (2019). The effect of atmospheric nudging on the stratospheric residual circulation in chemistry-climate models. *Atmospheric Chemistry and Physics*, *19*(17), 11559–11586. https://doi.org/10.5194/acp-19-11559-2019

Chung, S. H., & Seinfeld, J. H. (2005). Climate response of direct radiative forcing of anthropogenic black carbon. *Journal of Geophysical Research D: Atmospheres*, *110*(11), 1–25. https://doi.org/10.1029/2004JD005441

Clement, A., DiNezio, P., & Deser, C. (2011). Rethinking the ocean's role in the Southern Oscillation. *Journal of Climate*, *24*(15), 4056–4072. https://doi.org/10.1175/2011JCLI3973.1

Czaja, A., van der Vaart, P., & Marshall, J. (2002). A diagnostic study of the role of remote forcing in tropical Atlantic variability. *Journal of Climate*, *15*(22), 3280–3290. https://doi.org/10.1175/1520-0442(2002)015<3280:ADSOTR>2.0.CO;2

D'Orgeville, M., & Richard Peltier, W. (2009). Implications of both statistical equilibrium and global warming simulations with CCSM3. Part I: On the decadal variability in the North Pacific basin. *Journal of Climate*, *22*(20), 5277–5297. https://doi.org/10.1175/2009JCLI2428.1

Dai, A., Fyfe, J. C., Xie, S. P., & Dai, X. (2015). Decadal modulation of global surface temperature by internal climate variability. *Nature Climate Change*, *5*(6), 555–559. https://doi.org/10.1038/nclimate2605

Dai, X. G., & Wang, P. (2018). Identifying the early 2000s hiatus associated with internal climate variability. *Scientific Reports*, *8*(1), 13602. https://doi.org/10.1038/s41598-018-31862-z

Deser, C., Lehner, F., Rodgers, K. B., Ault, T., Delworth, T. L., DiNezio, P. N., Fiore, A., Frankignoul, C., Fyfe, J. C., Horton, D. E., Kay, J. E., Knutti, R., Lovenduski, N. S., Marotzke, J., McKinnon, K. A., Minobe, S., Randerson, J., Screen, J. A., Simpson, I. R., & Ting, M. (2020). Insights from Earth system model initial-

condition large ensembles and future prospects. *Nature Climate Change*, *10*(4), 277–286. https://doi.org/10.1038/s41558-020-0731-2

Deser, C., & Phillips, A. S. (2009). Atmospheric circulation trends, 1950-2000: The relative roles of sea surface temperature forcing and direct atmospheric radiative forcing. *Journal of Climate*, *22*(2), 396–413. https://doi.org/10.1175/2008JCLI2453.1

Deser, C., Sun, L., Tomas, R. A., & Screen, J. (2016). Does ocean coupling matter for the northern extratropical response to projected Arctic sea ice loss? *Geophysical Research Letters*, *43*(5), 2149–2157. https://doi.org/10.1002/2016GL067792

Deser, C., & Timlin, M. S. (1997). Atmosphere-ocean interaction on weekly timescales in the North Atlantic and Pacific. *Journal of Climate*, *10*(3), 393–408. https://doi.org/10.1175/1520-0442(1997)010<0393:AOIOWT>2.0.CO;2

Di Carlo, E., Ruggieri, P., Davini, P., Tibaldi, S., & Corti, S. (2022). ENSO teleconnections and atmospheric mean state in idealised simulations. *Climate Dynamics*. https://doi.org/10.1007/s00382-022-06261-w

Ding, S., Chen, W., Feng, J., & Grafa, H. F. (2017). Combined impacts of PDO and two types of La Niña on climate anomalies in Europe. *Journal of Climate*, *30*(9), 3253–3278. https://doi.org/10.1175/JCLI-D-16-0376.1

Dittus, A. J., Hawkins, E., Robson, J. I., Smith, D. M., & Wilcox, L. J. (2021). Drivers of Recent North Pacific Decadal Variability: The Role of Aerosol Forcing. *Earth's Future*, *9*(12). https://doi.org/10.1029/2021EF002249

Dittus, A. J., Hawkins, E., Wilcox, L. J., Sutton, R. T., Smith, C. J., Andrews, M. B., & Forster, P. M. (2020). Sensitivity of Historical Climate Simulations to Uncertain Aerosol Forcing. *Geophysical Research Letters*, *47*(13), e2019GL085806. https://doi.org/10.1029/2019GL085806

Dong, B., & Dai, A. (2015). The influence of the Interdecadal Pacific Oscillation on Temperature and Precipitation over the Globe. *Climate Dynamics*, *45*(9–10), 2667–2681. https://doi.org/10.1007/s00382-015-2500-x

Dong, B., Dai, A., Vuille, M., & Timm, O. E. (2018). Asymmetric modulation of ENSO teleconnections by the interdecadal Pacific oscillation. *Journal of Climate*, *31*(18), 7337–7361. https://doi.org/10.1175/JCLI-D-17-0663.1

Dong, L., Zhou, T., & Chen, X. (2014). Changes of Pacific decadal variability in the twentieth century driven by internal variability, greenhouse gases, and aerosols. *Geophysical Research Letters*, *41*(23), 8570–8577. https://doi.org/10.1002/2014GL062269

Dong, X., & Xue, F. (2016). Phase transition of the Pacific decadal oscillation and decadal variation of the East Asian summer monsoon in the 20th century. *Advances in Atmospheric Sciences 2016 33:3*, *33*(3), 330–338. https://doi.org/10.1007/S00376-015-5130-7

Dow, W. J., Maycock, A. C., Lofverstrom, M., & Smith, C. J. (2021). The effect of anthropogenic aerosols on the aleutian low. *Journal of Climate*, *34*(5), 1725–1741. https://doi.org/10.1175/JCLI-D-20-0423.1

DR, C. (1992). *Latent and Sensible Heat Flux Anomalies over the Northern Oceans: Driving the Sea Surface Temperature in: Journal of Physical Oceanography Volume 22 Issue 8 (1992)*. Journals.Ametsoc.Org. https://journals.ametsoc.org/view/journals/phoc/22/8/1520-0485_1992_022_0859_lashfa_2_0_co_2.xml

Dufresne, J. L., Foujols, M. A., Denvil, S., Caubel, A., Marti, O., Aumont, O., Balkanski, Y., Bekki, S., Bellenger, H., Benshila, R., Bony, S., Bopp, L., Braconnot, P., Brockmann, P., Cadule, P., Cheruy, F., Codron, F., Cozic, A., Cugnet, D., … Vuichard, N. (2013). Climate change projections using the IPSL-CM5 Earth System Model: From CMIP3 to CMIP5. *Climate Dynamics*, *40*(9–10), 2123–2165. https://doi.org/10.1007/s00382-012-1636-1

Edwards, J. M., & Slingo, A. (1996). Studies with a flexible new radiation code. I: Choosing a configuration for a large-scale model. *Quarterly Journal of the Royal Meteorological Society*, *122*(531), 689–719. https://doi.org/10.1256/smsqj.53106

Edwards, N. R., & Marsh, R. (2005). Uncertainties due to transport-parameter sensitivity in an efficient 3-D ocean-climate model. *Climate Dynamics*, *24*(4), 415–433. https://doi.org/10.1007/s00382-004-0508-8

Engardt, M., Simpson, D., Schwikowski, M., & Granat, L. (2017). Deposition of sulphur and nitrogen in Europe 1900–2050. Model calculations and comparison to historical observations. *Tellus, Series B: Chemical and Physical Meteorology*, *69*(1). https://doi.org/10.1080/16000889.2017.1328945

England, M. H., Mcgregor, S., Spence, P., Meehl, G. A., Timmermann, A., Cai, W., Gupta, A. Sen, Mcphaden, M. J., Purich, A., & Santoso, A. (2014). Recent intensification of wind-driven circulation in the Pacific and the ongoing warming hiatus. *Nature Climate Change*, *4*(3), 222–227. https://doi.org/10.1038/nclimate2106

Ervens, B., Turpin, B. J., & Weber, R. J. (2011). Secondary organic aerosol formation in cloud droplets and aqueous particles (aqSOA): A review of laboratory, field and model studies. In *Atmospheric Chemistry and Physics* (Vol. 11, Issue 21, pp. 11069–11102). https://doi.org/10.5194/acp-11-11069-2011

Esbensen, S. K. (1984). A comparison of intermonthly and interannual teleconnections in the 700 mb geopotential height field during the Northern Hemisphere winter. *Monthly Weather Review*, *112*(10), 2016–2032. https://doi.org/10.1175/1520-0493(1984)112<2016:ACOIAI>2.0.CO;2

Ewen, T. L., Weaver, A. J., & Eby, M. (2004). Sensitivity of the inorganic ocean carbon cycle to future climate warming in the UVic coupled model. *Atmosphere - Ocean*, *42*(1), 23–42. https://doi.org/10.3137/ao.420103

Eyring, V., Bony, S., Meehl, G. A., Senior, C. A., Stevens, B., Stouffer, R. J., & Taylor, K. E. (2016). Overview of the Coupled Model Intercomparison Project Phase 6 (CMIP6) experimental design and organization. *Geoscientific Model Development*, *9*(5), 1937–1958. https://doi.org/10.5194/gmd-9-1937-2016

Eyring, V., Gillett, N. P., Achuta Rao, K. M., Barimalala South Africa, R., Barreiro, M., Bock, L., Malinina, E., Ruiz, L., Sallée, J.-B., Santer, B. D., Trewin, B., Weigel, K., Zhang, X., Zhao, A., Halenka, T., Marengo Orsini Brazil, J. A., Mitchell, D., Gillett, N., Achuta Rao, K., … Zhou, B. (2021). *Chapter 3: Human Influence on the Climate System*. https://doi.org/10.1017/9781009157896.005

Fang, C., Wu, L., & Zhang, X. (2014). The impact of global warming on the pacific decadal oscillation and the possible mechanism. *Advances in Atmospheric Sciences*, *31*(1), 118–130. https://doi.org/10.1007/s00376-013-2260-7

Fathrio, I., Manda, A., Iizuka, S., Kodama, Y. M., & Ishida, S. (2018). Ocean heat budget analysis on sea surface temperature anomaly in western Indian Ocean during strong-weak Asian summer monsoon. *IOP Conference Series: Earth and Environmental Science*, *149*(1), 12014. https://doi.org/10.1088/1755-1315/149/1/012014

Fedorov, A. V. 2008. Ocean-atmosphere coupling. In: Oxford Companion to Global Change (eds. A. Goudie and D. Cuff), Oxford University Press, Oxford, Great Britain, pp. 369374.

Fereday, D. R., Chadwick, R., Knight, J. R., & Scaife, A. A. (2020). Tropical Rainfall Linked to Stronger Future ENSO-NAO Teleconnection in CMIP5 Models. *Geophysical Research Letters*, *47*(22). https://doi.org/10.1029/2020GL088664

Forster, P. M., Richardson, T., Maycock, A. C., Smith, C. J., Samset, B. H., Myhre, G., Andrews, T., Pincus, R., & Schulz, M. (2016). Recommendations for diagnosing effective radiative forcing from climate models for CMIP6. *Journal of Geophysical Research*, *121*(20), 12,460-12,475. https://doi.org/10.1002/2016JD025320

Fraedrich, K., Kirk, E., Luksch, U., & Lunkeit, F. (2005). The portable university model of the atmosphere (PUMA): Storm track dynamics and low-frequency variability. *Meteorologische Zeitschrift*, *14*(6), 735–745. https://doi.org/10.1127/0941-2948/2005/0074

Frankignoul, C., & Hasselmann, K. (1977). Stochastic climate models, Part II Application to sea-surface temperature anomalies and thermocline variability. *Tellus*, *29*(4), 289–305. https://doi.org/10.3402/tellusa.v29i4.11362

Frankignoul, C., & Reynolds, R. W. (1983). Testing a Dynamical Model for Mid-Latitude Sea Surface Temperature Anomalies. *Journal of Physical Oceanography*, *13*(7), 1131–1145. https://doi.org/10.1175/1520-0485(1983)013<1131:tadmfm>2.0.co;2

Fyfe, J. C., Meehl, G. A., England, M. H., Mann, M. E., Santer, B. D., Flato, G. M., Hawkins, E., Gillett, N. P., Xie, S. P., Kosaka, Y., & Swart, N. C. (2016). Making sense of the early-2000s warming slowdown. *Nature Climate Change*, *6*(3), 224–228. https://doi.org/10.1038/nclimate2938

Gan, B., Wu, L., Jia, F., Li, S., & Cai, W. (2017). On the response of the Aleutian low to greenhouse warming. *Journals.Ametsoc.Org*. https://journals.ametsoc.org /view /journals/clim/30/10/jcli-d-15-0789.1.xml

Gedalof, ev, Mantua, N. J., & Peterson, D. L. (2002). A multi-century perspective of variability in the Pacific Decadal Oscillation: new insights from tree rings and coral. *Z., N. J. Res. Lett*, *29*(24), 2204. https://doi.org/10.1029/2002GL015824

Geng, T., Yang, Y., & Wu, L. (2019). On the Mechanisms of Pacific Decadal Oscillation Modulation in a Warming Climate. *Journal of Climate*, *32*(5), 1443–1459. https://doi.org/10.1175/JCLI-D-18-0337.1

Gent, P. R., Danabasoglu, G., Donner, L. J., Holland, M. M., Hunke, E. C., Jayne, S. R., Lawrence, D. M., Neale, R. B., Rasch, P. J., Vertenstein, M., Worley, P. H., Yang, Z. L., & Zhang, M. (2011). The community climate system model version 4. *Journal of Climate*, *24*(19), 4973–4991. https://doi.org/10.1175/2011JCLI4083.1

Giamalaki, K., Beaulieu, C., Henson, S. A., Martin, A. P., Kassem, H., & Faranda, D. (2021). Future intensification of extreme Aleutian low events and their climate impacts. *Scientific Reports 2021 11:1*, *11*(1), 1–12. https://doi.org/10.1038/s41598-021-97615-7

Gollan, G., Greatbatch, R. J., & Jung, T. (2015). Origin of variability in Northern Hemisphere winter blocking on interannual to decadal timescales. *Geophysical Research Letters*, *42*(22), 10037–10046. https://doi.org/10.1002/2015GL066572

Grandey, B. S., Cheng, H., & Wang, C. (2016). Transient climate impacts for scenarios of aerosol emissions from Asia: A story of coal versus gas. *Journal of Climate*, *29*(8), 2849–2867. https://doi.org/10.1175/JCLI-D-15-0555.1

Green, J. S. A. (1984). Atmosphere-ocean dynamics. A. E. Gill. Academic Press (London). 1982. Pp. x + 662. £39.60/$60.00 (paperback $30.00). *Quarterly Journal of the Royal Meteorological Society*, *110*(463), 280–281. https://doi.org/10.1002/QJ.49711046322

Griesel, A., Levermann, A., Mignot, J., Hofmann, M., Montoya, M., Alexa, A. E., Ae, G., Ae, J. M., Ae, A. G., & Rahmstorf, S. (2005). The earth system model of intermediate complexity CLIMBER-3α. Part I: description and performance for present-day conditions. *Springer*, *25*(2–3), 237–263. https://doi.org/10.1007/s00382-005-0044-1

Gu, D., & Philander, S. G. H. (1997). Interdecadal climate fluctuations that depend on exchanges between the tropics and extratropics. *Science*, *275*(5301), 805–807. https://doi.org/10.1126/science.275.5301.805

Guan, B., & Nigam, S. (2008). Pacific Sea Surface Temperatures in the Twentieth Century: An Evolution-Centric Analysis of Variability and Trend. *Journal of Climate*, *21*(12), 2790–2809. https://doi.org/10.1175/2007JCLI2076.1

Haarsma, R., Roberts, M., … P. V.-G. M., & 2016, undefined. (n.d.). High resolution model intercomparison project (HighResMIP v1. 0) for CMIP6. *Gmd.Copernicus.Org*. Retrieved September 8, 2022, from https://gmd .copernicus.org/ articles/9/4185/2016/

Hannachi, A., Jolliffe, I. T., & Stephenson, D. B. (2007). Empirical orthogonal functions and related techniques in atmospheric science: A review. *International Journal of Climatology*, *27*(9), 1119–1152. https://doi.org/10.1002/JOC.1499

Hansen, J. (2005). Efficacy of climate forcings. *Journal of Geophysical Research*, *110*(D18), D18104. https://doi.org/10.1029/2005JD005776

Harvey, B. J., Cook, P., Shaffrey, L. C., & Schiemann, R. (2020). The Response of the Northern Hemisphere Storm Tracks and Jet Streams to Climate Change in the CMIP3, CMIP5, and CMIP6 Climate Models. *Journal of Geophysical Research: Atmospheres*, *125*(23), 1–10. https://doi.org/10.1029/2020JD032701

Held, I. M., Ting, M., & Wang, H. (2002). Northern winter stationary waves: Theory and modeling. *Journal of Climate*, *15*(16), 2125–2144. https://doi.org/10.1175/1520-0442(2002)015<2125:NWSWTA>2.0.CO;2

Henson, C., Market, P., Lupo, A., & Guinan, P. (2017). ENSO and PDO-related climate variability impacts on Midwestern United States crop yields. *International Journal of Biometeorology*, *61*(5), 857–867. https://doi.org/10.1007/s00484-016-1263-3

Hernández, A., Martin-Puertas, C., Moffa-Sánchez, P., Moreno-Chamarro, E., Ortega, P., Blockley, S., Cobb, K. M., Comas-Bru, L., Giralt, S., Goosse, H., Luterbacher, J., Martrat, B., Muscheler, R., Parnell, A., Pla-Rabes, S., Sjolte, J., Scaife, A. A., Swingedouw, D., Wise, E., & Xu, G. (2020). Modes of climate variability: Synthesis and review of proxy-based reconstructions through the Holocene. *Earth-Science Reviews*, *209*, 103286. https://doi.org/ 10.1016/J.EARSCIREV.2020.103286

Hersbach, H., Bell, B., Berrisford, P., Hirahara, S., Horányi, A., Muñoz-Sabater, J., Nicolas, J., Peubey, C., Radu, R., Schepers, D., Simmons, A., Soci, C., Abdalla, S., Abellan, X., Balsamo, G., Bechtold, P., Biavati, G., Bidlot, J., Bonavita, M., …

Thépaut, J. N. (2020). The ERA5 global reanalysis. *Quarterly Journal of the Royal Meteorological Society*, *146*(730), 1999–2049. https://doi.org/10.1002/qj.3803

Hodgson, D. A., Verleyen, E., Sabbe, K., Squier, A. H., Keely, B. J., Leng, M. J., Saunders, K. M., & Vyverman, W. (2005). Late Quaternary climate-driven environmental change in the Larsemann Hills, East Antarctica, multi-proxy evidence from a lake sediment core. *Quaternary Research*, *64*(1), 83–99. https://doi.org/10.1016/J.YQRES.2005.04.002

Hodnebrog, Ø., Myhre, G., Samset, B. H., Alterskjær, K., Andrews, T., Boucher, O., Faluvegi, G., Fläschner, D., Forster, P. M., Kasoar, M., Kirkevåg, A., Lamarque, J.-F., Olivié, D., Richardson, T. B., Shawki, D., Shindell, D., Shine, K. P., Stier, P., Takemura, T., … Watson-Parris, D. (2019). Increased water vapour lifetime due to global warming. In *Atmospheric Chemistry and Physics Discussions*. https://doi.org/10.5194/acp-2019-121

Hong, S. Y., & Chang, E. C. (2012). Spectral nudging sensitivity experiments in a regional climate model. *Asia-Pacific Journal of Atmospheric Sciences*, *48*(4), 345–355. https://doi.org/10.1007/s13143-012-0033-3

Hoskins, B. J., & Simmons, A. J. (1975). A multi-layer spectral model and the semi-implicit method. *Quarterly Journal of the Royal Meteorological Society*, *101*(429), 637–655. https://doi.org/10.1002/qj.49710142918

Hoskins, B. J., & Karoly, D. J. (1981). The steady linear response of a spherical atmosphere to thermal and orographic forcing. *Journal of the Atmospheric Sciences*, *38*(6), 1179–1196. https://doi.org/10.1175/1520-0469(1981)038<1179:TSLROA>2.0.CO;2

Hoskins, B. J., & Simmons, A. J. (1975). A multi-layer spectral model and the semi-implicit method. *Quarterly Journal of the Royal Meteorological Society*, *101*(429), 637–655. https://doi.org/10.1002/qj.49710142918

Hoskins, B. J., Simmons, A. J., & Andrews, D. G. (1977). Energy dispersion in a barotropic atmosphere. *Quarterly Journal of the Royal Meteorological Society*, *103*(438), 553–567. https://doi.org/10.1002/qj.49710343802

Hu, D., & Guan, Z. (2018). Decadal relationship between the stratospheric arctic vortex and pacific decadal oscillation. *Journal of Climate*, *31*(9), 3371–3386. https://doi.org/10.1175/JCLI-D-17-0266.1

Hu, S., & Fedorov, A. V. (2017). The extreme El Niño of 2015–2016 and the end of global warming hiatus. *Geophysical Research Letters*, *44*(8), 3816–3824. https://doi.org/10.1002/2017GL072908

Hua, W., Dai, A., & Qin, M. (2018). *Contributions of Internal Variability and External Forcing to the Recent Pacific Decadal Variations*. Geophysical Research Letters. https://doi.org/10.1029/2018GL079033

Hurrell, J. W., Holland, M. M., Gent, P. R., Ghan, S., Kay, J. E., Kushner, P. J., Lamarque, J. F., Large, W. G., Lawrence, D., Lindsay, K., Lipscomb, W. H., Long, M. C., Mahowald, N., Marsh, D. R., Neale, R. B., Rasch, P., Vavrus, S., Vertenstein, M., Bader, D., … Marshall, S. (2013). The community earth system model: A framework for collaborative research. *Bulletin of the American Meteorological Society*, *94*(9), 1339–1360. https://doi.org/10.1175/BAMS-D-12-00121.1

Hwang, S. O., Yeh, S. W., Oh, S. Y., & Lee, J. (2022). Recent weakening linkage between Arctic oscillation and Aleutian low during boreal winter and its impact on surface temperature over Eastern Eurasia. *Atmospheric Science Letters*, *23*(7). https://doi.org/10.1002/asl.1089

Iizuka, Y., Uemura, R., Fujita, K., Hattori, S., Seki, O., Miyamoto, C., Suzuki, T., Yoshida, N., Motoyama, H., & Matoba, S. (2018). A 60 Year Record of Atmospheric Aerosol Depositions Preserved in a High-Accumulation Dome Ice Core, Southeast Greenland. *Journal of Geophysical Research: Atmospheres*, *123*(1), 574–589. https://doi.org/10.1002/2017JD026733

Imbers, J., Lopez, A., Huntingford, C., & Allen, M. (2014). Sensitivity of climate change detection and attribution to the characterization of internal climate variability. *Journal of Climate*, *27*(10), 3477–3491. https://doi.org/10.1175/JCLI-D-12-00622.1

IPCC, Stocker, T. F., Qin, D., Plattner, G.-K., Tignor, M., Allen, S. K., Boschung, J., Nauels, A., Xia, Y., Bex, V., & Midgley, P. . (2013). *AR5 Climate Change 2013: The Physical Science Basis — IPCC*. https://www.ipcc.ch/report/ar5/wg1/

Iversen, T., Bentsen, M., Bethke, I., Debernard, J. B., Kirkevåg, A., Seland, Ø., Drange, H., Kristjansson, J. E., Medhaug, I., Sand, M., & Seierstad, I. A. (2013). The Norwegian Earth System Model, NorESM1-M – Part 2: Climate response and scenario projections. *Geoscientific Model Development*, *6*(2), 389–415. https://doi.org/10.5194/gmd-6-389-2013

Iwasaka, N., & Wallace, J. M. (1995). Large scale air sea interaction in the Northern Hemisphere from a view point of variations of surface heat flux by SVD analysis. *Journal of the Meteorological Society of Japan*, *73*(4), 781–794. https://doi.org/10.2151/jmsj1965.73.4_781

Jarraud, M., & Steiner, A. (2012). Summary for policymakers. In *Managing the Risks of Extreme Events and Disasters to Advance Climate Change Adaptation: Special Report of the Intergovernmental Panel on Climate Change* (Vol. 9781107025). https://doi.org/10.1017/CBO9781139177245.003

Jiang-Hua, W., Mahmood, R., & Shuanglin, L. (2013). Impact of European Black Carbon on East Asian Summer Climate. *Atmospheric and Oceanic Science Letters*, *6*(5), 375–380. https://doi.org/10.3878/j.issn.1674-2834.13.0037

Jin, F. F. (2001). Low-frequency modes of tropical ocean dynamics. *Journal of Climate*, *14*(18), 3874–3881. https://doi.org/10.1175/1520-0442(2001)014<3874:LFMOTO>2.0.CO;2

Joh, Y., & Di Lorenzo, E. (2019). Interactions between Kuroshio Extension and Central Tropical Pacific lead to preferred decadal-timescale oscillations in Pacific climate. *Scientific Reports*, *9*(1), 1–12. https://doi.org/10.1038/s41598-019-49927-y

Joh, Y., Di Lorenzo, E., Siqueira, L., & Kirtman, B. P. (2021). Enhanced interactions of Kuroshio Extension with tropical Pacific in a changing climate. *Scientific Reports*, *11*(1), 1–12. https://doi.org/10.1038/s41598-021-85582-y

Johnson, B. T., Haywood, J. M., & Hawcroft, M. K. (2019). Are Changes in Atmospheric Circulation Important for Black Carbon Aerosol Impacts on Clouds, Precipitation, and Radiation? *Journal of Geophysical Research: Atmospheres*, *124*(14), 7930–7950. https://doi.org/10.1029/2019JD030568

Joshi, M., Stringer, M., Van Der Wiel, K., O'Callaghan, A., & Fueglistaler, S. (2015). IGCM4: A fast, parallel and flexible intermediate climate model. *Geoscientific Model Development*, *8*(4), 1157–1167. https://doi.org/10.5194/gmd-8-1157-2015

Joshi, M., & Gregory, J. (2008). Dependence of the land-sea contrast in surface climate response on the nature of the forcing. *Geophysical Research Letters*, *35*(24), L24802. https://doi.org/10.1029/2008GL036234

Jung, T., Palmer, T. N., Rodwell, M. J., & Serrar, S. (2010). Understanding the anomalously cold European winter of 2005/06 using relaxation experiments. *Monthly Weather Review*, *138*(8), 3157–3174. https://doi.org/10.1175/2010MWR3258.1

Kajtar, J. B., Santoso, A., McGregor, S., England, M. H., & Baillie, Z. (2018). Model under-representation of decadal Pacific trade wind trends and its link to tropical Atlantic bias. *Climate Dynamics*, *50*(3–4), 1471–1484. https://doi.org/10.1007/s00382-017-3699-5

Kang, S. M., Held, I. M., Frierson, D. M. W., & Zhao, M. (2008). The response of the ITCZ to extratropical thermal forcing: Idealized slab-ocean experiments with a GCM. *Journal of Climate*, *21*(14), 3521–3532. https://doi.org/10.1175/2007JCLI2146.1

Kara, A. B., Rochford, P. A., & Hurlburt, H. E. (2000). An optimal definition for ocean mixed layer depth. *Journal of Geophysical Research: Oceans*, *105*(C7), 16803–16821. https://doi.org/10.1029/2000jc900072

Kasoar, M., Shawki, D., & Voulgarakis, A. (2018). Similar spatial patterns of global climate response to aerosols from different regions. *Npj Climate and Atmospheric Science*, *1*(1), 12. https://doi.org/10.1038/s41612-018-0022-z

Kasoar, M., Voulgarakis, A., Lamarque, J. F., Shindell, D. T., Bellouin, N., Faluvegi, G., & Tsigaridis, K. (2016). Regional and global temperature response to anthropogenic SO2 emissions from China in three climate models. *Atmospheric Chemistry and Physics*, *16*(15), 9785–9804. https://doi.org/10.5194/acp-16-9785-2016

Kay, J. E., Deser, C., Phillips, A., Mai, A., Hannay, C., Strand, G., Arblaster, J. M., Bates, S. C., Danabasoglu, G., Edwards, J., Holland, M., Kushner, P., Lamarque, J. F., Lawrence, D., Lindsay, K., Middleton, A., Munoz, E., Neale, R., Oleson, K., … Vertenstein, M. (2015). The community earth system model (CESM) large ensemble project : A community resource for studying climate change in the presence of internal climate variability. *Bulletin of the American Meteorological Society*, *96*(8), 1333–1349. https://doi.org/10.1175/BAMS-D-13-00255.1

Kelsey, A. (n.d.). Abrupt climate change and millennial-scale cycles: an astronomical mechanism. *Cp.Copernicus.Org*. https://doi.org/10.5194/cp-2022-49

Kirkevåg, A., Iversen, T., Seland, Ø., Hoose, C., Kristjánsson, J. E., Struthers, H., Ekman, A. M. L., Ghan, S., Griesfeller, J., Nilsson, E. D., & Schulz, M. (2013). Aerosol–climate interactions in the Norwegian Earth System Model – NorESM1-M. *Geoscientific Model Development*, *6*(1), 207–244. https://doi.org/10.5194/gmd-6-207-2013

Kirtman, B. P. (1997). Oceanic Rossby wave dynamics and the ENSO period in a coupled model. *Journal of Climate*, *10*(7), 1690–1704. https://doi.org/10.1175/1520-0442(1997)010<1690:ORWDAT>2.0.CO;2

Klimont, Z., Kupiainen, K., Heyes, C., Purohit, P., Cofala, J., Rafaj, P., Borken-Kleefeld, J., & Schöpp, W. (2017). Global anthropogenic emissions of particulate matter including black carbon. *Atmospheric Chemistry and Physics*, *17*(14), 8681–8723. https://doi.org/10.5194/acp-17-8681-2017

Knight, J. R., Maidens, A., Watson, P. A. G., Andrews, M., Belcher, S., Brunet, G., Fereday, D., Folland, C. K., Scaife, A. A., & Slingo, J. (2017). Global meteorological influences on the record UK rainfall of winter 2013-14. *Environmental Research Letters*, *12*(7). https://doi.org/10.1088/1748-9326/aa693c

Knutson, T. R., & Manabe, S. (1998). Model assessment of decadal variability and trends in the tropical Pacific Ocean. In *Journal of Climate* (Vol. 11, Issue 9). https://doi.org/10.1175/1520-0442(1998)011<2273:MAODVA>2.0.CO;2

Kooperman, G. J., Pritchard, M. S., Ghan, S. J., Wang, M., Somerville, R. C. J., & Russell, L. M. (2012). Constraining the influence of natural variability to improve estimates of global aerosol indirect effects in a nudged version of the Community Atmosphere Model 5. *Journal of Geophysical Research Atmospheres*, *117*(23), 23204. https://doi.org/10.1029/2012JD018588

Körper, J. (2016). El niÑo (Southern oscillation). *Encyclopedia of Earth Sciences Series*, *Part 2*, 216–217. https://doi.org/10.4135/9781446216187.n117

Kosaka, Y., & Xie, S. P. (2013). Recent global-warming hiatus tied to equatorial Pacific surface cooling. In *Nature* (Vol. 501, Issue 7467). https://doi.org/10.1038/nature12534

Kovilakam, M., & Mahajan, S. (2015). Black carbon aerosol-induced Northern Hemisphere tropical expansion. *Geophysical Research Letters*, *42*(12), 4964–4972. https://doi.org/10.1002/2015GL064559

Kremser, S., Thomason, L. W., von Hobe, M., Hermann, M., Deshler, T., Timmreck, C., Toohey, M., Stenke, A., Schwarz, J. P., Weigel, R., Fueglistaler, S., Prata, F. J., Vernier, J. P., Schlager, H., Barnes, J. E., Antuña-Marrero, J. C., Fairlie, D., Palm, M., Mahieu, E., … Meland, B. (2016). Stratospheric aerosol—Observations, processes, and impact on climate. In *Reviews of Geophysics* (Vol. 54, Issue 2, pp. 278–335). John Wiley & Sons, Ltd. https://doi.org/10.1002/2015RG000511

Kuntz, L. B., & Schrag, D. P. (2016). Impact of Asian aerosol forcing on tropical pacific circulation and the relationship to global temperature trends. *Journal of Geophysical Research*, *121*(24), 14403–14413. https://doi.org/ 10.1002/2016JD025430

Kushnir, Y., Scaife, A. A., Arritt, R., Balsamo, G., Boer, G., Doblas-Reyes, F., Hawkins, E., Kimoto, M., Kolli, R. K., Kumar, A., Matei, D., Matthes, K., Müller, W. A., O'Kane, T., Perlwitz, J., Power, S., Raphael, M., Shimpo, A., Smith, D., … Wu, B. (2019). Towards operational predictions of the near-term climate. *Nature Climate Change*, *9*(2), 94–101. https://doi.org/10.1038/s41558-018-0359-7

Kwon, Y. O., & Deser, C. (2007). North Pacific decadal variability in the community climate system model version 2. *Journal of Climate*, *20*(11), 2416–2433. https://doi.org/10.1175/JCLI4103.1

Kwon, Y. O., & Deser, C. (2007). North Pacific decadal variability in the community climate system model version 2. *Journal of Climate*, *20*(11), 2416–2433. https://doi.org/10.1175/JCLI4103.1

L'Heureux, M. L., Lee, S., & Lyon, B. (2013). Recent multidecadal strengthening of the Walker circulation across the tropical Pacific. *Nature Climate Change*, *3*(6), 571–576. https://doi.org/10.1038/nclimate1840

Lamarque, J. F., Bond, T. C., Eyring, V., Granier, C., Heil, A., Klimont, Z., Lee, D., Liousse, C., Mieville, A., Owen, B., Schultz, M. G., Shindell, D., Smith, S. J., Stehfest, E., van Aardenne, J., Cooper, O. R., Kainuma, M., Mahowald, N., McConnell, J. R., … van Vuuren, D. P. (2010). Historical (1850-2000) gridded anthropogenic and biomass burning emissions of reactive gases and aerosols: Methodology and application. *Atmospheric Chemistry and Physics*, *10*(15), 7017–7039. https://doi.org/10.5194/ACP-10-7017-2010

Latif, M., & Barnett, T. P. (1996). Decadal climate variability over the North Pacific and North America: Dynamics and predictability. *Journal of Climate*, *9*(10), 2407–2423. https://doi.org/10.1175/1520-0442(1996)009<2407:DCVOTN>2.0.CO;2

Latif, M., & Barnett, T. P. (1994). Causes of decadal climate variability over the North Pacific and North America. *Science*, *266*(5185), 634–637. https://doi.org/10.1126/science.266.5185.634

Lau, N. C., & Nath, M. J. (2000). Impact of ENSO on the variability of the Asian-Australian Monsoons as simulated in GCM experiments. *Journal of Climate*, *13*(24), 4287–4309. https://doi.org/10.1175/1520-0442(2000)013<4287:IOEOTV>2.0.CO;2

Lehodey, P., Alheit, J., Barange, M., Baumgartner, T., Beaugrand, G., Drinkwater, K., Fromentin, J. M., Hare, S. R., Ottersen, G., Perry, R. I., Roy, C., van der Lingen, C. D., & Werner, F. (2006). Climate variability, fish, and fisheries. In *Journal of Climate* (Vol. 19, Issue 20, pp. 5009–5030). American Meteorological Society. https://doi.org/10.1175/JCLI3898.1

Lewinschal, A., Ekman, A. M. L., & Körnich, H. (2013). The role of precipitation in aerosol-induced changes in northern hemisphere wintertime stationary waves. *Climate Dynamics*, *41*(3–4), 647–661. https://doi.org/10.1007/s00382-012-1622-7

Li, L. Z. X. (2006). Atmospheric GCM response to an idealized anomaly of the Mediterranean sea surface temperature. *Climate Dynamics*, *27*(5), 543–552. https://doi.org/10.1007/s00382-006-0152-6

Li, S., Wu, L., Yang, Y., Geng, T., Cai, W., Gan, B., Chen, Z., Jing, Z., Wang, G., & Ma, X. (2020). The Pacific Decadal Oscillation less predictable under greenhouse warming. In *Nature Climate Change* (Vol. 10, Issue 1, pp. 30–34). Nature Publishing Group. https://doi.org/10.1038/s41558-019-0663-x

Li, X., Cai, W., Meehl, G. A., Chen, D., Yuan, X., Raphael, M., Holland, D. M., Ding, Q., Fogt, R. L., Markle, B. R., Wang, G., Bromwich, D. H., Turner, J., Xie, S. P., Steig, E. J., Gille, S. T., Xiao, C., Wu, B., Lazzara, M. A., … Song, C. (2021). Tropical teleconnection impacts on Antarctic climate changes. In *Nature Reviews Earth and Environment* (Vol. 2, Issue 10, pp. 680–698). Nature Publishing Group. https://doi.org/10.1038/s43017-021-00204-5

Liakka, J., Nilsson, J., & Löfverström, M. (2012). Interactions between stationary waves and ice sheets: Linear versus nonlinear atmospheric response. *Climate Dynamics*, *38*(5–6), 1249–1262. https://doi.org/10.1007/s00382-011-1004-6

Liguori, G., & Di Lorenzo, E. (2019). Separating the North and South Pacific Meridional Modes Contributions to ENSO and Tropical Decadal Variability. *Geophysical Research Letters*, *46*(2), 906–915. https://doi.org/10.1029/2018GL080320

Liguori, G., McGregor, S., Arblaster, J. M., Singh, M. S., & Meehl, G. A. (2020). A joint role for forced and internally-driven variability in the decadal modulation of global warming. *Nature Communications*, *11*(1), 1–7. https://doi.org/10.1038/s41467-020-17683-7

Limpasuvan, V., & Hartmann, D. L. (2000). Wave-maintained annular modes of climate variability. *Journal of Climate*, *13*(24), 4414–4429. https://doi.org/10.1175/1520-0442(2000)013<4414:WMAMOC>2.0.CO;2

Lin, Y., Wang, Y., Pan, B., Hu, J., Liu, Y., & Zhang, R. (2016). Distinct impacts of aerosols on an evolving continental cloud complex during the RACORO field campaign. *Journal of the Atmospheric Sciences*, *73*(9), 3681–3700. https://doi.org/10.1175/JAS-D-15-0361.1

Litzow, M. A., Malick, M. J., Bond, N. A., Cunningham, C. J., Gosselin, J. L., & Ward, E. J. (2020). Quantifying a Novel Climate Through Changes in PDO-Climate and PDO-Salmon Relationships. *Geophysical Research Letters*, *47*(16), e2020GL087972. https://doi.org/10.1029/2020GL087972

Liu, L., Shawki, D., Voulgarakis, A., Kasoar, M., Samset, B. H., Myhre, G., Forster, P. M., Hodnebrog, Sillmann, J., Aalbergsjø, S. G., Boucher, O., Faluvegi, G., Iversen, T., Kirkevåg, A., Lamarque, J. F., Olivié, D., Richardson, T., Shindell, D., & Takemura, T. (2018). A PDRMIP Multimodel study on the impacts of regional aerosol forcings on global and regional precipitation. *Journal of Climate*, *31*(11), 4429–4447. https://doi.org/10.1175/JCLI-D-17-0439.1

Liu, Y., Sun, C., Kucharski, F., Li, J., Wang, C., & Ding, R. (2021). The North Pacific Blob acts to increase the predictability of the Atlantic warm pool. *Environmental Research Letters*, *16*(6), 064034. https://doi.org/10.1088/1748-9326/ac0030

Liu, Z., & Alexander, M. (2007). Atmospheric bridge, oceanic tunnel, and global climatic teleconnections. *Reviews of Geophysics*, *45*(2), RG2005. https://doi.org/10.1029/2005RG000172

Liu, Z., & Di Lorenzo, E. (2018). Mechanisms and Predictability of Pacific Decadal Variability. In *Current Climate Change Reports* (Vol. 4, Issue 2, pp. 128–144). https://doi.org/10.1007/s40641-018-0090-5

Lucas, C., Timbal, B., & Nguyen, H. (2014). The expanding tropics: A critical assessment of the observational and modeling studies. *Wiley Interdisciplinary Reviews: Climate Change*, *5*(1), 89–112. https://doi.org/10.1002/wcc.251

Lysne, J. A., Chang, P., & Giese, B. (1997). Impact of the extratropical Pacific on equatorial variability. *Geophysical Research Letters*, *24*(21), 2589–2592. https://doi.org/10.1029/97GL02751

Ma, P. L., Rasch, P. J., Fast, J. D., Easter, R. C., Gustafson, W. I., Liu, X., Ghan, S. J., & Singh, B. (2014). Assessing the CAM5 physics suite in the WRF-Chem model: Implementation, resolution sensitivity, and a first evaluation for a regional case study. *Geoscientific Model Development*, *7*(3), 755–778. https://doi.org/10.5194/gmd-7-755-2014

Ma, Z. (2007). The interdecadal trend and shift of dry/wet over the central part of North China and their relationship to the Pacific Decadal Oscillation (PDO). *Chinese Science Bulletin*, *52*(15), 2130–2139. https://doi.org/10.1007/s11434-007-0284-z

Madden, R. A. (2007). Large-scale, free Rossby waves in the atmosphere - An update. In *Tellus, Series A: Dynamic Meteorology and Oceanography* (Vol. 59, Issue 5, pp. 571–590). John Wiley & Sons, Ltd. https://doi.org/10.1111/j.1600-0870.2007.00257.x

Mahajan, S., Evans, K. J., Hack, J. J., & Truesdale, J. E. (2013). Linearity of climate response to increases in black carbon aerosols. *Journal of Climate*, *26*(20), 8223–8237. https://doi.org/10.1175/JCLI-D-12-00715.1

Mahajan, S., Saravanan, R., & Chang, P. (2009). The role of the wind-evaporation-sea surface temperature (WES) feedback in air-sea coupled tropical variability. *Atmospheric Research*, *94*(1), 19–36. https://doi.org/10.1016/j.atmosres.2008.09.017

Maher, N., Lehner, F., & Marotzke, J. (2020). Quantifying the role of internal variability in the temperature we expect to observe in the coming decades. *Environmental Research Letters*, *15*(5), 054014. https://doi.org/10.1088/1748-9326/ab7d02

Maher, N., Milinski, S., & Ludwig, R. (2021). Large ensemble climate model simulations: Introduction, overview, and future prospects for utilising multiple types of large ensemble. *Earth System Dynamics*, *12*(2), 401–418. https://doi.org/10.5194/esd-12-401-2021

Maher, N., Milinski, S., Suarez-Gutierrez, L., Botzet, M., Dobrynin, M., Kornblueh, L., Kröger, J., Takano, Y., Ghosh, R., Hedemann, C., Li, C., Li, H., Manzini, E., Notz, D., Putrasahan, D., Boysen, L., Claussen, M., Ilyina, T., Olonscheck, D., … Marotzke, J. (2019). The Max Planck Institute Grand Ensemble: Enabling the Exploration of Climate System Variability. *Journal of Advances in Modeling Earth Systems*, *11*(7), 2050–2069. https://doi.org/10.1029/2019MS001639

Mahmood, R., Donat, M. G., Ortega, P., Doblas-Reyes, F. J., & Ruprich-Robert, Y. (2021). Constraining Decadal Variability Yields Skillful Projections of Near-Term Climate Change. In *Geophysical Research Letters* (Vol. 48, Issue 24, p. e2021GL094915). John Wiley & Sons, Ltd. https://doi.org/10.1029/2021GL094915

Mahmood, R., & Li, S. (2014). Remote influence of South Asian black carbon aerosol on East Asian summer climate. *International Journal of Climatology*, *34*(1), 36–48. https://doi.org/10.1002/joc.3664

Manners, J., Edwards, J. M., Hill, P., & Thelen, J.-C. (2015). SOCRATES (Suite Of Community RAdiative Transfer codes based on Edwards and Slingo) Technical Guide. *Met Office, UK*. https://code.metoffice.gov.uk/trac/socrates.

Mantua, N. J., & Hare, S. R. (2002). The Pacific Decadal Oscillation. In *Journal of Oceanography* (Vol. 58, Issue 1, pp. 35–44). https://doi.org/10.1023/A:1015820616384

Mantua, N. J., Hare, S. R., Zhang, Y., Wallace, J. M., & Francis, R. C. (1997). A Pacific Interdecadal Climate Oscillation with Impacts on Salmon Production. *Bulletin of the American Meteorological Society*, *78*(6), 1069–1079. https://doi.org/10.1175/1520-0477(1997)078<1069:APICOW>2.0.CO;2

Marotzke, J. (2019). Quantifying the irreducible uncertainty in near-term climate projections. *Wiley Interdisciplinary Reviews: Climate Change*, *10*(1), e563. https://doi.org/10.1002/wcc.563

Marotzke, J., & Forster, P. M. (2015). Forcing, feedback and internal variability in global temperature trends. *Nature*, *517*(7536), 565–570. https://doi.org/10.1038/nature14117

Martin, Z., Orbe, C., Wang, S., & Sobel, A. (2021). The MJO–QBO relationship in a GCM with stratospheric nudging. *Journal of Climate*, *34*(11), 4603–4624. https://doi.org/10.1175/JCLI-D-20-0636.1

MacDonald, G. M., & Case, R. A. (2005). Variations in the Pacific Decadal Oscillation over the past millennium. *Geophysical Research Letters*, *32*(8), 1–4. https://doi.org/10.1029/2005GL022478

McCreary, J. P., & Peng Lu. (1994). Interaction between the subtropical and equatorial ocean circulations: the subtropical cell. *Journal of Physical Oceanography*, *24*(2), 466–497.https://doi.org/10.1175/1520-0485(1994)024<0466:IBTSAE>2.0.CO;2

McGraw, Z., Storelvmo, T., Samset, B. H., & Stjern, C. W. (2020). Global Radiative Impacts of Black Carbon Acting as Ice Nucleating Particles. *Geophysical Research Letters*, *47*(20), e2020GL089056. https://doi.org/10.1029/2020GL089056

McGregor, S., Timmermann, A., Stuecker, M. F., England, M. H., Merrifield, M., Jin, F. F., & Chikamoto, Y. (2014). Recent walker circulation strengthening and pacific cooling amplified by atlantic warming. In *Nature Climate Change* (Vol. 4, Issue 10). https://doi.org/10.1038/nclimate2330

McKenna, C. (2019). *The influence of Arctic sea-ice loss on mid-latitude weather and climate: exploring sensitivities and mechanisms*. https://nora.nerc.ac.uk/id/eprint/528404/

Meehl, G. A., & Stocker, T. F. (2007). Chapter 10. Global Climate Projections. *Climate Change 2007: The Physical Science Basis*, *November*, 747–846.

Meehl, G. A., Arblaster, J. M., Fasullo, J. T., Hu, A., & Trenberth, K. E. (2011). Model-based evidence of deep-ocean heat uptake during surface-temperature hiatus periods. *Nature Climate Change*, *1*(7), 360–364. https://doi.org/10.1038/nclimate1229

Meehl, G. A., Goddard, L., Boer, G., Burgman, R., Branstator, G., Cassou, C., Corti, S., Danabasoglu, G., Doblas-Reyes, F., Hawkins, E., Karspeck, A., Kimoto, M.,

Kumar, A., Matei, D., Mignot, J., Msadek, R., Navarra, A., Pohlmann, H., Rienecker, M., … Yeager, S. (2014). Decadal climate prediction an update from the trenches. *Bulletin of the American Meteorological Society*, *95*(2), 243–267. https://doi.org/10.1175/BAMS-D-12-00241.1

Meehl, G. A., Goddard, L., Murphy, J., Stouffer, R. J., Boer, G., Danabasoglu, G., Dixon, K., Giorgetta, M. A., Greene, A. M., Hawkins, E., Hegerl, G., Karoly, D., Keenlyside, N., Kimoto, M., Kirtman, B., Navarra, A., Pulwarty, R., Smith, D., Stammer, D., & Stockdale, T. (2009). Decadal Prediction. *Bulletin of the American Meteorological Society*, *90*(10), 1467–1486. https://doi.org/10.1175/2009bams2778.1

Meehl, G. A., Hu, A., Arblaster, J. M., Fasullo, J., & Trenberth, K. E. (2013). Externally forced and internally generated decadal climate variability associated with the interdecadal pacific oscillation. *Journal of Climate*, *26*(18), 7298–7310. https://doi.org/10.1175/JCLI-D-12-00548.1

Menon, S., Hansen, J., Nazarenko, L., & Luo, Y. (2002). Climate effects of black carbon aerosols in China and India. *Science*, *297*(5590), 2250–2253. https://doi.org/10.1126/science.1075159

Mo, K. C. (2000). Relationships between low-frequency variability in the Southern Hemisphere and sea surface temperature anomalies. *Journal of Climate*, *13*(20), 3599–3610. https://doi.org/10.1175/1520-0442(2000) 013<3599:RBLFVI>2.0.CO;2

Mochizuki, T., Ishii, M., Kimoto, M., Chikamoto, Y., Watanabe, M., Nozawa, T., Sakamoto, T. T., Shiogama, H., Awaji, T., Sugiura, N., Toyoda, T., Yasunaka, S., Tatebe, H., & Mori, M. (2010). Pacific decadal oscillation hindcasts relevant to near-term climate prediction. *Proceedings of the National Academy of Sciences of the United States of America*, *107*(5), 1833–1837. https://doi.org/10.1073/pnas.0906531107

Modak, A., & Bala, G. (2019). Efficacy of black carbon aerosols: The role of shortwave cloud feedback. *Environmental Research Letters*, *14*(8). https://doi.org/10.1088/1748-9326/ab21e7

Mohino, E., Janicot, S., & Bader, J. (2011). Sahel rainfall and decadal to multi-decadal sea surface temperature variability. *Climate Dynamics*, *37*(3), 419–440. https://doi.org/10.1007/s00382-010-0867-2

Murata, K., Kido, S., & Tozuka, T. (2020). Role of Reemergence in the Central North Pacific Revealed by a Mixed Layer Heat Budget Analysis. *Geophysical Research Letters*, *47*(13), e2020GL088194. https://doi.org/10.1029/2020GL088194

Myhre, G; Shindell, D; Pongratz, J. (2013). Anthropogenic and natural radiative forcing. In *Climate Change 2013 the Physical Science Basis: Working Group I Contribution to the Fifth Assessment Report of the Intergovernmental Panel on Climate Change* (Vol. 9781107057, pp. 659–740). Cambridge University Press. https://doi.org/10.1017/CBO9781107415324.018

Myhre, G., Forster, P. M., Samset, B. H., Hodnebrog, Sillmann, J., Aalbergsjø, S. G., Andrews, T., Boucher, O., Faluvegi, G., Fläschner, D., Iversen, T., Kasoar, M., Kharin, V., Kirkevag, A., Lamarque, J. F., Olivié, D., Richardson, T. B., Shindell, D., Shine, K. P., … Zwiers, F. (2017). PDRMIP: A precipitation driver and response model intercomparison project-protocol and preliminary results. *Bulletin of the American Meteorological Society*, *98*(6), 1185–1198. https://doi.org/10.1175/BAMS-D-16-0019.1

Myhre, G., Samset, B. H., Schulz, M., Balkanski, Y., Bauer, S., Berntsen, T. K., Bian, H., Bellouin, N., Chin, M., Diehl, T., Easter, R. C., Feichter, J., Ghan, S. J., Hauglustaine, D., Iversen, T., Kinne, S., Kirkeväg, A., Lamarque, J. F., Lin, G., … Zhou, C. (2013). Radiative forcing of the direct aerosol effect from AeroCom Phase II simulations. *Atmospheric Chemistry and Physics*, *13*(4), 1853–1877. https://doi.org/10.5194/acp-13-1853-2013

Myhre, G., Berglen, T. F., Myhre, C. E. L., & Isaksen, I. S. A. (2004). The radiative effect of the anthropogenic influence on the stratospheric sulfate aerosol layer. *Tellus B: Chemical and Physical Meteorology*, *56*(3), 294–299. https://doi.org/10.3402/tellusb.v56i3.16431

Nagano, A., & Wakita, M. (2019). Wind-driven decadal sea surface height and main pycnocline depth changes in the western subarctic North Pacific. *Progress in Earth and Planetary Science*, *6*(1), 1–26. https://doi.org/10.1186/s40645-019-0303-0

Neale, R. B., Chen, C., Lauritzen, P. H., Williamson, D. L., Conley, A. J., Smith, A. K., Mills, M., & Morrison, H. (2004). Description of the NCAR Community Atmosphere Model (CAM5.0). *Ncar/Tn-464+Str*, *June*, 214.

https://www.ccsm.ucar.edu/models/ccsm4.0/cam/docs/description/cam4_desc.pdf

Newman, M. (2007). Interannual to decadal predictability of tropical and North Pacific sea surface temperatures. *Journal of Climate*, *20*(11), 2333–2356. https://doi.org/10.1175/JCLI4165.1

Newman, M., Alexander, M. A., Ault, T. R., Cobb, K. M., Deser, C., Di Lorenzo, E., Mantua, N. J., Miller, A. J., Minobe, S., Nakamura, H., Schneider, N., Vimont, D. J., Phillips, A. S., Scott, J. D., & Smith, C. A. (2016). The Pacific decadal oscillation, revisited. *Journal of Climate*, *29*(12), 4399–4427. https://doi.org/10.1175/JCLI-D-15-0508.1

Newman, M., Compo, G. P., & Alexander, M. A. (2003). ENSO-forced variability of the Pacific decadal oscillation. In *Journal of Climate* (Vol. 16, Issue 23). https://doi.org/10.1175/1520-0442(2003)016<3853:EVOTPD>2.0.CO;2

Nguyen, H., Evans, A., Lucas, C., Smith, I., & Timbal, B. (2013). The hadley circulation in reanalyses: Climatology, variability, and Change. *Journal of Climate*, *26*(10), 3357–3376. https://doi.org/10.1175/JCLI-D-12-00224.1

Nidheesh, A. G., Lengaigne, M., Vialard, J., Izumo, T., Unnikrishnan, A. S., & Cassou, C. (2017). Influence of ENSO on the Pacific decadal oscillation in CMIP models. *Climate Dynamics*, *49*(9–10), 3309–3326. https://doi.org/10.1007/s00382-016-3514-8

Nonaka, M., Nakamura, H., Tanimoto, Y., Kagimoto, T., & Sasaki, H. (2005). Decadal Variability in the Kuroshio – Oyashio Extension Simulated in an. In *Journal of Climate* (Vol. 19). https://journals.ametsoc.org/doi/pdf/10.1175/JCLI3793.1

O'Callaghan, A., Joshi, M., … D. S.-G. R., & 2014, undefined. (2014). The effects of different sudden stratospheric warming types on the ocean. *Wiley Online Library*, *41*(21), 7739–7745. https://doi.org/10.1002/2014GL062179

Olonscheck, D., Rugenstein, M., & Marotzke, J. (2020). Broad Consistency Between Observed and Simulated Trends in Sea Surface Temperature Patterns. *Geophysical Research Letters*, *47*(10), e2019GL086773. https://doi.org/ 10.1029/ 2019GL086773

Orihuela-Pinto, B., England, M. H., & Taschetto, A. S. (2022). Interbasin and interhemispheric impacts of a collapsed Atlantic Overturning Circulation. *Nature Climate Change*, *12*(6), 558–565. https://doi.org/10.1038/s41558-022-01380-y

Osterberg, E. C., Winski, D. A., Kreutz, K. J., Wake, C. P., Ferris, D. G., Campbell, S., Introne, D., Handley, M., & Birkel, S. (2017). The 1200 year composite ice core record of Aleutian Low intensification. *Geophysical Research Letters*, *44*(14), 7447–7454. https://doi.org/10.1002/2017GL073697

Osterberg, E. C., Mayewski, P. A., Fisher, D. A., Kreutz, K. J., Maasch, K. A., Sneed, S. B., & Kelsey, E. (2014). Mount logan ice core record of tropical and solar influences on aleutian low variability: 500–1998 A.D. *Journal of Geophysical Research*, *119*(19), 11,189-11,204. https://doi.org/10.1002/2014JD021847

Otto-Bliesner, B. L., Brady, E. C., Fasullo, J., Jahn, A., Landrum, L., Stevenson, S., Rosenbloom, N., Mai, A., & Strand, G. (2016). Climate variability and change since 850 ce an ensemble approach with the community earth system model. *Bulletin of the American Meteorological Society*, *97*(5), 787–801. https://doi.org/10.1175/BAMS-D-14-00233.1

Oudar, T., Kushner, P. J., Fyfe, J. C., & Sigmond, M. (2018). No Impact of Anthropogenic Aerosols on Early 21st Century Global Temperature Trends in a Large Initial-Condition Ensemble. In *Geophysical Research Letters* (Vol. 45, Issue 17). https://doi.org/10.1029/2018GL078841

Overland, J. E., Adams, J. M., & Bond, N. A. (1999). Decadal variability of the Aleutian low and its relation to high-latitude circulation. *Journal of Climate*, *12*(5 II), 1542–1548. https://doi.org/10.1175/1520-0442(1999)012<1542:dvotal>2.0.co;2

Pachauri, R. K., Meyer, L., Hallegatte France, S., Bank, W., Hegerl, G., Brinkman, S., van Kesteren, L., Leprince-Ringuet, N., & van Boxmeer, F. (2014). Ottmar Edenhofer (Germany), Ismail Elgizouli (Sudan), Christopher B. Field (USA), Piers), Mark Howden (Australia). In *Ipcc*. Gian-Kasper Plattner. http://www.ipcc.ch.

Palmer, T., & Stevens, B. (2019). The scientific challenge of understanding and estimating climate change. In *Proceedings of the National Academy of Sciences of the United States of America* (Vol. 116, Issue 49, pp. 34390–34395). https://doi.org/10.1073/pnas.1906691116

Pan, X., Ichoku, C., Chin, M., Bian, H., Darmenov, A., Colarco, P., Ellison, L., Kucsera, T., Da Silva, A., Wang, J., Oda, T., & Cui, G. (2020). Six global biomass burning emission datasets: Intercomparison and application in one global aerosol model. *Atmospheric Chemistry and Physics*, *20*(2), 969–994. https://doi.org/10.5194/acp-20-969-2020

Papastefanou, C. (2006). Residence time of tropospheric aerosols in association with radioactive nuclides. *Applied Radiation and Isotopes*, *64*(1), 93–100. https://doi.org/10.1016/j.apradiso.2005.07.006

Peng, S., & Robinson, W. A. (2001). Relationships between atmospheric internal variability and the responses to an extratropical SST anomaly. *Journal of Climate*, *14*(13), 2943–2959. https://doi.org/10.1175/1520-0442(2001)014<2943:RBAIVA>2.0.CO;2

Philander, S. G. H., Gu, D., Halpern, D., Lambert, G., Lau, N. C., Li, T., & Pacanowski, R. C. (1996). Why the ITCZ is mostly north of the equator. *Journal of Climate*, *9*(12),2958–2972.https://doi.org/10.1175/1520-0442(1996)009<2958:WTIIMN>2.0.CO;2

Philander, S. G. H. (1983). El Niño Southern Oscillation phenomena. *Nature 1983 302:5906*, *302*(5906), 295–301. https://doi.org/10.1038/302295a0

Pickart, R. S., Moore, G. W. K., Macdonald, A. M., Renfrew, I. A., Walsh, J. E., & Kessler, W. S. (2009). Seasonal evolution of Aleutian low pressure systems: Implications for the North Pacific subpolar circulation. *Journal of Physical Oceanography*, *39*(6), 1317–1339. https://doi.org/10.1175/2008JPO3891.1

Pierce, D. W., Barnett, T. P., & Latif, M. (2000). Connections between the Pacific Ocean Tropics and midlatitudes on decadal timescales. *Journal of Climate*, *13*(6),1173–1194.https://doi.org/10.1175/1520-0442(2000)013<1173:CBTPOT>2.0.CO;2

Pinault, J. L. (2022). A Review of the Role of the Oceanic Rossby Waves in Climate Variability. *Journal of Marine Science and Engineering*, *10*(4). https://doi.org/10.3390/jmse10040493

Pinault, J. L. (2012). Global warming and rainfall oscillation in the 5-10 yr band in Western Europe and Eastern North America. *Climatic Change*, *114*(3–4), 621–650. https://doi.org/10.1007/s10584-012-0432-6

Pinault, J. L. (2018). Modulated response of subtropical gyres: Positive feedback loop, subharmonic modes, resonant solar and orbital forcing. *Journal of Marine Science and Engineering*, *6*(3), 107. https://doi.org/10.3390/JMSE6030107

Pinault, J. L. (2022). A Review of the Role of the Oceanic Rossby Waves in Climate Variability. In *Journal of Marine Science and Engineering* (Vol. 10, Issue 4, p. 493). Multidisciplinary Digital Publishing Institute. https://doi.org/ 10.3390/jmse10040493

Pinault, J. L. (2018). Regions subject to rainfall oscillation in the 5-10 year band. *Climate*, *6*(1), 2. https://doi.org/10.3390/cli6010002

Ping Chang, & Philander, S. G. (1994). A coupled ocean-atmosphere instability of relevance to the seasonal cycle. *Journal of the Atmospheric Sciences*, *51*(24), 3627–3648. https://doi.org/10.1175/1520-0469(1994)051<3627:acoior>2.0.co;2

Pohl, B., & Crétat, J. (2014). On the use of nudging techniques for regional climate modeling: Application for tropical convection. *Climate Dynamics*, *43*(5–6), 1693–1714. https://doi.org/10.1007/s00382-013-1994-3

Qin, M., Dai, A., & Hua, W. (2020). Aerosol-forced multidecadal variations across all ocean basins in models and observations since 1920. In *Science Advances* (Vol. 6, Issue 29). American Association for the Advancement of Science. https://doi.org/10.1126/sciadv.abb0425

Qiu, B. (2002). The Kuroshio Extension system: Its large-scale variability and role in the midlatitude ocean-atmosphere interaction. *Journal of Oceanography*, *58*(1), 57–75. https://doi.org/10.1023/A:1015824717293

Qiu, B. (2003). Kuroshio extension variability and forcing of the Pacific decadal oscillations: Responses and potential feedback. *Journal of Physical Oceanography*, *33*(12), 2465–2482. https://doi.org/10.1175/2459.1

Quaas, J., Jia, H., Smith, C., Albright, A. L., Aas, W., Bellouin, N., Boucher, O., Doutriaux-Boucher, M., Forster, P. M., Grosvenor, D., Jenkins, S., Klimont, Z., Loeb, N. G., Ma, X., Naik, V., Paulot, F., Stier, P., Wild, M., Myhre, G., & Schulz, M. (2022). Robust evidence for reversal of the trend in aerosol effective climate forcing. *Atmospheric Chemistry and Physics*, *22*(18), 12221–12239. https://doi.org/10.5194/acp-22-12221-2022

Ramana, M. V., Ramanathan, V., Feng, Y., Yoon, S. C., Kim, S. W., Carmichael, G. R., & Schauer, J. J. (2010). Warming influenced by the ratio of black carbon to sulphate and the black-carbon source. *Nature Geoscience*, *3*(8), 542–545. https://doi.org/10.1038/ngeo918

Ramanathan, V., Chung, C., Kim, D., Bettge, T., Buja, L., Kiehl, J. T., Washington, W. M., Fu, Q., Sikka, D. R., & Wild, M. (2005). Atmospheric brown clouds: Impacts on South Asian climate and hydrological cycle. *Proceedings of the National Academy of Sciences of the United States of America*, *102*(15), 5326–5333. https://doi.org/10.1073/pnas.0500656102

Rayner, N. A.; Parker, D. E.; Horton, E. B.; Folland, C. K.; Alexander, L. V.; Rowell, D. P.; Kent, E. C.; Kaplan, A. (2003) Global analyses of sea surface temperature, sea ice, and night marine air temperature since the late nineteenth century J. Geophys. Res.Vol. 108, No. D14, 4407 10.1029/2002JD002670 (pdf ~9Mb)

Reis, S., Grennfelt, P., Klimont, Z., Amann, M., ApSimon, H., Hettelingh, J. P., Holland, M., LeGall, A. C., Maas, R., Posch, M., Spranger, T., Sutton, M. A., & Williams, M. (2012). From acid rain to climate change. *Science*, *338*(6111), 1153–1154. https://doi.org/10.1126/SCIENCE.1226514/SUPPL_FILE/1226514.REIS.SM.PDF

Richardson, T. B., Forster, P. M., Andrews, T., Boucher, O., Faluvegi, G., Fläschner, D., Hodnebrog, Kasoar, M., Kirkevåg, A., Lamarque, J. F., Myhre, G., Olivié, D., Samset, B. H., Shawki, D., Shindell, D., Takemura, T., & Voulgarakis, A. (2018). Drivers of precipitation change: An energetic understanding. *Journal of Climate*, *31*(23), 9641–9657. https://doi.org/10.1175/JCLI-D-17-0240.1

Richardson, T. B., Forster, P. M., Smith, C. J., Maycock, A. C., Wood, T., Andrews, T., Boucher, O., Faluvegi, G., Fläschner, D., Hodnebrog, Ø., Kasoar, M., Kirkevåg, A., Lamarque, J. -F., Mülmenstädt, J., Myhre, G., Olivié, D., Portmann, R. W., Samset, B. H., Shawki, D., … Watson-Parris, D. (2019). Efficacy of Climate Forcings in PDRMIP Models. *Journal of Geophysical Research: Atmospheres*, *124*(23), 12824–12844. https://doi.org/10.1029/2019JD030581

Richter, J. H., Deser, C., & Sun, L. (2015). Effects of stratospheric variability on El Niñ. *Environmental Research Letters*, *10*(12). https://doi.org/10.1088/1748-9326/10/12/124021

Ridley, J. K., Blockley, E. W., Keen, A. B., Rae, J. G. L., West, A. E., & Schroeder, D. (2018). The sea ice model component of HadGEM3-GC3.1. *Geoscientific Model Development*, *11*(2), 713–723. https://doi.org/10.5194/gmd-11-713-2018

Riemer, N., Ault, A. P., West, M., Craig, R. L., & Curtis, J. H. (2019). Aerosol Mixing State: Measurements, Modeling, and Impacts. *Reviews of Geophysics*, *57*(2), 187–249. https://doi.org/10.1029/2018RG000615

Risbey, J. S., Lewandowsky, S., Langlais, C., Monselesan, D. P., O'Kane, T. J., & Oreskes, N. (2014). Well-estimated global surface warming in climate projections selected for ENSO phase. In *Nature Climate Change* (Vol. 4, Issue 9). https://doi.org/10.1038/nclimate2310

Rodionov, S. N., Overland, J. E., & Bond, N. A. (2005). The Aleutian low and winter climatic conditions in the Bering Sea. Part I: Classification. *Journal of Climate*, *18*(1), 160–177. https://doi.org/10.1175/JCLI3253.1

Rossby, C. G. (2020). Relation between variations in the intensity of the zonal circulation of the atmosphere and the displacements of the semi permanent centers of action. In *Journal of Marine Research* (Vol. 78, Issue 1, p. 41). https://ci.nii.ac.jp/naid/10025024081/

Rotstayn, L. D., & Lohmann, U. (2002). Tropical rainfall trends and the indirect aerosol effect. *Journal of Climate*, *15*(15), 2103–2116. https://doi.org/10.1175/1520-0442(2002)015<2103:TRTATI>2.0.CO;2

Sabine, C., Bala, G., Bopp, L., Brovkin, V., Canadell, J., Chhabra, A., DeFries, R., Galloway, J., Heimann, M., Jones, C., Le Quéré, C., Myneni, R., Piao, S., Thornton, P., Qin, D., Plattner, G., Tignor, M., Allen, S., Boschung, J., … Bala, G. (2013). Contribution of Working Group I to the Fifth Assessment Report of the Intergovernmental Panel on Climate Change Coordinating Lead Authors: Lead Authors. *Josep Canadell (Australia), Abha Chhabra*, 255–315.

Saha, S., Moorthi, S., Pan, H. L., Wu, X., Wang, J., Nadiga, S., Tripp, P., Kistler, R., Woollen, J., Behringer, D., Liu, H., Stokes, D., Grumbine, R., Gayno, G., Wang, J., Hou, Y. T., Chuang, H. Y., Juang, H. M. H., Sela, J., … Goldberg, M. (2010). The NCEP climate forecast system reanalysis. *Bulletin of the American Meteorological Society*, *91*(8), 1015–1057. https://doi.org/10.1175/2010BAMS3001.1

Samset, B. H., & Myhre, G. (2015). Climate response to externally mixed black carbon as a function of altitude. *Journal of Geophysical Research*, *120*(7), 2913–2927. https://doi.org/10.1002/2014JD022849

Samset, B. H., Myhre, G., Forster, P. M., Hodnebrog, Andrews, T., Faluvegi, G., Fläschner, D., Kasoar, M., Kharin, V., Kirkevåg, A., Lamarque, J. F., Olivié, D., Richardson, T., Shindell, D., Shine, K. P., Takemura, T., & Voulgarakis, A. (2016). Fast and slow precipitation responses to individual climate forcers: A PDRMIP multimodel study. *Geophysical Research Letters*, *43*(6), 2782–2791. https://doi.org/10.1002/2016GL068064

Samset, B. H., Myhre, G., Schulz, M., Balkanski, Y., Bauer, S., Berntsen, T. K., Bian, H., Bellouin, N., Diehl, T., Easter, R. C., Ghan, S. J., Iversen, T., Kinne, S., Kirkeväg, A., Lamarque, J. F., Lin, G., Liu, X., Penner, J. E., Seland, O., … Zhang, K. (2013). Black carbon vertical profiles strongly affect its radiative forcing uncertainty. *Atmospheric Chemistry and Physics*, *13*(5), 2423–2434. https://doi.org/10.5194/acp-13-2423-2013

Samset, B. H., Lund, M. T., Bollasina, M., Myhre, G., & Wilcox, L. (2019). Emerging Asian aerosol patterns. In *Nature Geoscience* (Vol. 12, Issue 8, pp. 582–584). Nature Publishing Group. https://doi.org/10.1038/s41561-019-0424-5

Samset, B. H., & Myhre, G. (2011). Vertical dependence of black carbon, sulphate and biomass burning aerosol radiative forcing. *Geophysical Research Letters*, *38*(24). https://doi.org/10.1029/2011GL049697

Samyn, D., Vega, C., Motoyama, H., & Pohjola, V. (2012). Nitrate and sulfate anthropogenic trends in the 20th century from five svalbard ice cores. In *Arctic, Antarctic, and Alpine Research* (Vol. 44, Issue 4, pp. 490–499). Taylor & Francis. https://doi.org/10.1657/1938-4246-44.4.490

Sardeshmukh, P. D., & Hoskins, B. J. (1988). The generation of global rotational flow by steady idealized tropical divergence. *Journal of the Atmospheric Sciences*, *45*(7),1228–1251.https://doi.org/10.1175/1520-0469(1988)045<1228:TGOGRF> 2.0.CO;2

Scaife, A. A., Comer, R. E., Dunstone, N. J., Knight, J. R., Smith, D. M., MacLachlan, C., Martin, N., Peterson, K. A., Rowlands, D., Carroll, E. B., Belcher, S., & Slingo, J. (2017). Tropical rainfall, Rossby waves and regional winter climate predictions. *Quarterly Journal of the Royal Meteorological Society*, *143*(702), 1–11. https://doi.org/10.1002/qj.2910

Schmidt, G. A., Kelley, M., Nazarenko, L., Ruedy, R., Russell, G. L., Aleinov, I., Bauer, M., Bauer, S. E., Bhat, M. K., Bleck, R., Canuto, V., Chen, Y. H., Cheng, Y., Clune, T. L., Del Genio, A., De Fainchtein, R., Faluvegi, G., Hansen, J. E., Healy, R. J., … Zhang, J. (2014). Configuration and assessment of the GISS ModelE2 contributions to the CMIP5 archive. *Journal of Advances in Modeling Earth Systems*, *6*(1), 141–184. https://doi.org/10.1002/2013MS000265

Schmidt, G. A., Ruedy, R., Hansen, J. E., Aleinov, I., Bell, N., Bauer, M., Bauer, S., Cairns, B., Canuto, V., Cheng, Y., Del Genio, A., Faluvegi, G., Friend, A. D., Hall, T. M., Hu, Y., Kelley, M., Kiang, N. Y., Koch, D., Lacis, A. A., … Yao, M. S. (2006). Present-day atmospheric simulations using GISS ModelE: Comparison to in situ, satellite, and reanalysis data. In *Journal of Climate* (Vol. 19, Issue 1, pp. 153–192). American Meteorological Society. https://doi.org/10.1175/JCLI3612.1

Schneider, N., & Cornuelle, B. D. (2005). The forcing of the Pacific Decadal Oscillation. *Journal of Climate*, *18*(21), 4355–4373. https://doi.org/10.1175/JCLI3527.1

Schneider, N., Miller, A. J., & Pierce, D. W. (2002). Anatomy of North Pacific decadal variability. In *Journal of Climate* (Vol. 15, Issue 6). https://doi.org/10.1175/1520-0442(2002)015<0586:AONPDV>2.0.CO;2

Seager, R., Kushnir, Y., Naik, N. H., Cane, M. A., & Miller, J. (2001). Wind-driven shifts in the latitude of the Kuroshio-Oyashio extension and generation of SST anomalies on decadal timescales. *Journal of Climate*, *14*(22), 4249–4265. https://doi.org/10.1175/1520-0442(2001)014<4249:WDSITL>2.0.CO;2

Seager, R., Henderson, N., & Cane, M. (2022). Persistent Discrepancies between Observed and Modeled Trends in the Tropical Pacific Ocean. *Journal of Climate*, *35*(14), 4571–4584. https://doi.org/10.1175/JCLI-D-21-0648.1

Seager, R., Ting, M., Held, I., Kushnir, Y., Lu, J., Vecchi, G., Huang, H. P., Harnik, N., Leetmaa, A., Lau, N. C., Li, C., Velez, J., & Naik, N. (2007). Model projections of an imminent transition to a more arid climate in southwestern North America. *Science*, *316*(5828), 1181–1184. https://doi.org/10.1126/science.1139601

Sen Roy, S. (2006). The impacts of ENSO, PDO, and local SSTS on winter precipitation in India. *Physical Geography*, *27*(5), 464–474. https://doi.org/10.2747/0272-3646.27.5.464

Shaffrey, L. C., Stevens, I., Norton, W. A., Roberts, M. J., Vidale, P. L., Harle, J. D., Jrrar, A., Stevens, D. P., Woodage, M. J., Demory, M. E., Donners, J., Clark, D.

B., Clayton, A., Cole, J. W., Wilson, S. S., Connolley, W. M., Davies, T. M., Iwi, A. M., Johns, T. C., … Martin, G. M. (2009). U.K. HiGEM: The new U.K. high-resolution global environment model - Model description and basic evaluation. *Journal of Climate*, *22*(8), 1861–1896. https://doi.org/10.1175/2008JCLI2508.1

Sherman, P., Gao, M., Song, S., Archibald, A. T., Luke Abraham, N., Lamarque, J. F., Shindell, D., Faluvegi, G., & McElroy, M. B. (2021). Sensitivity of modeled Indian monsoon to Chinese and Indian aerosol emissions. *Atmospheric Chemistry and Physics*, *21*(5), 3593–3605. https://doi.org/10.5194/ACP-21-3593-2021

Shindell, D. T., Voulgarakis, A., Faluvegi, G., & Milly, G. (2012). Precipitation response to regional radiative forcing. *Atmospheric Chemistry and Physics*, *12*(15), 6969–6982. https://doi.org/10.5194/acp-12-6969-2012

Simon, A., Gastineau, G., Frankignoul, C., Rousset, C., & Codron, F. (2021). Transient climate response to Arctic Sea ice loss with two ice-constraining methods. *Journal of Climate*, *34*(9), 3295–3310. https://doi.org/10.1175/JCLI-D-20-0288.1

Smirnov, D., Newman, M., & Alexander, M. A. (2014). Investigating the role of ocean-atmosphere coupling in the North Pacific ocean. *Journal of Climate*, *27*(2), 592–606. https://doi.org/10.1175/JCLI-D-13-00123.1

Smith, A., & Jahn, A. (2019). Definition differences and internal variability affect the simulated Arctic sea ice melt season. *Cryosphere*, *13*(1), 1–20. https://doi.org/10.5194/tc-13-1-2019

Smith, D. M., Booth, B. B. B., Dunstone, N. J., Eade, R., Hermanson, L., Jones, G. S., Scaife, A. A., Sheen, K. L., & Thompson, V. (2016). Role of volcanic and anthropogenic aerosols in the recent global surface warming slowdown. *Nature Climate Change*, *6*(10), 936–940. https://doi.org/10.1038/nclimate3058

Smith, S. J., & Andres, R. (2004). Historical Sulfur Dioxide Emissions 1850-2000 : Methods and Results. *Methods*, *January*. http://www.ntis.gov/ordering.htm

Smith, S. J., Van Aardenne, J., Klimont, Z., Andres, R. J., Volke, A., & Delgado Arias, S. (2011). Anthropogenic sulfur dioxide emissions: 1850-2005. *Atmospheric Chemistry and Physics*, *11*(3), 1101–1116. https://doi.org/10.5194/acp-11-1101-2011

Song, F., Zhou, T., & Qian, Y. (2014). Responses of East Asian summer monsoon to natural and anthropogenic forcings in the 17 latest CMIP5 models. *Geophysical Research Letters*, *41*(2), 596–603. https://doi.org/10.1002/2013GL058705

Sprintall, J., Cravatte, S., Dewitte, B., Du, Y., & Gupta, A. Sen. (2020). ENSO Oceanic Teleconnections. In *Geophysical Monograph Series* (Vol. 253, pp. 337–357). American Geophysical Union (AGU). https://doi.org/10.1002/9781119548164.ch15

Stan, C., Straus, D. M., Frederiksen, J. S., Lin, H., Maloney, E. D., & Schumacher, C. (2017). Review of Tropical-Extratropical Teleconnections on Intraseasonal Time Scales. In *Reviews of Geophysics* (Vol. 55, Issue 4, pp. 902–937). John Wiley & Sons, Ltd. https://doi.org/10.1002/2016RG000538

Stephenson, D. B., Hannachi, A., & O'Niell, A. (2004). On the existence of multiple climate regimes. *Quarterly Journal of the Royal Meteorological Society*, *130*(597 PART B), 583–605. https://doi.org/10.1256/qj.02.146

Stjern, C. W., Samset, B. H., Myhre, G., Forster, P. M., Hodnebrog, Ø., Andrews, T., Boucher, O., Faluvegi, G., Iversen, T., Kasoar, M., Kharin, V., Kirkevåg, A., Lamarque, J.-F., Olivié, D., Richardson, T., Shawki, D., Shindell, D., Smith, C. J., Takemura, T., & Voulgarakis, A. (2017). Rapid Adjustments Cause Weak Surface Temperature Response to Increased Black Carbon Concentrations. *Journal of Geophysical Research: Atmospheres*, *122*(21), 11,462-11,481. https://doi.org/10.1002/2017JD027326

Stohl, A., & Sodemann, H. (2010). Characteristics of atmospheric transport into the Antarctic troposphere. *Journal of Geophysical Research Atmospheres*, *115*(D2), 1–16. https://doi.org/10.1029/2009JD012536

Straus, D. M., & Shukla, J. (2002). Does ENSO force the PNA? In *Journal of Climate* (Vol. 15, Issue 17). https://doi.org/10.1175/1520-0442(2002)015<2340:DEFTP>2.0.CO;2

Suarez-Gutierrez, L., Li, C., Müller, W. A., & Marotzke, J. (2018). Internal variability in European summer temperatures at 1.5 °c and 2 °c of global warming. *Environmental Research Letters*, *13*(6), 064026. https://doi.org/10.1088/1748-9326/aaba58

Sugimoto, S., & Hanawa, K. (2009). Decadal and interdecadal variations of the Aleutian Low activity and their relation to upper oceanic variations over the North

Pacific. *Journal of the Meteorological Society of Japan*, *87*(4), 601–614. https://doi.org/10.2151/jmsj.87.601

Sun, J., & Wang, H. (2006). Relationship between Arctic Oscillation and Pacific Decadal Oscillation on decadal timescale. *Chinese Science Bulletin*, *51*(1), 75–79. https://doi.org/10.1007/s11434-004-0221-3

Sun, T., & Okumura, Y. M. (2019). Role of stochastic atmospheric forcing from the south and North Pacific in tropical Pacific decadal variability. *Journal of Climate*, *32*(13), 4013–4038. https://doi.org/10.1175/JCLI-D-18-0536.1

Szopa, S., V. Naik, B. Adhikary, P. Artaxo, T. Berntsen, W.D. Collins, S. Fuzzi, L. Gallardo, A. Kiendler-Scharr, Z. Klimont, H. Liao, N. Unger, and P. Zanis, 2021: Short-Lived Climate Forcers. In Climate Change 2021: The Physical Science Basis. Contribution of Working Group I to the Sixth Assessment Report of the Intergovernmental Panel on Climate Change [Masson-Delmotte, V., P. Zhai, A. Pirani, S.L. Connors, C. Péan, S. Berger, N. Caud, Y. Chen, L. Goldfarb, M.I. Gomis, M. Huang, K. Leitzell, E. Lonnoy, J.B.R. Matthews, T.K. Maycock, T. Waterfield, O. Yelekçi, R. Yu, and B. Zhou (eds.)]. Cambridge University Press, Cambridge, United Kingdom and New York, NY, USA, pp. 817–922, doi:10.1017/9781009157896.008.

Taguchi, B., Xie, S. P., Schneider, N., Nonaka, M., Sasaki, H., & Sasai, Y. (2007). Decadal variability of the Kuroshio Extension: Observations and an eddy-resolving model hindcast. *Journal of Climate*, *20*(11), 2357–2377. https://doi.org/10.1175/JCLI4142.1

Takahashi, C., & Watanabe, M. (2016). Pacific trade winds accelerated by aerosol forcing over the past two decades. *Nature Climate Change*, *6*(8), 768–772. https://doi.org/10.1038/nclimate2996

Takahashi, C., & Watanabe, M. (2016). Pacific trade winds accelerated by aerosol forcing over the past two decades. *Nature Climate Change*, *6*(8), 768–772. https://doi.org/10.1038/nclimate2996

Takemura, T., Egashira, M., Matsuzawa, K., Ichijo, H., O'Ishi, R., & Abe-Ouchi, A. (2009). A simulation of the global distribution and radiative forcing of soil dust aerosols at the Last Glacial Maximum. In *Atmospheric Chemistry and Physics* (Vol. 9, Issue 9). https://doi.org/10.5194/acp-9-3061-2009

Takemura, T., Nozawa, T., Emori, S., Nakajima, T. Y., & Nakajima, T. (2005). Simulation of climate response to aerosol direct and indirect effects with aerosol transport-radiation model. *Journal of Geophysical Research D: Atmospheres*, *110*(2), 1–16. https://doi.org/10.1029/2004JD005029

Takemura, T., & Suzuki, K. (2019). Weak global warming mitigation by reducing black carbon emissions. *Scientific Reports*, *9*(1), 1–6. https://doi.org/10.1038/s41598-019-41181-6

Tang, T., Shindell, D., Samset, B. H., Boucher, O., Forster, P. M., Hodnebrog, Ø., Myhre, G., Sillmann, J., Voulgarakis, A., Andrews, T., Faluvegi, G., Fläschner, D., Iversen, T., Kasoar, M., Kharin, V., Kirkeväg, A., Lamarque, J. F., Olivié, D., Richardson, T., … Takemura, T. (2018). Dynamical response of Mediterranean precipitation to greenhouse gases and aerosols. *Atmospheric Chemistry and Physics*, *18*(11), 8439–8452. https://doi.org/10.5194/ACP-18-8439-2018

Taylor, K. E., Stouffer, R. J., & Meehl, G. A. (2012). An overview of CMIP5 and the experiment design. In *Bulletin of the American Meteorological Society* (Vol. 93, Issue 4, pp. 485–498). https://doi.org/10.1175/BAMS-D-11-00094.1

Telford, P. J., Braesicke, P., Morgenstern, O., & Pyle, J. A. (2008). Technical note: Description and assessment of a nudged version of the new dynamics Unified Model. *Atmospheric Chemistry and Physics*, *8*(6), 1701–1712. https://doi.org/10.5194/acp-8-1701-2008

Teng, H., Washington, W. M., Branstator, G., Meehl, G. A., & Lamarque, J. F. (2012). Potential impacts of Asian carbon aerosols on future US warming. *Geophysical Research Letters*, *39*(11), n/a-n/a. https://doi.org/10.1029/2012GL051723

Ting, M. (1994). Maintenance of Northern Summer Stationary Waves in a GCM. *Journal of the Atmospheric Sciences*, *51*(22), 3286–3308. https://doi.org /10.1175/ 1520-0469(1994)051 <3286:monssw>2.0.co;2

Tourre, Y. M., Kushnir, Y., & White, W. B. (1999). Evolution of interdecadal variability in sea level pressure, sea surface temperature, and upper ocean temperature over the Pacific Ocean. *Journal of Physical Oceanography*, *29*(7), 1528–1541. https://doi.org/10.1175/1520-0485(1999)029<1528:EOIVIS>2.0.CO;2

Trenberth, K. E., Branstator, G. W., Karoly, D., Kumar, A., Lau, N.-C., & Ropelewski, C. (1998). Progress during TOGA in understanding and modeling global teleconnections associated with tropical sea surface temperatures. In *Journal of*

Geophysical Research: Oceans (Vol. 103, Issue C7). https://doi.org/10.1029/97jc01444

Trenberth, K. E., Fasullo, J. T., Branstator, G., & Phillips, A. S. (2014). Seasonal aspects of the recent pause in surface warming. *Nature Climate Change*, *4*(10), 911–916. https://doi.org/10.1038/nclimate2341

Trenberth, K. E., & Hoar, T. J. (1996). The 1990-1995 El Niño-Southern Oscillation event: Longest on record. *Geophysical Research Letters*, *23*(1), 57–60. https://doi.org/10.1029/95GL03602

Trenberth, K. E., & Hurrell, J. W. (1994). Decadal atmosphere-ocean variations in the Pacific. *Climate Dynamics*, *9*(6), 303–319. https://doi.org/10.1007/BF00204745

Tung, K. K., Chen, X., Zhou, J., & Li, K. F. (2018). Interdecadal variability in pan-Pacific and global SST, revisited. *Climate Dynamics*, *52*(3–4), 2145–2157. https://doi.org/10.1007/s00382-018-4240-1

Undorf, S., Bollasina, M. A., Booth, B. B. B., & Hegerl, G. C. (2018). Contrasting the Effects of the 1850–1975 Increase in Sulphate Aerosols from North America and Europe on the Atlantic in the CESM. *Geophysical Research Letters*, *45*(21), 11,930-11,940. https://doi.org/10.1029/2018GL079970

Undorf, S., Polson, D., Bollasina, M. A., Ming, Y., Schurer, A., & Hegerl, G. C. (2018). Detectable Impact of Local and Remote Anthropogenic Aerosols on the 20th Century Changes of West African and South Asian Monsoon Precipitation. *Journal of Geophysical Research: Atmospheres*, *123*(10), 4871–4889. https://doi.org/10.1029/2017JD027711

Verma, T., Saravanan, R., Chang, P., & Mahajan, S. (2019). Tropical Pacific Ocean Dynamical Response to Short-Term Sulfate Aerosol Forcing. *Journal of Climate*, *32*(23), 8205–8221. https://doi.org/10.1175/JCLI-D-19-0050.1

Vimont, D. J. (2005). The contribution of the interannual ENSO cycle to the spatial pattern of decadal ENSO-like variability. In *Journal of Climate* (Vol. 18, Issue 12). https://doi.org/10.1175/JCLI3365.1

Vimont, D. J., Battisti, D. S., & Hirst, A. C. (2001). Footprinting: A seasonal connection between the tropics and mid-latitudes. *Geophysical Research Letters*, *28*(20), 3923–3926. https://doi.org/10.1029/2001GL013435

Vimont, D. J., Battisti, D. S., & Hirst, A. C. (2002). Pacific interannual and interdecadal equatorial variability in a 1000-Yr simulation of the CSIRO coupled general circulation model. *Journal of Climate*, *15*(2), 160–178. https://doi.org/10.1175/1520-0442(2002)015<0160:PIAIEV>2.0.CO;2

Vimont, D. J., Wallace, J. M., & Battisti, D. S. (2003). The seasonal footprinting mechanism in the Pacific: Implications for ENSO. *Journal of Climate*, *16*(16), 2668–2675.https://doi.org/10.1175/1520-0442(2003)016<2668:TSFMIT>2.0 .CO;2

Wallace, J. M., & Gutzler, D. S. (1981). Teleconnections in the geopotential height field during the Northern Hemisphere winter. *Monthly Weather Review*, *109*(4), 784–812. https://doi.org/10.1175/1520-0493(1981)109<0784:TITGHF>2.0.CO;2

Walters, D. N., Williams, K. D., Boutle, I. A., Bushell, A. C., Edwards, J. M., Field, P. R., Lock, A. P., Morcrette, C. J., Stratton, R. A., Wilkinson, J. M., Willett, M. R., Bellouin, N., Bodas-Salcedo, A., Brooks, M. E., Copsey, D., Earnshaw, P. D., Hardiman, S. C., Harris, C. M., Levine, R. C., … Vidale, P. L. (2014). The Met Office Unified Model Global Atmosphere 4.0 and JULES Global Land 4.0 configurations. *Geoscientific Model Development*, *7*(1), 361–386. https://doi.org/10.5194/gmd-7-361-2014

Wang, H., Easter, R. C., Rasch, P. J., Wang, M., Liu, X., Ghan, S. J., Qian, Y., Yoon, J.-H., Ma, P.-L., & Vinoj, V. (2013). Sensitivity of remote aerosol distributions to representation of cloud–aerosol interactions in a global climate model. *Geoscientific Model Development*, *6*(3), 765–782. https://doi.org/10.5194/gmd-6-765-2013

Wang, H., Kumar, A., Wang, W., & Xue, Y. (2012). Seasonality of the Pacific decadal oscillation. *Journal of Climate*, *25*(1), 25–38. https://doi.org/10.1175/ 2011JCLI4092.1

Wang, Y., Le, T., Chen, G., Yung, Y. L., Su, H., Seinfeld, J. H., & Jiang, J. H. (2020). Reduced European aerosol emissions suppress winter extremes over northern Eurasia. *Nature Climate Change*, *10*(3), 225–230. https://doi.org/10.1038/ s41558-020-0693-4

Wang, Y., Wang, M., Zhang, R., Ghan, S. J., Lin, Y., Hu, J., Pan, B., Levy, M., Jiang, J. H., & Molina, M. J. (2014). Assessing the effects of anthropogenic aerosols on Pacific storm track using a multiscale global climate model. *Proceedings of the*

National Academy of Sciences of the United States of America, *111*(19), 6894–6899. https://doi.org/10.1073/pnas.1403364111

Watanabe, M., Kamae, Y., Yoshimori, M., Oka, A., Sato, M., Ishii, M., Mochizuki, T., & Kimoto, M. (2013). Strengthening of ocean heat uptake efficiency associated with the recent climate hiatus. *Geophysical Research Letters*, *40*(12), 3175–3179. https://doi.org/10.1002/grl.50541

Watanabe, M., Shiogama, H., Tatebe, H., Hayashi, M., Ishii, M., & Kimoto, M. (2014). Contribution of natural decadal variability to global warming acceleration and hiatus. *Nature Climate Change*, *4*(10), 893–897. https://doi.org/10.1038/nclimate2355

Watanabe, M., Suzuki, T., O'Ishi, R., Komuro, Y., Watanabe, S., Emori, S., Takemura, T., Chikira, M., Ogura, T., Sekiguchi, M., Takata, K., Yamazaki, D., Yokohata, T., Nozawa, T., Hasumi, H., Tatebe, H., & Kimoto, M. (2010). Improved climate simulation by MIROC5: Mean states, variability, and climate sensitivity. *Journal of Climate*, *23*(23), 6312–6335. https://doi.org/10.1175/2010JCLI3679.1

Watson, P. A. G., Weisheimer, A., Knight, J. R., & Palmer, T. N. (2016). The role of the tropical West Pacific in the extreme Northern Hemisphere winter of 2013/2014. *Journal of Geophysical Research*, *121*(4), 1698–1714. https://doi.org/10.1002/2015JD024048

Weare, B. C., Navato, A. R., & Newell, R. E. (1976). Empirical Orthogonal Analysis of Pacific Sea Surface Temperatures. *Journal of Physical Oceanography*, *6*(5), 671–678. https://doi.org/10.1175/1520-0485(1976)006<0671:eoaops>2.0.co;2

Webb, D. J. (1996). An ocean model code for array processor computers. *Computers and Geosciences*, *22*(5), 569–578. https://doi.org/10.1016/0098-3004(95)00133-6

Wei, Y., Yu, H., Huang, J., He, Y., Yang, B., Guan, X., & Liu, X. (2018). Comparison of the Pacific Decadal Oscillation in climate model simulations and observations. *International Journal of Climatology*, *38*, e99–e118. https://doi.org/10.1002/joc.5355

Westervelt, D. M., Horowitz, L. W., Naik, V., Golaz, J. C., & Mauzerall, D. L. (2015). Radiative forcing and climate response to projected 21st century aerosol decreases. *Atmospheric Chemistry and Physics*, *15*(22), 12681–12703. https://doi.org/10.5194/acp-15-12681-2015

Wilcox, L., Dunstone, N., Lewinschal, A., Bollasina, M., Ekman, A., & Highwood, E. (2019). Mechanisms for a remote response to Asian anthropogenic aerosol in boreal winter. *Atmospheric Chemistry and Physics*, *19*(14), 9081–9095. https://doi.org/10.5194/acp-19-9081-2019

Wills, R. C. J., Dong, Y., Proistosecu, C., Armour, K. C., & Battisti, D. S. (2022). Systematic Climate Model Biases in the Large-Scale Patterns of Recent Sea-Surface Temperature and Sea-Level Pressure Change. *Geophysical Research Letters*, *49*(17), e2022GL100011. https://doi.org/10.1029/2022GL100011

Wills, R. C. J., Battisti, D. S., Proistosescu, C., Thompson, L. A., Hartmann, D. L., & Armour, K. C. (2019). Ocean Circulation Signatures of North Pacific Decadal Variability. *Geophysical Research Letters*, *46*(3), 1690–1701. https://doi.org/10.1029/2018GL080716

Wills, R. C. J., White, R. H., & Levine, X. J. (2019). Northern Hemisphere Stationary Waves in a Changing Climate. *Current Climate Change Reports*, *5*(4), 372–389. https://doi.org/10.1007/s40641-019-00147-6

Wood, T., McKenna, C. M., Chrysanthou, A., & Maycock, A. C. (2020). Role of sea surface temperature patterns for the Southern Hemisphere jet stream response to CO2forcing. *Environmental Research Letters*, *16*(1). https://doi.org/10.1088/1748-9326/abce27

World Meteorological Organization (WMO). (2021). *FAQs - Climate | World Meteorological Organization*. https://public.wmo.int/en/about-us/frequently-asked-questions/climate

Wu, Z., Huang, N. E., Wallace, J. M., Smoliak, B. V., & Chen, X. (2011). On the time-varying trend in global-mean surface temperature. *Climate Dynamics*, *37*(3), 759–773. https://doi.org/10.1007/s00382-011-1128-8

Xie, S. P., Deser, C., Vecchi, G. A., Collins, M., Delworth, T. L., Hall, A., Hawkins, E., Johnson, N. C., Cassou, C., Giannini, A., & Watanabe, M. (2015). Towards predictive understanding of regional climate change. *Nature Climate Change*, *5*(10), 921–930. https://doi.org/10.1038/nclimate2689

Xie, S. P., & Tanimoto, Y. (1998). A pan-Atlantic decadal climate oscillation. *Geophysical Research Letters*, *25*(12), 2185–2188. https://doi.org/10.1029/98GL01525

Xie, S.-P. (2004). *The Shape of Continents, Air-Sea Interaction, and the Rising Branch of the Hadley Circulation*. 121–152. https://doi.org/10.1007/978-1-4020-2944-8_5

XIE, S. -PING, & PHILANDER, S. G. H. (1994). A coupled ocean-atmosphere model of relevance to the ITCZ in the eastern Pacific. *Tellus A*, *46*(4), 340–350. https://doi.org/10.1034/j.1600-0870.1994.t01-1-00001.x

Xu, B., Cao, J., Hansen, J., Yao, T., Joswia, D. R., Wang, N., Wu, G., Wang, M., Zhao, H., Yang, W., Liu, X., & He, J. (2009). Black soot and the survival of Tibetan glaciers. *Proceedings of the National Academy of Sciences of the United States of America*, *106*(52), 22114–22118. https://doi.org/10.1073/pnas.0910444106

Yan, H., Zhu, Z., Wang, B., Zhang, K., Luo, J., Qian, Y., & Jiang, Y. (2021). Tropical African wildfire aerosols trigger teleconnections over mid-to-high latitudes of Northern Hemisphere in January. *Environmental Research Letters*, *16*(3). https://doi.org/10.1088/1748-9326/abe433

Yang, Y., Smith, S. J., Wang, H., Lou, S., & Rasch, P. J. (2019). Impact of Anthropogenic Emission Injection Height Uncertainty on Global Sulfur Dioxide and Aerosol Distribution. *Journal of Geophysical Research: Atmospheres*, *124*(8), 4812–4826. https://doi.org/10.1029/2018JD030001

Yeh, S. W., Cai, W., Min, S. K., McPhaden, M. J., Dommenget, D., Dewitte, B., Collins, M., Ashok, K., An, S. Il, Yim, B. Y., & Kug, J. S. (2018). ENSO Atmospheric Teleconnections and Their Response to Greenhouse Gas Forcing. *Reviews of Geophysics*, *56*(1), 185–206. https://doi.org/10.1002/2017RG000568

Yu, B., Zhang, X., Li, G., & Yu, W. (2022). Interhemispheric asymmetry of climate change projections of boreal winter surface winds in CanESM5 large ensemble simulations. *Climatic Change*, *170*(3–4), 1–20. https://doi.org/10.1007/s10584-022-03313-2

Zelinka, M. D., Andrews, T., Forster, P. M., & Taylor, K. E. (2014). Quantifying components of aerosol-cloud-radiation interactions in climate models. *Journal of Geophysical Research: Atmospheres*, *119*(12), 7599–7615. https://doi.org/10.1002/2014JD021710

Zhang, C. (2005). Madden-Julian Oscillation. In *Reviews of Geophysics* (Vol. 43, Issue 2, pp. 1–36). https://doi.org/10.1029/2004RG000158

Zhang, D., & McPhaden, M. J. (2006). Decadal variability of the shallow Pacific meridional overturning circulation: Relation to tropical sea surface temperatures in observations and climate change models. *Ocean Modelling*, *15*(3–4), 250–273. https://doi.org/10.1016/j.ocemod.2005.12.005

Zhang, H., Zhao, S., Wang, Z., Zhang, X., & Song, L. (2016). The updated effective radiative forcing of major anthropogenic aerosols and their effects on global climate at present and in the future. *International Journal of Climatology*, *36*(12), 4029–4044. https://doi.org/10.1002/joc.4613

Zhang, J., Liu, J., Tao, S., & Ban-Weiss, G. A. (2015). Long-range transport of black carbon to the Pacific Ocean and its dependence on aging timescale. *Atmos. Chem. Phys*, *15*, 11521–11535. https://doi.org/10.5194/acp-15-11521-2015

Zhang, K., O'Donnell, D., Kazil, J., Stier, P., Kinne, S., Lohmann, U., Ferrachat, S., Croft, B., Quaas, J., Wan, H., Rast, S., & Feichter, J. (2012). The global aerosol-climate model ECHAM-HAM, version 2: Sensitivity to improvements in process representations. *Atmospheric Chemistry and Physics*, *12*(19), 8911–8949. https://doi.org/10.5194/acp-12-8911-2012

Zhang, K., Wan, H., Liu, X., Ghan, S. J., Kooperman, G. J., Ma, P. L., Rasch, P. J., Neubauer, D., & Lohmann, U. (2014). Technical note: On the use of nudging for aerosol-climate model intercomparison studies. *Atmospheric Chemistry and Physics*, *14*(16), 8631–8645. https://doi.org/10.5194/acp-14-8631-2014

Zhang, L., & Delworth, T. L. (2016). Simulated Response of the pacific decadal oscillation to climate change. *Journal of Climate*, *29*(16), 5999–6018. https://doi.org/10.1175/JCLI-D-15-0690.1

Zhang, L., & Delworth, T. L. (2015). Analysis of the characteristics and mechanisms of the pacific decadal oscillation in a suite of coupled models from the geophysical fluid dynamics laboratory. *Journal of Climate*, *28*(19), 7678–7701. https://doi.org/10.1175/JCLI-D-14-00647.1

Zhang, Y., Xie, S. P., Kosaka, Y., & Yang, J. C. (2018). Pacific decadal oscillation: Tropical Pacific forcing versus internal variability. *Journal of Climate*, *31*(20), 8265–8279. https://doi.org/10.1175/JCLI-D-18-0164.1

Zhang, Y., Yu, S. Y., Amaya, D. J., Kosaka, Y., Stuecker, M. F., Yang, J. C., Lin, X., & Fan, L. (2022). Atmospheric Forcing of the Pacific Meridional Mode: Tropical

Pacific-Driven Versus Internal Variability. *Geophysical Research Letters*, *49*(7), e2022GL098148. https://doi.org/10.1029/2022GL098148

Zhao, S., & Suzuki, K. (2019). Differing impacts of black carbon and sulfate aerosols on global precipitation and the ITCZ location via atmosphere and ocean energy perturbations. *Journal of Climate*, *32*(17), 5567–5582. https://doi.org/10.1175/JCLI-D-18-0616.1

Zhao, Y., Newman, M., Capotondi, A., Lorenzo, E. Di, & Sun, D. (2021). Removing the effects of tropical dynamics from north pacific climate variability. *Journal of Climate*, *34*(23), 9249–9265. https://doi.org/10.1175/JCLI-D-21-0344.1

Zhong, Y., & Liu, Z. (2009). On the mechanism of Pacific multidecadal climate variability in CCSM3: The role of the subpolar North Pacific Ocean. *Journal of Physical Oceanography*, *39*(9), 2052–2076. https://doi.org/10.1175/2009JPO4097.1

Zhong, Y., Liu, Z., & Jacob, R. (2008). Origin of Pacific multidecadal variability in Community Climate System Model, Version 3 (CCSM3): A combined statistical and dynamical assessment. *Journal of Climate*, *21*(1), 114–133. https://doi.org/10.1175/2007JCLI1730.1

Zhu, Y., & Wang, H. (2010). The relationship between the aleutian low and the Australian summer monsoon at interannual time scales. *Advances in Atmospheric Sciences*, *27*(1), 177–184. https://doi.org/10.1007/s00376-009-8144-1

Appendix

Nudging code

```
#! /bin/ksh
set -xve
set +v
############################################## USER SWITCHES.

echo $SRCSTORE

RUNNAME=$1.igcm4
RPATH='/nobackup/eewjd/forte2_march5'
NUPDATE=yes               # Nupdate to a new code, or re-use
existing one

OROGRAPHY=cmip_tiling_arctic

SRCSTORE=$RPATH/source/igcm4/igcm4-forte-code/SRCSTORE
RUNSTORE=$RPATH/run_dirs/igcm4
COMPDIR=$RPATH/source/igcm4/compdir
EXPDIR=$RUNSTORE/$RUNNAME
OASISCLIMDIR=$RPATH/source/oasis/toyclim/wkdir.basic
ProgLib=$RPATH/source/igcm4/igcm_mpi.npl

###############################################
COMPILE=yes                    # Nupdate and compile (yes/no)
###############################################
OASISCLIMDIR=$RPATH/source/oasis/toyclim/wkdir.basic

NETCDF_ROOT=$NETCDF_HOME
NETCDFLIB=$NETCDF_ROOT/lib
NETCDFINC=$NETCDF_ROOT/include

PVM_ROOT=$RPATH/source/pvm3
PVM_ARCH=LINUX64
PVMLIB=$PVM_ROOT/lib/$PVM_ARCH

MPILIB=$MPI_HOME/lib
MPIINC=$MPI_HOME/include

###############################################
# Linux directories
KD=$RPATH/source/igcm4/kd # position of KD directory

CLIMDIR=$RPATH/source/igcm4/data/CLIMDATA/NEW
NUPDATE=$RPATH/source/igcm4/nupdate/nupdate
NUDGREF=$RPATH/source/igcm4/data/CLIMDATA/NEW/nudg/forte2_jun10_
input_jun5mask_y163_tr_sc
OROGDIR=$RPATH/source/igcm4/data/OROG
INIDATA=$RPATH/source/igcm4/data

EXEC=L20-$RUNNAME         # Name of the executable
#                         # to be created if COMPILE=yes

############################################## UPDATE DIRECTIVES.
```

```
#
[ ! -d $EXPDIR ]   &&   mkdir -p $EXPDIR
cd $COMPDIR
[ ! -d $EXPDIR/climdata ]   &&   mkdir -p $EXPDIR/climdata
cat  <<  /EOF  >  updates
*READ ${SRCSTORE}/T42L20-m.upd
*READ ${SRCSTORE}/forte/T42-runoff-real_snow_ice-m.upd
*READ ${SRCSTORE}/forte/T42-av-accumulate-tile-m.upd
*READ ${SRCSTORE}/morcrette3_1_1_swv-m.upd
*READ ${SRCSTORE}/igcm_radclouds_sebal_2012-m.upd
*READ ${SRCSTORE}/forte/T42L20-forte-m.upd
*READ ${SRCSTORE}/forte/surfacetype2012-forte-m.upd
*READ ${SRCSTORE}/forte/T42-common_tile-m.upd
*READ ${SRCSTORE}/forte/T42-tiling-m.upd
*READ ${SRCSTORE}/forte/runscript-m.upd
*READ ${SRCSTORE}/forte/T42-oasis-m.upd
*READ ${SRCSTORE}/forte/oasis-backend-m.upd
*READ ${SRCSTORE}/forte/T42L20_misc_common.upd
*IDENT T42IGCM4
*DEF ABOVE_V1,ONLY_V3
*/
*/ T42L20 topography, vegetation and ocean heatflux
*/
*D PARAM1.8
      INTEGER, PARAMETER :: NHEM=2
*D PARAM1.11
      INTEGER, PARAMETER :: MM=42
*D PARAM1.16
      INTEGER, PARAMETER :: NL=20
*D PARAM1.18
      INTEGER, PARAMETER :: MG=128
*D PARAM1.21
      INTEGER, PARAMETER :: JG=32
*D PARAM1.24
      INTEGER, PARAMETER :: NTRAC=1
*D PARAM1.35,36
      INTEGER, PARAMETER :: NWJ2=462
*D PARAM1.47
      INTEGER, PARAMETER :: npe=32
*D PARAM1.50
      INTEGER, PARAMETER :: NLEVRF=3
*D PARAM3.12
      INTEGER, PARAMETER :: Px=8
/EOF
# Updates for spinup executable
cp updates updates_spin
cat  <<  /EOF  >>  updates_spin
*READ ${SRCSTORE}/chg_read_nl.upd
*READ ${SRCSTORE}/forte/spinup-forte-m.upd
/EOF

# Updates for continuation executable
cp updates updates_cont
cat  <<  /EOF  >>  updates_cont
*READ ${SRCSTORE}/forte/restart-forte-m.upd

*/ =====================================
*/ NUDGING EDITS
*/ =====================================
```

```
*/
*/ ---------------------------------------
*/ Add ININDG
*/ Initialises nudging reference state
*/ ---------------------------------------
*/
*/ --- Add required parameters for nudging ---
*/
*I GRIDPA3.46
      REAL :: FPLG3(MGx,NHEM,JGy)

*D GRIDPA3.14
     & ,TRAG3,FPLG3,TRANLG3

*I OUTCON.42
      REAL :: DNUDG(NL)
      REAL :: SPNUDG
      REAL :: DNDMAX
      REAL :: KNUDG(NL)
      REAL :: KMX
      REAL :: KMN
      REAL :: TAUND

      !wd edits
      COMPLEX :: UNDGI2(NL,MGx,NHEM,JGy)
      COMPLEX :: UNDGI3(NL,MGx,NHEM,JGy)
      COMPLEX :: UNDGJ2(NL,MGx,NHEM,JGy)
      COMPLEX :: UNDGJ3(NL,MGx,NHEM,JGy)

      COMPLEX :: VNDGI2(NL,MGx,NHEM,JGy)
      COMPLEX :: VNDGI3(NL,MGx,NHEM,JGy)
      COMPLEX :: VNDGJ2(NL,MGx,NHEM,JGy)
      COMPLEX :: VNDGJ3(NL,MGx,NHEM,JGy)

      COMPLEX :: TNDGI2(NL,MGx,NHEM,JGy)
      COMPLEX :: TNDGI3(NL,MGx,NHEM,JGy)
      COMPLEX :: TNDGJ2(NL,MGx,NHEM,JGy)
      COMPLEX :: TNDGJ3(NL,MGx,NHEM,JGy)

      COMPLEX :: SPNDGI2(1,MGx,NHEM,JGy)
      COMPLEX :: SPNDGI3(1,MGx,NHEM,JGy)
      COMPLEX :: SPNDGJ2(1,MGx,NHEM,JGy)
      COMPLEX :: SPNDGJ3(1,MGx,NHEM,JGy)

      COMPLEX :: DUMNDGI2(NL,MGx,NHEM,JGy)
      COMPLEX :: DUMNDGI3(NL,MGx,NHEM,JGy)
      COMPLEX :: DUMNDGJ2(NL,MGx,NHEM,JGy)
      COMPLEX :: DUMNDGJ3(NL,MGx,NHEM,JGy)

      COMPLEX :: TIMERAMPNDGI2(NL,MGx,NHEM,JGy)
      COMPLEX :: TIMERAMPNDGI3(NL,MGx,NHEM,JGy)
      COMPLEX :: TIMERAMPNDGJ2(NL,MGx,NHEM,JGy)
      COMPLEX :: TIMERAMPNDGJ3(NL,MGx,NHEM,JGy)


      LOGICAL :: LNUDG
      LOGICAL :: LNDCYC
      LOGICAL :: LNUDGGP
*/
```

```
*/ --- Now call ININDG in initialisation subroutine ---
*/ --- INITAL and add ININDG subroutine code ---
*/
*I INITAL.62
      CALL ININDG
*DECK ININDG
!=====================================================
! Initialises nudging reference state
!=====================================================

      SUBROUTINE ININDG
      IMPLICIT NONE
!
*CALL PARAM1
*CALL PARAM2
*CALL PARAM3
*CALL BLANK
*CALL MPIDECK
*CALL BATS
*CALL RESTOR
*CALL OUTCON
*CALL LEGAU
!-----------------------------------------------------
! Local variables
!-----------------------------------------------------
! Loop variable
      INTEGER :: iCol2,L,IHEM,J,iRow2,iPe,IN,IM,I,JH
      INTEGER :: countLHEM,countHEM,countJ
! MPI variables
      INTEGER, PARAMETER :: TagRef=100000
      INTEGER, PARAMETER :: TagRefJ=100001
      INTEGER(KIND=Type) :: iTagJ
! Nudging variables
      REAL :: RDAY
      REAL :: KTND
      REAL :: RNT1,RNT2
      REAL :: DOYC
      REAL :: BEGDOY1
      character*3 :: bday
      character*31 :: UA10,VA10,T10,SP10
      character*31 :: UA11,VA11,T11,SP11
      character*31 :: UA20,VA20,T20,SP20
      character*31 :: UA21,VA21,T21,SP21

      REAL :: uan10(NL,MGx,NHEM,JGy)
      REAL :: uan11(NL,MGx,NHEM,JGy)
      REAL :: uan20(NL,MGx,NHEM,JGy)
      REAL :: uan21(NL,MGx,NHEM,JGy)

      REAL :: van10(NL,MGx,NHEM,JGy)
      REAL :: van11(NL,MGx,NHEM,JGy)
      REAL :: van20(NL,MGx,NHEM,JGy)
      REAL :: van21(NL,MGx,NHEM,JGy)

      REAL :: tn10(NL,MGx,NHEM,JGy)
      REAL :: tn11(NL,MGx,NHEM,JGy)
      REAL :: tn20(NL,MGx,NHEM,JGy)
      REAL :: tn21(NL,MGx,NHEM,JGy)
```

```
      REAL :: spn10(1,MGx,NHEM,JGy)
      REAL :: spn11(1,MGx,NHEM,JGy)
      REAL :: spn20(1,MGx,NHEM,JGy)
      REAL :: spn21(1,MGx,NHEM,JGy)

      character*31 :: DUM10
      character*31 :: DUM11
      character*31 :: DUM20
      character*31 :: DUM21
      REAL :: dumn10(NL,MGx,NHEM,JGy)
      REAL :: dumn11(NL,MGx,NHEM,JGy)
      REAL :: dumn20(NL,MGx,NHEM,JGy)
      REAL :: dumn21(NL,MGx,NHEM,JGy)

      character*31 :: TIMERAMP10
      character*31 :: TIMERAMP11
      character*31 :: TIMERAMP20
      character*31 :: TIMERAMP21
      REAL :: timerampn10(NL,MGx,NHEM,JGy)
      REAL :: timerampn11(NL,MGx,NHEM,JGy)
      REAL :: timerampn20(NL,MGx,NHEM,JGy)
      REAL :: timerampn21(NL,MGx,NHEM,JGy)


!-----------------------------------------------------
  203 FORMAT(15F12.2)
      NAMELIST/INNUDG/
LNUDG,LNDCYC,LNUDGGP,KINND,DNUDG,SPNUDG,DNDMAX
     +                  ,KNUDG,KMX,KMN,TAUND
      !-------------------------------------------------------------
--------
      !-------------------------------------------------------------
--------
      ! Variables are set on PE 0 and then passed to the other
PEs
      !-------------------------------------------------------------
--------
      !!!MYPE.EQ.0-
      IF (MYPE.EQ.0) THEN
       !-------------------------------------------------------------
--------
       !-------------------------------------------------------------
--------
       ! Set default values and override as desired through
       ! NAMELIST input
       !-------------------------------------------------------------
--------
       LNUDG=.FALSE.
       LNDCYC=.FALSE.
       LNUDGGP=.FALSE.
       KINND=-1
       SPNUDG=0.
       DNDMAX=-1.
       KMX=0.
       KMN=0.
       TAUND=0.
       ! Init these as 0:
       UNDGI2 = 0.
       UNDGI3 = 0.
```

```
       UNDGJ2 = 0.
       UNDGJ3 = 0.

       VNDGI2 = 0.
       VNDGI3 = 0.
       VNDGJ2 = 0.
       VNDGJ3 = 0.

       TNDGI2 = 0.
       TNDGI3 = 0.
       TNDGJ2 = 0.
       TNDGJ3 = 0.

       SPNDGI2 = 0.
       SPNDGI3 = 0.
       SPNDGJ2 = 0.
       SPNDGJ3 = 0.

       DUMNDGI2 = 0.
       DUMNDGI3=0.
       DUMNDGJ2 = 0.
       DUMNDGJ3 = 0.

       TIMERAMPNDGI2 = 0.
       TIMERAMPNDGI3=0.
       TIMERAMPNDGJ2 = 0.
       TIMERAMPNDGJ3 = 0.

       DO 31 L=1,NL
        DNUDG(L) = 0.
        KNUDG(L) = 0.
   31  CONTINUE
       !---------------------------------------------------------
--------
       ! Read NAMELISTs, overwrite defaults and write them out
       !---------------------------------------------------------
--------
       READ(7,INNUDG)
       WRITE(2,INNUDG)
       !---------------------------------------------------------
--------
       ! Set up nudging parameters if need be
       !---------------------------------------------------------
--------
       IF (LNUDGGP) THEN
        RDAY = WW/PI2
        KTND = (24./TAUND)*RDAY
        KNUDG = ((SIGMA) - KMN)/(KMX - KMN)
        DO 25 L=1,NL
         IF (KNUDG(L).LT.0.0) THEN
          KNUDG(L) = 0.0
         ELSE IF (KNUDG(L).GT.1.0) THEN
          KNUDG(L) = 1.0
         ENDIF
   25   CONTINUE
        DO 24 L=1,NL
         IF (KNUDG(L).GT.0.0) THEN
          DNUDG(L) = KTND*KNUDG(L)/WW
         ELSE
```

```
          DNUDG(L) = 0.0
         ENDIF

          PRINT *,'DNUDG(1)=',DNUDG(1)
          PRINT *,'DNUDG(2)=',DNUDG(2)
          PRINT *,'DNUDG(3)=',DNUDG(3)
          PRINT *,'DNUDG(4)=',DNUDG(4)
          PRINT *,'DNUDG(5)=',DNUDG(5)
          PRINT *,'DNUDG(6)=',DNUDG(6)
          PRINT *,'DNUDG(7)=',DNUDG(7)
          PRINT *,'DNUDG(8)=',DNUDG(8)
          PRINT *,'DNUDG(9)=',DNUDG(9)
          PRINT *,'DNUDG(10)=',DNUDG(10)
          PRINT *,'DNUDG(11)=',DNUDG(11)
          PRINT *,'DNUDG(12)=',DNUDG(12)
          PRINT *,'DNUDG(13)=',DNUDG(13)
          PRINT *,'DNUDG(14)=',DNUDG(14)
          PRINT *,'DNUDG(15)=',DNUDG(15)
          PRINT *,'DNUDG(16)=',DNUDG(16)
          PRINT *,'DNUDG(17)=',DNUDG(17)
          PRINT *,'DNUDG(18)=',DNUDG(18)
          PRINT *,'DNUDG(19)=',DNUDG(19)
          PRINT *,'DNUDG(20)=',DNUDG(20)



   24    CONTINUE
         SPNUDG=DNUDG(NL)
         WRITE(2,203) DNUDG
        ENDIF
       ENDIF
       !-------------------------------------------------------
--------
       ! Pass information from PE 0 to other PEs
       !-------------------------------------------------------
--------
       IF (NPE.GT.1) THEN
        iSend=0
        nBuffSize=1
        CALL MPI_BARRIER(MPI_COMM_WORLD,ierr)
        CALL MPI_BCAST(LNUDG,nBuffSize,ParaLog,iSend,
     &                 MPI_COMM_WORLD,ierr)
        CALL MPI_BCAST(LNDCYC,nBuffSize,ParaLog,iSend,
     &                 MPI_COMM_WORLD,ierr)
        CALL MPI_BCAST(LNUDGGP,nBuffSize,ParaLog,iSend,
     &                 MPI_COMM_WORLD,ierr)
        CALL MPI_BCAST(KINND,nBuffSize,ParaInt,iSend,
     &                 MPI_COMM_WORLD,ierr)
        CALL MPI_BCAST(SPNUDG,nBuffSize,ParaReal,iSend,
     &                 MPI_COMM_WORLD,ierr)
        CALL MPI_BCAST(DNDMAX,nBuffSize,ParaReal,iSend,
     &                 MPI_COMM_WORLD,ierr)
        nBuffSize=NL
        CALL MPI_BCAST(DNUDG,nBuffSize,ParaReal,iSend,
     &                 MPI_COMM_WORLD,ierr)
        CALL MPI_BARRIER(MPI_COMM_WORLD,ierr)
       ENDIF
       !-------------------------------------------------------
--------
```

```
      ! Read in grid-point nudging fields
      !-------------------------------------------------------
--------
      ! If a nudging run read in reference state
      ! to nudge towards
      !-------------------------------------------------------
--------
      IF (LNUDGGP) THEN
       !-------------------------------------------------------
--------
       ! Grid point nudging
       !-------------------------------------------------------
--------
       ! First two records are
       ! the BEGDOY and +1 (there are 360 records in total)
        WRITE(bday, '(i3)') NINT(BEGDOY)
        UA10='ua_d'//trim(adjustl(bday))//
     &                 '_0_dims.dat'
        UA11='ua_d'//trim(adjustl(bday))//
     &                 '_1_dims.dat'

        VA10='va_d'//trim(adjustl(bday))//
     &                 '_0_dims.dat'
        VA11='va_d'//trim(adjustl(bday))//
     &                 '_1_dims.dat'

        T10='temp_d'//trim(adjustl(bday))//
     &                 '_0_dims.dat'
        T11='temp_d'//trim(adjustl(bday))//
     &                 '_1_dims.dat'

        SP10='ps_d'//trim(adjustl(bday))//
     &                 '_0_dims.dat'
        SP11='ps_d'//trim(adjustl(bday))//
     &                 '_1_dims.dat'

        DUM10='dum_d'//trim(adjustl(bday))//
     &                 '_0_dims.dat'
        DUM11='dum_d'//trim(adjustl(bday))//
     &                 '_1_dims.dat'

        TIMERAMP10='dum_d'//trim(adjustl(bday))//
     &                  '_0_dims.dat'
        TIMERAMP11='dum_d'//trim(adjustl(bday))//
     &                  '_1_dims.dat'


        BEGDOY1=BEGDOY+1
        WRITE(bday, '(i3)') NINT(BEGDOY1)
        UA20='ua_d'//trim(adjustl(bday))//
     &                 '_0_dims.dat'
        UA21='ua_d'//trim(adjustl(bday))//
     &                 '_1_dims.dat'

        VA20='va_d'//trim(adjustl(bday))//
     &                 '_0_dims.dat'
        VA21='va_d'//trim(adjustl(bday))//
     &                 '_1_dims.dat'
```

```
        T20='temp_d'//trim(adjustl(bday))//
     &                 '_0_dims.dat'
        T21='temp_d'//trim(adjustl(bday))//
     &                 '_1_dims.dat'

        SP20='ps_d'//trim(adjustl(bday))//
     &                 '_0_dims.dat'
        SP21='ps_d'//trim(adjustl(bday))//
     &                 '_1_dims.dat'

        DUM20='dum_d'//trim(adjustl(bday))//
     &                 '_0_dims.dat'
        DUM21='dum_d'//trim(adjustl(bday))//
     &                 '_1_dims.dat'

        TIMERAMP20='timeramp_d'//trim(adjustl(bday))//
     &                  '_0_dims.dat'
        TIMERAMP21='timeramp_d'//trim(adjustl(bday))//
     &                  '_1_dims.dat'
        !-------------------------------------------------------
--------
        ! Time-varying zonal mean state;
        ! read in first two records
        ! to set up cubic spline interpolation
        !-------------------------------------------------------
--------
        IF (MYPE.EQ.0) print *, '* READING FILE: ', UA10
        CALL READCLIM(UA10,NL,.FALSE.,uan10)
        IF (MYPE.EQ.0) print *, '* READING FILE: ', UA11
        CALL READCLIM(UA11,NL,.FALSE.,uan11)
        IF (MYPE.EQ.0) print *, '* READING FILE: ', UA20
        CALL READCLIM(UA20,NL,.FALSE.,uan20)
        IF (MYPE.EQ.0) print *, '* READING FILE: ', UA21
        CALL READCLIM(UA21,NL,.FALSE.,uan21)

        IF (MYPE.EQ.0) print *, '* READING FILE: ', VA10
        CALL READCLIM(VA10,NL,.FALSE.,van10)
        IF (MYPE.EQ.0) print *, '* READING FILE: ', VA11
        CALL READCLIM(VA11,NL,.FALSE.,van11)
        IF (MYPE.EQ.0) print *, '* READING FILE: ', VA20
        CALL READCLIM(VA20,NL,.FALSE.,van20)
        IF (MYPE.EQ.0) print *, '* READING FILE: ', VA21
        CALL READCLIM(VA21,NL,.FALSE.,van21)

        IF (MYPE.EQ.0) print *, '* READING FILE: ', T10
        CALL READCLIM(T10,NL,.FALSE.,tn10)
        IF (MYPE.EQ.0) print *, '* READING FILE: ', T11
        CALL READCLIM(T11,NL,.FALSE.,tn11)
        IF (MYPE.EQ.0) print *, '* READING FILE: ', T20
        CALL READCLIM(T20,NL,.FALSE.,tn20)
        IF (MYPE.EQ.0) print *, '* READING FILE: ', T21
        CALL READCLIM(T21,NL,.FALSE.,tn21)

        IF (MYPE.EQ.0) print *, '* READING FILE: ', SP10
        CALL READCLIM(SP10,1,.FALSE.,spn10)
        IF (MYPE.EQ.0) print *, '* READING FILE: ', SP11
        CALL READCLIM(SP11,1,.FALSE.,spn11)
        IF (MYPE.EQ.0) print *, '* READING FILE: ', SP20
        CALL READCLIM(SP20,1,.FALSE.,spn20)
```

```
        IF (MYPE.EQ.0) print *, '* READING FILE: ', SP21
        CALL READCLIM(SP21,1,.FALSE.,spn21)

        IF (MYPE.EQ.0) print *, '* READING FILE: ', DUM10
        CALL READCLIM(DUM10,NL,.FALSE.,dumn10)
        IF (MYPE.EQ.0) print *, '* READING FILE: ', DUM11
        CALL READCLIM(DUM11,NL,.FALSE.,dumn11)
        IF (MYPE.EQ.0) print *, '* READING FILE: ', DUM20
        CALL READCLIM(DUM20,NL,.FALSE.,dumn20)
        IF (MYPE.EQ.0) print *, '* READING FILE: ', DUM21
        CALL READCLIM(DUM21,NL,.FALSE.,dumn21)

        IF (MYPE.EQ.0) print *, '* READING FILE: ', TIMERAMP10
        CALL READCLIM(DUM10,NL,.FALSE.,timerampn10)
        IF (MYPE.EQ.0) print *, '* READING FILE: ', TIMERAMP11
        CALL READCLIM(DUM11,NL,.FALSE.,timerampn11)
        IF (MYPE.EQ.0) print *, '* READING FILE: ', TIMERAMP20
        CALL READCLIM(DUM20,NL,.FALSE.,timerampn20)
        IF (MYPE.EQ.0) print *, '* READING FILE: ', TIMERAMP21
        CALL READCLIM(DUM21,NL,.FALSE.,timerampn21)

        !-------------------------------------------------------
--------
        ! Write all the data in UNDGI etc. onto PEs
        ! uan10/11 and uan20/21 are : uan10(NL,MGx,NHEM,JGy)
        ! UNDGI2/3 and UNDGJ2/3 are : UNDGI2(NL,MGx,NHEM,JGy)
        ! Fill UNDG arrays with values from uan arrays ...
        ! Need to multiply by cos lat and non-dimnesionalise
        !-------------------------------------------------------
--------
         DO IM=1,JGyy(iRow)
          DO IHEM=1,NHEM
           DO IN=1,MGxx(iCol)
            DO L=1,NL
            UNDGI2(L,IN,IHEM,IM) =
     &         (uan10(L,IN,IHEM,IM))*
     &          (CS(JJ1(iRow)+IM,1)/CV)

            UNDGI3(L,IN,IHEM,IM) =
     &         (uan11(L,IN,IHEM,IM))*
     &          (CS(JJ1(iRow)+IM,1)/CV)

            UNDGJ2(L,IN,IHEM,IM) =
     &         (uan20(L,IN,IHEM,IM))*
     &          (CS(JJ1(iRow)+IM,1)/CV)

            UNDGJ3(L,IN,IHEM,IM) =
     &         (uan21(L,IN,IHEM,IM))*
     &          (CS(JJ1(iRow)+IM,1)/CV)

            VNDGI2(L,IN,IHEM,IM) =
     &         (van10(L,IN,IHEM,IM))*
     &          (CS(JJ1(iRow)+IM,1)/CV)

            VNDGI3(L,IN,IHEM,IM) =
     &         (van11(L,IN,IHEM,IM))*
     &          (CS(JJ1(iRow)+IM,1)/CV)

            VNDGJ2(L,IN,IHEM,IM) =
```

```
&         (van20(L,IN,IHEM,IM))*
&          (CS(JJ1(iRow)+IM,1)/CV)

       VNDGJ3(L,IN,IHEM,IM) =
&         (van21(L,IN,IHEM,IM))*
&          (CS(JJ1(iRow)+IM,1)/CV)


       TNDGI2(L,IN,IHEM,IM) =
&         ((tn10(L,IN,IHEM,IM)
&         + 273.15 - 250.0)
&          /CT)

    TNDGI3(L,IN,IHEM,IM) =
&         tn11(L,IN,IHEM,IM)
&          /CT

       TNDGJ2(L,IN,IHEM,IM) =
&         ((tn20(L,IN,IHEM,IM)
&         + 273.15 - 250.0)
&           /CT)


       TNDGJ3(L,IN,IHEM,IM) =
&         tn21(L,IN,IHEM,IM)
&          /CT

       SPNDGI2(1,IN,IHEM,IM) =
&         (spn10(1,IN,IHEM,IM))
&          /1.0E5

       SPNDGI3(1,IN,IHEM,IM) =
&         spn11(1,IN,IHEM,IM)
&          /1.0E5

       SPNDGJ2(1,IN,IHEM,IM) =
&         (spn20(1,IN,IHEM,IM))
&          /1.0E5

       SPNDGJ3(1,IN,IHEM,IM) =
&         spn21(1,IN,IHEM,IM)
&          /1.0E5

       DUMNDGI2(L,IN,IHEM,IM) =
&         dumn10(L,IN,IHEM,IM)
       DUMNDGI3(L,IN,IHEM,IM) =
&         dumn11(L,IN,IHEM,IM)
       DUMNDGJ2(L,IN,IHEM,IM) =
&         dumn20(L,IN,IHEM,IM)
       DUMNDGJ3(L,IN,IHEM,IM) =
&         dumn21(L,IN,IHEM,IM)

       TIMERAMPNDGI2(L,IN,IHEM,IM) =
&         timerampn10(L,IN,IHEM,IM)
       TIMERAMPNDGI3(L,IN,IHEM,IM) =
&         timerampn11(L,IN,IHEM,IM)
       TIMERAMPNDGJ2(L,IN,IHEM,IM) =
&         timerampn20(L,IN,IHEM,IM)
       TIMERAMPNDGJ3(L,IN,IHEM,IM) =
```

```
     &        timerampn21(L,IN,IHEM,IM)

          ENDDO
         ENDDO
        ENDDO
        ENDDO
       ENDIF

       END

*/
*/ ---------------------------------------
*/ Add READNDG
*/ Reads in subsequent records for time-
*/ dependent nudging reference states
*/ ---------------------------------------
*/
*/
*/ --- Now call READNDG in main program ---
*/ --- MLTRI and add READNDG subroutine code ---
*/

*D OUTCON.16
     &          ,KOUTE,KOUTH,KOUTR,KINND,KINN
*I OUTCON.41
       INTEGER :: KINND
       INTEGER :: KINN
       REAL :: NDGI
       REAL :: NDGJ
       REAL :: NDGI3
       REAL :: NDGJ3
       REAL :: NDFAC
       REAL :: DUM
       REAL :: TIMERAMP
       COMPLEX :: REF
,REF0,REFT

*D OUTCON.7
     &
,TOUT2,LSPO,LGPO,NDGI,NDGJ,NDGI3,NDGJ3,UNDGI2,UNDGI3,UNDGJ2,
     &
UNDGJ3,LNUDGGP,KMX,KMN,TAUND,DNDMAX,SPNUDG,DUMNDGI2,DUMNDGI3,
     &
DUMNDGJ2,DUMNDGJ3,NDFAC,REF,REF0,DUM,VNDGI2,VNDGI3,VNDGJ2,
     &  VNDGJ3,TNDGI2,TNDGI3,TNDGJ2,TNDGJ3,SPNDGI2,SPNDGI3,
     &  SPNDGJ2,SPNDGJ3,DNUDG,REFT,TIMERAMPNDGI2,TIMERAMPNDGI3,
     &  TIMERAMPNDGJ2,TIMERAMPNDGJ3,TIMERAMP



*I MGRMLT.18
*CALL OUTCON
*CALL RESTOR
*CALL BATS

*I MGRMLT.41

!--------------TEST-------------TEST--------
!-----------------------------------------
```

```
! Calling READNDG to make adjustments to PLG3
!-------------------------------------------
!-------------------------------------------


            KINN=MOD(KOUNT,ITSPD)
            IF (KINN.EQ.0) KINN=ITSPD
!               PRINT *,'KINN=',KINN
            IF (KINND.GT.0.AND.KINN.EQ.KINND) THEN
               CALL READNDG
            ENDIF
            IF (KINND.GT.0) THEN
               NDGI=REAL(KINN)/REAL(KINND)
               NDGI3=(NDGI**3 - NDGI)/6.
               NDGJ=1.-NDGI
               NDGJ3=(NDGJ**3 - NDGJ)/6.
            ENDIF

*I DGRMLT.125
            !-------------------------------------------------
            ! Update zonal mean nudging, cubic spline
            ! interpolating factors, for time-dependent nudging
            ! reference states
            !-------------------------------------------------

            KINN=MOD(KOUNT,ITSPD)
            IF (KINN.EQ.0) KINN=ITSPD
!               PRINT *,'KINN=',KINN
            IF (KINND.GT.0.AND.KINN.EQ.KINND) THEN
               CALL READNDG
            ENDIF
            IF (KINND.GT.0) THEN
               NDGI=REAL(KINN)/REAL(KINND)
               NDGI3=(NDGI**3 - NDGI)/6.
               NDGJ=1.-NDGI
               NDGJ3=(NDGJ**3 - NDGJ)/6.
            ENDIF


*DECK READNDG
!=====================================================
! Read subsequent record for nudging reference state
!=====================================================
      SUBROUTINE READNDG
      IMPLICIT NONE
!
*CALL PARAM1
*CALL PARAM2
*CALL PARAM3
*CALL BLANK
*CALL MPIDECK
*CALL BATS
*CALL RESTOR
*CALL OUTCON
*CALL LEGAU
!-----------------------------------------------------
! Local variables
!-----------------------------------------------------
! End of nudg.bin file error variable
```

```
      INTEGER :: IOS
! Loop variable
      INTEGER :: I,II,iCol2,iRow2,L,IHEM,J,iPe,IM,IN
      INTEGER :: JH
      INTEGER :: countLHEM,countHEM,countJ
! MPI variables
      INTEGER, PARAMETER :: TagRef=10000
! Nudging variables
      REAL :: RNT1,RNT2
      REAL :: DOY1
      COMPLEX :: UU,VV,UUU,VVV
      COMPLEX :: AA,BB,CC,SS,RR,TT
      COMPLEX :: ABC,DEF
      character*3 :: dy
      character*31 :: UA20,UA21,DUM20,DUM21
      character*31 :: TIMERAMP20,TIMERAMP21
      character*31 :: VA20,VA21,T20,T21,SP20,SP21

      REAL :: uan20(NL,MGx,NHEM,JGy)
      REAL :: uan21(NL,MGx,NHEM,JGy)

      REAL :: van20(NL,MGx,NHEM,JGy)
      REAL :: van21(NL,MGx,NHEM,JGy)
      REAL :: tn20(NL,MGx,NHEM,JGy)
      REAL :: tn21(NL,MGx,NHEM,JGy)
      REAL :: spn20(1,MGx,NHEM,JGy)
      REAL :: spn21(1,MGx,NHEM,JGy)

      REAL :: dumn20(NL,MGx,NHEM,JGy)
      REAL :: dumn21(NL,MGx,NHEM,JGy)

      REAL :: timerampn20(NL,MGx,NHEM,JGy)
      REAL :: timerampn21(NL,MGx,NHEM,JGy)

      !-------------------------------------------------------------
--------
      ! If a nudging run read in next record and update linear
      ! interpolation parameter
      !-------------------------------------------------------------
--------
      IF (LNUDGGP) THEN
        !-----------------------------------------------------------
--------
        ! Read in on PE 0
        !-----------------------------------------------------------
--------
         DOY1=DOY-1
         WRITE(dy, '(i3)') NINT(DOY1)

         UA20='ua_d'//trim(adjustl(dy))//
     &                '_0_dims.dat'
         IF (MYPE.EQ.0) print *, '* READING FILE: ', UA20
         CALL READCLIM(UA20,NL,.FALSE.,uan20)
         UA21='ua_d'//trim(adjustl(dy))//
     &                '_1_dims.dat'
         IF (MYPE.EQ.0) print *, '* READING FILE: ', UA21
         CALL READCLIM(UA21,NL,.FALSE.,uan21)

         VA20='va_d'//trim(adjustl(dy))//
```

```
     &                '_0_dims.dat'
          IF (MYPE.EQ.0) print *, '* READING FILE: ', VA20
          CALL READCLIM(VA20,NL,.FALSE.,van20)
          VA21='va_d'//trim(adjustl(dy))//
     &                '_1_dims.dat'
          IF (MYPE.EQ.0) print *, '* READING FILE: ', VA21
          CALL READCLIM(VA21,NL,.FALSE.,van21)

          T20='temp_d'//trim(adjustl(dy))//
     &                '_0_dims.dat'
          IF (MYPE.EQ.0) print *, '* READING FILE: ', T20
          CALL READCLIM(T20,NL,.FALSE.,tn20)
          T21='temp_d'//trim(adjustl(dy))//
     &                '_1_dims.dat'
          IF (MYPE.EQ.0) print *, '* READING FILE: ', T21
          CALL READCLIM(T21,NL,.FALSE.,tn21)

          SP20='ps_d'//trim(adjustl(dy))//
     &                '_0_dims.dat'
          IF (MYPE.EQ.0) print *, '* READING FILE: ', SP20
          CALL READCLIM(SP20,1,.FALSE.,spn20)
          SP21='ps_d'//trim(adjustl(dy))//
     &                '_1_dims.dat'
          IF (MYPE.EQ.0) print *, '* READING FILE: ', SP21
          CALL READCLIM(SP21,1,.FALSE.,spn21)

          DUM20='dum_d'//trim(adjustl(dy))//
     &                '_0_dims.dat'
          IF (MYPE.EQ.0) print *, '* READING FILE: ', DUM20
          CALL READCLIM(DUM20,NL,.FALSE.,dumn20)
          DUM21='dum_d'//trim(adjustl(dy))//
     &                '_1_dims.dat'
          IF (MYPE.EQ.0) print *, '* READING FILE: ', DUM21
          CALL READCLIM(DUM21,NL,.FALSE.,dumn21)

          TIMERAMP20='timeramp_d'//trim(adjustl(dy))//
     &                 '_0_dims.dat'
          IF (MYPE.EQ.0) print *, '* READING FILE: ', TIMERAMP20
          CALL READCLIM(TIMERAMP20,NL,.FALSE.,timerampn20)
          TIMERAMP21='timeramp_d'//trim(adjustl(dy))//
     &                 '_1_dims.dat'
          IF (MYPE.EQ.0) print *, '* READING FILE: ', TIMERAMP21
          CALL READCLIM(TIMERAMP21,NL,.FALSE.,timerampn21)


         !-------------------------------------------------------
--------
         ! Write all the data in ZNDGI etc. onto PEs
         !-------------------------------------------------------
--------
          DO IM=1,JGyy(iRow)
           DO IHEM=1,NHEM
            DO IN=1,MGxx(iCol)
             DO L=1,NL
                 UNDGJ2(L,IN,IHEM,IM) = (uan20(L,IN,IHEM,IM))*
     &          (CS(JJ1(iRow)+IM,1)/CV)

                 UNDGJ3(L,IN,IHEM,IM) = (uan21(L,IN,IHEM,IM))*
     &          (CS(JJ1(iRow)+IM,1)/CV)
```

```
                VNDGJ2(L,IN,IHEM,IM) =
     &                 (van20(L,IN,IHEM,IM))*
     &          (CS(JJ1(iRow)+IM,1)/CV)

                VNDGJ3(L,IN,IHEM,IM) =
     &                 (van21(L,IN,IHEM,IM))*
     &          (CS(JJ1(iRow)+IM,1)/CV)

                TNDGJ2(L,IN,IHEM,IM) =
     &                 ((tn20(L,IN,IHEM,IM)
     &                 + 273.15 - 250.0)
     &            /CT)

                TNDGJ3(L,IN,IHEM,IM) =
     &                 tn21(L,IN,IHEM,IM)
     &                          /CT

                SPNDGJ2(1,IN,IHEM,IM) =
     &                 (spn20(1,IN,IHEM,IM))
     &                           /1.0E5
                SPNDGJ3(1,IN,IHEM,IM) =
     &                 spn21(1,IN,IHEM,IM)
     &                           /1.0E5


                DUMNDGJ2(L,IN,IHEM,IM) = dumn20(L,IN,IHEM,IM)
                DUMNDGJ3(L,IN,IHEM,IM) = dumn21(L,IN,IHEM,IM)

                TIMERAMPNDGJ2(L,IN,IHEM,IM) =
timerampn20(L,IN,IHEM,IM)
                TIMERAMPNDGJ3(L,IN,IHEM,IM) =
timerampn21(L,IN,IHEM,IM)


            ENDDO
           ENDDO
          ENDDO
         ENDDO
         !-------------------------------------------------------
--------
         ! Need to swap UNDGI etc and UNDGJ etc arrays
         ! around so the I's contain the most recent
         ! record and J's contain the previous record
         !-------------------------------------------------------
--------
          DO IHEM=1,NHEM
           DO IM=1,JGyy(iRow)
            DO IN=1,MGxx(iCol)
             DO L=1,NL
             UU=UNDGI2(L,IN,IHEM,IM)
             UNDGI2(L,IN,IHEM,IM)=UNDGJ2(L,IN,IHEM,IM)
             UNDGJ2(L,IN,IHEM,IM)=UU

             VV=UNDGI3(L,IN,IHEM,IM)
             UNDGI3(L,IN,IHEM,IM)=UNDGJ3(L,IN,IHEM,IM)
             UNDGJ3(L,IN,IHEM,IM)=VV
!
```

```
              RR=VNDGI2(L,IN,IHEM,IM)
              VNDGI2(L,IN,IHEM,IM)=VNDGJ2(L,IN,IHEM,IM)
              VNDGJ2(L,IN,IHEM,IM)=RR

              SS=VNDGI3(L,IN,IHEM,IM)
              VNDGI3(L,IN,IHEM,IM)=VNDGJ3(L,IN,IHEM,IM)
              VNDGJ3(L,IN,IHEM,IM)=SS
!

              TT=TNDGI2(L,IN,IHEM,IM)
              TNDGI2(L,IN,IHEM,IM)=TNDGJ2(L,IN,IHEM,IM)
              TNDGJ2(L,IN,IHEM,IM)=TT

              AA=TNDGI3(L,IN,IHEM,IM)
              TNDGI3(L,IN,IHEM,IM)=TNDGJ3(L,IN,IHEM,IM)
              TNDGJ3(L,IN,IHEM,IM)=AA
!

              BB=SPNDGI2(1,IN,IHEM,IM)
              SPNDGI2(1,IN,IHEM,IM)=SPNDGJ2(1,IN,IHEM,IM)
              SPNDGJ2(1,IN,IHEM,IM)=BB

              CC=SPNDGI3(1,IN,IHEM,IM)
              SPNDGI3(1,IN,IHEM,IM)=SPNDGJ3(1,IN,IHEM,IM)
              SPNDGJ3(1,IN,IHEM,IM)=CC
!

              UUU=DUMNDGI3(L,IN,IHEM,IM)
              DUMNDGI3(L,IN,IHEM,IM)=DUMNDGJ3(L,IN,IHEM,IM)
              DUMNDGJ3(L,IN,IHEM,IM)=UUU

              VVV=DUMNDGI3(L,IN,IHEM,IM)
              DUMNDGI3(L,IN,IHEM,IM)=DUMNDGJ3(L,IN,IHEM,IM)
              DUMNDGJ3(L,IN,IHEM,IM)=VVV

              ABC=TIMERAMPNDGI3(L,IN,IHEM,IM)

TIMERAMPNDGI3(L,IN,IHEM,IM)=TIMERAMPNDGJ3(L,IN,IHEM,IM)
              TIMERAMPNDGJ3(L,IN,IHEM,IM)=ABC

              DEF=TIMERAMPNDGI3(L,IN,IHEM,IM)

TIMERAMPNDGI3(L,IN,IHEM,IM)=TIMERAMPNDGJ3(L,IN,IHEM,IM)
              TIMERAMPNDGJ3(L,IN,IHEM,IM)=DEF

            ENDDO
           ENDDO
          ENDDO
         ENDDO

       ENDIF

       END

*/
*/ ---------------------------------------
*/ Edit DGRMLT to include nudging
*/ Applies nudging in grid-point space
*/ ---------------------------------------
```

```
*/
*/ --- Add required nudging parameters ---
*/
*I DGRMLT.176

      !-------------------------------------------------------
--------
      ! Apply nudging in grid point space
      ! DOY (Day of year) sets calendar days over which nudging
is
      ! switched on
      ! DAY.GE. sets nudging to start in first winter (not
immediately)
      !-------------------------------------------------------
--------
      IF (LNUDGGP) THEN
       IF (DOY.LE.90.OR.DOY.GE.300) THEN
       IF (DAY.GE.72451) THEN
       !-------------------------------------------------------
--------
       ! Nudging applies across all zonal wavenumbers
       !-------------------------------------------------------
--------
       IF (DAY.GT.DNDMAX.OR.DNDMAX.LE.0.) THEN
        NDFAC = 1.
       ELSE IF (DAY.GT.0) THEN
        NDFAC = SIN(PI*DAY/(2*DNDMAX))**2
       ELSE
        NDFAC = 0.
       END IF
       !-------------------------------------------------------
--------
       ! Loop
       !-------------------------------------------------------
--------

         DO L=1,NL
          DO IHEM=1,NHEM
            DO I=1,MGxx(iCol)
             DUM=NDGI*DUMNDGI2(L,I,IHEM,JH) +
     &          NDGI3*DUMNDGI3(L,I,IHEM,JH) +
     &          NDGJ*DUMNDGJ2(L,I,IHEM,JH) +
     &          NDGJ3*DUMNDGJ3(L,I,IHEM,JH)

             TIMERAMP=NDGI*TIMERAMPNDGI2(L,I,IHEM,JH) +
     &          NDGI3*TIMERAMPNDGI3(L,I,IHEM,JH) +
     &          NDGJ*TIMERAMPNDGJ2(L,I,IHEM,JH) +
     &          NDGJ3*TIMERAMPNDGJ3(L,I,IHEM,JH)

             REF=NDGI*UNDGI2(L,I,IHEM,JH) +
     &          NDGI3*UNDGI3(L,I,IHEM,JH) +
     &          NDGJ*UNDGJ2(L,I,IHEM,JH) +
     &          NDGJ3*UNDGJ3(L,I,IHEM,JH)

            FUG3(I,IHEM,JH,L) = FUG3(I,IHEM,JH,L)
     &          -(NDFAC*DNUDG(L)*TIMERAMP*DUM*(UG3(I,IHEM,JH,L)-
REF))
```

```
              REF=NDGI*VNDGI2(L,I,IHEM,JH) +
     &           NDGI3*VNDGI3(L,I,IHEM,JH) +
     &           NDGJ*VNDGJ2(L,I,IHEM,JH) +
     &           NDGJ3*VNDGJ3(L,I,IHEM,JH)

             FVG3(I,IHEM,JH,L) = FVG3(I,IHEM,JH,L)
     &           -(NDFAC*DNUDG(L)*TIMERAMP*DUM*(VG3(I,IHEM,JH,L)-
REF))

             REFT=NDGI*TNDGI2(L,I,IHEM,JH) +
     &           NDGI3*TNDGI3(L,I,IHEM,JH) +
     &           NDGJ*TNDGJ2(L,I,IHEM,JH) +
     &           NDGJ3*TNDGJ3(L,I,IHEM,JH)


             TNLG3(I,IHEM,JH,L) = TNLG3(I,IHEM,JH,L)
     &           -(NDFAC*DNUDG(L)*TIMERAMP*DUM*
     &                   (TG3(I,IHEM,JH,L)-T0(L)-REFT))


              ENDDO
             ENDDO
            ENDDO

      ENDIF
      ENDIF
      ENDIF

*/
*/ ---------------------------------------
*/ Edit MGRMLT to include nudging
*/ Applies nudging to VPG3 grid-point space
*/ ---------------------------------------
*/
*/ --- Add required nudging parameters ---
*/
*I MGRMLT.102

      !-------------------------------------------------------------
--------
      ! Apply nudging in grid point space
      ! DOY (Day of year) sets calendar days over which nudging
is
      ! switched on
      ! DAY.GE. sets nudging to start in first winter (not
immediately)
      !-------------------------------------------------------------
--------
      IF (LNUDGGP) THEN
       IF (DOY.LE.90.OR.DOY.GE.300) THEN
       IF (DAY.GE.72451) THEN
       !-------------------------------------------------------------
--------
       ! Nudging applies across all zonal wavenumbers
       !-------------------------------------------------------------
--------
       IF (DAY.GT.DNDMAX.OR.DNDMAX.LE.0.) THEN
        NDFAC = 1.
       ELSE IF (DAY.GT.0) THEN
```

```
         NDFAC = SIN(PI*DAY/(2*DNDMAX))**2
        ELSE
         NDFAC = 0.
        END IF
        !-------------------------------------------------------
--------
        ! Loop
        !-------------------------------------------------------
--------
             DO I=1,MGxx(iCol)
              DUM=NDGI*DUMNDGI2(NL-1,I,IHEM,J) +
     &           NDGI3*DUMNDGI3(NL-1,I,IHEM,J) +
     &           NDGJ*DUMNDGJ2(NL-1,I,IHEM,J) +
     &           NDGJ3*DUMNDGJ3(NL-1,I,IHEM,J)

              TIMERAMP=NDGI*TIMERAMPNDGI2(NL-1,I,IHEM,J) +
     &           NDGI3*TIMERAMPNDGI3(NL-1,I,IHEM,J) +
     &           NDGJ*TIMERAMPNDGJ2(NL-1,I,IHEM,J) +
     &           NDGJ3*TIMERAMPNDGJ3(NL-1,I,IHEM,J)

              REF=NDGI*SPNDGI2(1,I,IHEM,J) +
     &           NDGI3*SPNDGI3(1,I,IHEM,J) +
     &           NDGJ*SPNDGJ2(1,I,IHEM,J) +
     &           NDGJ3*SPNDGJ3(1,I,IHEM,J)

             VPG3(I,IHEM,J)=VPG3(I,IHEM,J)
     &           +(NDFAC*SPNUDG*TIMERAMP*DUM*
     &            (SPG3(I,IHEM,J)-(REF-1.0)))

          ENDDO
       ENDIF
       ENDIF
       ENDIF
/EOF
#
############################################## NAMELIST DATA.
#
cat  <<  /EOF  >  $EXPDIR/data.template
 &INPPL
 &END
 &INPRN
 DAYS=dummy_NDAYS2RUN,
 BEGDAY=dummy_BEGDAY,
 KITS=0,
 TSPD=72,
 PNU=0.02,
 TDISS=0.166666666667,
 NDEL=6,
 BEGDOY=0.0,
 LFLUX=.TRUE.,
 LSTRETCH=.TRUE.,
 L22L=.FALSE.,LCLIM=.FALSE.,LPERPET=.FALSE.,LOROG=.TRUE.,
 LSHORT=.FALSE.,LBALAN=.FALSE.,
 LRSTRT=dummy_LRSTRT,
 LRESTIJ=.FALSE.,
 LNOISE=.FALSE.,
 LMASCOR=.TRUE.,LMASPRT=.FALSE.,LMASOLD=dummy_LMASOLD
 &END
 &INPOP
```

```
 RNTAPE=1.0,
 DAYP=10,
 NCKNTIN=dummy_OUTPUTEVERY,
 DAYH=dummy_AOUTPUTEVERY,
 DAYR=dummy_RESTARTEVERY,
 KOUNTE=1,
 NLAT=32,
 NTRACO=1,RNTAPO=1.0
 &END
 &INPHYS
LBL=.TRUE.,LCR=.TRUE.,LLR=.TRUE.,LCUBM=.TRUE.,LCBADJ=.TRUE.,
      LRD=.TRUE.,LVD=.TRUE.,LSL=.TRUE.,LOC=.TRUE.,
      LNOICE=.FALSE.,LOLDBL=.FALSE.,LNNSK=.TRUE.,LCOND=.FALSE.
 &END
 &INMORCGAS VMRCO2=285.0E-6,VMRCH4=0.70E-6,VMRN2O=270.0E-9,
      VMRCFC11=0.0,VMRCFC12=0.0,NEXOTIC=.TRUE.
 &END
 &INPRS
 &END
 &INPRSIJ
 &END
 &INPBL
 KBAL=0,LTBAL=.FALSE.,TMEAN=20*250.0
 &END
 &INQ LRH=.FALSE., LNSURF=.FALSE.
 &END
 &INNUDG LNUDG=.FALSE.,LNUDGGP=.TRUE.,KINND=72,
      KMX=0.92000,KMN=0.16983,TAUND=6.0
 &END
/EOF
#
############################################## ERROR PROCESSING
FUNCTION.
#
ABORT ()
{
echo '!!!!!!!!!! ERROR PROCESSING !!!!!!!!!!'
set +e
\cp fort.2 $EXPDIR/results_fail
exit 1
}
#
############################################### COMPILE PROGRAM.
#
cd $COMPDIR

if [ $COMPILE = yes ]
then
    fc='mpif90'
    fflags='-i4 -r8 -O3 -xHOST -align -fp-model source  -fpe0 -
traceback'

# Spinup
   $NUPDATE  -p ${ProgLib}  -c igcm4_mpi_spin     \
            -i updates_spin                      \
            -f -o sq -s igcm4_mpi.src      ||  ABORT NUPDATE
    $fc $fflags -c igcm4_mpi_spin.f -I$NETCDFINC -I$MPIINC ||
ABORT $fc
```

```
  # linking bit
    $fc $fflags -o $EXPDIR/${EXEC}_spin \
      $OASISCLIMDIR/Clim/*.o \
      igcm4_mpi_spin.o \
      -L$KD \
      -lsun'fft1' -lsun'blas1' -lsun'util1' \
      -lsun'aux1' \
      -L$NETCDFLIB -lhdf5 -lhdf5_hl -lcurl -lnetcdff -lnetcdf -
L$PVMLIB -lfpvm3 -lgpvm3 -lpvm3\
      -L$MPILIB -lmpi || ABORT ${FC}


# Restart
   $NUPDATE  -p ${ProgLib}  -c igcm4_mpi_cont     \
            -i updates_cont                      \
            -f -o sq -s igcm4_mpi.src      ||  ABORT NUPDATE
    $fc $fflags -c igcm4_mpi_cont.f -I$NETCDFINC -I$MPIINC ||
ABORT $fc

  # linking bit
    $fc $fflags -o $EXPDIR/${EXEC}_cont \
      $OASISCLIMDIR/Clim/*.o \
      igcm4_mpi_cont.o \
      -L$KD \
      -lsun'fft1' -lsun'blas1' -lsun'util1' \
      -lsun'aux1' \
      -L$NETCDFLIB -lhdf5 -lhdf5_hl -lcurl -lnetcdff -lnetcdf -
L$PVMLIB -lfpvm3 -lgpvm3 -lpvm3\
      -L$MPILIB -lmpi || ABORT ${FC}

fi


cd $EXPDIR
echo "Making links:" $PWD
     [ -r climdata ] && \rm -f climdata/*.dat
     ln -s $CLIMDIR/*.dat climdata

     [ -r orogdata ] && \rm -f orogdata
     ln -s $OROGDIR orogdata

     [ -f input.dat ] && \rm -f input.dat
     \cp $INIDATA/restart.12 input.dat
     [ -f RestartSurface.dat ] && \rm -f RestartSurface.dat
     \cp $INIDATA/restart.17 RestartSurface.dat

     [ -f column.dat ] && \rm -f column.dat
     [ -f vegetation.dat ] && \rm -f vegetation.dat
     ln -s $INIDATA/vegetation.260x32.171011 vegetation.dat
     [ -f flxocean ] && \rm -f flxocean
     \cp $INIDATA/flxocean flxocean
     [ -f topog_gwd.dat ] && \rm -f topog_gwd.dat
     ln -s $INIDATA/topog_gwd.T42.dat topog_gwd.dat

     ln -s $NUDGREF/*.dat climdata

# before running keep a copy of this runscript in the output
directory
      cp $RPATH/source/igcm4/$0 $EXPDIR/
```

```
      cp $COMPDIR/igcm4_mpi_????.f $EXPDIR/
  exit 0                                          # Successful
termination.
#
############################################## END OF JOB.
```